DISSERTATION

Twin-atom beam generation in a one-dimensional Bose gas

Ausgeführt zum Zwecke der Erlangung des akademischen Grades eines Doktors der Naturwissenschaften

unter der Leitung von

o. Univ.-Prof. Dipl.-Ing. Dr. techn. Hannes-Jörg Schmiedmayer

E141, Atominstitut

eingereicht an der Technischen Universität Wien
Fakultät für Physik

von

Dipl.-Phys. Robert Bücker

Matrikelnummer: 0746192
Lerchenfelder Str. 88-90/15, 1080 Wien

Wien, am 30. Jänner 2013

Robert Bücker

Gutachter:

Jörg Schmiedmayer

Christoph Westbrook

Abstract

One of the most fascinating aspects of quantum physics is particle-wave duality, leading to striking analogies in the behavior of light and matter. Wave-like phenomena of matter on a macroscopic scale are especially pronounced in quantum-degenerate atomic gases. In these, strongly populated matter-wave modes give rise to coherence properties resembling those of laser light, enabling interferometry and homodyne measurements with Bose-Einstein condensates. In recent years, numerous experiments and theory proposals have been developed to extend this analogy into the realm of quantum optics, highlighting the complex interplay of wave and particle aspects of a degenerate atom gas. In quantum optics, a powerful theory framework is readily available, and numerous ground-breaking experiments with non-classical light have been performed. The realization of similar experiments using matter waves holds promise for both fundamental tests of quantum mechanics, and future metrology applications. This approach is promoted by the intrinsic atom-atom interactions in a condensate, that allow to efficiently access non-classical quantum states, without the need for non-linear media as in light optics.

In this thesis, a scheme to generate twin-atom beams, confined to a one-dimensional wave-guide geometry on an atom chip, was realized. The twin beams emerge from a degenerate one-dimensional Bose gas, propagate as wave packets with opposite momenta, and show quantum correlations that ideally lead to complete suppression of relative population fluctuations (number squeezing). This process, which operates in a strongly Bose-enhanced regime, is in close analogy to twin-photon beam generation in an optical parametric oscillator, a key tool in both fundamental and applied photonics. In our experiment, using time-of-flight fluorescence imaging, almost perfect number squeezing between the twin beams is observed, for the first time in the regime of high mode population. Furthermore, the dynamics of the stimulated twin-beam emission is analyzed quantitatively, and good agreement with a newly developed theoretical model is found.

In analogy to a pumped gain medium in optics, the starting point of the twin-beam emission process is a population-inverted state in the transverse vibrational degree of freedom of the elongated confinement. The preparation and characterization of this source state, which resembles a Fock state of a single-particle system, is the second main result of this thesis. To reach the pumped state, we apply a purely mechanical technique, where the transverse wave function of the condensate is controlled by displacement of the anharmonic trapping potential. The precise trajectory of the trap motion is obtained from quantum optimal control theory, which has been applied to the excitation of a condensate for the first time. By time-resolved observation of the system response, excellent agreement between experiment and theory, and a near-unit efficiency of the excitation process is obtained. Also, an effective two-level description is developed, that allows to capture the dynamics in an intuitive way.

The availability of quantum-correlated twin-atom beams opens up a plethora of research opportunities towards strongly entangled many-body states, enabling both fundamental experiments, and quantum-enhanced metrology techniques.

Zusammenfassung

Einer der faszinierendsten Aspekte der Quantenphysik ist der Teilchen-Welle-Dualismus, der zahlreiche Analogien im Verhalten von Licht und Materie zur Folge hat. Wellenartige Phänomene auf makroskopischer Skala treten insbesondere in quantenentarteten Atomgasen auf. Dort führen stark besetzte Materiewellen-Moden zu Kohärenzeigenschaften ähnlich denen eines Lasers, was Experimente wie Interferometrie und Homodyn-Messungen ermöglicht. In den letzten Jahren wurden zahlreiche Experimente und Theorievorschläge entwickelt, um diese Analogie in den Bereich der Quantenoptik auszudehnen, wo das komplexe Zusammenspiel zwischen Wellen- und Teilchenaspekten des entarteten Atomgases besonders klar hervortritt. Die Quantenoptik liefert hierzu mächtige Theoriewerkzeuge, und viele bahnbrechende Experimente wurden mit nichtklassischem Licht durchgeführt. Die Umsetzung solcher Experimente mit Materiewellen verspricht sowohl fundamentale Tests der Quantenmechanik, als auch neuartige Messverfahren. Dieser Ansatz wird durch die intrinsichen Atom-Atom-Wechselwirkungen in einem Kondensat begünstigt, die nichtklassische Zustände zugänglich machen, ohne dass, wie in der Lichtoptik, ein nichtlineares Medium benötigt wird.

In dieser Dissertation wurde ein experimentelles Schema zur Erzeugung von Strahlen aus Zwillingsatomen, die in einer Wellenleiter-Geometrie gefangen sind, implementiert. Die Zwillingsstrahlen entstehen in einem entarteten, eindimensionalen Bose-Gas, bewegen sich von dort aus mit entgegengesetztem Impuls, und weisen Quantenkorrelationen auf, die im Idealfall zu vollständig unterdrückten Fluktuationen der relativen Besetzung führen (*Number Squeezing*). Dieser stark Bose-verstärkte Prozess verläuft analog zur Erzeugung von Zwillingsstrahlen aus Photonen in einem optischen parametrischen Oszillator, einem zentralen Baustein der grundlegenden und angewandten Photonik. Mit Hilfe von Flugzeit-Fluoreszenzabbildung wurde in unserem Experiment, erstmals im Regime starker Modenbesetzungen, ein nahezu perfektes *Number Squeezing* gezeigt. Weiterhin wurde die Dynamik des Emissionsprozesses untersucht, und gute Übereinstimmung mit einem neu entwickelten Modell beobachtet.

Ähnlich einem gepumpten Lasermedium, ist der Anfangszustand der Zwillingsatom-Erzeugung durch eine Besetzungsinversion gekennzeichnet, hier in den transversalen Vibrationszuständen der elongierten Falle. Die Präparation und Charakterisierung dieses Ausgangszustands ist ein zweites Hauptergebnis dieser Dissertation. Um die Vibrationsanregung zu erreichen, wurde ein rein mechanisches Schema angewandt, bei dem die transversale Wellenfunktion durch Bewegung des anharmonischen Fallenpotentials kontrolliert wird. Die Bestimmung der genauen Trajektorie erfolgte mithilfe der Theorie der optimalen Quantenkontrolle, die hierbei erstmals auf die Anregung eines Kondensates angewandt wurde. Durch zeitaufgelöste Beobachtung der Reaktion des Systems konnte exzellente Übereinstimmung zwischen Experiment und Theorie, sowie eine Anregung mit nahezu perfekter Effizienz erreicht werden. Weiterhin wird eine effektive Zweizustands-Näherung entwickelt, die die Dynamik der Anregung auf intuitive Weise beschreibt.

Die Verfügbarkeit von quantenkorrelierten Zwillingsatom-Strahlen eröffnet eine Reihe von Forschungsmöglichkeiten hin zu stark verschränkten Vielteilchenzuständen, die sowie grundlegende Experimente, als auch Messverfahren jenseits der klassischen Limits ermöglichen.

Contents

Acknowledgments

During the years I have been working at the Atominstitut, I recognized more and more that performing exciting and successful science is not about fancy lasers or elegant maths, but about collaboration, communication, and having lots of coffee with colleagues. Fortunately, conditions were optimal for me, and I am indebted to all those many people, that turned my time in Vienna into an enjoyable and inspiring experience. First of all, specials thanks go to all my past and present lab mates at the Rb-II machine for fabulous teamwork through all ups and downs, and the entire atom chip group for all the discussions and mutual support, a pleasant atmosphere, and phenomenal breakfasts. In particular, I would like to thank...

...Jörg Schmiedmayer for sharing his enthusiasm, curiosity, and intuition for physics, and giving me the opportunity to freely explore all ideas that came up. Without his ongoing support and encouragement, this thesis would not have been possible.

...Thorsten Schumm, who – apart from being an awesome teacher in the lab, an absolutely reliable organizer, and a most helpful proofreader – was always available without complaining when I needed advice, reassurance, or simply a beer.

...Aurélien Perrin for helping me in understanding what I am actually doing time and again.

...The first-generation Rb-II crew: Stephanie Manz, Thomas Betz, Christian Koller, Aurélien Perrin, and Wolfgang Rohringer. I'm continuously reminiscing about those good ol' days of wedged screws, fried diodes, loud music, heavy swearing, sudden inspiration and those magic ich-bin-sehr-zufrieden moments.

...The next-generation Rb-II crew: Tarik Berrada, Sandrine van Frank, and Jean-François Schaff for great collaboration, and being forgiving about my non-French and reminiscing about those good ol' days. C'était un honneur et un plaisir pour moi de travailler avec vous (...well, I guess).

...Stephan Schneider for taking care of all the annoying stuff, and our good vacuum.

Also outside the Praterreaktor I enjoyed great collaboration with, and support from various people. I am grateful to...

...Julian Grond and Ulrich Hohenester for the fruitful theory collaboration, that eventually lead to the results presented in this thesis.

...Jan Chwedeńczuk and Tomasz Wasak for helpful discussions and calculations on the twin-beam correlation properties.

...Vladan Vuletić for giving me the opportunity to work in his group at MIT. I enjoyed discussing with him a lot, and was also impressed by his technical skills.

...Kristi Beck and Wenlan Chen, who made the three months in Vladan's lab a really enjoyable time, and whose patience with a complete newbie in serious locking electronics must be applauded.

...my advisory committee, Ehud Altman and Christoph Nägerl, for numerous helpful discussions.

...Chris Westbrook for being my thesis referee.

...Thomas Gasenzer, Boris Nowak, and Sebastian Erne. Even though unrelated to the topics of this thesis, I tremendously enjoyed the collaboration on quantum turbulence, and I'm looking forward to the things to come.

...the CoQuS grad school for financial and organizational support.

Beyond physics, the number of people who helped me in writing this thesis (without explicitly aiming for that, probably) may be even much larger. This includes my parents, who always unconditionally supported me, all those cute little siblings, and my entire family. Finally, I want to thank all my friends who were patient about me babbling nerdy stuff, the population of Vienna's coziest kitchen for making it feel like home, and Thea Hoffmann-Axthelm for... well, everything.

1. Introduction

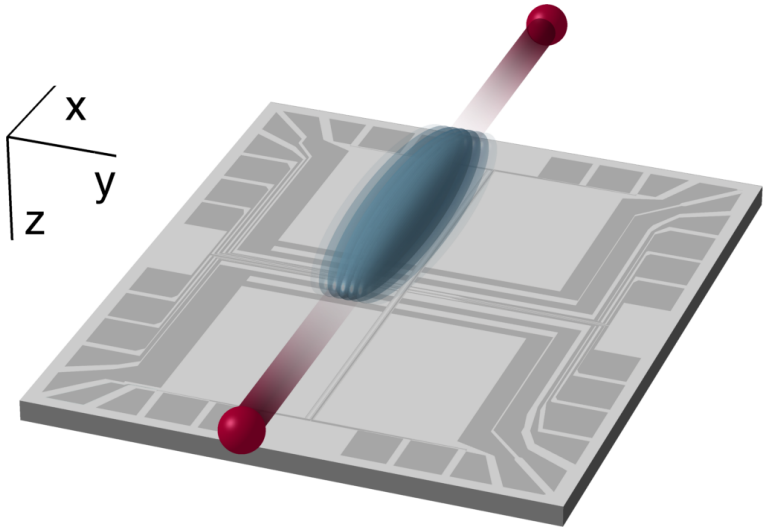

Figure 1.1.: Illustration of the experiment described in this thesis. A one-dimensional Bose gas (blue) trapped on an atom chip (not drawn to scale), is excited by means of fast transverse motion, which leads to longitudinal emission of a quantum-correlated pair of twin-beams.

To a great extent, the appeal of ultracold atom experiments lies in their ability to model and extend schemes and concepts known from other areas of physics, ranging from simulation of condensed matter systems in lattice experiments [1–4] to universal behavior at phase transitions and turbulence [5–7]. Their versatility is enabled by the unique combination of tunability of fundamental parameters, abundance of manipulation techniques, and the ability to observe the experiment result by simply taking photographs [8].

In this thesis, two (at first sight) rather different ways of employing a gas of ultracold atoms – quantum atom optics, and optimal quantum control – have been combined in a chip-based experiment. The former relates to fundamental aspects of quantum physics, highlighting particle-wave duality and the equivalence of light and matter, but also holds promise for future high-precision metrology techniques. The latter is concerned with how quantum systems in general can be driven in an efficient way, to obtain a desired final state or operation; an approach which is rather known from NMR or chemical physics.

Our main goal was to realize a bright source of single-mode twin-atom beams for quantum atom optics experiments [9], similar to the well-known technique of producing twin-photon beams using an optical parametric oscillator [10]. In the above figure, which subsumes the implemented experiment, the twin beams are shown in red. They are produced in a stimulated emission process, and emerge along the longitudinal

direction x from a one-dimensional quasi-condensate (blue), which has been excited to provide the necessary energy. Near-perfect quantum correlations between the beams are demonstrated in this thesis.

The quantum control aspect came up when searching for a suitable way to prepare an excited source state – the pumped gain medium in the language of the optics analogy. It turned out that, given the specific abilities of our experimental setup, a rather novel approach to tackle this problem was most efficient, the exploration of which became a secondary objective of this thesis. To obtain the "pumped" state with almost unit fidelity, we employ an all-mechanical scheme of spatially displacing the condensate wave function along its transverse direction y. The protocol for achieving efficient excitation has been derived from quantum optimal control theory [11], which for the first time has been applied to an excitation process in an ultracold atom system.

In this brief chapter, building on some basic theory concepts that will be introduced in chapter 2, the context of each of these two aspects is introduced, before the actual experimental scheme is described.

1.1. Twin-atom beams as a resource for quantum atom optics

Particle-wave duality, the interplay between wave and particle aspects of both light and matter, is at the heart of quantum physics. Soon after the wave character of matter had been proposed by de Broglie [12], interference of electrons [13] and atoms [14] was found, and matter-wave interferometry has now become a major field in physics [15]. From the viewpoint of matter-wave optics, a Bose-Einstein condensate is strongly reminiscent of laser light. Both can appropriately be described as a macroscopically occupied bosonic field mode, that behaves similar to a classical wave, coining the term "atom laser" for a propagating BEC [16, 17]. Indeed, one of the first experiments with Bose-Einstein condensates has been, to demonstrate interference of two independent condensates [18], implying a collective (but random [19]) phase. Matter-wave interferometry can benefit from using condensates due to their high brightness and narrow momentum distribution, and phase-coherent beam splitters have been implemented [20, 21], even though, at the relatively high densities in a condensate, complications arise from inter-atomic interactions [19, 22, 23].

Conversely, the corpuscular nature of light is especially evident in typical quantum optics experiments [24], that involve measurement of correlation functions as introduced by Glauber [25]. In several key experiments, such as refs. [26–30], purely classical (i.e., non-quantized) theories of light were ruled out by violation of classical inequalities [31]. By now, quantum optics provides versatile tools for engineering all kinds of exotic quantum states [24], which have reached the level of first applications. Apart from the quest for quantum computing [32] and communication [33], where non-classical light is a key ingredient to many proposed schemes, also metrology devices such as interferometers can be enhanced to the sub-shot-noise level by quantum correlations [34–37], which has e.g. recently been implemented for gravitational wave sensing [38, 39].

Quantum atom optics While the corpuscular nature of *matter* is hardly surprising, the toolbox of quantum optics can still be fruitfully applied to matter waves, in

particular to ultracold atoms, where the quantum state populations are macroscopic, and wave-like phenomena such as interference and diffraction prevail. In the formalism of "second quantization", indistinguishable particles are treated as quanta of a matter-wave field, in complete analogy to a quantized light field. This means, that in principle all the theoretical machinery of quantum optics can be readily applied to matter waves, giving rise to the field of *quantum atom optics* [9], where (mostly) atomic counterparts to quantum optics schemes are studied. One obvious first step is to apply Glauber's definition of coherence [25] to ultracold gases [40], and second-order (or even higher) correlation measurements have become a standard tool of cold atom physics by now. For instance, it has been shown, that second-order correlations of the atomic field are changed drastically when crossing the condensation temperature, just as light when the emitting medium is passing its lasing threshold [41–43].

One strong difference to light optics arises from the *interactions* of atoms in an ultracold gas, making the system's evolution non-linear in field amplitudes. In (light) quantum optics, such non-linearites correspond to higher-order susceptibilities in media, that give rise to effective interactions between photons, which is the main building block for generation of non-classical states [24]. This suggests, that non-classical[1] states of matter-wave fields can be obtained by setting up an appropriately conceived experimental situation, and just have the system undergo its inherent non-linear evolution. Indeed, in recent years an ever-increasing number of such schemes have been proposed and implemented, with the goal of both studying fundamental quantum effects, and achieving gain for metrology.

Spin squeezing One way of reaching quantum-correlated states in condensates is that of spin squeezing [44–47]. There, a pair of conjugate collective variables, usually population imbalance $\hat{N}_-$ and relative phase $\hat{\varphi}$ between two spatial modes or internal states with N_+ atom in total, are mapped to the components of an effective spin system with spin length $\leq N_+/2$. The quantum uncertainty of a spin measurement is then re-distributed between the two components, similarly to a squeezed interferometer in optics [34] (where field quadratures correspond to the spin components). The most common scheme to implement such a state in a condensate starts from a minimum-uncertainty *coherent spin state*, where each atom is placed in the same single-particle state, that is a superposition of the two modes. Then, the system evolves under an evolution that is non-linear in one of the spin variables, e.g. using state-selective interactions, giving rise to a term $\chi\hat{N}_-^2$ in the total Hamiltonian, which deforms the uncertainty distribution of the effective spin (one-axis twisting) [47]. This leads to a final state, that is strongly non-separable in the single-atom basis [46], and can reduce projection noise in the final readout of the interferometric signal below the shot-noise level [45]. This scheme has been realized using numerous techniques, in both internal (hyperfine) [48,49] and external [50–52] states of condensates. Similar states have been produced in non-condensed atom clouds using interaction with non-classical light [53], or one-axis twisting due to cavity-mediated interactions [54, 55]. Very recently, the spin-squeezing concept was applied to a more complex three-component system [56].

[1] Here, as generally in quantum optics, "non-classical" refers to effects that arise from the *particle* nature of quantum fields, which in the case of atomic matter-wave fields is somewhat contrary to some typical notion of "quantum-ness". In ref. [9], the term "quantum-correlated", which will be occasionally used in this thesis, is suggested as a more precise alternative.

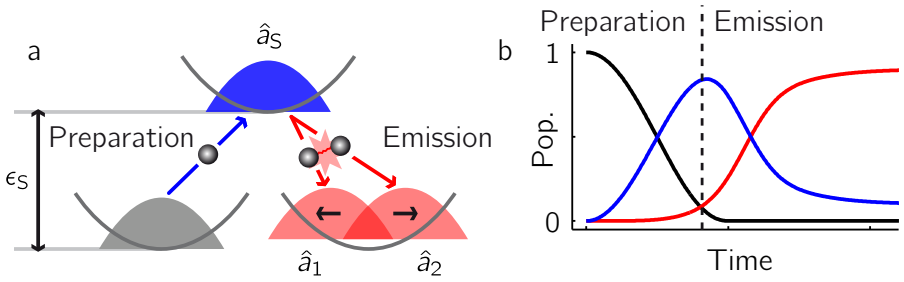

Figure 1.2.: Illustration of twin-atom beam production in the two-mode limit with a degenerate source mode (S = S′). (a) Initially, the system is prepared in a source state (blue, represented by a field operator $\hat{a}_S$), which is unstable with respect to a two-body relaxation process. The character of this source state differs among the various schemes mentioned in the text. Then, driven by a two-body process as described by eq. 1.1, pair-correlated atoms are emitted into the modes $\hat{a}_{1,2}$. For external-state schemes, the source mode typically carries some kind of excess energy ϵ_S, which is converted into kinetic energy, yielding twin beams moving in opposite direction. (b) Typical temporal dynamics of the process, including the initial preparation of the source state. The process stops, once the source state is depleted (as shown here), or the overlap of the involved modes vanishes.

Twin-atom beams Another branch of quantum atom optics experiments is dealing with correlated emission into paired modes, similar to photon pair creation in nonlinear crystals as used for down-conversion or four-wave mixing [57]. In the simplest case of a single pair of correlated modes, the system is driven by a coupling term in the Hamiltonian of the form

$$\hat{H}_{\mathrm{TM}} = \kappa[\hat{a}_1^\dagger \hat{a}_2^\dagger \hat{a}_S \hat{a}_{S'} + \mathrm{H.c.}], \tag{1.1}$$

where appropriately prepared source modes S, S′ (which may be identical, such as in our experiment) emit population into the initially empty modes 1, 2 (signal and idler), which acquire an exactly correlated population (two-mode squeezed state [57]). The process is illustrated in fig. 1.2. In a realistic setting, often many more final modes are accessible, and the dynamics of the process may become rather complex.

The proposed and experimentally realized schemes can be categorized following different criteria. One division can be made between schemes, where the two input modes are either different (as in four-wave mixing) or identical (similar to down-conversion),[2] which however is of limited importance for the properties of the correlated modes only. Also, the involved modes may differ in either their internal (typically magnetization) or external state, which leads to the process being governed by conservation of magnetization or momentum (phase-matching), respectively.

A key distinction is given by the number of paired modes and their typical (final) populations, both of which depend on the specific setting of the experiment, concerning e.g. length and time scales, and, crucially for the case of external states, the

[2] Of course, except for the case of molecular dissociation [58–60], still *two* source particles are extracted from the source instead of a single pump photon in down-conversion (also suggesting the term *degenerate* four-wave mixing). However, this has little effect on the description otherwise.

geometry of the involved modes. One limiting case is that of only two (or very few) twin modes, which acquire populations $\gg 1$, similar to the output of an optical parametric oscillator (OPO) in light optics, which is emitting a bright, quantum-correlated pair of beams [10]. In this case, the emission is strongly stimulated, and depletion of the source mode(s) may become perceivable. This regime has been reached in the experiment presented in this thesis. Other experiments with motional states in the stimulated regime have employed four-wave mixing processes generated by Bragg gratings [61, 62] or RF outcoupling [63, 64], or dynamical instabilities in optical lattices, where the modified dispersion relation allows to engineer appropriate phase-matching conditions [65–68]. Analogous schemes have been developed for internal atomic states, which provide direct means of mixing the twin-modes (using resonant radio-frequency and microwave pulses), to study their properties at the quadrature level [56, 69–72]. At the other extreme there are experiments, where the modes, into which emission can occur, are much less restricted, and many of them become weakly occupied. This has been reached by collision of two condensates in free space [73–76], dissociation of molecules [58, 59], or collisional de-excitation similar to this thesis, albeit in a two-dimensional (and hence, less restricted) geometry [77]. In many of those experiments, quantum correlations were detected, either by sub-binomial statistics of population imbalances (number squeezing) [70–72, 74, 78], or stronger-than-classical second order correlations [76]. Both approaches are employed in this thesis, to demonstrate the strong quantum correlations in the twin-beam system we have implemented.

Applications for twin atoms As for spin-squeezed states, twin-atom states are candidates both for fundamental tests of quantum mechanics, and quantum-enhanced interferometry. For the latter application, especially the case of a highly populated two-mode system, which corresponds to a twin-Fock state $|N_+/2, N_+/2\rangle$ seems promising. Clearly, the framework of spin-squeezed states [45] is inappropriate here, as the mean spin length of a twin-Fock state is zero due to the undefined relative phase: The readout of the acquired phase in a twin-Fock interferometer, which is encoded in the fluctuations of the signal, necessitates other means than observing fringes directly. However, interferometry approaching the Heisenberg sensitivity limit seems feasible in this way [37, 79]. Also for condensates, twin-Fock interferometers have been proposed [80, 81], and recently implemented using internal-state twin-atoms [70]. A generalized definition of "useful" many-body entanglement (which is equivalent to the ability for sub-shot-noise interferometry) has been given in ref. [82], that is based on quantum Fisher information, and encompasses, among others, both twin-Fock and spin squeezed states.

On the other hand, strategies have been proposed to perform fundamental experiments of quantum optics with atoms, such as preparation of EPR states [83, 84]. In refs. [85, 86], the use of spinor condensates has been discussed, where internal and external degrees of freedom are combined to obtain entanglement on the single-particle level, in a way similar to polarization-entangled photons [87]. Another recently proposed scheme in the weakly populated regime goes along the lines of classical two-particle interference experiments [30, 88], to obtain an EPR state in momentum and position of atom pairs [89].

In the opposite regime of large mode populations, continuous-variable (CV) entan-

glement in the two-mode quadratures of the twin-modes [90, 91] is expected, again leading to the generation of an EPR state. However, such a state cannot be detected by density correlation measurements (as presented in this thesis) alone [92]: quadrature measurements have to be performed, that necessitate some phase reference (local oscillator). For internal states, such a measurement has been experimentally realized in ref. [71], where the source state was also used as a local oscillator to probe the phase of the twin modes by homodyning, and CV entanglement could be demonstrated. Similar experiments with external-state twin beams have been proposed, using molecular dissociation [60], or few-mode four-wave mixing with subsequent Bragg pulses [92], which effectively are used as linear optical elements for recombination and homodyning.

Twin atoms on a chip In this thesis, we will present a promising novel technique to produce external-state twin-atom beams in a few-mode one-dimensional geometry, trapped on an atom chip. For the first time, quantum correlations in the strongly populated regime are demonstrated, by observation of almost perfectly suppressed population imbalance fluctuations between the twin beams. Furthermore, the Bose-enhanced dynamics of the stimulated population growth, governed by eq. (1.1), is studied in detail, and a theoretical description for the process is derived, that is able to quantitatively explain our findings in an intuitive way. While further experimental tools will be necessary to prove entanglement (e.g. following ref. [92]) or metrology gain (similar to ref. [70]), such measurements seem feasible in the foreseeable future.

1.2. Preparing the source: optimal control of a condensate wave function

One rather unique aspect of our recipe for twin-beam creation is the way the source state is prepared. The basic principle is that of de-excitation from a transversely excited vibrational state, by means of two-body collisions. In lower-dimensional geometries, the "frozen" degrees of freedom (see sec. 2.4) are usually eliminated from the theoretical description as far as possible. For the one-dimensional case present in our experiment, the Lieb-Liniger Hamiltonian (2.31), the transverse state affects a single static parameter (the effective interaction constant g_{1d}) only. The transverse levels define the highest energy scale of the system, and the corresponding states strongly resemble discrete single-particle states, with only weak modification due to atom-atom interactions [93].

Vibrational de-excitation and twin atoms We exploit the approximate de-coupling of transverse and longitudinal degrees of freedom, by using a condensate as a gain medium, which is not in the transverse ground state, but has been transferred to an excited eigenstate of its non-linear Hamiltonian [94], which in the non-interacting limit is a Fock state of an oscillator ("vibrational inversion"). This does not change the one-dimensional description: along the longitudinal direction, the "pumped" cloud remains close to its equilibrium state, and the transverse excitation effectively represents an internal degree of freedom. However, the total state is highly excited, obviously, and will decay by inelastic collisions. If the transverse levels are energetically non-

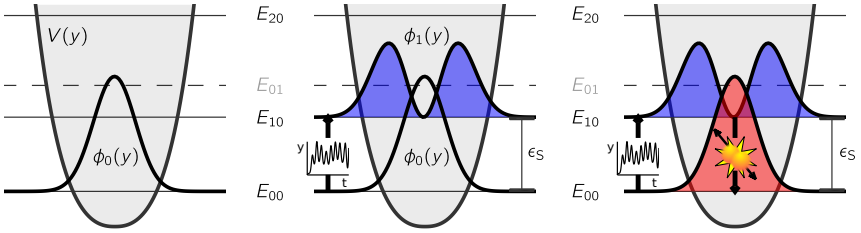

Figure 1.3.: Using vibrational de-excitation for twin-beam production. The potential along the transverse coordinate y, which is perpendicular to the direction drawn in fig. 1.2(a) and has a stronger confinement by orders of magnitude, is shown with its first few energy levels (where the two indices count the levels along y and z, respectively). Initially (left panel), the condensate is in its transverse ground state ϕ_0. Then (center), by means of an excitation pulse (inset), the condensate is transferred to the first excited state ϕ_1, which has an excess energy ϵ_S per atom and acts as the twin-beam source. Finally (right), the atoms can decay back into the ground state, where they release the excess energy into kinetic energy of twin atoms in the longitudinal direction.

equidistant with increasing level spacings (as e.g. for a box potential), and we have populated the lowest-lying excited state, atoms can only be scattered into the transverse ground state (vibrational de-excitation). Due to energy, momentum, and parity conservation, this process must happen pair-wise, and a twin-beam emission process will start, where longitudinal high-momentum modes will be populated strongly with twin-atoms (fig. 1.3).

A typical way to address vibrational states in general is that of using sidebands of optical or microwave transitions. Indeed, in ref. [77], collisional de-excitation has been demonstrated in a two-dimensional condensate, where excited states along the axial (strongly confined) direction have been populated using a Raman transfer. In our experiment, we took a rather different approach, and achieved the vibrational inversion using a modulation (translation) of the confinement potential, steering the dynamics of the transverse wave function.[3] After the modulation sequence, the condensate has been "shaken" with near-unity efficiency into the first excited state, which does not have any residual dynamics but that of de-excitation.

Optimal control of a quantum system The precise excitation protocol has been obtained from quantum optimal control theory (OCT) [11, 95, 96]. OCT provides a framework for determining optimized driving sequences to actively manipulate a quantum system in any desired way with high fidelity. One typical task is the precise control of spin evolution in an NMR spectroscopy experiment [97–99]. Other exciting applications are the shaping of laser pulses for controlling chemical reactions [100–102], or optimizing solid-state quantum gates [103–108]. While protocols exist, that optimize the complete adiabaticity of parameter changes [109, 110], most optimal control sequences are highly non-adiabatic. Typically, they either drive rapid transitions be-

[3] This transverse condensate mode is strongly populated; hence, in contrast to the quantized description of the previous section, it can be treated as a classical wave with mean-field interactions, which is governed by the Gross-Pitaevskii equation (2.15).

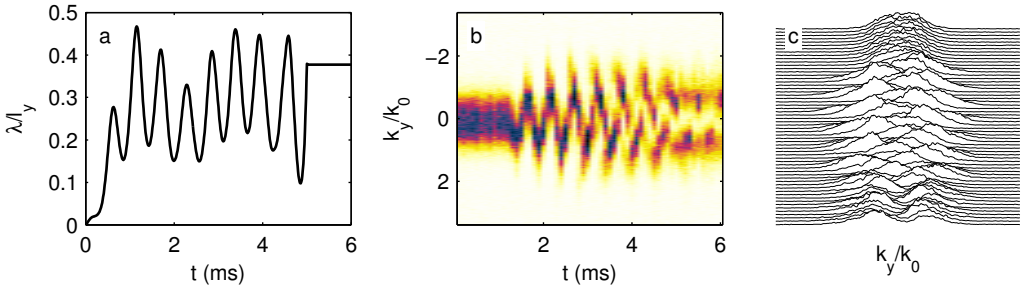

Figure 1.4.: Optimal control of the condensate wavefunction. (a) Optimized trajectory of the transverse trap minimum along y, normalized to the typical oscillator length l_y. (b, c) Measured response of the system: Momentum distribution dynamics $\tilde{n}_{\mathrm{k}}(y,t)$ shown as false-color and stacked plots, respectively.

tween different quantum states, or provide "shortcuts to adiabaticity", where the system ends up in its new ground state after a change of its parameters, even though this change is performed too fast for the system to sustain an adiabatic evolution. Both kinds of transformation usually involve complex quantum interference between many transiently populated eigenstates, which however lead to the desired outcome in the end. For the rapid transitions, the *quantum speed limit* [111–113] may be approached, which sets the upper limit to how fast a system can evolve in its Hilbert space. This may be highly relevant for quantum computation, where fast gate times are required to outrun decoherence.

Ultracold atoms, due to their relatively large length and time scales and good isolation from the environment, offer excellent means to dynamically control parameters, as well as to probe the response to the applied control by the powerful imaging techniques available. So far, most applications of optimized quantum control in condensates were aiming for shortcuts to adiabaticity, e.g. to transport or deform condensates without undesired excitation [110, 114–121]. On the theory side, these approaches are based either on self-similar solutions for the evolution of a condensate [122, 123], or numerical solution of the Gross-Pitaevskii equation (2.15). However, also state preparation beyond the mean-field level has been proposed, including entanglement generation and storage [124, 125], number-squeezed states [126], or cooling [127].

Optimal control on a chip For the vibrational inversion we are aiming for in this thesis, a mean-field Gross-Pitaevskii approach was appropriate, which has been developed initially to optimize fast splitting of a chip-trapped BEC [114]. However, instead of reaching the new ground state of a transformed (split) system in a non-adiabatic way, we now use the algorithm (see appendix A) to populate the first excited eigenstate of the initial system, by means of a transient excitation, where the system is driven by mechanical motion of the anharmonic trap, see fig. 1.4(a). The response can be monitored in the experiment by measuring the momentum distribution using time-of-flight imaging, see fig. 1.4(b,c). It will be demonstrated that we reach the vibrational inversion state with an efficiency close to 100% , which to our knowledge represents the first successful use of OCT for the preparation of exotic many-body states of Bose-Einstein condensates. The dynamics of the process is studied in detail

by means of time-of-flight imaging, and excellent agreement between experiment and numerical simulations is found. Furthermore, we will deduce an approximate description, that allows to map the dynamics of the many-body wave function to a driven two-level system, where the excitation process corresponds to a π-pulse that transfers all population to the excited state.

1.3. Structure of this thesis

This thesis is structured as follows:

- In chapter 2, fundamental theoretical concepts are introduced that will be relied on in the remainder of the thesis. This mainly comprises the basic description of Bose-Einstein condensates of interacting particles, with a focus on one-dimensional systems.
- Chapter 3 starts by describing the hardware of the experiment setup this thesis was carried out at, before explaining some of the key techniques that have been used. The focus will be on aspects that have not been thoroughly described in previous theses yet.
- The second part of the thesis specializes on the twin-beam emission and optimal control experiments. It starts with chapter 4, where a theoretical description of twin-beam production in general, and specifically for our case, is developed.
- Chapter 5, which is the central part of this thesis, describes in detail the novel experiments performed, and their results.
- Finally, in chapter 6 some ideas for future experiments, extending the ones implemented in this thesis, are sketched, together with some recently obtained preliminary results.
- Various more technical explanations, including the derivation of the optimal control sequence, are given in appendices.

Part I.

Foundations and Tools

2. Theory of cold Bose gases

In this chapter, some basic theoretical concepts are introduced, which are fundamental for the more specific theory and experiments presented in part II of this thesis. After introducing the phenomenon of Bose-Einstein condensation in its original thermodynamic formulation, the description is more and more extended up to the basic formalism used for trapped, interacting Bose gases. A brief section recapitulates the definition of correlation functions, which will be essential at various places. Finally, the one-dimensional Bose gas is introduced, leading to the theoretical description of a quasi-condensate, which is the main "raw material" for the experiments presented in this thesis.

2.1. Ideal Bose gas

In 1924, a peculiarity of Bosonic statistics has been pointed out by Bose and Einstein, namely, that under certain conditions even for non-zero temperatures T, almost all particles occupy the single-particle ground state of the system [128]. Using the grand canonical ensemble, the Bosonic occupation number for a single-particle state with energy ϵ_i is given by

$$N_i(\epsilon_i, \mu, T) = \frac{1}{e^{\beta(\epsilon_i - \mu)} - 1} = \frac{z e^{-\beta\epsilon_i}}{1 - z e^{-\beta\epsilon_i}}, \tag{2.1}$$

with the inverse temperature $\beta = (k_\mathrm{B} T)^{-1}$. The chemical potential μ (or, equivalently, the fugacity $z = e^{\beta\mu}$) is implicitly determined by the constraint of a fixed particle number N:

$$N = \sum_{i=0}^{\infty} N_i(\epsilon_i, \mu, T). \tag{2.2}$$

For decreasing temperatures, the occupation numbers rise, and μ has to increase accordingly, to keep N fixed. However, from eq. (2.1) it is evident, that the chemical potential μ cannot exceed the lowest single-particle state ϵ_min. Depending on the level structure ϵ_i, at a sufficiently low temperature T, the occupation numbers may reach their limit $\{\exp[\beta(\epsilon_i - \epsilon_\mathrm{min})] - 1\}^{-1}$; the excited states are said to be saturated. To still fulfill eq. (2.2), the occupation of the absolute single-particle ground state, which is unlimited as $\mu \to \epsilon_\mathrm{min}$, has to become macroscopic, giving rise to the phenomenon of Bose-Einstein condensation (BEC).

In the thermodynamic limit of $N \to \infty$ and the system volume $V \to \infty$, keeping the density N/V constant, one can smooth out the discrete level structure and replace the summation by an integral. However, due to its divergence at $\mu \to \epsilon_\mathrm{min}$, the absolute ground state population N_0 is not being accounted for properly in the continuous approximation, and has to be separated, hence:

$$N - N_0 = \int_0^\infty D(\epsilon) N(\epsilon, \mu, T) \mathrm{d}\epsilon, \tag{2.3}$$

with a density of states $D(\epsilon)$, which typically has a power-law dependence on ϵ, that is determined by the confinement and dimensionality of the system. For cold atoms, the most experimentally relevant case is that of a harmonically trapped gas, which will be discussed in the following.[1]

2.1.1. BEC in a harmonic trap

Consider a harmonic potential in d dimensions with potential and energy levels as:

$$V = \frac{m}{2}\sum_{i=1}^{d}\omega_i^2 x_i^2 \qquad \epsilon_{\{n\}} = \sum_{i=1}^{d} n_i \hbar\omega_i,$$

omitting the zero-point energy, which only adds a global offset. The thermodynamic limit is now expressed by letting: $\omega_\mathrm{h} = \prod_{i=1}^{d}\omega_i^{1/d} \to 0$, keeping $N\omega_\mathrm{h}^d$ constant. For this case the density of states can be written as [130]:

$$D(\epsilon) = \frac{\epsilon^{d-1}}{(d-1)!\prod_{i=1}^{d}\hbar\omega_i}, \tag{2.4}$$

indicating that the dimensionality of the system will have a strong impact on the properties of eq. (2.3). To obtain the condition for Bose-Einstein condensation, we set the chemical potential to its maximum allowed value $\mu = 0$, insert (2.4) into (2.3) and perform the integration. For $d = 3$, the integral converges and we obtain

$$N - N_0 = g_3(1)\left(\frac{k_\mathrm{B}T}{\hbar\omega_\mathrm{h}}\right), \tag{2.5}$$

with the Bose (or polylogarithm) function $g_3(1) \approx 1.2$, implying that for temperatures $T < T_\mathrm{3d}$ with

$$k_\mathrm{B}T_\mathrm{3d} = \hbar\omega_\mathrm{h}[N/g_3(1)]^{1/3} \tag{2.6}$$

there is a ground state population $N_0 > 0$ and, hence, Bose-Einstein condensation. The condensed fraction is given by $N_0/N = 1 - (T/T_\mathrm{1d})^3$. As we assumed the thermodynamic limit as $N\omega_\mathrm{h}^3$ being kept constant, T_3d is independent of the system size. It is thus equivalent to the intuitive notion of the degeneracy criterion $n_0^{1/3}\lambda_\mathrm{dB} \sim 1$ being fulfilled for the peak density n_0, where

$$\lambda_\mathrm{dB} = \sqrt{\frac{2\pi\hbar^2}{mk_\mathrm{B}T}} \tag{2.7}$$

is the thermal de Broglie wave length, i.e. single-particle wave packets start to "overlap" near the trap center at $T \sim T_\mathrm{3d}$.

On the other hand, a highly relevant case in this thesis is $d = 1$, where the density of states (2.4) becomes independent of ϵ (as the harmonic trap level spacing does not depend on the energy and there is no degeneracy). In that case, the integral (2.3) diverges for $\mu = 0$, implying the absence of condensation.[2] However, this statement remains valid only in the thermodynamic limit $\omega_\mathrm{h} \to 0, N \to \infty$, as will be explained in the following section.

[1] See [129] for a more general treatment valid for different confinements.
[2] Note, that this does not hold for power-law potentials stronger than harmonic [131].

2.1.2. Finite-size and anisotropic BEC

Despite being convenient to evaluate, ignoring the discreteness of energy levels in the thermodynamic limit leads to deviations from the exact results at smaller atom numbers ($N \sim 10^4$ and below) and, even more crucially, strong anisotropy of the trap geometry. In ref. [132], the continuous approximation (2.3) is omitted; instead the chemical potential μ is obtained numerically from the implicit equation (2.2), allowing to directly calculate N_0. While there is strictly speaking no phase transition in a finite-size system, the behavior in terms of the condensed fraction N_0/N is found to be very similar to the thermodynamic limit, apart from a (downwards) shift of $T_{3\mathrm{d}}$, depending on the trap anisotropy:

$$\frac{\delta T_{3\mathrm{d}}}{T_{3\mathrm{d}}} \approx 1 - 0.73 \frac{\bar{\omega}}{\omega_{\mathrm{h}}} N^{-1/3}, \tag{2.8}$$

where $\bar{\omega} = (\omega_1 + \omega_2 + \omega_3)/3$ may be very different from ω_{h} for strongly anisotropic traps.

However, when $k_{\mathrm{B}}T \ll \hbar\omega_\perp$ in an elongated trap with $\omega_\perp \equiv \omega_2 = \omega_3 \gg \omega \equiv \omega_1$, and the perpendicular degrees are frozen out, in contrast to the result of the continuous approximation, it is found that the ground state *can* be macroscopically populated. As a critical temperature for this one-dimensional finite-size condensation,

$$k_{\mathrm{B}}T_{1\mathrm{d}} = \hbar\omega \frac{N}{\ln(2N)} \tag{2.9}$$

is found. In the thermodynamic limit, $T_{1\mathrm{d}} \to \infty$, i.e. the absence of BEC in an infinite one-dimensional system is restored. As will be discussed in sec. 2.4, physics in degenerate one-dimensional gases is mostly determined by inter-particle interactions, making the finite-size condensation hard to observe for realistic experimental parameters [133].

Another remarkable property of the strongly elongated ideal gas is the presence of a two-step condensation [134]. It is predicted, that in certain ranges of aspect ratio and atom number where $k_{\mathrm{B}}T_{3\mathrm{d}} > k_{\mathrm{B}}T_{1\mathrm{d}}, \hbar\omega_\perp$, a *transverse condensation* can occur. In this case, the ground state along the transverse directions becomes macroscopically populated and a discontinuity in specific heat is observed at $T_{3\mathrm{d}}$, but many quantum states remain occupied along the longitudinal direction, before full condensation occurs as $T_{1\mathrm{d}}$. This constitutes a regime of effective dimensional reduction of the system, despite $k_{\mathrm{B}}T > \hbar\omega_\perp$ (i.e., no actual "freezing out" of transverse degrees of freedom). For realistic experimental parameters in an atom chip experiment, there is a competition between two-step condensation and interaction-driven crossover effects (quasi-condensation, see sec. 2.4), which has been studied in [135]. In the context of our experiment as described below, this effect is important as it ensures that a mean-field description of the excitation dynamics, which is a purely transverse process (see appendix A and sec. 5.4), are satisfied even in the case of temperatures, which do not ensure quasi-condensation in the entire system. There, for typical trap parameters and $N = 700$ atoms, $T_{3\mathrm{d}} \approx 120\,\mathrm{nK}$.

2.2. Interacting Bose gas

While the phenomenon of condensation is predicted already for non-interacting bosons, even in three dimensions many of the crucial properties of a BEC are affected by the

interactions of their constituents. In low-dimensional systems, for realistic experimental parameters, interactions play an even much stronger role; in fact, many of the rich regimes of quantum degeneracy in such systems are completely absent for an ideal gas. Thus, before studying the case of a one-dimensional Bose gas in more detail, we introduce the general description of an interacting Bose gas and some typical approaches to derive its behavior from theory.

In the occupation number representation (or "second quantization") formalism, the most general Hamiltonian for an interacting Bose gas writes:

$$\hat{H}_{\mathrm{tot}} = \int \mathrm{d}\mathbf{r}\hat{\Psi}^\dagger(\mathbf{r},t)\hat{H}_0\hat{\Psi}(\mathbf{r},t) + \frac{1}{2}\iint \mathrm{d}\mathbf{r}\mathrm{d}\mathbf{r}'\hat{\Psi}^\dagger(\mathbf{r},t)\hat{\Psi}^\dagger(\mathbf{r}',t)V(\mathbf{r}-\mathbf{r}')\hat{\Psi}(\mathbf{r}',t)\hat{\Psi}(\mathbf{r},t), \tag{2.10}$$

where $\hat{H}_0 = -\hbar^2\nabla^2/(2m) + V_{\mathrm{ext}}(\mathbf{r},\mathbf{t})$ is the single-particle Hamiltonian with the confinement potential $V_{\mathrm{ext}}(\mathbf{r},\mathbf{t})$, and $V(\mathbf{r}-\mathbf{r}')$ denotes the two-particle interaction potential as a function of particle distance. The Bose field operator can be written as a sum of single-particle annihilation operators $\hat{a}_i$ corresponding to modes with wave functions $\psi_i(\mathbf{r},t)$:

$$\hat{\Psi}(\mathbf{r},t) = \sum_{i=1}^{M}\psi_i(\mathbf{r},t)\hat{a}_i(t). \tag{2.11}$$

For low-energetic scattering as it appears in ultracold systems, only the s-wave scattering channel, characterized by the single parameter of the scattering length a_{s}, remains: If $na_{\mathrm{s}}^3 \ll 1$, and $\lambda_{\mathrm{dB}} \gg a_{\mathrm{s}}$, atoms are unlikely to encounter each other on a scale a_{s}, which would allow txhem to probe the potential $V(\mathbf{r}-\mathbf{r}')$, and we only have to account for the influence of scattering on the asymptotic scattering states at long distances, which is a mere phase shift [130]. Thus, in most instances[3] we can replace $V(\mathbf{r}-\mathbf{r}')$ by a "pseudopotential", that mimics the effect of the actual interaction by a contact potential $g\delta(\mathbf{r}-\mathbf{r}')$, with the interaction constant $g = 4\pi\hbar^2 a/m$. Instead of eq. 2.10, we obtain

$$\hat{H}_{\mathrm{tot}} = \int \mathrm{d}\mathbf{r}\left[\hat{\Psi}^\dagger(\mathbf{r},t)\hat{H}_0\hat{\Psi}(\mathbf{r},t) + \frac{g}{2}\hat{\Psi}^\dagger(\mathbf{r},t)\hat{\Psi}^\dagger(\mathbf{r},t)\hat{\Psi}(\mathbf{r},t)\hat{\Psi}(\mathbf{r},t)\right], \tag{2.12}$$

which will serve as starting point for most theoretical considerations in the remainder of this manuscript.

Using the Heisenberg picture for time evolution, the Bose field operator $\hat{\Psi}$ evolves according to the Heisenberg equation as:

$$\begin{aligned} i\hbar\frac{\partial}{\partial t}\hat{\Psi}(\mathbf{r},t) &= \left[\hat{\Psi}(\mathbf{r},t), \hat{H}_{\mathrm{tot}}\right] \\ &= \hat{H}_0\hat{\Psi}(\mathbf{r},t) + g\hat{\Psi}^\dagger(\mathbf{r},t)\hat{\Psi}(\mathbf{r},t)\hat{\Psi}(\mathbf{r},t). \end{aligned} \tag{2.13}$$

Apart from particularly simple systems, such as the one discussed in sec. 4.2, the full Heisenberg equation for the interacting Bose gas is non-linear and considered numerically intractable. One very common approach to enable approximate solutions for

[3] see e.g. [130, 136] for a discussion of cases, where this does not apply.

(partially) condensed systems, is to separate a single, suitably identified condensate mode $\hat{\Psi}_0(\mathbf{r},t)$, that has a macroscopic population N_0, from the rest of the field operator. Assuming $N_0 - 1 \approx N_0$ (classical limit), one can replace the operator for that mode by a classical complex field $\psi_0(\mathbf{r},t)$:

$$\begin{aligned}\hat{\Psi}(\mathbf{r},t) &= \psi_0(\mathbf{r},t) + \hat{\delta}(\mathbf{r},t) \\ &= \sqrt{n_0(\mathbf{r},t)} + \sum_{i=1}^{\infty} \psi_i(\mathbf{r},t)\hat{a}_i(t),\end{aligned} \tag{2.14}$$

where $\hat{\delta}(\mathbf{r},t)$, which now holds all the remaining operators, is assumed to be small and we used the condensate density $n_0(\mathbf{r},t) = |\psi_0(\mathbf{r},t)|^2$ (we arbitrarily chose zero global phase for the condensate). This ansatz, which is conceptually similar to the identification of a condensed state in the ideal case, is known as the *Bogoliubov approximation* [137].[4] We can now substitute eq. (2.14) into eq. (2.13), and expand the result in increasing orders of $\hat{\delta}, \hat{\delta}^\dagger$ [136]. The zeroth-order result, where $\hat{\Psi}$ is completely replaced by the classical field ψ_0 leads to the famous Gross-Pitaevskii equation (GPE):

$$i\hbar\frac{\partial}{\partial t}\psi_0(\mathbf{r},t) = \left[-\frac{\hbar^2}{2m}\nabla^2 + V_{\text{ext}}(\mathrm{r},t) + g|\psi_0(\mathbf{r},t)|^2\right]\psi_0(\mathbf{r},t), \tag{2.15}$$

which is a non-linear Schrödinger equation, that appropriately captures the behavior of the "condensate wave function" $\psi_0(\mathbf{r},t)$ [138] for a broad range of problems, and is widely used throughout the field of ultracold Bose gases. It will serve as the main tool to calculate the dynamics of a driven condensate in appendix A and sec. 5.4.

For a static system, the trivial time dependence $\psi_0(\mathbf{r},t) = \psi(\mathbf{r})e^{-i\mu t/\hbar}$ with the chemical potential μ can be eliminated to obtain the time-independent GPE:

$$\mu\psi_0(\mathbf{r}) = \left[-\frac{\hbar^2}{2m}\nabla^2 + V_{\text{ext}}(\mathrm{r}) + g|\psi_0(\mathbf{r},t)|^2\right]\psi_0(\mathbf{r}). \tag{2.16}$$

In typical condensate experiments, where the chemical potential μ exceeds the trap level spacing $\hbar\omega_{\mathrm{h}}$, the kinetic energy term in the time-independent GPE can be safely neglected, leading to the Thomas-Fermi (TF) approximation for the condensate density $n_0(\mathbf{r})$:

$$n_0(\mathbf{r}) = \begin{cases} g^{-1}[\mu - V_{\text{ext}}(\mathbf{r})] & : \mu > V_{\text{ext}}(\mathbf{r}) \\ 0 & : \text{otherwise} \end{cases}, \tag{2.17}$$

which is the inverted parabola profile typical for a BEC. Its radius R_i along direction i follows from the condition $V_{\text{ext}}(R) = \mu$, hence:

$$R_i = \sqrt{\frac{2\mu}{m\omega_i^2}} = l_i\sqrt{\frac{2\mu}{\hbar\omega_i}} \gg l_i, \tag{2.18}$$

[4] Note, that this approximation breaks the phase symmetry of the initial problem [the fied operator acquires a non-zero expectation value $\psi_0(\mathbf{r},t)$], and hence allows violation of particle number conservation. This will be a major limitation in the context of chapter 4, where the populations of the modes described by $\hat{\delta}$ may become large, without the condensate population N_0 being depleted simultaneously.

where $l_i = \sqrt{\hbar/m\omega_i}$ denotes the harmonic oscillator length.

Note, that in a low dimensional system as described above, the Thomas-Fermi approximation may fail along the transverse directions, as $\hbar\omega_\perp > \mu$ and kinetic energy cannot be neglected or even becomes dominant. See refs. [93, 139] for a discussion of this dimensional crossover.

2.2.1. Excitation spectrum of a condensate

We now take a very brief look at how to obtain the excitation spectrum of the condensate at negligible temperature. See e.g. ref. [136] for a systematic overview of current approaches that go far beyond the simple approximation shown here, and are also valid for higher temperatures.

Collective modes can be obtained by adding a weak perturbation $\delta\psi$ on top of the condensate wave function in eq. (2.15), and neglecting any terms that are non-linear in $\delta\psi$ [140]. Equivalently, one can insert the field operator in Bogoliubov approximation [eq. (2.14)] into the system Hamiltonian (2.12), and neglect any terms higher than quadratic in $\hat{\delta}$. While all linear terms in $\hat{\delta}$ vanish, the quadratic contribution writes

$$\hat{H}_\delta = \int \mathrm{d}\mathbf{r} \left[\hat{\delta}^\dagger(\hat{H}_0 + 2g|\psi_0|^2)\hat{\delta} + \frac{g}{2}([\psi_0^*]^2\hat{\delta}\hat{\delta} + \psi_0^2\hat{\delta}^\dagger\hat{\delta}^\dagger)\right], \tag{2.19}$$

omitting arguments $\mathbf{r}, t$ for brevity. This expression can be diagonalized by expressing $\hat{\delta}$ in terms of *quasi-particle* operators $\hat{b}_i(t)$ instead of the single-particle operators $\hat{a}_i(t)$:

$$\hat{\delta}(\mathbf{r}, t) = \sum_{i=1}^{\infty} \left[u_i(\mathbf{r})\hat{b}_i(t) + v_i^*(\mathbf{r})\hat{b}_i^\dagger(t)\right], \tag{2.20}$$

where the functions $u(\mathbf{r})$ and $v(\mathbf{r})$ are determined by the Bogoliubov-de Gennes equations [140, 141]:

$$\begin{aligned}\left[\hat{H}_0 + 2gn_0(\mathrm{r}) - \mu\right] u_i(\mathbf{r}) + g[\psi_0(\mathbf{r})]^2 v_i(\mathbf{r}) &= \epsilon_i u_i(\mathbf{r}) \\ \left[\hat{H}_0 + 2gn_0(\mathrm{r}) - \mu\right] v_i(\mathbf{r}) + g[\psi_0^*(\mathbf{r})]^2 u_i(\mathbf{r}) &= -\epsilon_i v_i(\mathbf{r}).\end{aligned} \tag{2.21}$$

For weakly interacting particles, the energy of the Bogoliubov excitations in a condensate is then given by

$$\hat{H}_\delta = \sum_{i=1}^{\infty} \epsilon_i \hat{b}_i^\dagger \hat{b}_i. \tag{2.22}$$

Inserting de Boguliubov-de Gennes equations into the time-independent GPE (2.16) for a uniform system ($V_{\mathrm{ext}} = 0$) yields the quasi-particle dispersion relation (i.e., energy for a quasi-particle with momentum $p \equiv |\mathrm{p}|$:

$$E(p) = \sqrt{\frac{p^2}{2m}\left[\frac{p^2}{2m} + 2\mu\right]} = \sqrt{\left(\frac{p^2}{2m}\right)^2 + (cp)^2}, \tag{2.23}$$

with the speed of sound $c = \sqrt{\mu/m}$. Hence, while low-momentum quasi-particles behave as phonons with a linear dispersion $E = cp$, they change to free particles with

quadratic dispersion at energies large compared to the chemical potential μ. Equivalently, the crossover occurs, once the wavelength of excitations $\lambda_i = \hbar/p_i$ becomes comparable to the correlation, or healing length $\xi_\mathrm{h} = \hbar/\sqrt{m\mu}$. Qualitatively, this notion also holds for one-dimensional systems, see sec. 2.4.

For trapped systems, the lowest-lying collective modes have $\lambda_i \sim R$ and correspond to bulk excitations [8, 141–144], such as a "sloshing" dipolar excitation (which corresponds to a quasi-classical oscillation of the cloud in the trap, maintaining its shape), or "breathing" modes, where the cloud width oscillates. It can be shown exactly, that in a harmonically trapped system, for any kind of interactions, the dipolar excitation decouples from the rest of the condensate dynamics, and leaves the system unperturbed in an oscillating reference frame [145, 146], a concept that will become important in sec. 5.4. At higher wavelengths $\lambda_i \ll R_\mathrm{TF}$, the excitations again correspond to sound-like phonons or, at $\lambda_i \ll \xi_\mathrm{h}$, free particles.

2.3. Correlation functions and coherence

In this section, we introduce the definition of *correlation functions*, which will be of great importance in the following theory sections, as well as for the experiment analysis in chapter 5. In quantum optics, correlation functions are among the most valuable tools to access the coherence and quantum correlation properties of light, following the definition of Glauber [25]. Of coarse, they can be readily applied to study the coherence of matter wave fields, too [40]. In terms of a quantum field $\hat{\Psi}(x,t)$, a n-th order correlation function, characterizing the n-th order coherence of a light or matter wave can be written as[5]

$$G^{(n)}(x_1 \dots x_{2n}) = \langle \hat{\Psi}^\dagger(x_1)\hat{\Psi}^\dagger(x_2)\cdots\hat{\Psi}(x_n)^\dagger\hat{\Psi}(x_{n+1})\hat{\Psi}(x_{n+2})\cdots\hat{\Psi}(x_{2n})\rangle\,. \tag{2.24}$$

For light, the ability to detect single photons using photomultipliers or single-photon counting photodiodes has made correlation functions experimentally accessible and enabled unambiguous proofs for the quantum nature of light [24, 25]. Especially the second-order correlation with creation and annihilation operators at corresponding positions, $G^{(2)}(x_1,x_2) = \langle\hat{\Psi}^\dagger(x_1)\hat{\Psi}^\dagger(x_2)\hat{\Psi}(x_1)\hat{\Psi}(x_2)\rangle$, is a simple and powerful tool to characterize non-classical properties of fields. This includes photon anti-bunching [27], and most prominently, the violation of inequalities that apply for classical field variables, such as the Cauchy-Schwarz [26, 31] and Bell [28, 147, 148] inequalities.

A fully coherent field is characterized by all its correlation functions factorizing into products of the first-order coherence [149], e.g. for the second-order correlation:

$$G^{(2)}_\mathrm{coh}(x_1,x_2) = G^{(1)}(x_1,x_1)G^{(1)}(x_2,x_2) = \langle\hat{n}(x_1)\rangle\,\langle\hat{n}(x_2)\rangle\,, \tag{2.25}$$

with the density $\hat{n}(x) = \hat{\Psi}^\dagger(x)\hat{\Psi}(x)$. More generally, a field is called coherent to n-th order, if all correlation functions $G^{(k)}$ for $k \le n$ factorize into densities. It is natural then to make higher-order correlation functions independent of occupations, by normalizing them to densities, defining:

$$g^{(n)}(x_1\cdots x_{2n}) = \frac{G^{(n)}(x_1\cdots x_{2n})}{\prod_{i=1}^{2n}\sqrt{\langle\hat{n}(x_i)\rangle}}, \tag{2.26}$$

[5] For the sake of brevity, here and in the following, the time-dependence of fields will not be explicitly noted. The coordinates x hence shall be understood as points in space *and* time, $x \equiv (\mathbf{r},t)$.

or specifically:

$$g^{(2)}(x_1, x_2) = \frac{G^{(2)}(x_1, x_2)}{\langle \hat{n}(x_1) \rangle \langle \hat{n}(x_2) \rangle}, \tag{2.27}$$

hence, $g^{(n)}(x_1 \dots x_{2n}) = 1 \forall n, x_i$ for a fully coherent state.

In a stationary and homogeneous (or locally approximated, sec. 2.4.3) system, it is very common to write averaged correlation functions as a function of the *distance* between points, e.g.:

$$g^{(1)}(\delta x) = \frac{\int G^{(1)}(x, x+\delta x) \mathrm{d}x}{\int \sqrt{\hat{n}(x) \langle \hat{n}(x+\delta x) \rangle} \mathrm{d}x} \tag{2.28}$$

$$g^{(2)}(\delta x) = \frac{\int G^{(2)}(x, x+\delta x) \mathrm{d}x}{\int \langle \hat{n}(x) \rangle \langle \hat{n}(x+\delta x) \rangle \, \mathrm{d}x} \tag{2.29}$$

The mean-field approximation, i.e. setting $\hat{\delta}(x) = 0$ and $\hat{\Psi}(x) = \psi_0(x)$ in eq. 2.14, is equivalent to *assuming* a coherent state for the matter-wave field, which is hence described appropriately by the GPE, eq. 2.15. In density matrix expansion methods such as that detailed in sec. 4.4, higher-order correlation functions are assumed to factorize as in a coherent field, whereas more complex behavior is allowed for the first (or first few) orders. On the other hand, a thermally distributed (i.e., incoherent) light or matter wave field has $g^{(2)}(x, x) = 2$, which corresponds to photon bunching in the classical Hanbury Brown-Twiss (HBT) experiment [150, 151].

For quasi-condensates, as relevant for this thesis, intermediate cases of $g^{(2)}(x, x) \gtrsim 1$ are typical (sec. 2.4.2), which in the Bogoliubov picture of eq. 2.14 correspond to random interference of $\hat{\delta}(x)$ with the condensate $\psi_0(x)$ and each other. For such systems, second order correlation measurements have been performed in various configurations, mostly focused on HBT-like bunching of particles, and its dependence on the temperature and geometry of the matter wave field [41–43, 64, 152–154]. Note that, however, HBT bunching can still be described in terms of second-order interference of partially coherent classical fields, in contrast to anti-bunching or violations of classical inequalities, where a quantum viewpoint has to be assumed.

2.4. One-dimensional degenerate Bose gas

Over the last years, improved atom trapping techniques such as optical lattices [155–158] and atom chips (see sec. 3.1.2) have enabled detailed studies of Bose gases in the one-dimensional regime, which is a remarkable example for an exactly solvable many-body system [159–161]. The typical conditions for considering a system as one-dimensional are defined by a "freeze-out" of both thermal and interaction energy scales, which are small compared to the transverse trapping strength: $\mu, k_\mathrm{B}T \ll \hbar\omega_\perp$.[6] Along its tranversal directions y, z, the condition $\mu \ll \hbar\omega_\perp$ invalidates the Thomas-Fermi description, and the wave function approaches the single-particle ground state of the confining potential ϕ_0 [93], which for a harmonic trap is a Gaussian with radius

[6] However, as discussed in various experimental and theoretical works, also crossover regions having $\mu \sim \hbar\omega$ [93, 162–164] and/or $k_\mathrm{B}T \sim \hbar\omega$ [133, 135, 165, 166], can be described by slightly modified one-dimensional theories.

$l_\perp = \sqrt{\hbar/(m\omega_\perp)}$. In most situations,[7] the scattering length is well below that radius, $a_\mathrm{s} \ll l_\perp$, implying that the interactions between atoms still have a three-dimensional character [168]. One can then derive an effective one-dimensional interaction constant g_1d by integrating over the transverse wave functions $\phi(y)$ and $\phi(z)$:

$$g_\mathrm{1d} = g \int |\phi(y)|^4 \,\mathrm{d}y \int |\phi(z)|^4 \,\mathrm{d}z \approx 2\hbar\omega_\perp a_\mathrm{s}, \tag{2.30}$$

where the approximation is valid if the transverse wave functions are almost equal to the single-particle harmonic oscillator ground states $\phi(x) \approx \phi_0(x), \phi(y) \approx \phi_0(y)$. A more general expression will be introduced in sec. 4.1.1.

2.4.1. Regimes of a 1d Bose gas

Compared to the 3d case, the ultra-cold 1d Bose gas shows a larger variety of physical regimes. This is to some extent due to the absence of true condensation in the thermodynamic limit (see above), which would mask the rich interplay of interaction and kinetic effects appearing in a degenerate, yet not condensed system. For the moment, we consider the homogeneous case, i.e. a gas of infinite extent (or, somewhat less fictitious, confined to a ring- or box-shaped potential). Its properties are fully defined by the Lieb-Liniger Hamiltonian, which is essentially a one-dimensional version of eq. (2.12):

$$\hat{H}_\mathrm{1d} = \int \mathrm{d}x \left[-\frac{\hbar^2}{2m} \hat{\Psi}^\dagger(x) \frac{\partial^2}{\partial x^2} \hat{\Psi}(x) + \frac{g_\mathrm{1d}}{2} \hat{\Psi}^\dagger(x) \hat{\Psi}^\dagger(x) \hat{\Psi}(x) \hat{\Psi}(x) \right]. \tag{2.31}$$

The regime of a 1d gas can be characterized by two dimensionless parameters, γ and t, which depend on the linear density n and the temperature T. First, we define the Lieb-Liniger parameter γ that quantifies the interaction strength, by relating to each other the typical interaction energy per particle $g_\mathrm{1d} n$, and the kinetic energy scale associated with the density $\hbar^2 n^2/m$:

$$\gamma = \frac{g_\mathrm{1d} n}{\hbar^2 n^2/m} = \frac{m g_\mathrm{1d}}{\hbar^2 n}. \tag{2.32}$$

The second parameter is the temperature T, which can be written in a dimensionless way by defining:

$$t = \frac{2\hbar^2 k_\mathrm{B} T}{m g_\mathrm{1d}^2}. \tag{2.33}$$

Another crucial temperature scale is given by the degeneracy condition $\lambda_\mathrm{dB} n_\mathrm{1d} \sim 1$ (see eq. (2.7)). As a convention, the according degeneracy temperature T_d is defined using the energy $\hbar^2 n^2/(2m)$ associated with the density :

$$T_\mathrm{d} = \frac{\hbar^2 n^2}{2m k_\mathrm{B}}, \qquad t_\mathrm{d} = \frac{1}{\gamma^2}. \tag{2.34}$$

Coarsely, three regimes are distinguished, which can be characterized in terms of their correlation functions [169, 170], and have been studied both theoretically [170–

[7] See e.g. [167] for a notable exception.

176] and experimentally [153, 156–158, 165, 166, 177–182] in quite some detail. Remarkably, *all* of those are encompassed by the exact solution of the Lieb-Liniger model [159, 160] and the Yang-Yang thermodynamic equations [183], the latter giving access to the equation of state, and the same-position second-order correlation function [see eq. (2.29)] $g^{(2)} \equiv g^{(2)}(\delta x = 0)$.

- For $\gamma \gg 1, t \ll 1$, we have a *Tonks-Girardeau* gas [184], which has been realized in optical lattice experiments [156–158, 180], and approached in an atom chip setup recently [182]. The physics here is dominated by strong interactions, leading to a phenomenon of "fermionization", where the bosons avoid occupying the same spatial position (anti-bunching), hence $g^{(2)} \to 0$ similar to ideal fermions. The fact that a *low* density (as $\gamma \propto n^{-1}$) leads to this strong repulsion may seem counterintuitive. It can be understood qualitatively by considering, that avoiding atom overlap becomes favorable, once the required kinetic energy $\hbar^2 n^2/m$ falls below the interaction energy $g_{1\mathrm{d}} n$ that would be caused by overlapping atoms.

- For $t > \gamma^{-3/2}$ (or, equivalently, $T > T_{\mathrm{co}} = \sqrt{\gamma} T_{\mathrm{d}}$) and $\gamma \ll 1$, we are in the *near-ideal* [169], or *decoherent* [170] regime. Here, interactions play a much weaker role, and as in a thermal Bose gas (or, equivalently, in a thermal light field), $g^{(2)} \approx 2$. The near-ideal regime further divides into a *classical* and a *degenerate* range, where the border lies at the degeneracy temperature T_{d}. These subregimes differ strongly in their first-order coherence properties: For the classical, near-ideal gas, the first-order correlation functions $g^{(1)}(\delta x)$ [see eq. (2.28)] drops off as a Gaussian on the scale of the thermal de Broglie wave length. For a degenerate gas, first-order coherence spreads out further, and $g^{(1)}(\delta x)$ decays exponentially on a scale given by $n\lambda_{\mathrm{dB}}^2$, i.e. enhanced by the degeneracy $n\lambda_{\mathrm{dB}}$ compared to the classical range.

- At $\gamma \ll 1, t \ll t_{\mathrm{co}} = \gamma^{-3/2}$ one enters the *quasi-condensate* regime [185]. It is characterized by suppressed density fluctuations, hence $g^{(2)} = 1 + T/(2T_{\mathrm{co}}) \approx 1$, whereas $g^{(1)}(\delta x)$ still decays exponentially due to a fluctuating phase [186, 187], preventing true coherence, or long range order (see below). However, the scale of the decay given by the coherence length λ_{T} is now longer and exceeds the healing length: $\lambda_{\mathrm{T}} \gg \xi_{\mathrm{h}} = \hbar/\sqrt{mng_{1\mathrm{d}}}$. The chemical potential of a quasi-condensate is positive and simply given by $\mu = g_{1\mathrm{d}} n$. At very low temperatures $t \ll \gamma^{-1}$, or $k_{\mathrm{B}} T < \mu$, also the contribution of quantum fluctuations may become significant on short length scales [175]. In this thesis, we will mostly be concerned with quasi-condensates (with a brief exception in sec. 5.6), which will be discussed in more detail in the following.

2.4.2. Quasi-condensates

Given the suppression of density fluctuations in the quasi-condensate regime, the field operator is often written in the form $\hat{\psi}(x) = \sqrt{n(x) + \hat{\delta n}(x)} \exp[i\hat{\theta}]$, where density fluctuation and phase operator are conjugate: $[\hat{\delta n}(x), \hat{\theta}(x')] = i\delta(x - x')$. See ref. [188] for a rigorous definition of the operators. In that paper, this approach was used to

extend the Bogoliubov theory of elementary excitations (as sketched in sec. 2.2.1) to quasi-condensates, where a similar dispersion relation for quasi-particles is found. In agreement with the thermodynamic result [170], it indeed turns out that the contribution of both phononic and free-particle excitations to density fluctuations are suppressed by a factor $\langle \hat{\delta n}^2 \rangle / n^2 \approx T/T_{\mathrm{co}}$.

The exponential decay of the first-order coherence is hence mostly due to fluctuations of the phase. Integrating over contributions from thermally populated modes,[8] the decay of phase coherence can be expressed as:

$$\left\langle [\hat{\theta}(x) - \hat{\theta}(x+\delta x)]^2 \right\rangle \approx \frac{\delta x}{l_\phi}, \qquad l_\phi = \frac{\hbar^2 n}{mT}. \tag{2.35}$$

If we neglect density fluctuations, and assume Gaussian phase fluctuations, the resulting first-order coherence decay can be expressed as

$$g^{(1)}(\delta x) = e^{-\frac{1}{2}\left\langle [\hat{\theta}(x)-\hat{\theta}(x+\delta x)]^2 \right\rangle} \approx e^{-\frac{\delta x}{\lambda_{\mathrm{T}}}}, \qquad \lambda_{\mathrm{T}} = \frac{2\hbar^2 n}{mT} = 2l_\phi, \tag{2.36}$$

with the *thermal coherence length* λ_{T}, which is by construction much larger than the healing length: $\xi_{\mathrm{h}} \ll \lambda_{\mathrm{T}} \lesssim R$.

Th expression (2.36) also predicts the momentum distribution $\tilde{n}(k)$ (with $p = \hbar k$) of the quasi-condensate. The Wiener-Khinchine theorem states that the power spectral density of a function (the randomly fluctuating wave function, in our case) equals the Fourier transform of its autocorrelation, and thus:

$$\tilde{n}(k) = \mathcal{F}\left[g^{(1)}(\delta x)\right] \approx \frac{1}{2\pi}\int \mathrm{d}\delta x e^{-\frac{\delta x}{\lambda_{\mathrm{T}}} - ik\delta x} = \frac{\lambda_{\mathrm{T}}/\pi}{1+\lambda_{\mathrm{T}}^2 k^2}, \tag{2.37}$$

i.e., the momentum distribution, which has been studied e.g. in refs. [165,166,189,190] follows a Lorentzian shape.[9]

2.4.3. Trapped 1d gas

Up to now, we have been discussing the one-dimensional Bose gas in the homogeneous case. To date, experimental realizations have been using (approximately) harmonic confinement, yielding an inhomogeneous density. In the next section, a direct derivation of $g(1)(x, x')$ for a harmonically trapped quasi-condensate will be given. Before, we briefly introduce the more general *local density approximation* (LDA), which can account for the changing values of parameters, including the regime-changing $\gamma, \mu, T_{\mathrm{d}}$ and T_{co}. Assuming that the density varies slowly on the relevant length scales, the basic approach of the LDA is to consider the gas locally homogeneous, and apply the treatment as given above, varying the parameters accordingly. Still, the entire gas is in thermal equilibrium with temperature T and the global chemical potential μ_0. Locally, properties are determined by a *local* chemical potential, that is shifted by the

[8] As a consequence, this treatment does *not* comprise the regime of quantum-noise driven phase fluctuations [179], which however only becomes relevant at very short length scales [175].

[9] Obviously, this can only hold up to a certain cutoff momentum, as otherwise the kinetic energy density, given by the variance or $\tilde{n}(k)$, would be infinite. Indeed, at $k \sim l_\perp^{-1}$, excitations lose their one-dimensional character, which invalidates the quasi-condensate approach.

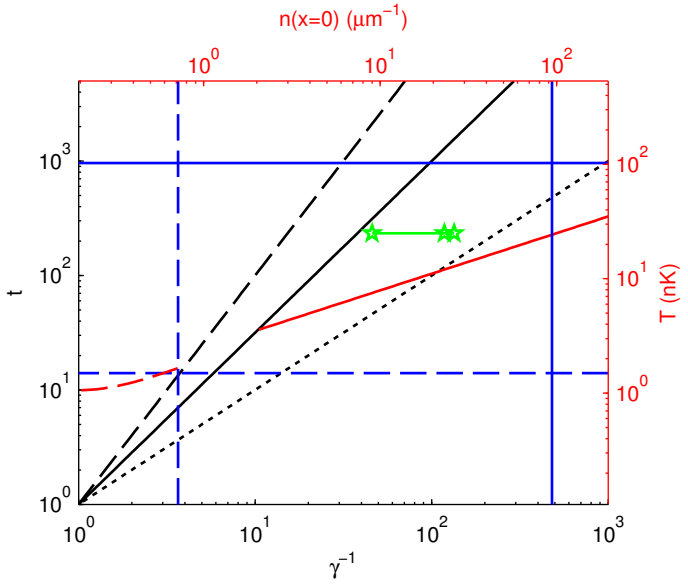

Figure 2.1.: Phase diagram of a weakly interacting one-dimensional Bose gas, as function of γ^{-1}, t (lower and left axes) and n, T (upper and right axes), the latter assuming trapping frequencies $\omega_x = 16.3\,\mathrm{Hz}, \omega_\perp = 2140\,\mathrm{Hz}$, ^{87}Rb and n being the peak density. Black lines: homogeneous/LDA crossover lines, dashed: T_d, solid: T_co, dotted μ/k_B. Red lines: finite-size crossover lines. Solid: T_ϕ (assuming a TF profile), dashed: T_1d (assuming a single-particle ground state profile) Solid blue lines: dimensional crossovers $k_\mathrm{B}T = \hbar\omega_\perp$ (horizontal) and $g_\mathrm{1d}n = \hbar\omega_\perp$ (vertical). Dashed blue lines: LDA validity/finite-size condensation temperature limit (horizontal) and $\mu = \hbar\omega_\mathrm{x}$, $l_\mathrm{x} = \xi_\mathrm{h}$ (vertical). Green line: Estimated range for twin-beam source at $N = 800, T = 25\,\mathrm{nK}$. Markers correspond to the peak density and densities that are exceeded by 50% and 95% of the atom population, respectively.

trapping potential: $\mu(x) = \mu_0 - V_{\mathrm{ext}}(x)$. As a simple example, a quasi-condensate with equation of state $\mu = g_{1\mathrm{d}} n$ acquires a Thomas-Fermi density profile with radius $R = \sqrt{2\mu_0/m\omega_x^2} \propto N^{1/3}$, and $n(x=0) \propto N^{2/3}$, similar to the 3d case (sec. 2.2). However, at the edges where $n(x) \to 0$, the gas leaves the quasi-condensate regime, invalidating $\mu(x) \propto n(x)$, and smoothing out the discontinuity at the edges of the TF parabola.

In ref. [133], a detailed analysis of both the validity limit of the LDA, and the crossover from interaction-induced quasi-condensation to finite-size ideal condensation (see sec. 2.1.2) is given. It is found that both are equivalent (essentially given by the condition that $l_x \gg \xi_{\mathrm{h}}$), and that for realistic parameters in an atom-chip experiment using ^{87}Rb (see fig. 2.1) reaching finite-size ideal condensation seems elusive, and the LDA holds. Furthermore it is found, that the criterion for quasi-condensation in a harmonic trap reads:

$$N_{\mathrm{co}} \approx \frac{T}{\hbar\omega_{\mathrm{x}}} \ln\left(\frac{\hbar^2 T}{m g_{1\mathrm{d}}^2}\right)^{1/3} \tag{2.38}$$

In a trapped quasi-condensate, another characteristic temperature is introduced by the condition, that the first-order coherence length λ_{T} [eq. 2.36] may exceed the typical condensate radius R. In this case, long-range order (in the sense of $g^{(1)}(\delta x) = 1 \forall \delta x$) is approached over the entire system size. One can speak again of a finite-size condensate, even though this effect is very different from the ideal one-dimensional condensation in a finite system (sec. 2.1.2). The condition $\lambda_{\mathrm{T}} \sim R$ leads to the definition:

$$T_\phi = \frac{2n\hbar^2}{m k_{\mathrm{B}} R} \sim \hbar^2 \sqrt{\frac{2\mu_0 \omega_x^2}{m g_{1\mathrm{d}}^2}}. \tag{2.39}$$

In fig. 2.1, the crossover conditions discussed are shown for parameters used in the experiments presented in this thesis. The green markers represent the source cloud for twin-beam production, assuming a LDA viewpoint: the leftmost point indicates the density, that is exceeded by 95% of the total population, whereas the rightmost point is the peak density $\mu_0/g_{1\mathrm{d}}$. It is observed, that almost the entire cloud can be considered as a quasi-condensate with thermal phase fluctuations.

2.4.4. Single-particle density matrix and Penrose-Onsager mode

Having found that the gas we will have to deal with is almost entirely in the quasi-condensate regime, we can use the true finite-size (i.e., non-LDA) quasi-condensate theory developed in ref. [191]. There, the phase operator $\hat{\theta}(x)$ as defined above is decomposed into thermally occupied eigenmodes. Those are given by Legendre polynomials $P_j(x)$, having an energy spectrum ϵ_j as given below. The coherence properties are defined in terms of the single-particle density matrix $\rho(x, x') = \langle \hat{\Psi}(x) \hat{\Psi}(x') \rangle$ [192, 193], which is equivalent to Glauber's non-normalized first-order correlation function $G^{(1)}(x, x')$ as defined in eq. (2.24). Moreover, it can be seen as a restricted density matrix, where all but one particle in the system have been traced out (see sec. 4.4). By

construction, its diagonal is equal to the line density: $n_{1\mathrm{d}}(x) = \rho(x,x)$. One obtains:

$$\begin{aligned}
\rho(x,x') &= \sqrt{n(x)n(x')}\exp\left[-\langle[\hat{\theta}(x)-\hat{\theta}(x')]^2\rangle/2\right], \qquad (2.40)\\
\langle[\hat{\theta}(x)-\hat{\theta}(x')]^2\rangle &= \sum_{j=1}^{\infty}\frac{g_{1\mathrm{d}}(j+1/2)}{2\epsilon_j R}\left[P_j(x/R)-P_j(x'/R)\right]^2(1+2N_j^{(\mathrm{B})})\\
&\approx \frac{4T_\mathrm{d}}{3\hbar\omega_\mathrm{x}}\left|\log\left[\frac{(1-x'/R)(1+x/R)}{(1+x'/R)(1-x/R)}\right]\right|,\\
\epsilon_j &= \hbar\omega_\mathrm{x}\sqrt{j(j+1)} \qquad N_j^{(\mathrm{B})} = [\exp(\epsilon_j/T)-1]^{-1}.
\end{aligned}$$

R and μ are Thomas-Fermi radius and chemical potential, respectively. In the third line, an approximation has been made, where quantum fluctuations are neglected (i.e., only thermal fluctuations remain), which is well satisfied for length scales of interest [175]. The single-particle density matrix is directly related to $g^{(1)}(\delta x)$ as discussed above [eq. (2.36)], but, crucially, instead of $\delta x = |x-x'|$ only, it is now explicitly defined for two arbitrary points x, x' in the inhomogeneous system.

An alternative notion to that of the quasi-condensate as a phase-fluctuating BEC, is provided by decomposing the total system into the eigenmodes of its single-particle density matrix, also known as *natural orbitals* [193]. In this picture, quasi-condensation is equivalent to the appearance of a macroscopic eigenvalue of the single-particle density matrix, generalizing the notion of condensation of an ideal gas into a single-particle eigenstate. The corresponding mode, called *Penrose-Onsager* (PO) mode [136, 183, 194], now comprises the first-order coherent, long-range-ordered part of the system, and can be split from the rest of the field:

$$\rho(x,x') = N_\mathrm{c}\psi_\mathrm{c}^*(x)\psi_\mathrm{c}(x') + \rho_\mathrm{th}(x,x'). \qquad (2.41)$$

Its population N_c is always lower than that that of the quasi-condensate N_qc; the latter is defined by the part of the system that has suppressed density fluctuations, i.e., for a system sufficiently below T_co, we have $N_\mathrm{qc} \approx N$, see sec. 2.4.2. In eq. (2.41), $\rho_\mathrm{th}(x,x')$ denotes the "thermal" component of the quasi-condensate, however, it shall be noted, that this is a very different concept from e.g. a (transversely excited) thermal cloud around a (quasi-)condensate, or the non-degenerate "thermal" portions of a one-dimensional gas (sec. 2.4.1).

For our system, if the parameters are known, one can numerically compute population N_c and wave function $\psi_\mathrm{c}(x)$ of the PO mode (and higher modes). The decomposition of the system into a long-range-ordered and an incoherent part will be the key to quantitatively understand twin-beam emission in sec. 5.5.

Some results for typical values are shown in fig. 2.2. There, it has been used that the single-particle density matrix can be easily transformed into momentum space [193], or propagated in free expansion for a certain time of flight t_tof, during which the cloud expands ballistically [174]:

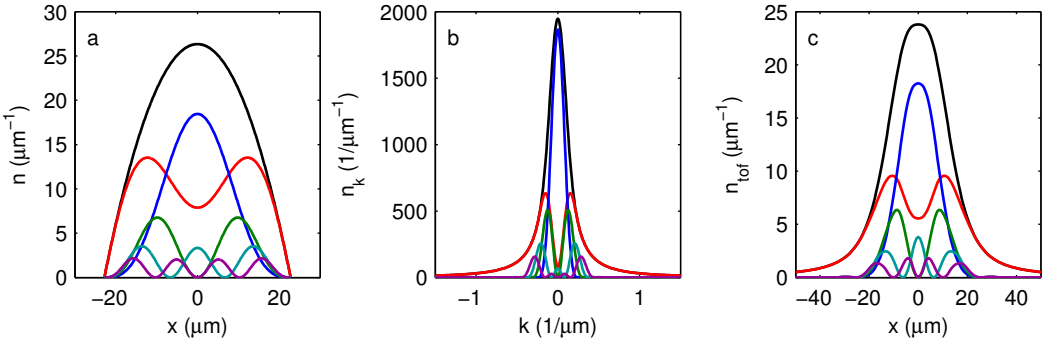

Figure 2.2.: Single-particle eigenmodes (natural orbitals) of quasi-condensate density matrix, shown in (a) real space, (b) momentum space, (c) real space after 46 ms of ballistic propagation. Note that the shown spatial range in (c) corresponds to the shown momentum range in (b) as $x_{\max} = \hbar k_{\max} t_{\mathrm{tof}}/m$. Parameters are $N = 800, T = 25\,\mathrm{nK}$. Black lines: total density. Blue lines: PO mode density. Red lines: non-PO density. Other lines: densities of three largest non-PO modes.

$$\tilde{\rho}(k,k') \propto \iint e^{-ikx} e^{-ik'x'} \rho(x,x') \mathrm{d}x \mathrm{d}x', \tag{2.42}$$

$$\begin{aligned} \rho(x,x';t_{\mathrm{tof}}) &\propto \iint e^{i(kx-\hbar t_{\mathrm{tof}} k^2/2m)} e^{i(k'x'-\hbar t_{\mathrm{tof}} k'^2/2m)} \tilde{\rho}(k,k') \mathrm{d}k \mathrm{d}k' \\ &\propto \iint e^{i\frac{m}{2\hbar t_{\mathrm{tof}}}(x-x'')^2} e^{i\frac{m}{2\hbar t_{\mathrm{tof}}}(x'-x''')^2} \rho(x'',x''') \mathrm{d}x'' \mathrm{d}x'''. \end{aligned} \tag{2.43}$$

It can be observed, that while the PO mode spreads over most of the condensate length spatially, its momentum distribution is very narrow compared to the total quasi-condensate, corresponding to the absence of a fluctuating phase. In time of flight at $t_{\mathrm{tof}} = 46\,\mathrm{ms}$, an intermediate case is reached.

3. Experimental implementation

In this chapter, a brief description of the experimental setup (Rb-II) at which the measurements presented in this thesis have been performed, will be given. The focus will be on aspects that are of particular importance for the excitation and twin-beam emission scheme, and on recent updates that are not sufficiently covered in previous theses. While sec. 3.1 focuses on the different hardware parts, some experimental techniques typically used are sketched in sec. 3.2. For more detailed information, the reader is referred to the following theses, which have been carried out both in Heidelberg (from 2002 to 2006) and in Vienna (starting from 2007), and spawned a large series of publications [21, 78, 153, 179, 195–206]:

- The initial design of the Rb-II machine, and a lot of practical aspects concerning atom chip experiments are covered in the PhD theses of Peter Krüger [207] and Stephan Wildermuth [208]. Some more specific information can be found in diploma theses written by Harald Gimpel [209], Christiane Becker [210], Sebastian Haupt [211], and Sebastian Hofferberth [212].

- In Thorsten Schumm's [213] and Sebastian Hofferberth's [214] PhD theses, radio-frequency dressed potentials have been implemented for the first time, which are a key technique for the experiments in the present work. Also, extensive information on different trap geometries can be found there.

- Manufacturing techniques for atom chips, including that in our experiment [200], have been discussed by Sönke Groth [215].

- After the move to Vienna, several changes have been made to the setup, including a new atom chip. The upgrades performed alongside the reconstruction are detailed in PhD theses by Stephanie Manz [216] and Thomas Betz [217], and the author's diploma thesis [218], that are specifically recommended for information about the general setup, radio-frequency dressing, and imaging systems, respectively.

- The experiment control system is described in the diploma theses of Mihael Brajdic [219] and Wolfgang Rohringer [220], the latter including a novel approach for automatized experiment optimization, using a genetic algorithm.

3.1. Hardware of the Rb-II machine

In the following, the several hardware parts of the Rb-II setup will be described, with some more details and characterizations at points that are particularly relevant for the experiments in this thesis.

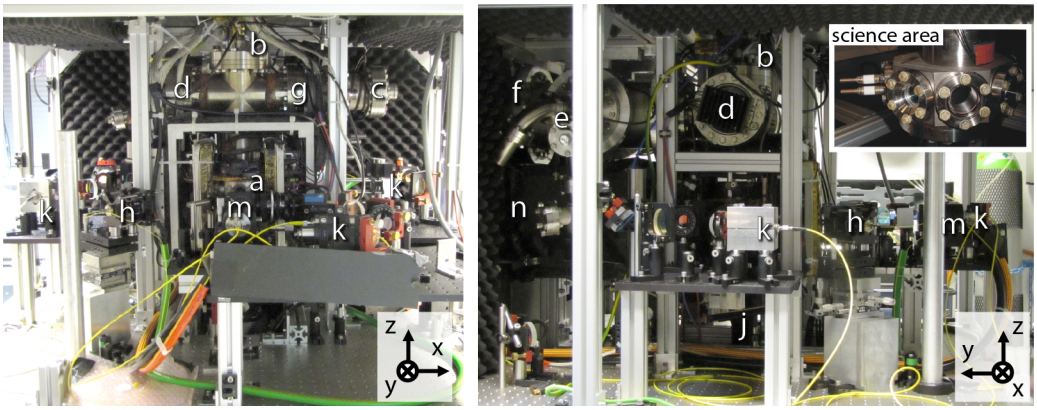

Figure 3.1.: Picture of the Rb-II setup. Left: front view, right: side view. a: science area, surrounded by Helmholtz coil pairs, b: chip mounting flange, c: Ti-sublimation pump, d: LIAD viewport, e: cluster flange with vacuum valve and ion gauge, f (behind panel): ion getter pump, g: NEG pump, h: light sheet illumination oxptics, j: light sheet objective (facing upwards), k: various fiber couplers for optical pumping beams, m: fiber coupler for absorption imaging, n (behind panel): absorption imaging camera. Inset: science area (octagon) with viewports and dispenser current feedthrough (left), photograph taken before assembly of the experiment setup.

3.1.1. Vacuum chamber and atom source

Compared to previous setups, the basic design of the experiment apparatus was simplified by using a single vacuum chamber only; all steps of the experimental sequence (see sec. 3.2.3) take place at the same position. The stainless steel chamber as depicted in fig. 3.1 can be roughly separated in a large-volume upper area, that mostly contains devices to maintain vacuum, and a lower part where the actual science takes places. The upper part contains a large-volume ion getter pump,[1] a water-cooled tube containing Titanium filaments (Titanium sublimation pump, TSP) which are heated every few weeks, a passive non-evaporative getter (NEG) pump,[2] an ion vacuum gauge, a valve to attach a turbo molecular pump, and a large viewport with a rubidium dispenser directly behind, to be used as a light-induced desorption source (LIAD), which however has not been implemented yet. A large flange allows to insert the chip mounting (see sec. 3.1.2), which places the chip hanging upside-down into the lower (science) area of the chamber. There, it is surrounded by an octagon-shaped chamber (see inset of fig. 3.1), containing anti-reflection coated viewports with at least 1" of clear aperture on seven of its faces, and Rubidium dispensers on the eights. The viewports provide optical access for the magneto-optical trap (MOT), optical pumping, and imaging beams. At the bottom of the chamber, a large window provides further optical access for fluorescence imaging and MOT beams.

For experiments with Bose-Einstein condensates, a low background pressure of the order of 10^{-11}mbar is required to prevent loss and heating during evaporative cooling due to collisions with room-temperature background atoms. On the other hand, for efficient loading of the magneto-optical trap, a higher Rubidium vapor pressure (on the order of some 10^{-9}mbar) is necessary. This is achieved by pulsing of the Rubidium dispensers at the beginning of each experiment cycle, emitting Rubidium vapor at a few 100° C.

The low-velocity tail of this thermal distribution can be captured by the MOT. After typically 17 s, the dispensers are switched off, and the MOT is held for another 1.5 s to allow the vacuum pumps to capture the remaining Rubidium vapor. At this point, the actual cooling sequence starts, which will be described in sec. 3.2.3.

3.1.2. Atom chip

At the heart of the Rb-II setup lies a double-layer gold atom chip [221], which will be described in the following. More general remarks on trapping and manipulation techniques for atom chips can be found in secs. 3.2.1 and 3.2.2.

Rb-II chip design The atom chip which is in use at Rb-II since the move to Vienna has been designed and manufactured in collaboration with the group of I. Bar-Joseph at the Weizmann institute. It provides gold wires on two layers, that are insulated from each other to allow wire crossings. Details on the manufacturing technology are explained in ref. [200] and the thesis of Sönke Groth [215]. Characterization in the actual experiment, including an assessment of its practical performance is given in Stephanie Manz' PhD thesis [216]. The basic layout is sketched in fig. 3.2, some

[1] Varian StarCell, 500 L/s
[2] SAES Getters

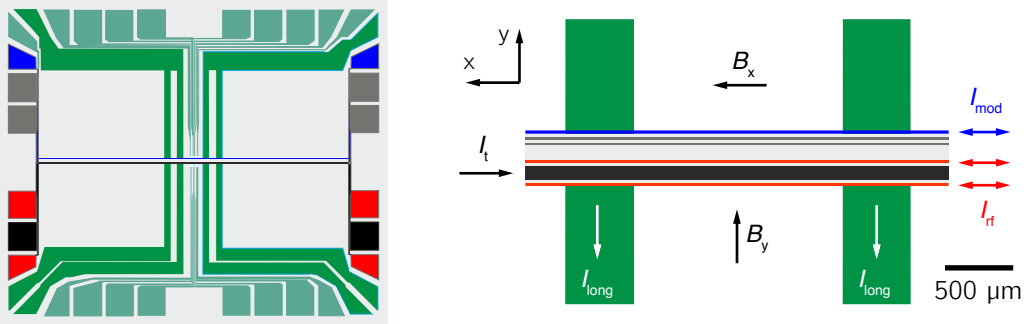

Figure 3.2.: Chip wire schematic, viewed along z. Left: overview. Connection pads are placed all around the chip, with central regions spared to avoid obstruction of imaging beam paths. The red, green, blue, and black pads and wires correspond to the wires used for the experiments in this thesis. Faint green wires connect to the inner part of the lower chip layer which contains electron-beam lithographed sub-micron structures. Right: inner part, where the actual experiment takes place. Black: main trapping wire. Green: longitudinal confinement wires. Red: radio-frequency wires. Blue: trap position modulation wire.

photos are shown in fig. 3.3. As the main structure for trapping, it uses a straight wire (along x) of 80 µm width on the upper chip layer in conjunction with a pair of perpendicular (along y) wires on the lower layer, of 500 µm width. The latter provide weak longitudinal confinement along x. Wires running alongside the trapping wire can be used as antennae for radio-frequency dressing (see sec. 3.2.2), as well as additional modulations. Both will be key ingredients to the experiments performed in the present thesis. In addition to the wide longitudinal confinement wires, the lower chip layer contains an area manufactured by electron beam lithography, comprising sub-micron structures for creation of versatile potential landscapes. Of those, only two 18 µm wide wires have been actually used, that allow to prepare crossed-wire dimple traps for traps with low, tunable aspect ratio, allowing to span both three- and one-dimensional regimes of Bose gases (see sec. 2.4), as in ref. [43]. Also, they can be used to excite collective longitudinal modes for trap characterization, as will be described below. All DC chip wires are driven by custom-designed current sources, the supply voltages of which are provided by car batteries to reduce noise that might be introduced from the power network.

Chip mounting and copper wires The chip mounting structure as shown in fig. 3.3(a-c) is hanging upside down in the vacuum chamber. It is based on a vacuum flange with feedthroughs for high-current (up to 60 A) copper wires, a 36-pin connector for low-current chip wires, and cooling water. Connected to the feedthroughs are rigid copper rods and thin, Kapton-insulated wires, that lead to the upper (or, once mounted in the experiment, lower) part of the mounting. There, chip wire connection pins and big copper wire structures (see panel c) are embedded into a block machined from a ceramic material (Shapal), that provides good heat conductivity while being electrically insulating. The chip is glued on top of this block, and connected using aluminum wires that have been attached using ultrasonic bonding, to minimize mechanical and

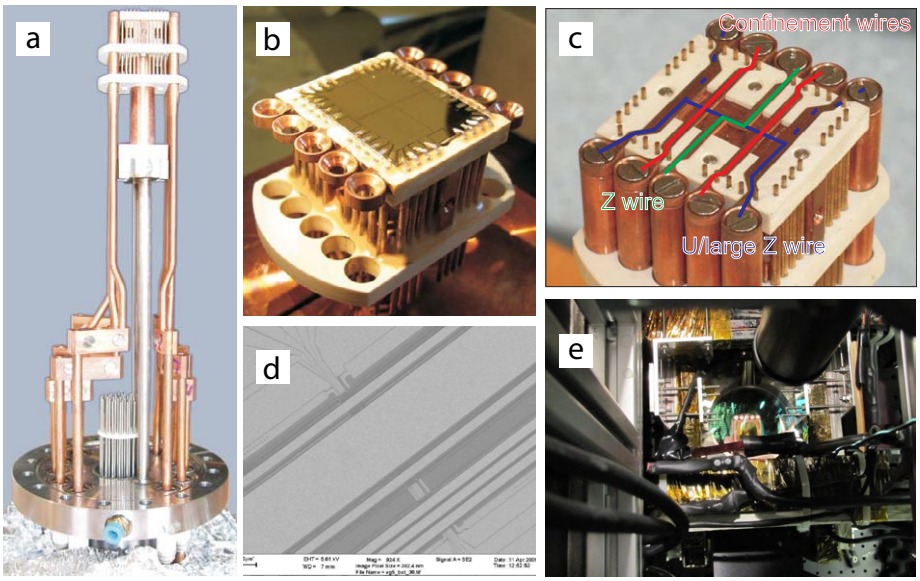

Figure 3.3.: Photos of the atom chip and its mounting. (a) Chip mounting structure. At the bottom, the vacuum flange with feedthroughs for high-current copper rods and chip wires is seen. The steel tube in the center can be used for water cooling. Near the top, the copper rods and chip connection pins are guided by a custom-machined ceramic (Shapal) block. (b) Atom chip, glued to ceramic mounting block. Near the edges of the atom chip, bond wires between connection pins and pads on the chip are seen. (c) Copper structures underneath the atom chip. Z-, U- and outer confinement wires are traced in green, blue, and red, respectively. (d) SEM image of the chip center, where the central trap wire (width 80 µm) and parallel 10 µm-wires cross the electron-beam lithographed area. (e) Picture of chip built into the vacuum chamber, taken from below. Coils for magnetic fields are surrounding the chamber; in the top right corner the imaging objective for fluorescence imaging is seen, which is placed close to the vacuum window when operating.

thermal stress during the connection process.

The copper wires embedded in the mounting block are used to provide inhomogeneous magnetic fields as needed during different parts of the experimental sequence (sec. 3.2.3):

- The largest structure has an H-shape with a broad (1 cm) central part [blue lines in fig. 3.3(c)] along the x-direction. Its shape is optimized for creating a quadrupole field as needed for the magneto-optical trap (MOT) next to the chip surface. This is achieved by connecting the structure in a U-shaped geometry, and superimposing an external homogeneous field in the yz-plane [195, 210]. Moreover, the structure is used as an antenna for radio-frequency evaporation.
- In the central part, a smaller Z-shaped structure is placed, separated from the H-structure by a thin gap (green line). In conjunction with external fields along y and x, running current through it creates a Ioffe-Pritchard field configuration [8] for the first stage of magnetic trapping and evaporative cooling.
- On each side of the Z-structure, straight wires running along y are placed, that can be used for a multitude of tasks, such as providing additional longitudinal confinement, or pulsed application of an inhomogeneous field for Stern-Gerlach-type separation of magnetic states during expansion.

3.1.3. Laser system

While in an atom chip experiment the trapping and evaporative cooling of atoms is achieved solely by magnetic means, lasers are still needed for pre-cooling, optical pumping, and imaging of the atoms. In our setup, two principal laser sources are used, the frequencies of which are tuned next to the resonances between the two hyperfine states $F = 1, 2$ of the electronic ground state $5^2S_{1/2}$, with the electronic excited state $5^2P_{3/2}$, respectively. Hence, the frequencies of both lasers differ by the hyperfine level spacing of $\nu_{\mathrm{hf}} = 6.83\,\mathrm{GHz}$. The hyperfine level separations of the electronic excited state are small enough to be addressed by frequency-shifting elements later in the beam paths. Both lasers are external cavity diode lasers (ECDLs). While for the $F = 1$ source ("repumper") a simple high-power diode laser[3] is sufficient, the $F = 2$ source ("cooler"), which has to drive the main cooling transition of the MOT, uses a master oscillator/powered amplifier (MOPA) configuration,[4] where a relatively weak ECDL laser seeds a high-power tapered amplifier (TA). Both lasers are independently locked to Doppler-free saturation spectroscopies using Rubidium vapor cells, and coupled into single-mode fibers. At the fiber output, we typically obtain $\sim 50\,\mathrm{mW}$ of optical power from the repumper laser, and $\sim 500\,\mathrm{mW}$ from the cooler.

Subsequently, both lasers are distributed between different paths by half-wave plates and polarizing beam splitters. Each path is then guided through acusto-optical modulators (AOMs) that allow to shift the frequency, and rapidly switch the power of each beam. For the cooler and imaging paths, double-pass AOMs are used for shifting the frequency over some tens of MHz during the experimental cycle, without the need for geometrical readjustment. In fig. 3.4, the optical setup is shown schematically; fig. 3.5

[3] Toptica Photonics, DL100
[4] Toptica Photonics, TA100

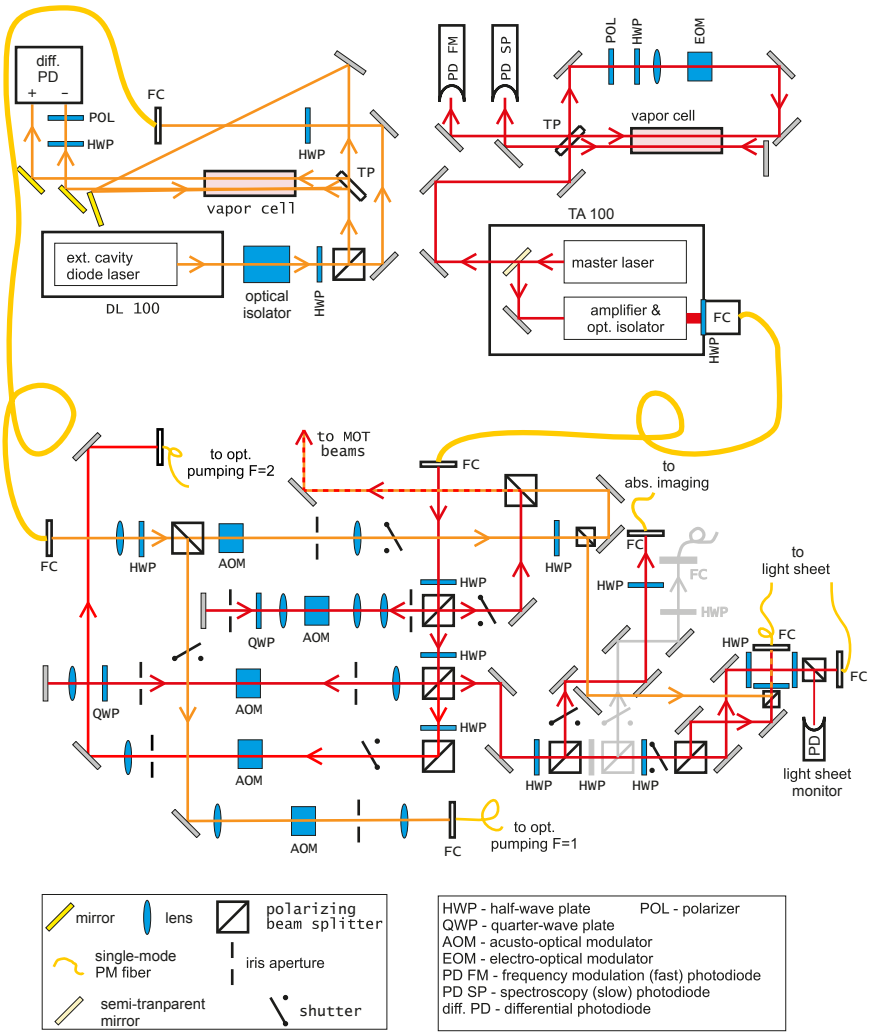

Figure 3.4.: Laser setup (updated version of fig. 2.2 in ref. [218]). Red and orange lines indicate $F = 2$ (cooler) and $F = 1$ (repumper) beam paths, respectively. The greyed-out parts belong to the former longitudinal imaging, which is not in use currently. The upper part of the drawing shows the laser spectroscopy setups for the $F = 1$ (left) and $F = 2$ (right) lasers, which are placed in a separate box to provide better thermal and acoustic isolation from the environment. The $F = 2$ laser uses a dual spectroscopy setup to simultaneously provide a normal Doppler-free spectroscopy and an additional path for Pound-Drever-Hall locking using an EOM for sideband modulation [209]. Both lasers are coupled into single-mode polarization-maintaining fibers and brought to the AOM and beam distribution setup shown in the lower part. Finally the beams are guided to their destinations by free-field beam lines (MOT) or single-mode fibers (imaging, optical pumping).

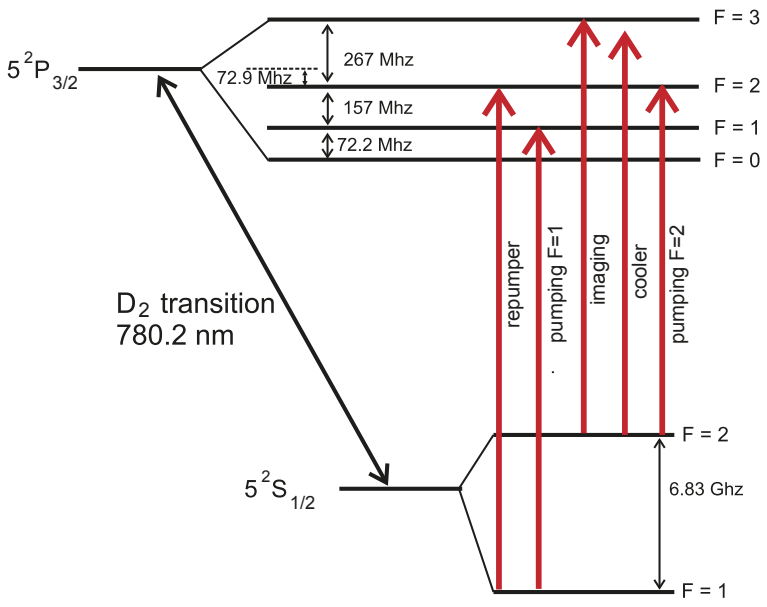

Figure 3.5.: Hyperfine levels of the Rubidium-87 D2 line. Red lines indicate the transitions addressed by the different laser beam paths. (updated version of fig. 3.3 in ref. [216]).

depicts the frequencies of the beam paths. In sec. 3.2.3 the application of each of the beams will be explained.

3.1.4. External fields

During all phases of the experimental sequence, homogeneous offset fields are needed to complement the inhomogenoeus fields created by the chip and copper structure wires. Those are provided by external Helmholtz coil pairs.

Coil setup Around the science area of the chamber, two complete sets of coil pairs along each spatial direction are mounted (amounting to 12 coils in total, see fig. 3.1). One of those sets is fabricated from thick (cross sections of tens of mm^2) wires and allows to create homogeneous offset fields up to some tens of Gauss. The second set uses thin wires and is used to provide small offset fields up to a few Gauss. Having two sets of coils is convenient especially during points in the experiment cycle, where fast switching between field configuration (both in magnitude and direction) are required on a time scale that cannot be met by the output regulation of the current sources, given the high inductive load. Also, it allows to use unipolar supplies,[5] and a good matching of their voltage and current ranges to the requirement for the respective coil. A fast switch-off time of the coils (typically below 0.1 ms) is achieved using additional solid-state (FET) switches [222], which can stand up to 60 A of continuous current, and induced voltages up to 400 V during rapid switch-off.

[5] HP/Agilent 65xx series, with the exception of the small vertical coil, where a bipolar supply (High-Finesse BCS-5/5) is still advantageous.

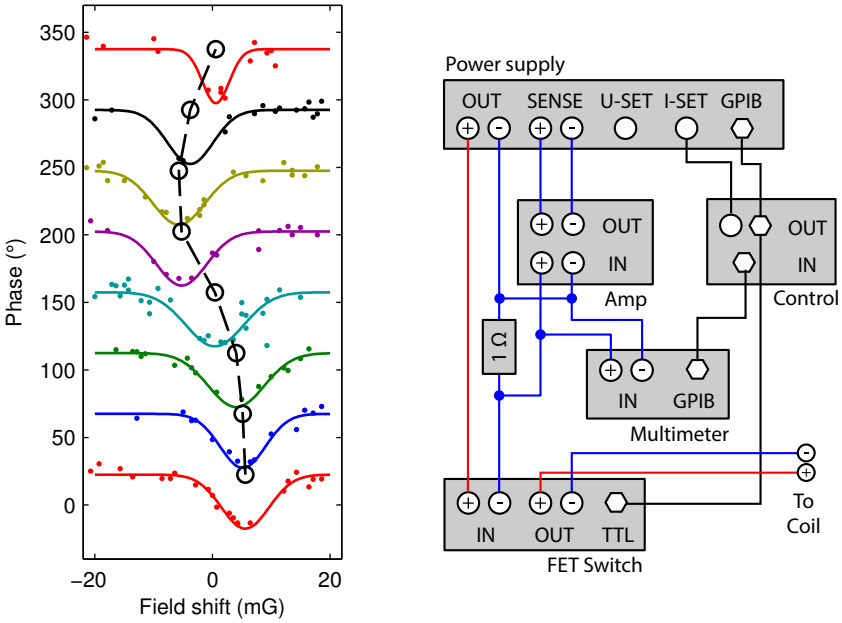

Figure 3.6.: Stabilization of the Ioffe field. Left: trap bottom spectroscopy measurement (see sec. 3.2.2), taken with direct current stabilization at the power supply (i.e., without using the external test resistor), and binned according to the power network phase during the short (1 ms) radio-frequency pulse (dots). For each bin, the points are normalized and re-scaled; their vertical base line shift corresponds to the phase of the power network that the bin is centered on. The black dashed lines with circles indicates the peak position of atom loss, as determined from Gaussian fits (solid lines). The x-axis is given in magnetic field corresponding to the applied radio frequency, shifted by an arbitrary amount. Right: schematic of the stabilization circuit finally used in the experiment. Empty round and hexagonal symbols represent analog and digital control connectors, respectively.

Ioffe field stabilization Most of the coil (and copper wire) power supplies run in current-stabilized mode, with set points controlled by analog inputs of the power supplies. At the expense of potentially increased low-frequency noise, this provides direct control and good drift stability of the magnetic fields (that would be affected by thermal drifts and the non-ohmic resistance of the solid-state switches otherwise), and thus reproducibility of experiments over a long time span.

The single exception is the small x-directed coil ("Ioffe" coil), which serves to control the offset field, and hence the atomic Larmor frequency ν_L, of the chip trap (see sec. 3.2.1). For this coil, long-term stability and rejection of low-frequency noise at the sub-Milligauss level are of utmost importance, especially when using dressed traps, where the potential shape is defined by the detuning of the radio frequency with respect to the Larmor frequency (see sec. 3.2.2). While the former goal would be achievable using output current stabilization (as for the other fields), the latter is compromised due to the inductive load and the output capacity of the supply forming a resonant

circuit with quality factor

$$Q = \frac{1}{R}\sqrt{\frac{L}{C}} \approx \frac{1}{3.3\ \Omega}\sqrt{\frac{4.5\,\mathrm{mH}}{550\,\mu\mathrm{F}}} \approx 0.9, \tag{3.1}$$

that may lead to ringing of the stabilization electronics, specifically at the 50 Hz power network frequency. This quality factor exceeds the specification of the used power supply of $Q \leq 0.5$. Indeed, when measuring the low-frequency noise spectrum in the coil circuit, a dramatic peak at 50 Hz is found, that disappears when stabilizing the clamp voltage of the supply instead. First runs of the optimal control excitation (see sec. 5.4) yielded unsatisfying results due to poor shot-to-shot stability of the dressed potential (see fig. 3.11), that stems from the random relative phase of the power network at the time where the excitation sequence is applied. Also, running short-pulsed trap bottom (Larmor frequency) measurements (see sec. 3.2.2) when recording the power network phase at the end of each experimental cycle revealed a phase-dependent shift of ~ 10 mG peak-to-peak amplitude (fig. 3.6).

To mitigate this issue while keeping good long-term reproducibility, we chose to insert a high-precision test resistor[6] in series with the coil and the switch, and feeding back the voltage drop over the resistor into the voltage sensing port of the power supply. The supply is set to stabilize the voltage drop, effectively restoring a current stabilization, which was found to be much less prone to ringing, presumably due to the large test resistance of 1 Ω. Using this method, and analog (CV) control of the voltage set point, a decrease of the ringing peak at 50 Hz by −22 dB was achieved, sufficient to run the excitation sequence successfully. Later, this scheme was improved further, by disabling the analog voltage control circuit entirely, and instead programming the power supply set point digitally (using a GPIB connection), see fig. 3.6 (left).[7] A further reduction by −18 dB was found, leading to a rejection of ringing similar to that achieved with clamp voltage stabilization. Due to insufficient resolution of the digital control, an additional amplification (of the order of 10) of the resistor voltage drop had to be introduced, using a low-noise pre-amplifier,[8] and yielding an effective set point resolution of ~ 1 mG. During early phases of the experiment, where offset fields lower than the final one are required but low-frequency noise is acceptable, the current is stabilized by the power supply directly, in order to avoid re-programming the supply during the cycle.

To ensure proper operation and long-term stability, the test resistor voltage drop is monitored during the final phase of the cycle using a multimeter.[9] In each experiment cycle, 100 measurements of 6 ms averaging time each are taken in rapid succession. Mean and standard deviation of the outcomes are automatically recorded, where a magnitude of the latter of more than some tens of ppm (or, in absolute numbers, tens of Microgauss) indicates a malfunction. Additionally, the phase of the power network at the end of the experiment is recorded in each cycle. A data set is considered invalid, if any significant correlation between this value and a single-shot observable (such as atom number, temperature or shape of the cloud) is found in post-processing.

[6] Isabellenhütte RUG-Z, temperature coefficient < 1 ppm/K

[7] This second scheme has been used in all measurements presented in chapter 5, except for data set Sqz.

[8] Stanford SR560, or Femto DLPVA

[9] Keithley 2000

3.1.5. AC electronics

In the experiment, modulated currents are needed for various purposes; for the experiments presented in this thesis, this comprises radio-frequency fields for evaporative cooling ($0.5 - 20$ MHz) and dressed potentials ($\sim 800\,\mathrm{kHz}$), as well as chip currents for trap position modulation (DC $-$ 4 kHz).

Signal generation As initial signal sources for all modulated currents in the experiment, digital arbitrary waveform generators[10] are used. They are set to a sequenced mode: once a TTL trigger is received, a programmed series of arbitrary wave forms is played back with a given number of loops at each step. In this way, even for long and complex sequences, such as the radio-frequency ramp for evaporative cooling which lasts several seconds, each single sample at the output (at a sampling rate of tens of MHz) is explicitly defined. The way the sequence is composed differs among the various applications:

- For radio-frequency dressing, the sequence consists of short waveforms, containing a single sinusoidal cycle each, that are looped to fill a given time with a constant signal, and longer waveforms, e.g. containing amplitude ramps at the beginning and end of the dressing field application. The phase of the wave can be defined arbitrarily, affecting the behavior after switching off the potential [217]. In this way, also complex sequences of trap deformations with various intermediate ramps can be realized, as e.g. needed for interferometry schemes [223]. A two-channel generator with independent waveform sequences, but locked sample clocks is used, to be able to address the two dressing antenna wires (see sec. 3.2.2) independently in terms of phase and amplitude.

- The radio-frequency signal needed for evaporative cooling cannot be synthesized in this way, as the frequency is constantly changing for several seconds, and the internal memory of the generator is not sufficient to store each single sample during this time.

  Instead, we program a sequence of cosine waveforms, that span the appropriate frequency range, creating a ramp of discrete frequency steps, where the length of each step is determined by the number of loops. Over most of the range, the frequencies of the waves are distributed roughly exponentially, i.e. keeping the relative step size constant. For the lowest frequencies (few hundreds of kHz), the step size is decreased further, down to a value of $\sim 0.5\,\mathrm{kHz}$, below the typical transverse level spacing of elongated traps. The final evaporation frequency, which controls atom number and temperature of the prepared gas, can be set to arbitrary accuracy, using a slight adjustment of the sample clock. While this sequenced scheme requires some rather complex programming (especially given certain restrictions of the generator that shall not be discussed here), it allows for completely arbitrary frequency ramp shapes, that are of crucial importance to achieve efficient cooling (see sec. 3.2.3).

- For trap position modulation such as the excitation sequence in the experiments presented in part II of this thesis, a simple sequence of two waveforms is sufficient,

[10] Tabor Electronics, WonderWave series

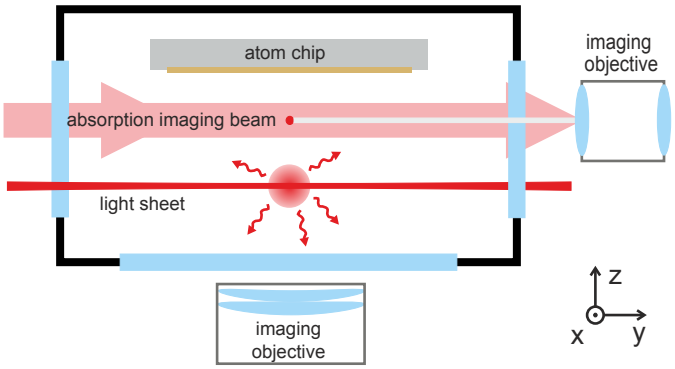

Figure 3.7.: Sketch of imaging systems (modified version of fig. 3.9 in ref. [216]). Having been released from the chip trap, the cloud falls in $-z$-direction. For expansion times roughly between 1.5 ms and 25 ms, the attenuation of an absorption beam due to the atoms can be imaged. If fluorescence imaging is used, after an expansion time of 46 ms, the atoms pass a thin light sheet in the xy-plane, and start emitting photons. They are imaged using an objective sitting underneath the vacuum chamber, facing upwards. (The different parts shown are not drawn to scale.)

the position modulation ("shaking") sequence itself being the first, and a constant value corresponding to the final position of the trap being the second. The latter is looped for the remainder of the experiment cycle time.

Signal transmission Each output of the dressing generator is driving its respective chip wire without further amplification. The connection is made through additional RF-switches,[11] and 1:1 isolation transformers,[12] the latter providing a floating ground for the chip wires. On the secondary side of the transformer, inductive current probes[13] are placed, allowing to monitor the AC current through the chip wires. The evaporation RF signal is fed to the copper U-structure [fig. 3.3(c)] capacitively, achieving a current of up to 200 mA peak-to-peak amplitude. For the modulation wire, the generator signal is fed through a custom-made DC isolation amplifier into the control input of a battery-driven current source identical to those used for the DC chip wires. The isolation amplifier is necessary for galvanic isolation of the generator output from the chip wire, but limits the bandwidth of the applied signal to $\lesssim 4$ kHz. The impact of this filtering will be discussed in sec. 5.4.1.

3.1.6. Cameras

Besides an auxiliary camera to image the fluorescence of the MOT and optical molasses, two independent imaging systems are implemented in the experiment, see fig. 3.7. Detailed technical information about both can be found in the author's diploma thesis [218], and only few basic characteristics shall be repeated here. In sec. 5.1, some more practical aspects of using the two systems are discussed.

[11] MiniCircuits ZX80-DR230-S+
[12] MiniCircuits T1-1T
[13] Tektronix CT-6

Absorption imaging A high-resolution absorption imaging system is placed along the y-axis, allowing to take images at expansion times extending from roughly 1.5 ms to 25 ms. At even shorter times, reflections of the imaging light at the chip surface cause distortions (which could possibly be mitigated using a tilted imaging beam [224]). The objective is composed of two stock doublet lenses, each operating at near-infinite conjugate ratio. Using one-inch optics at $\sim$ 100 mm working distance, it reaches a numerical aperture (NA) of 0.12. The focal lengths are arranged to obtain a magnification of $\times 3.78$ and an object space pixel size of 3.44 µm. Calibration of the pixel size, which is crucial for quantitative image analysis (see sec. 3.2.4) is performed using the light sheet beams as a ruler, which are made visible by fluorecence from thermal background atoms. A cooled, back-illuminated CCD camera[14] with 1024×1024 pixels resolution provides a field of view of $\sim$ 3 mm edge length, which is sufficient to image warm thermal clouds at the beginning of evaporation after short expansion times. Also, the CCD supports frame-transfer readout, allowing to take two images (absorption and reference) in rapid succession (tens of ms).

Fluorescence imaging The system mainly used for the experiments presented below uses a unique fluorescence scheme, where atoms fall through a thin (20 µm waist radius) light sheet after tens of ms of expansion [202]. Some of the emitted fluorescence photons are captured by an objective placed underneath the vacuum chamber. This method avoids the problem of blurring due to finite depth of field, that would occur if the entire (expanded) cloud was imaged simultaneously with a high-NA objective. Also, it becomes possible to take slice images by pulsing the sheet only briefly [43]. Given the NA of the objective of 0.34, the transmission of all surfaces, and the quantum efficiency of the used EMCCD camera,[15] about 2% of the emitted photons are detected. For typical parameters, this gives us $\sim$ 12 detected photons per atom, which, given the extremely low background of the system, is sufficient for single-atom sensitivity [202]. The intensity of the light sheet is stabilized using a photodiode (see fig. 3.4), that receives some light separated off the beams going to the light sheet launchers (via single-mode fibers), which is read out in each experimental cycle, feeding back on the RF power setting of the respective AOM.

Compared to the first version as presented in ref. [218], the imaging objective has been modified to adapt to more recent experiment requirements, doubling the magnification to $\times 4$, to yield an object-space pixel size of 4 µm. At the expense of a smaller field of view, the reduced pixel size provides a higher oversampling of the inherent resolution limit (see sec. 3.2.4), simplifying several analysis schemes (such as shot-noise rejection, see appendix C). Some characteristics of the objective are collected in fig. 3.8. The main change with respect to the initial $\times 2$ version is the last lens in the beam path. In the first version, a positive meniscus lens close to the CCD was used to reduce magnification. This lens has been replaced by a negative meniscus lens closer to the front group of elements, which changes the system from a retro-focus to a (weak) tele-photo configuration, doubling magnification, while leaving the rest of the design unchanged. As becomes clear from the lower left panel in fig. 3.8, the depth of field of the objective matches the light sheet thickness well: within the defocus

[14] Roper Scientific MicroMax 1024 BFT
[15] Andor iXon+ 897

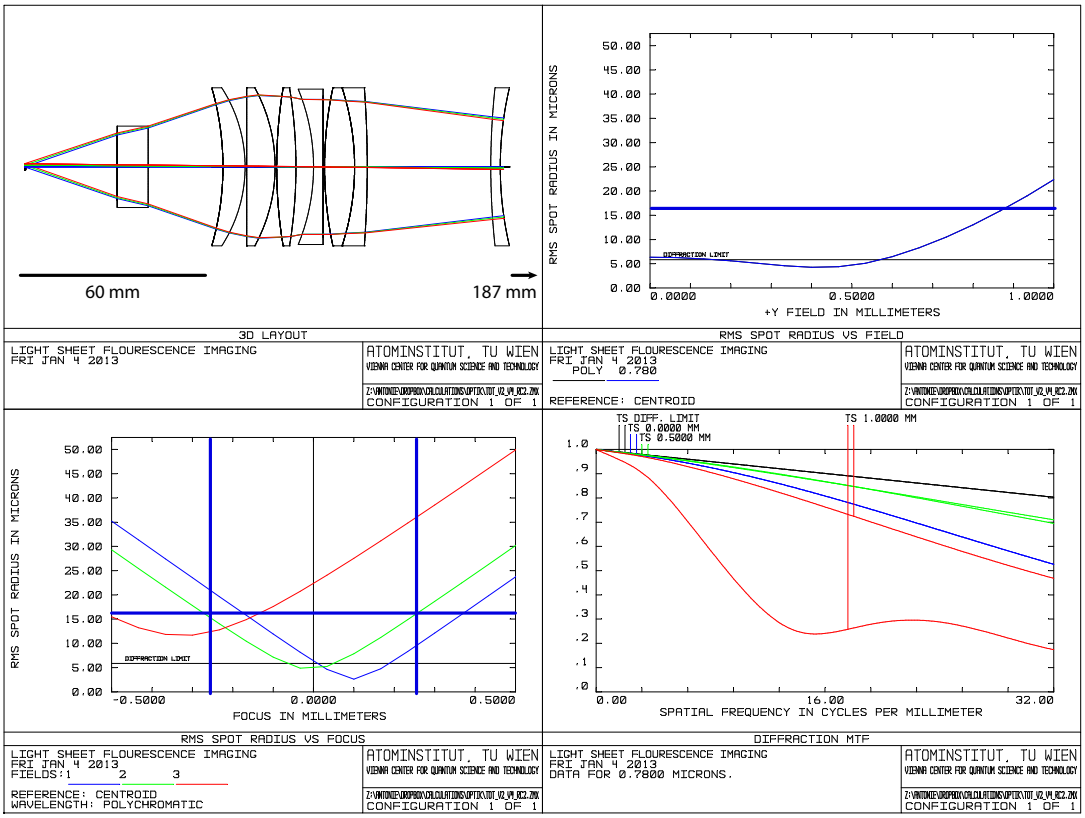

Figure 3.8.: Design and simulated performance of updated light sheet objective with $\times 4$ magnification. Upper left: layout of the objective. Apart from the last lens in the beam path, the design is near-identical to the $\times 2$ magnification version as explained in detail in ref. [218]. The image plane is located at $\sim 187\,\mathrm{mm}$ distance from the last lens. All plots are given in image-space units. Upper right: geometric (ray-tracing) RMS spot size of a point source in the conjugate plane, as a function of distance from the optical axis within the field of view. Over most of the field of view, the spot size remains below the camera pixel size of $16\,\mu\mathrm{m}$ (blue line), and is comparable to the diffraction limit (Airy disk radius, black line). Lower left: geometric spot size of point sources at three different field positions (blue, red and green: 0, 0.5, and 1 mm from optical axis in object space), as a function of focus position. The horizontal blue line indicates the pixel size. Vertical lines represent the waist ($1/e^2$ radius) of the light sheet, transferred to image space. Lower right: modulation transfer function (MTF) for the three field positions (including diffraction effects). For each field position, the sagittal (S) and tangential (T) function is shown (see e.g. [218] for further explanation). Black line is the diffraction limit. The upper limit of the frequency axis corresponds to the Nyquist frequency of the pixel grid.

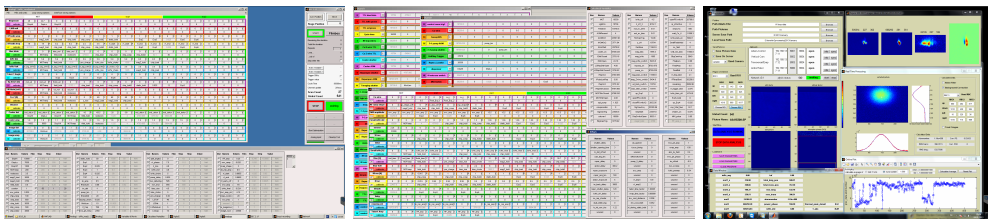

Figure 3.9.: Screenshots of principal experiment control interfaces. Left and center: sequencer control. Each of the colorful rows represents a single analog or digital channel, with columns corresponding to time steps. For analog steps, constant values or ramps are allowed. Grey windows contain variables that can be used to modify the cycle at multiple points consistently in a programmed way, and enable automatic parameter scans. Right: data acquisition, displaying images taken in the previous cycle, and several data extracted from the images or other signal sources.

range corresponding to the sheet thickness (blue vertical lines), the ray-tracing spot size mostly remains below the CCD pixel size (blue horizontal line), which in turn is matched to the best achievable resolution considering atom diffusion (see sec. 3.2.4).

3.1.7. Computer control

The central control device of the experiment is a stand-alone real-time computer,[16] equipped with 32 analog (16 bit, up to ±10 V) and 64 digital (TTL) output channels. For each experiment cycle, the sequences for all channels are transmitted from a control computer via an Ethernet connection; after transmission, the system is running independently. A time resolution of 25 µs step size is achieved, with negligible jitter. The only devices to some extent independent from the central sequencer are the arbitrary waveform generators (see sec. 3.1.5), which only receive a single TTL trigger to start their stored sequences. It has been found, that the jitter between the generator clocks and the main sequencer clock is negligible on the sub-microsecond level for the required sequence lengths of few seconds.

Programming the main sequencer, waveform generators, and several other devices that are read out or initialized via digital connections, as well as image acquisition, storage and simple processing is handled by various specifically written Matlab programs. Those run distributed over a couple of computers, and communicate via shared folders and UDP messages in an internal lab network. Most of the functionality is accessible by two complex graphical user interfaces for sequence programming, and data acquisition (fig. 3.9). Functions to run automated parameter scans are included, hence, the experiment can run unattended for an arbitrary time, which is practically limited, among others, by the stability of the laser locks, and the capacity of the car batteries used for chip currents.

[16] Jäger ADwin Pro. Details of adopting the ADwin system for our experiment can be found in theses by Mihael Brajdic [219] and Wolfgang Rohringer [220].

3.2. Condensate preparation, manipulation and detection

In this section, some key techniques needed for the experiments presented in chapter 5 are outlined; references to more in-depth discussions will be given at appropriate points.

3.2.1. Magnetic trapping on a chip

Soon after first proposals and realizations of atom trapping using free-standing wires [225–230], it was realized that micro-fabricated wires on chip provide even better control over potential landscapes, and stronger confinement due to high current densities [231,232]. First demonstrations of Bose-Einstein condensation were achieved soon after [233,234]. By now, atom chips have become one of the major approaches to trapping and manipulating neutral atoms, enabling both fundamental and applied research by virtue of their versatility and robustness. Besides some earlier reviews [235, 236], an exhaustive overview over basic concepts, wire geometries, and the numerous applications of atom chips is given in a recently published book [221], which also includes a chapter about experiments using dressed potentials performed at the Rb-II setup.

Static chip traps At magnetic field strengths $|\mathbf{B}|$, where the Zeeman shift is small compared to the hyperfine level splitting, nuclear and electronic spin of the Rubidium atoms remain coupled to a total angular momentum $\mathbf{F}$. The motion of an atom can then be described by the Hamiltonian

$$\hat{H} = \frac{\hat{\mathbf{p}}^2}{2m} + g_\mathrm{F}\mu_\mathrm{B}\hat{\mathbf{F}}\cdot\mathbf{B}(\hat{\mathbf{r}}) \tag{3.2}$$

with the momentum $\mathbf{p}$, mass m, Bohr magneton μ_B, and the g-factor g_F characteristic for the internal state of the atom. The Larmor, or precession frequency of an atom at position $\mathbf{r}$ is then given by $\nu_\mathrm{L} = h^{-1}g_\mathrm{F}\mu_\mathrm{B}|\mathbf{B}(\mathbf{r})|$. If the relative change rate of the magnetic field strength remains small compared to the Larmor frequency, i.e.: $\dot{\mathbf{B}}/|\mathbf{B}| \ll \nu_\mathrm{L}$, the precession of the atoms can follow the external field adiabatically. In quantum terms, the atoms remain in their magnetic state m_F, whereas the quantization axis with respect to which the state is defined, continuously adjusts itself to the local field. Eq. (3.2) then simplifies to:

$$\hat{H} = \frac{\hat{\mathbf{p}}^2}{2m} + V_\mathrm{mag}(\hat{\mathbf{r}}) \tag{3.3}$$

$$V_\mathrm{mag}(\hat{\mathbf{r}}) = m_\mathrm{F}g_\mathrm{F}\mu_\mathbf{B}|\mathbf{B}(\hat{\mathbf{r}})|. \tag{3.4}$$

As Maxwell's equations rule out maxima of magnetic field strength in free space [237], only magnetic states with a positive value of the product $m_\mathrm{F}g_\mathrm{F}$ (weak-field seekers) can be trapped. For ^{87}Rb, this restricts the choice to the states $|F=1, m_\mathrm{F}=-1\rangle$, $|F=2, m_\mathrm{F}=1\rangle$, and $|F=2, m_\mathrm{F}=2\rangle$, the first of which is usually used in our experiment. It has $m_\mathrm{F}g_\mathrm{F} = 1/2$, and hence a magnetic moment of $m_\mathrm{F}g_\mathrm{F}\mu_\mathrm{B} = 0.70\,\mathrm{MHz/G}$.

An important consequence of the adiabaticity condition $\dot{\mathbf{B}}/|\mathbf{B}| \ll \nu_\mathrm{L}$ is, that points of zero field have to be avoided, as spin flips (Majorana losses [238]) may occur there. For an ultracold cloud of atoms, which has a high density near the trap minimum, this rules out a simple quadrupole field, which has a linear dependence of the field

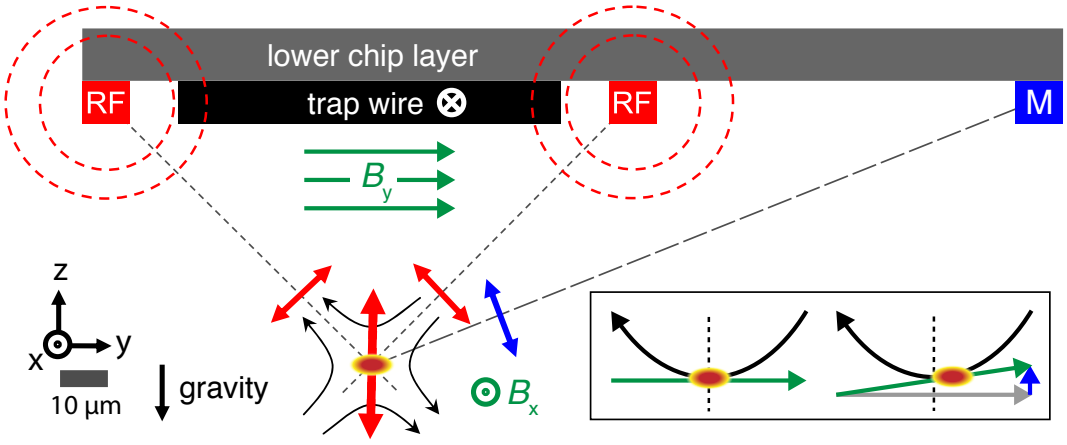

Figure 3.10.: Main figure: Schematic of the atom chip layout (see ref. [200] for details). The waveguide potential is formed by the current I_t through the trap wire along $-x$ and a static bias field B_y, adding up to quadrupole field (bent bent arrows). On a separate chip layer, currents I_H in broad wires along y (not shown, see fig. 3.2) provide weak longitudinal confinement and a constant field along x. An external offset field along B_x, perpendicular to the figure plane, is added, to define the Larmor frequency at the trap minimum ν_L. The radio frequency dressing currents I_{RF} are applied to wires (RF) in parallel to the trapping wire, leading to a RF field along z (red arrows). The resulting anisotropic transverse potential is shown as ellipse in the center of the quadrupole. Finally, the modulation of the trap position is accomplished by a current in an auxiliary wire (M), leading to a magnetic field, aligned at $\sim 19°$ with respect to the z-axis (blue arrow). Inset: Field configuration for trap position modulation. The transverse trap position is defined by cancellation of the chip wire field (black) and the bias field (green). Adding a weak field along z (blue) tilts the bias field slightly, leading to a horizontal shift of the trap minimum.

on all spatial directions, and hence vanishes at the center. However, several other solutions have been found [8], the most popular of which is the Ioffe-Pritchard configuration [239], which is realized in our atom chip traps.

The standard configuration for the radial gradient part of a Ioffe-Pritchard field is a single current-carrying wire (shown blue in figs. 3.10 and 3.2), the inhomogeneous field of which is canceled by an external field (bias) in the yz-plane at exactly one position. Assuming an infinitely thin wire carrying a current I_t, and a bias field along y, its distance d along z from the wire is given by the relation:

$$B_\mathrm{y} = \frac{\mu_0}{2\pi}\frac{I}{d} = 2000\,\mathrm{G} \times \frac{I_\mathrm{t}/\mathrm{A}}{d/\mu\mathrm{m}}. \tag{3.5}$$

Around this minimum, a two-dimensional quadrupole configuration with axes tilted by 45° with respect to y, z is created (black arrows in fig. 3.10), with a field gradient $\mathrm{d}B/\mathrm{d}r = \mu_0/(2\pi)I_\mathrm{t}/d^2$. By adding a homogeneous field along x, which lifts the magnetic zero in the center of the quadrupole, a two-dimensional harmonic confinement is obtained, which e.g. can be used to guide atoms [240–242]. The transverse trapping frequencies $\nu_\mathrm{y}, \nu_\mathrm{z}$ achieved in this way are typically in the kHz range, which is beyond what can be conveniently achieved with external coils.

To obtain a complete Ioffe-Pritchard configuration, confinement along x has to be added. In our experiment, this is done by means of a H-configuration, where two wires along y (shown as green stripes in fig. 3.2) cross the trapping wire on a separate chip layer. A simpler option would be a single wire bent into a Z-shape, which has been used previously in our experiment, and which we still implement for the macroscopic trapping wires (see sec. 3.1.2). In principle, the H-configuration allows to adjust the transverse and longitudinal confinement of the atoms independently; however, this turned out to be mostly superfluous due to wire corrugation effects (see below). Alternatively, using a single thin wire along y near the chip center (dimple), which runs current in opposite direction to the H-wires, crossed-wire traps with stronger confinement along x can be built. This ability has been used to vary the aspect ratio of traps over a large range in ref. [43]. In either case, a certain constant offset field along x is already created by the longitudinal confinement, which however can be further adjusted using an external ("Ioffe") field B_x (see sec. 3.1.4). The total field ("trap bottom") defines the Larmor frequency at the trap center ν_L, which must be high enough to fulfill the adiabaticity criterion as explained above. The finally resulting potential landscape can be calculated numerically using a finite-element simulation, with the wire currents and external fields as input parameters.

Trap position modulation For the experiments presented in this thesis, the ability to rapidly move the potential minimum in the yz-plane along an optimized trajectory $\lambda(t)$, in order to excite vibrational states, is crucial. In an atom chip trap, this can be achieved easily by running small modulated currents through wires, changing the field configuration and position of the trap minimum. The simplest possible solution would be to put a slight modulation on the main trapping wire, which shifts the position of the trap minimum along z, following eq. 3.5. Indeed, this scheme has been implemented successfully. However, preparation of higher vibrational states along z has the disadvantage, that the excitation dynamics cannot be monitored using the light

sheet imaging system, which integrates over the z-direction. Furthermore, additional electronics connected to the chip wire is necessary, which may contribute to technical noise, and thus, undesirable heating of the atoms.

Instead, the movement is accomplished by applying a current to an auxiliary wire running parallel to the main trapping wire at a distance of 140 µm (shown in blue in figs. 3.2 and 3.10), creating a field mostly aligned along z for typical trap distances. As depicted in the inset of fig. 3.10, the additional magnetic field along z causes a slight tilt of the Bias field B_y. The trap minimum position, which is given by the point where the bias field cancels that of the trapping wire, is displaced along y. Still, the y-component of the modulation field causes a slight proportional movement along z. However, as confirmed by two-dimensional simulations of the excitation process (see sec. 5.4), the anisotropy of the transverse potential suppresses any significant influence on the excitation along y. For the field geometry which has been used in the final experiment, the movement of the trap minimum caused by the current can be calculated from simulations as 26 nm/mA along y and 9 nm/mA along z.

Potential corrugation A severe limit on the versatility of chip-based trapping potentials is imposed by the inhomogeneity of current flow through the trap wire, typically caused by imperfection of the wire edges or the grain size of the wire material [243–246]. Specifically for our chip [200], additional modulation is caused by the height "jumps" of the trap wire at the crossing points with wires on the lower chip layer [see fig. 3.3(d)], which are necessary to make room for insulating pads. All those contributions become more significant for traps placed in close proximity to the chip, which are desirable especially for experiments with one-dimensional systems (see sec. 2.4) due to the high achievable field gradients, and hence, transverse trap frequencies.[17] In practice, the inhomogeneities cause an irregular, but temporally stable corrugation of the trapping potential, most significantly along the longitudinal (x) axis. In images of trapped atom clouds, this effect can be clearly observed as a correspondingly modulated density distribution, up to a complete fragmentation [196, 203, 249, 250].

For the atom clouds used in this thesis, temperature and chemical potential are on the order of the typical modulation depth of corrugations on the micrometer length scale. At such low energies, the effective longitudinal potential is mostly given by corrugation effects, and the condensate forms in the lowest-lying potential "dip" in the irregular landscape. This results in a significantly stronger longitudinal confinement near the end of the cooling sequence than expected from the chip current configuration. The remaining effect of the H-wires (see above) becomes less important; in fact, the final condensate remains trapped even without any current sent through them. A more detailed characterization of corrugation effects in our chip can be found in Stephanie Manz' PhD thesis [216]; practically, longitudinal confinement weaker than $\nu_x \sim 15$ Hz seems elusive to achieve in a simple wire trap even at only moderate ($\nu_{y,z} \sim 2$ kHz) transverse trap frequencies.

[17] One possibility to mitigate this issue is to use temporally modulated field configurations [166, 182, 247, 248]. However, this forbids the usage of external offset fields (which could not be modulated at high enough frequencies), complicating the chip design.

3.2.2. Potential preparation using radio-frequency dressing

The experiment presented in part II of this thesis relies on the ability to excite non-classical (Fock) states of the transverse confinement potential. However, in a quantum harmonic oscillator, all states that can be addressed by simple displacement of the potential are quasi-classical coherent states [57]. This statement also holds for a harmonically trapped interacting many-body system, where a quasi-classical collective oscillation at the trap frequency fully decouples from more complex internal dynamics [145, 146, 251]. Hence, transferring the condensate population into an excited, stationary state necessitates an *anharmonic* potential along the displacement direction y, where the decoupling of collective and internal dynamics breaks down. Furthermore, to be robust against excitation in the perpendicular direction z, anisotropy in the transverse plane of the potential is required, causing a detuning of trap levels between the directions.

Initially, the Ioffe-Pritchard field configuration as created by the chip wires (plus external offset fields, see fig. 3.10) is rotationally symmetric in the yz-plane, and provides harmonic trapping transversely, as discussed before. To choose appropriate parameters for the static field trap, we tested various configurations of chip currents and external fields, and judged them in terms of observed fragmentation, confinement strength, and heating rate. The trap finally implemented uses wire currents of $I_\mathrm{t} = 1\,\mathrm{A}$ and $I_\mathrm{H} = 0.5\,\mathrm{A}$, with a Bias field of $B_\mathrm{y} \approx 34\,\mathrm{G}$ and a Ioffe field of $B_\mathrm{x} \approx 1\,\mathrm{G}$. For an atom in state $|F = 1, m_\mathrm{F} = -1\rangle$, this yields a transverse trap frequency of $\nu_0 = 4.1\,\mathrm{kHz}$ in both directions, and a trap position of $d \sim 49\,\mu\mathrm{m}$. The longitudinal confinement is strongly affected by corrugations, see sec. 3.2.1 and has a frequency on the order of 30 Hz.

To introduce anharmonicity and anisotropy, we apply radio-frequency dressing [21, 197, 198, 252–254]. This technique, which was pioneered at the Rb-II machine [21], is typically used for splitting of the transverse potential into a double well, enabling interferometry [21, 223], homodyne detection of phase fluctuations [179, 198, 255], or studying Bosonic Josephson junctions [204]. Detailed explanations of this technique and its implementation at Rb-II can be found in previous theses [213, 214, 217]. In brief, the atoms are irradiated by a radio-frequency (RF) near field $\mathbf{B}_\mathrm{RF}(\mathbf{r})$ with linear magnetic polarization, the frequency ν_RF of which is red-detuned by tens of kHz with respect to the atomic Larmor frequency ν_L. The RF field mixes the Zeeman levels (quantum numbers m_F) of the hyperfine manifold, coupling them to dressed states with effective quantum numbers $\tilde{m}_\mathrm{F}$, that adiabatically connect to the initial (bare) states. Once dressing is applied, the momentary decomposition into bare states depends on detuning from the local Larmor frequency $\Delta(\mathbf{r})$ and coupling strength (Rabi frequency) $\Omega(\mathbf{r})$. Both quantities are position-dependent, the latter because of the changing RF polarization with respect to the local magnetic field that modulates the coupling strength. Similarly to the adiabatic approximation for static fields introduced above, the state decomposition follows the momentary position of the atoms, giving rise to a spatially dependent energy shift. In rotating-wave approximation [254], the resulting

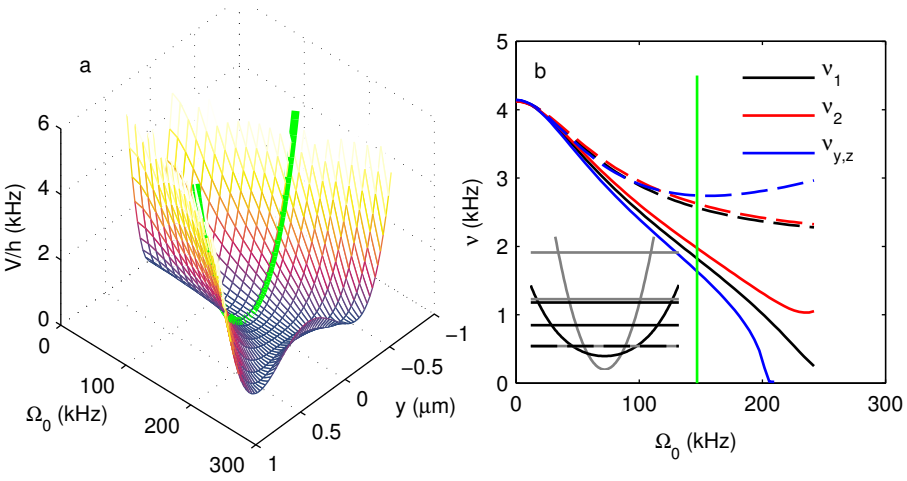

Figure 3.11.: Effects of RF dressing on the transverse trapping potential. (a) Potential along the y (displacement) direction, as a function of RF Rabi frequency. The detuning with respect to the minimum Larmor frequency ν_L is $\Delta_0 = -55\,\mathrm{kHz}$. At dressing strengths above $\Omega_0 \sim 180\,\mathrm{kHz}$, splitting of the single potential into a double well occurs. (b) Shift of single-particle trap levels vs. dressing strength. Solid and dashed lines correspond to perpendicular (y) and parallel (z) directions with respect to the RF polarization, respectively. Blue: frequency of harmonic part, as defined in eq. (3.6). Black, red: first and second level spacing of single-particle eigenstates. Inset: initial (grey) and dressed (black) potential, each with their first three energy levels. The green lines in both panels mark the setting used for the experiments.

potential landscape up to a constant is given by:

$$\begin{aligned} V_\mathrm{RF}(\mathbf{r})/h &= \sqrt{\Omega(\mathbf{r})^2 + \Delta(\mathbf{r})^2} \\ \Delta(\mathbf{r}) &= \nu_\mathrm{RF} - V_\mathrm{mag}(\mathbf{r})/h \\ \Omega(\mathbf{r}) &= \frac{1}{2}\mu_\mathrm{B}\tilde{m}_\mathrm{F} B_{\mathrm{RF},\perp}(\mathbf{r}), \end{aligned}$$

where $B_{\mathrm{RF},\perp}(\mathbf{r}) = |\mathbf{B}(\mathbf{r}) \times \mathbf{B}_\mathrm{RF}(\mathbf{r})|/|\mathbf{B}(\mathbf{r})|$ denotes the RF field component perpendicular to the local static field. To emit the radio-frequency field, we use two chip wires running in parallel to the trapping wire as antennae (see red lines in figs. 3.10 and 3.2). The dressing is most effective along the direction perpendicular to the RF polarization; in our case, applying a polarization along the vertical axis z leads to a deformation mostly along y.

In Fig. 3.11(a), the potential along y is shown as a function of dressing strength, expressed as coupling Ω_0 near the trap center. At sufficiently strong coupling, splitting of the potential into a double well occurs. However, at lower coupling, this technique also allows for the introduction of anharmonicity and anisotropy to a single trap, as needed for our scheme. In the experiment, we apply an RF field of $B_\mathrm{RF} = 0.84\,\mathrm{G}$ peak-to-peak amplitude, leading to a coupling $\Omega_0 = 147\,\mathrm{kHz}$, at a frequency red-detuned by $\Delta_0 = -54\,\mathrm{kHz}$ near the trap minimum with $\nu_\mathrm{L} = 824\,\mathrm{kHz}$. The procedure to obtain these parameters will be explained below.

The resulting potential is shown as a green line in fig. 3.11(a). Even though the

rotating-wave approximation holds well for the used dressing strength [198], the high sensitivity of the excitation protocol to the exact potential shape calls for an exact calculation by means of a Floquet analysis [256]. Along the transverse directions the result can be approximated by a sixth-order polynomial of the form

$$V_6(y,z)/h = \frac{\nu_\mathrm{y}}{2}\left(\frac{y}{l_\mathrm{y}}\right)^2 + \sigma_\mathrm{y}\left(\frac{y}{l_\mathrm{y}}\right)^4 + \xi_\mathrm{y}\left(\frac{y}{l_\mathrm{y}}\right)^6 \tag{3.6}$$

$$+ \frac{\nu_\mathrm{z}}{2}\left(\frac{z}{l_\mathrm{z}}\right)^2 + \sigma_\mathrm{z}\left(\frac{z}{l_\mathrm{z}}\right)^4 + \xi_\mathrm{z}\left(\frac{z}{l_\mathrm{z}}\right)^6. \tag{3.7}$$

In this expression, the lengths $l_{\mathrm{y,z}} = \sqrt{h/(m\nu_{\mathrm{y,z}})}/(2\pi)$ correspond to the characteristic length of the harmonic part. The parameters are given by:

$$\begin{aligned} \nu_\mathrm{y} &= 1655\,\mathrm{Hz}; & \nu_\mathrm{z} &= 2751\,\mathrm{Hz} \\ \sigma_\mathrm{y} &= 78.2\,\mathrm{Hz} & \sigma_\mathrm{z} &= -69.6\,\mathrm{Hz} \\ \xi_\mathrm{y} &= -0.96\,\mathrm{Hz} & \xi_\mathrm{z} &= 9.1\,\mathrm{Hz} \\ l_\mathrm{y} &= 265\,\mathrm{nm} & l_\mathrm{z} &= 206\,\mathrm{nm}. \end{aligned} \tag{3.8}$$

Along y, the sixth-order term ξ_y is negligibly small, and the description reduces to a Duffing oscillator [257].

By solving the Schrödinger equation for a single atom trapped in the dressed potential, the single-particle trap levels of the dressed potential can be obtained. The first two level spacings $\nu_{1,2}$ along y and z are shown in fig. 3.11(b). For the used parameters (as marked by a green line), the initial degeneracy of the level spacings is lifted, and we obtain the excitation energies (zero-point energy subtracted) $[E_{10}, E_{20}, E_{01}, E_{02}, E_{11}]/h = [1.84, 3.83, 2.58, 5.21, 4.42]$ kHz with E_{ij} denoting the i-th and j-th state along y and z, respectively. The relevant level spacings along y will be denoted by $\nu_1 = 1.84\,\mathrm{kHz}, \nu_2 = 1.99\,\mathrm{kHz}$, $\nu_3 \approx 2.10\,\mathrm{kHz}$, the first level spacing along z is $\nu_1^{(z)} = 2.58\,\mathrm{kHz}$.

To apply the theory of one-dimensional Bose gases (sec. 2.4), the eigenfunctions of the Schrödinger equation can be inserted into the equation for the 1-dimensional interaction constant. (2.30). We obtain $g_\mathrm{1d} = h \cdot 0.023\,\mathrm{Hz\,\mu m}$, or, equivalently, an effective transverse trap frequency of $\omega_\perp = g_\mathrm{1d}/(2\hbar a_\mathrm{s}) = 2\pi \cdot 2.14\,\mathrm{kHz}$.

Trap characterization In the laboratory, compliance with the simulated potential has to be ensured, given the limited accuracy to which experimental parameters, such as field strengths and currents, can be set, and the extreme sensitivity of our excitation scheme (sec. 5.4.1). The initial static trap can be characterized in terms of its transverse trap frequency ν_0, and the central Larmor frequency ν_L (trap bottom). The former is measured by observation of a collective dipole mode (sloshing), which is excited by a brief kink in the trap wire current (less than 1% of its normal value of $I_\mathrm{t} = 1\,\mathrm{A}$), see fig. 3.12(a). The horizontal position of the cloud in absorption images oscillates at the trap frequency, which can be fit with high precision. As a second characteristic, the trap bottom ν_L can be measured using RF spectroscopy, where a weak radio frequency pulse (Rabi frequency $\lesssim 1\,\mathrm{kHz}$, duration typically $\lesssim 20\,\mathrm{ms}$) is applied while the cooled cloud is held in the trap. If the RF pulse frequency matches ν_L, strong

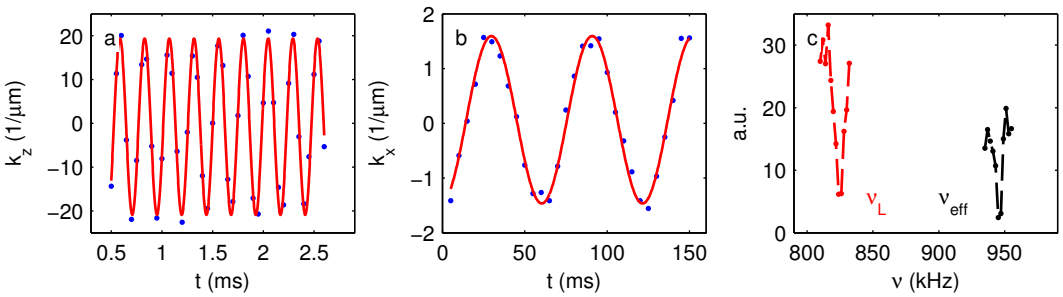

Figure 3.12.: Trap characterization. (a) Blue points: measured peak transverse momentum of a condensate excited by a brief displacement of the harmonic (static) trap, and released after some hold time t. The frequency of the collective mode equals the trap frequency, from a fit (red line) we obtain $\nu_0 = 4.105(10)\,\mathrm{kHz}$. (b) Longitudinal sloshing mode in the dressed trap, measured in the light sheet after excitation using the dimple wire. The fit yields $\nu_\mathrm{x} = 16.35(20)\,\mathrm{Hz}$. (c) RF spectroscopies in the static (red) and dressed (black) traps, indicating the Larmor frequency ν_L, and the effective trap bottom ν_eff.

atom loss occurs due to transfer into untrapped magnetic states, see fig. 3.12(c). Of the four parameters which determine the transverse shape and position of a static trap, $I_\mathrm{t}, I_\mathrm{H}, B_\mathrm{y}, B_\mathrm{x}$, the two currents are known to high accuracy in the experiment. Hence, the two fields can be uniquely inferred, once ν_L and ν_0 have been measured, such that experiment and finite-element simulation can be matched. The obtained values are used as input to the Floquet dressed potential calculation.

Concerning the RF parameters, while ν_RF can be directly set, the RF field strength is determined by the AC current in the RF wires. This current is not measurable with sufficient precision due to the specifications of the used AC current probes, and the signal generator running in voltage-stabilized mode. However, similarly to the static case, using a weak probe RF, transitions to untrapped states can be driven [fig. 3.12(c)], which are much more numerous in a dressed trap due to higher-order transitions to different dressed manifolds [198, 258]. Selecting the first transition above ν_L, which will also be used for evaporative cooling (see sec. 3.2.3) yields an effective dressed trap bottom ν_eff, which can be compared to simulations. Using this procedure, it is easy to reach a trap that roughly matches the simulation. However, in contrast to the static strap, a more precise characterization using a collective mode cannot be performed. Unlike for harmonic confinement, no stable dipole mode which maintains the internal mode structure is supported in an anharmonic potential [146, 251], and dephasing occurs. The resulting frequencies are significantly modified by many-body effects (see sec. 5.4.2) and cannot directly be related to the initial trap potential. Instead, we take a somewhat more pragmatic approach, and adjust the relevant experiment parameters directly, by comparing the observed response to the excitation ramp used in our experimental scheme to the one determined numerically, as shown in sec. 5.4.1. Once all other values have been set as good as possible using the methods shown in fig. 3.12, excellent agreement can be reached by fine-tuning I_RF or B_x, which have very similar influence on the potential shape [see eq. (5.29) and fig. 5.14].

Along the longitudinal x-axis, the trap confinement is strongly affected by wire imperfections (see previous section), which are not accounted for in simulations (which would predict a frequency of 7.7 Hz due to the H-wire current). However, we can apply a similar method as for the static transverse trap frequency, and excite a collective mode along the longitudinal direction. This is accomplished most conveniently by sending a brief current pulse through the dimple wire running along y. In light sheet images, sloshing oscillations of the trapped quasicondensate are observed. We obtain $\nu_{\mathrm{x}} = 16.4\,\mathrm{Hz}$, as shown in fig. 3.12(b).

3.2.3. Experiment sequence

We will now briefly go through the steps necessary to prepare a degenerate gas trapped near the chip, which is the starting point for all experiments shown in chapter 5. More detailed analysis of the sequence parts can be found in a previous thesis [214]. The cycle time of the experiment is usually set to 36 s, which is mostly limited by the collection of atoms in the pulsed magneto-optical trap.

Magneto-optical trap As in virtually all experiments with cold atoms, a magneto-optical trap (MOT) serves as a starting point to collect and pre-cool atoms [259]. In our case, the MOT is loaded directly from background gas, while the partial pressure of Rubidium in the chamber is increased by running current through pulsed thermal dispensers, which are placed in the science area, close to the chip (fig. 3.1). In contrast to the usual configuration using six beams and a quadrupole magnetic field, a mirror U-MOT [195] is implemented. Two of the beams are replaced by reflections from the gold chip surface, creating a beam alignment tilted by 45° with respect to the chip surface. Furthermore, the quadrupole field is substituted by a homogeneous (external) field in the yz plane, together with current through a U-shaped structure [fig. 3.3(c)]. While the light field is typically quite distorted by scattering off the chip wires, iterative optimization of beam positions and field strengths allows to obtain a regularly shaped MOT with large diameter, that provides a stable starting point of the experimental cycle over several weeks of operation. Typically, the MOT is run with $\sim 220\,\mathrm{mW}$ of cooler light in the four beams, at a $\sim -20\,\mathrm{MHz}$ detuning from the $F = 2 \leftrightarrow F' = 3$ (cycling) transition (fig. 3.5). Repumping light resonant with the $F = 1 \leftrightarrow F' = 2$ transition is superimposed before beam distribution (see fig. 3.4). The MOT is loaded for typically 18 s. For the last 2 s, the current in the dispensers is extinguished, to allow them to cool down (aided by water cooling) and to reduce the background pressure in the chamber, enabling high life times of the magnetic traps. During this time, the power in the cooling beams is reduced, to suppress light-induced collisions.

MOT transfer and molasses After loading of the MOT is finished, the fields and cooler detuning are ramped within 200 ms, to compress and move the MOT to a position closer to the chip, which is matched in position and size (mode-matching) to the first stage of magnetic trapping. Then, the external magnetic fields used for the MOT are extinguished within less than 100 µs. Simultaneously, the detuning is ramped to $\sim -70\,\mathrm{MHz}$ for sub-Doppler polarization gradient cooling (optical molasses, [259]). As the experiment has no dedicated set of ambient field compensation coils, the small coil set (see sec. 3.1.4) is used during molasses, to cancel all remaining fields. Still,

at any position close enough to the chip to enable loading to the magnetic trap, the molasses light field is heavily affected by chip structures, visible as a shadow pattern in the molasses. This causes rapid loss of atoms, limiting the duration of the molasses phase to $\sim 4\,\mathrm{ms}$.

Magnetic trap loading After optical cooling, atoms reside in the $F = 2$ manifold at random magnetic orientation. To pump them into $|F = 1, m_\mathrm{F} = -1\rangle$, we apply a weak field along y as quantization axis, and irradiate the atoms simultaneously with two pumping beams for $\lesssim 1\,\mathrm{ms}$. The first contains light near $F = 2 \leftrightarrow F' = 2$ ("pumping $F = 2$" in figs. 3.4 and 3.5), and is sent along x circularly polarized, i.e. containing all polarizations with respect to the magnetic quantization axis. After few scattered photons, atoms will fall into the $F = 1$ manifold and become dark for this beam. The second beam ("pumping $F = 1$") is tuned to $F = 1 \leftrightarrow F' = 1$ and sent with σ^- polarization (with respect to the quantization field) along y. This pumps atoms into $|F = 1, m_\mathrm{F} = -1\rangle$, where they will go dark for both beams. Should the atoms fall back into $F = 2$ before, they get repumped by the first beam, and the process is restarted.

Finally, all light is switched off, and the first magnetic trap field configuration is ramped up within 5 ms. This first "Z-trap" does not yet use the atom chip (which could achieve a rather small trap volume only), but the free-standing Z-shaped wire beneath it (see sec. 3.1.2), in conjunction with external fields in y (Bias) and $-x$ (anti-Ioffe) direction. The anti-Ioffe field counteracts the offset field of the Ioffe-Pritchard configuration created by the Z-wire and Bias field alone, to obtain a sufficiently deep trap. The initial values of the Z-current and field are set to enable good mode-matching with the molasses. They are ramped to their final values, which correspond to a confinement of $\nu_{\mathrm{y,z}} \sim 200\,\mathrm{Hz}, \nu_\mathrm{x} \sim 20\,\mathrm{Hz}$, within 2 s. During this ramp, for 10 ms, a strong laser pulse on the $F = 2 \leftrightarrow F' = 3$ transition is applied, to kick any remaining atoms in $F = 2$ out of the trap.

After compression of the Z-trap, evaporative cooling [260] starts, using an RF "knife" that induces spin flips to untrapped states at a trap position where the local Larmor frequency is resonant with the RF radiation [8], effectively regulating the trap depth. See sec. 3.1.5 for the technical implementation. Starting from a cloud of $N \sim 5 \times 10^6$ atoms at a temperature of $T \sim 100\,\mu\mathrm{K}$, evaporation in the Z-trap reduces both by approximately a factor of 2 (see fig. 3.13), increasing the phase space density $n_0 \lambda_\mathrm{dB}^3$ (see sec. 2.1.1) by a factor ~ 3.5 within $\sim 4\,\mathrm{s}$.

Chip trap Within 650 ms, the gas is now transferred into the chip trap, which still has trap parameters comparable to the Z-trap ($\nu_\mathrm{x} \approx 18\,\mathrm{Hz}$, $\nu_{\mathrm{y,z}} \approx 800\,\mathrm{Hz}$). The anti-Ioffe field and Z-wire current are ramped down during this time, while the Bias field is strongly decreased and the Ioffe field for the chip trap is ramped up. The latter is created by the small coil pair and points along $+x$, in order to *increase* the offset field of the chip H-trap. Within the first 100 ms of the transfer, the chip wires are ramped up to their final values. After the transfer, evaporation continues for another 3 s down to $\sim 20\,\mu\mathrm{K}$ (fig. 3.13). Finally, the trap is transformed into the final static trap. The high transverse frequencies of several kHz enable very efficient evaporation, where the central density n_0 [fig. 3.13(c)] increases rapidly (runaway cooling), and a unit phase

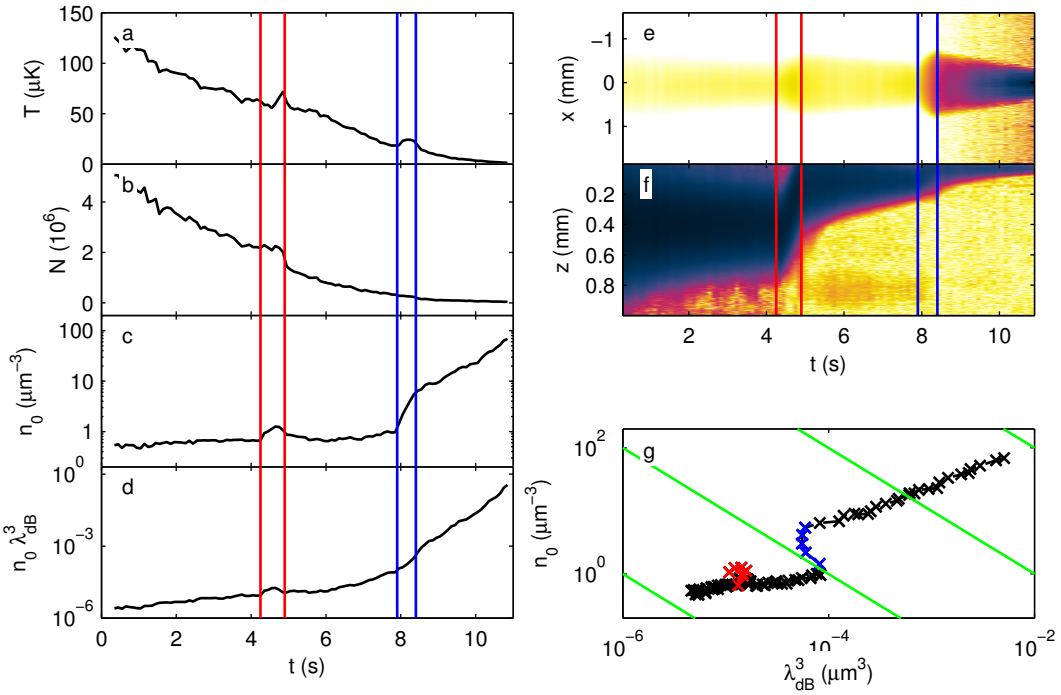

Figure 3.13.: Analysis of evaporative cooling of atoms down to slightly above degeneracy. Data has been derived from stopping the experiment sequence at a time t after beginning evaporation, and taking absorption images after 1.5 ms and 10 ms of expansion. (a-d) Temperature T, total atom number N, peak density n_0, and peak phase-space density $n_0\lambda_{\mathrm{dB}}^3$ during the evaporation process. Red and blue lines indicate the chip loading and chip compression, respectively. (e) False-color plot of the 3d density in the trap center $n(x; y = z = 0)$, as a function of the longitudinal position x, measured after 1.5 ms of expansion. The color scale is logarithmic and spans the same range as panel (c). (f) Transverse line density $n_{1\mathrm{d}}(z)$, logarithmic color scale (a.u.). (g) Path of evaporative cooling, as a function of central density n_0 and thermal de Broglie wavelength λ_{dB}. Red and blue ranges correspond to chip loading and compression, respectively. Green lines indicate phase space densities of $10^{-6}, 10^{-4}, 10^{-2}$, and 1.

space density is approached. Depending on the particular experiment, the cloud is either evaporated further and a condensate forms, or the trap is deformed once more using RF dressing (sec. 3.2.2), in which the final cooling occurs. For the experiments presented in this thesis, mostly the latter scheme has been used, to avoid excitation of collective modes of the condensate during the final deformation.

To achieve the highest possible phase space densities after evaporation, it is crucial to adjust the shapes of the cooling ramps. Using the sequenced RF generators (sec. 3.1.5), this is easy to implement. Typically, curves that interpolate between a linear and exponential decay are used, where a more exponential shape is especially useful near the crossover to a one-dimensional system (sec. 2.4), where near-integrability slows down thermalization [203, 261, 262].

3.2.4. Detection and image analysis

Besides their superior controllability, one major asset of ultracold atoms as an experimental system is the ability to detect the outcome of experiments by simply taking photographs. The typically interesting length scales of several micrometers requires imaging optics of only modest complexity (see e.g. [218]). Furthermore, alkali atoms (or any other laser-coolable species) provide near-closed optical transitions with high scattering cross sections, enabling strong signals in absorption or fluorescence detection, with visibility down to the single-atom level [263–267]. Also, non-optical imaging methods, such as electron microscopy [268] and micro-channel plates with meta-stable atoms [269] have been used. As mentioned in sec. 3.1.6, at the Rb-II both absorption [224] and light sheet fluorescence imaging [202] systems are available, see fig. 3.7 for a sketch of the geometry. In this thesis, absorption imaging is mainly used for calibration and characterization measurements, whereas the actual results are all obtained using the light sheet. We will first discuss how to obtain reliable atom numbers from absorption imaging, before compiling a few relevant characteristics of the light sheet system, which has been described in much more detail in the author's diploma thesis [218] and a more recent publication [202].

Measuring density in absorption imaging Absorption imaging has become the workhorse technique for imaging of cold atoms, due to its good signal-to-noise ratio and straightforward implementation. An excellent general discussion of absorption imaging in the context of a very similar atom chip experiment can be found in the PhD thesis of Michael Gring [270]; the resolution of time-of-flight absorption imaging is derived in appendix A.3 of ref. [202].

When taking an absorption image, the atom cloud is illuminated from behind by a brief ($\sim 50\,\mu$s, typically) pulse of light, resonant with the cycling transition ($F = 2 \leftrightarrow F' = 3$). Each atom scatters a few hundreds of photons, attenuating the beam (which in our case travels along y and has an intensity profile $I_{\mathrm{in}}(x, z)$) following Beer-Lambert's law:

$$\frac{I_{\mathrm{out}}(x, z)}{I_{\mathrm{in}}(x, z)} = e^{-\sigma_{\mathrm{s}} n(x,z)}, \tag{3.9}$$

where $n(x, z)$ denotes the column density of the (expanded) atom cloud and σ_{s} the resonant scattering cross section of the used transition. The attenuated beam profile

$I_{\mathrm{out}}(x,z)$ is then imaged on a CCD chip using some objective optics.

In the experiments presented below, the most important application of absorption imaging is to accurately determine atom numbers. Assuming that the imaged density of atoms is constant over the area A covered by a single camera pixel i (with A defined in object space), it follows, that the number of atoms N_i imaged on that pixel can be calculated as

$$N_i = \frac{A}{\sigma_{\mathrm{s}}} \ln\left(\frac{S_{0,i}}{S_i}\right), \tag{3.10}$$

where S_i and $S_{0,i}$ correspond to the number of counts (in arbitrary units) detected in that pixel in the presence or absence of atoms, respectively; $\frac{A}{\sigma_{\mathrm{s}}}$ equals the number of atoms in the pixel column needed to achieve unit optical density. As mentioned in sec. 3.1.6, the object-space pixel size $\sqrt{A}$ can be very accurately determined in the experiment, giving $A = 11.8\,\mu\mathrm{m}^2$. The value of σ_{s} is complex to evaluate in general, as pumping processes between magnetic sub-levels occur [271]. Reducing the problem to a two-level description can be achieved by applying a magnetic quantization field along the optical axis, and using circularly polarized light, which quickly pumps the atoms into a maximally polarized state. If the Larmor frequency of the quantization field exceeds the coupling to the imaging light (with a Rabi frequency of typically a few MHz), the atoms remain fluorescing on the transition $|F=2, m_{\mathrm{F}}=2\rangle \leftrightarrow |F=3, m_{\mathrm{F}}=3\rangle$ (for σ^+-polarized light), and the process can be described in terms of simple optical Bloch equations [272]. In the limit of low intensity, we then have $\sigma_{\mathrm{s}} = 3\lambda^2/(2\pi) \approx 0.291\,\mu\mathrm{m}^2$ [271], and hence $A/\sigma_{\mathrm{s}} \approx 40.8$. Once the light intensity approaches the saturation intensity of $I_{\mathrm{sat}} = 1.67\,\mathrm{mW/cm}^2$, the response of the atoms becomes non-linear, which has to be avoided for absorption imaging.[18] To properly set all parameters in the experiment, it is helpful that any other possible sub-level configuration will result in lower scattering rates. Thus, maximizing the observed absorption signal, varying polarization and power of the imaging light, and strength of the quantization field, ensures validity of this analysis.

Practically, to obtain the images, four shots are taken in each cycle. The first one is the actual absorption image, containing the attenuated beam with signal S_i on each pixel. As the atoms are initially in the $F = 1$ hyperfine state, also some repumping light is switched on, that runs perpendicular to the optical axis, and hence does not directly enter the camera. This imaging process is destructive, due to the recoil imposed on the atoms by each scattered photon. Tens of ms after, a second image of the illumination beam is taken, however, the atoms have moved away from the field of view by now, so that the initial beam profile $I_{\mathrm{in}}(x,z)$ is observed as pixel signals $S_{0,i}$. Once, camera readout is finished (which typically takes $\sim 2\,\mathrm{s}$), a second pair of images is taken, where the imaging light is switched off. These images are used to subtract background signal originating from the camera baseline, and stray light which mostly originates from scattering of the repumper beam at the chip wires.

Calibration of light sheet images Most measurements at the Rb-II experiment are performed using light sheet fluorescence imaging [202], mainly for two reasons: Firstly,

[18] An alternative approach explicitly using high intensities, which allows imaging of very dense clouds with high precision, has been developed in ref. [273].

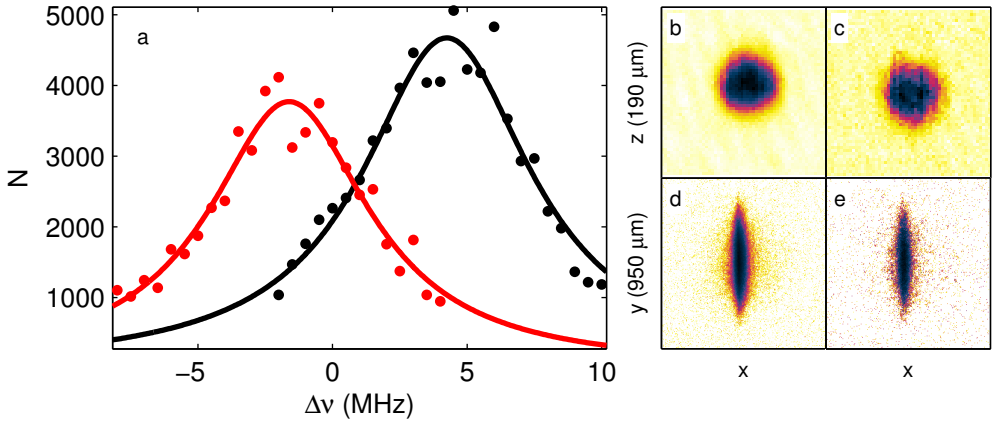

Figure 3.14.: Atom number calibration. (a) Influence of quantization field on absorption imaging. Red and black points correspond to images of identically prepared clouds, imaged with σ^+ light without and with quantization field, as a function of imaging frequency (arbitrary zero point). An increase of detected atom number by $\sim 25\%$ is found, if a field of 4.2 G is applied. Further increase of the field does not lead to any change. Lines are Lorentzian fits. (b-e) Images of quasicondensates with ~ 4600 atoms, taken with absorption imaging after 6 ms expansion time (b,c) or light sheet imaging (d,e). (b,d) Show averages over 7 shots each, (c,e) are typical single images. The light sheet images are shown on a logarithmic color scale. A set of such images can be used to calibrate the number of photons m detected from each atom during fluorescence imaging.

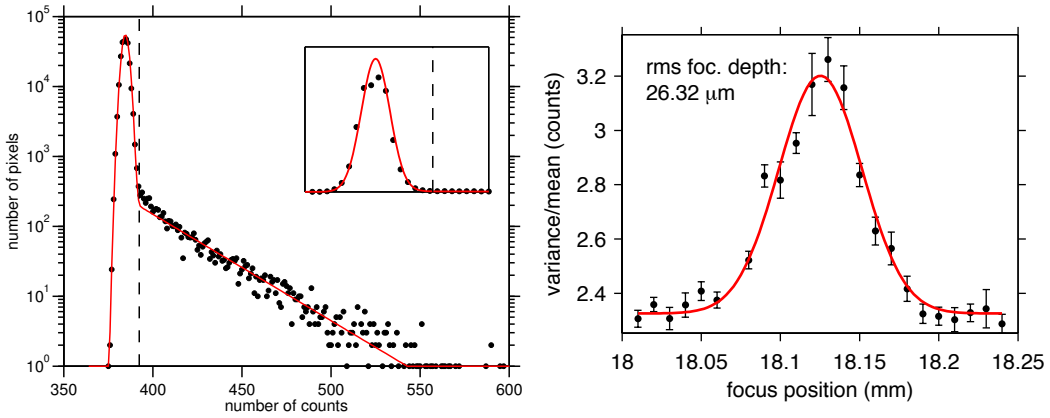

Figure 3.15.: Light sheet camera calibration and focusing. Figures taken from ref. [202] (C1, B1). Left: Histogram of pixel counts for an image taken without light. In the linear plot (inset), only a broadened baseline (readout noise) is visible. However, in the logarithmic plot, the exponential tail due to single-photoelectron events is visible. Its slope yields the gain factor g of the EM amplification. Right: focusing of the light sheet. The ratio $\Delta\hat{S}^2/S$ for a large thermal cloud (covering almost the entire field) is slightly above 2 due to photon shot noise $\Delta_{\mathrm{sn}}\hat{S}$ and residual inhomogeneous density. Near the focus of the system, the value rises due to visibility of atom shot noise, i.e. the "grain" that is caused by the discreteness of atom detection. This coincides with the visibility of the atom shot noise peak in measured correlation functions, see sec. 5.3.

the long expansion of $t_{\mathrm{tof}} = 46\,\mathrm{ms}$ allows to approach the far field (see 5.1), allowing to estimate the initial momentum distribution of the clouds. This is crucial for the experiment scheme used in this thesis. Absorption imaging at such long expansion times would be impractical due to the high sensitivity and depth of field required. Secondly, the high dynamic range of the system, which ranges from single atoms to dense condensates, allows to work with very low atom numbers, typically less than 1000. Thus, even at moderate trap anisotropy (aspect ratios of $\nu_{\mathrm{y,z}}/\nu_{\mathrm{x}} \sim 150$ are typically achievable), clouds deep in the one-dimensional regime with negligible population of transverse states (sec. 2.4) can be worked with.

To infer column densities $n(x, y)$ from pictures taken by the EMCCD camera, it is necessary to calibrate the raw signal. This is done in three steps:

- First, the number of photons which have impinged on each pixel $\hat{P}$ is derived from the number of digital counts $\hat{C}$. As the gain factor g of the electron multiplying unit of the camera may drift over time [274], we calibrate it for each single shot. This is done by taking a second (calibration) picture without any light, directly after the actual fluorescence image, which hence contains technical noise only. In an EMCCD camera, this is mainly given by clock-induced charges (CIC), which cannot be distinguished from actual photons, whereas readout noise is negligible. As the probability of two CIC events in the same pixel on a single shot is negligible, one can make a histogram of $\hat{C}$ for the calibration picture, and fit it by an exponential $g^{-1}\exp(-\hat{C}/g)$ (see appendix C in ref. [202]), which

is expected for the number of counts caused by a single photoelectron after amplification [275], to obtain g. The gain factor g, relating counts in one pixel to the most probable number of photons, can be inferred from the exponential decay constant.

- Apart from the fluorescence light emitted by the atoms, a background offset signal $\hat{b}$ is caused by CIC, as well as stray light from the light sheet beams, and fluorescence photons which have been reflected by the atom chip. As this background is homogeneous over the entire image, it can be calibrated from the image edges, outside the range where atoms are detected.

- Finally, the estimated photon density has to be converted into an estimation for the column density of the expanded atom cloud. This is done by regularly running calibration scans, where pictures of identically prepared clouds are taken using absorption and fluorescence imaging alternately [see fig. 3.14(b-e)] and deriving the expected number of detected photons m from a single atom. For typically chosen settings (resonant light, peak intensity of the light sheet $\sim I_{\mathrm{sat}}$), this value is typically around $m \approx 12$.

Noise of light sheet imaging Both the number of photons detected from each atom, and the number of counts caused by each photon are random variables, the distribution of which needs to be taken into account when analyzing correlations as done in sec. 5.2 and 5.3. Especially for the central result of this thesis, near-perfect number squeezing between two atomic wave packets (fig. 5.4), it is crucial to precisely know the amount of additional fluctuations due to detection noise. Fortunately, the derivation is relatively easy.

Neglecting additional fluctuations due to spatial diffusion (see below), the variance of detected photons is simply given by photon shot noise. As emission from each atom is independent, this means, that for $\hat{P}$ being a random variable for the number of primary photons detected on a certain area of the CCD with expectation value P, the variance due to shot noise is $\Delta_{\mathrm{sn}}\hat{P}^2 = P$. In the electron-multiplication (EM) register of the EMCCD, which sits between photosensors and readout, the signal sequentially passes $R \sim 500$ amplification stages, where an impact ionization probability of $p \sim 1\%$ leads to an electron avalanche growing as $(1+p)^R$. In the limit of low p and large R, the distribution at the output of the register is well understood; the simple outcome is, that the variance of the initial photon shot noise is doubled by the amplification process (excess noise [275]). Here and in the following chapters, we will work with an "effective" photon number $\hat{S}$, which is actually a best-guess inferred from the signal after the stochastic EM amplification, i.e. $\hat{S} = \hat{C}/g$ with the digital counts $\hat{C}$ and the gain factor g. Its expectation value is simply $S = P$. Hence, it can be treated just as a normal photon number, with the exception, that its shot noise is increased by excess noise: $\Delta_{\mathrm{sn}}\hat{S}^2 = 2S$. The second contribution to detection noise is that from background signal $\hat{b}$, which becomes dominant especially for regions with very low density. As mentioned above, background signal (CIC and stray light) is indistinguishable from actual signal. Hence, from analogous considerations, we expect a variance $\Delta\hat{b}^2 \approx \Delta_{\mathrm{sn}}\hat{b}^2 = 2b$, where the actually measured $\Delta\hat{b}^2$ is slightly higher ($2.14 \times b$, typically) which might be due to residual readout noise. For the total detection noise, we arrive

at

$$\Delta_{\mathrm{n}}\hat{S}^2 = 2S + \Delta\hat{b}^2. \tag{3.11}$$

This relation motivates, why for small atom numbers fluorescence imaging is much more sensitive than absorption: while for absorption imaging, the ultimate limit is defined by the shot noise of imaging light, and the noise is only weakly dependent on the actual signal, in fluorescence imaging the main contribution of noise scales with the signal itself, and single-atom visibility is only limited by background. In our case, the single-atom signal-to-background ratio can be calculated to be on the order of 10 [202].

Resolution In contrast to absorption imaging, where the resolution is limited by optical effects (diffraction and finite depth of field), the resolution of the light sheet imaging is fundamentally limited by the diffusion of atoms while being detected. Each atom interacts with the light sheet for $\sim 100\,\mu\mathrm{s}$, during which (depending on the sheet intensity, which is typically similar to I_{sat}), it scatters up to 1000 photons. This imposes a random walk in momentum space due to the recoil of $v_{\mathrm{r}} \approx 6\,\mathrm{mm/s}$ transferred by each absorbed or emitted photon. Emission is assumed to be into full solid angle, whereas photons are absorbed from the two counter-propagating elliptical beams forming the light sheet. Hence, the diffusion of each atom is expected to be stronger along the direction of light sheet propagation, which is at an 45° angle with respect to the y and x axes, which is indeed observed in both Monte Carlo simulations and experiments (see e.g. fig. 5 in ref. [202]). Another subtlety arises from the effect, that unlike in usual imaging systems, where the response to a single emitter (point spread function, PSF) always has the same shape (apart from shot noise), the fluorescence patterns of the single atoms are highly irregular. This has the consequence, that the centroid of each single fluorescence pattern, which has a typical RMS size of $r_{\mathrm{a}} \sim 6\,\mu\mathrm{m}$, may be displaced with respect to the initial unperturbed position by a typical amount of $r_{\mathrm{c}} \sim 3\,\mu\mathrm{m}$ (centroid deviation, see fig. 1(b) in ref. [202]). The actual resolution of the system is hence worse than what could be expected from the size of fluorescence patterns.

These characteristics become very apparent when working with second-order correlation functions (see secs. 2.3 and 5.3) derived from light sheet images, where both the atom shot noise peak and other correlation features are observed, see fig. 3.16. The atom shot noise peak originates from correlations between photon pairs scattered by the *same* atom, and hence has a width[19] $\tilde{r}_{\mathrm{a}} = \sqrt{2}r_{\mathrm{a}}$. On the other hand, for correlation features that arise from photon pairs scattered by *different* atoms, the centroid deviation does contribute to the resolution. In ref. [43], where HBT correlations (sec. 2.3) have been measured for clouds close to condensation, this distinction has been observed nicely: here, the width of the atom shot noise peak is significantly smaller than that of certain atom-atom correlation features, which would have negligible width without imaging. This latter width corresponds to the resolution relevant for all imaging analysis; in fact, measuring HBT correlations is up to now the most reliable way to characterize the light sheet resolution in the experiment itself.

[19] We assume a Gaussian shape of the peak, in which case the width of the auto-correlation is enhanced by a factor $\sqrt{2}$

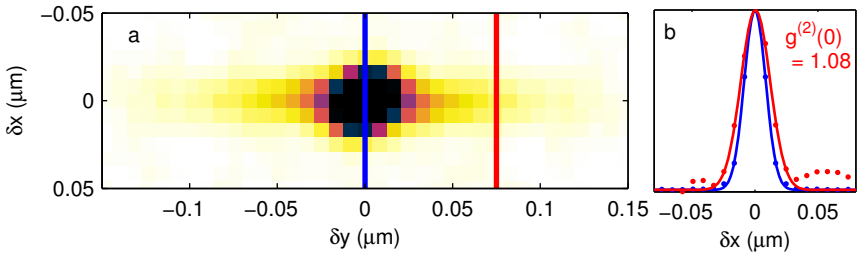

Figure 3.16.: HBT bunching peak in $\tilde{g}^{(2)}(\delta x, \delta y)$ of a thermal cloud just before condensation, observed with light sheet imaging. Data as in fig. 2(a) from ref. [43]. See e.g. sec. 5.3 for definitions and more explanation on how to derive this function. In the center, a large peak due to atom shot noise is given, the width of which [see blue profile in (b)] is determined by the RMS size of single atom fluorescence patterns. Note the sligly elliptic shape, which is elongated in the propagation direction of the light sheet beams. Underneath the shot noise peak, the actual HBT bunching effect is visible, which is strongly anisotropic due to the geometry of the initial trap – any finite size along δx is due to imaging resolution. A longitudinal cut through it [red line in (b)] reveals, that the width of the HBT peak is increased with respect to the shot noise peak, which is due to the centroid deviation as described in the text.

Part II.

Twin-atom beams and optimal control of motional states

4. Twin-beam production in a matter-wave

In this chapter, relying on the general theory of cold Bose gases outlined in chapter 2, several approaches to theoretically capture the emission of twin-atom beams in our specific experimental situation will be explained.

4.1. General formulation of the problem

As mentioned above, the interactions of condensate matter waves can be exploited to provide the non-linearity to populate the twin-mode (which we will equivalently refer to as "twin beams", highlighting the analogy to propagating light wave packets). This can be seen if we start from the Hamiltonian (2.12) for a Bose gas with point-like interactions in second quantization:

$$\begin{aligned}\hat{H}_{\mathrm{tot}} = &\int \mathrm{d}^3\mathbf{r}\hat{\Psi}^\dagger(\mathbf{r},t)\left[-\hbar^2\nabla^2/(2m) + V(\mathbf{r},t)\right]\hat{\Psi}(\mathbf{r},t) \\ &+ \frac{g}{2}\int \mathrm{d}^3\mathbf{r}\hat{\Psi}^\dagger(\mathbf{r},t)\hat{\Psi}^\dagger(\mathbf{r},t)\hat{\Psi}(\mathbf{r},t)\hat{\Psi}(\mathbf{r},t),\end{aligned} \tag{4.1}$$

and assume our bosonic matter-wave field $\Psi(\mathbf{r},t)$ to be comprised of M modes, which can be written in real space as (2.11):

$$\hat{\Psi}(\mathbf{r},t) = \sum_{i=1}^{M}\psi_i(\mathbf{r},t)\hat{a}_i.$$

Instead of using the Bogoliubov approximation as in eq. (2.14), which is not necessarily applicable (see below), we now directly insert this equation into the interaction term of the Hamiltonian (4.1), and obtain

$$\hat{H}_{\mathrm{int}} = \frac{1}{2}\sum_{ijlm}\kappa_{ijlm}\hat{a}_i^\dagger\hat{a}_j^\dagger\hat{a}_l\hat{a}_m, \tag{4.2}$$

where the summation runs from 1 to M for each of the indices i,j,l,m, and we have defined state-specific coupling constants:

$$\kappa_{ijlm}(t) = g\int \mathrm{d}^3\mathbf{r}\psi_i^*(\mathbf{r},t)\psi_j^*(\mathbf{r},t)\psi_l(\mathbf{r},t)\psi_m(\mathbf{r},t). \tag{4.3}$$

We will drop the explicit time dependence in the following, unless stated.

Terms containing the same combination of states in the creation and annihilation operators, respectively (irrespective of order, due to symmetrization), represent elastic scattering within that pair of states, effectively leading to energy shifts:

$$\hat{H}_{\mathrm{el}} = \frac{1}{2}\sum_i\kappa_{iiii}\hat{N}_i^2 + 2\sum_{i<j}\kappa_{ijij}\hat{N}_i\hat{N}_j, \tag{4.4}$$

with $\hat{N} = \hat{a}^\dagger \hat{a}$ being the particle number operator of each mode, respectively. The other terms correspond to inelastic scattering between the states, i.e. contain unequal pairs of modes in the creation and annihilation operators, respectively:

$$\hat{H}_{\mathrm{sc}} = \frac{1}{2} \sum_{\{i,j\} \neq \{l,m\}} \kappa_{ijlm} \hat{a}_i^\dagger \hat{a}_j^\dagger \hat{a}_l \hat{a}_m, \tag{4.5}$$

and inelastic scattering that may occur in the system solely depends on the coupling constants κ.

Let us assume the modes to be plane waves with wave vectors $\mathbf{k}_i$. Then, the integrand in eq. (4.3) has an oscillating phase factor: $\exp(-i\mathbf{\Delta}_{ijlm}\mathbf{r})$, where $\mathbf{\Delta}_{ijlm} = \mathbf{k}_i + \mathbf{k}_j - \mathbf{k}_l - \mathbf{k}_m$. For an infinite, homogeneous system, the integration leads to a non-zero κ_{ijlm} only for

$$\mathbf{\Delta}_{ijlm} = 0 \Rightarrow \mathbf{k}_i + \mathbf{k}_j = \mathbf{k}_l + \mathbf{k}_m, \tag{4.6}$$

enforcing momentum conservation, also known as *phase matching* in quantum optics. In finite-size (or otherwise inhomogeneous, e.g. phase-fluctuating, see sec. 2.4.2) systems, the integration in eq. (4.5) runs over finite limits only, weakening this restricition.

Similarly, energy conservation is required to enable population transfer during the evolution of the system:

$$\epsilon_i + \epsilon_j \approx \epsilon_l + \epsilon_m, \tag{4.7}$$

where in the case of free particles with mass m in identical internal states $\epsilon_i = |\mathbf{k}_i|^2/2m$, neglecting energy shifts arising from $\hat{H}_{\mathrm{el}}$. However, a strict conservation is only valid in the limit of vanishing coupling κ_{ijlm}. For finite coupling, the scattering will occur on a timescale of $1/(\kappa_{ijlm}N)$, where N denotes the typical mode population. From energy-time uncertainty, a power broadening of energy conservation on the order of $\kappa_{ijlm}N$ is expected, and indeed obtained when solving the equations of motion for the system, as will be detailed in the following sections of this chapter.

4.1.1. One-dimensional twin beam system

In the following, we will narrow the description to the case of twin-beam emission from a *single* source state (labeled by index S) in a one-dimensional geometry along direction x: $\mathbf{k}_i = k_i \hat{\mathbf{e}}_x$. The twin-beam modes $\phi_i(x)$, the number and type of which is not restricted at this point, are labeled by i, j. If we neglect inelastic scattering within the twin-beam modes, the inelastic scattering Hamlitonian (4.5) can now be simplified for multi-mode twin-beam dynamics:

$$\hat{H}_{\mathrm{MM}} = \frac{1}{2} \sum_{i,j} \kappa_{ij} \hat{a}_i^\dagger \hat{a}_j^\dagger \hat{a}_{\mathrm{S}}^2 + \mathrm{H.c.}, \tag{4.8}$$

where we introduced the shorthand notation $\kappa_{ij} \equiv \kappa_{ijSS}$.

As outlined in the introduction, in our experiment, the source mode is a one-dimensional quasi-condensate (sec. 2.4), which is in the first transversely excited state along y (vibrational inversion) with a transverse wave function $\phi_1(y)\phi_0(z)$. We denote

its longitudinal wave function as $\psi_{\mathrm{S}}(x)$.[1] On the other hand, the twin-beam modes are in the transverse ground state $\phi_0(y)\phi_0(z)$. Scattering into other combinations of transverse states (which would be allowed by momentum and parity conservation) is inhibited due to the anharmonicity of the potential (see sec. 3.2.2): The increasing level spacings make all other processes energetically inaccessible. After defining the transverse overlaps

$$\alpha_{mn} = \int |\phi_0(z)|^4 |\phi_m(y)|^2 |\phi_n(y)|^2 \mathrm{d}y\mathrm{d}z \tag{4.9}$$
$$\beta_{mn} = \int |\phi_0(z)|^4 [\phi_m^*(y)]^2 [\phi_n(y)]^2 \mathrm{d}y\mathrm{d}z.$$

we obtain coupling constants

$$\kappa_{ij} = g\beta_{01} \int \psi_i^*(x)\psi_j^*(x)[\psi_{\mathrm{S}}(x)]^2 \mathrm{d}x. \tag{4.10}$$

In this chapter, for the transverse states, we assume the single-particle eigenstates of the anharmonic potential prepared as described in sec. 3.2.2, neglecting the deformation due to interactions (as opposed to the treatment in sec. 5.4). As these functions are real-valued, we have $\alpha_{mn} = \beta_{mn}$, and from solving the Schrödinger equation for the potential (3.6), we obtain $\alpha_{00} = 2.96\,\mu\mathrm{m}^{-2}, \alpha_{11} = 2.31\,\mu\mathrm{m}^{-2}, \alpha_{01} = 1.54\,\mu\mathrm{m}^{-2}$, independent of the actual occupation of the transverse states.[2] The chemical potential of the excited source cloud (with zero-point energy subtracted) is then given by the single-particle level spacing, plus the mean field energy of a quasi-condensate at peak (line) density $n_{1\mathrm{d}}(0)$ (see sec. 2.4.1):

$$\mu_1 = h\nu_1 + g\alpha_{11} n_{1\mathrm{d}}(0). \tag{4.11}$$

The multi-mode inelastic scattering Hamiltonian (4.8) retains products of four field operators from the general many-body Hamiltonian (4.1). This makes the resulting Heisenberg equation of motion non-linear in field operators, and thus numerically intractable. A classical mean field approximation [such as the Gross-Pitaevskii equation (2.15)] is unable to include empty or weakly occupied modes [136], as for scattering into those, quantum fluctuations arising from commutators of field operators (which vanish in classical theories) have to be included.

4.1.2. Overview of approximations

In the remainder of this chapter, several beyond-mean-field approaches to approximating a solution and describing the experiment will be discussed:

- In sec. 4.2 we analyze the case of only a single pair of resonant twin-beam modes, which provides qualitative insight, and allows for an exact solution that is compared to the approximated results.

[1] We generally define the transverse wave functions to be normalized to unity, whereas the longitudinal wave functions are normalized to their population.

[2] Note, that in this nomenclature, $g_{1\mathrm{d}} = \alpha_{nn} g$ for a condensate in state n, generalizing eq. (2.30).

- Sec. 4.3 describes how the system can be treated within the Bogoliubov approximation, eq. 2.14. Only the twin-beam modes are retained as quantum fields, allowing for linearized equations of motion for the field operators in the spirit of sec. 2.2.1, that can be solved numerically even in the multi-mode case. This allows for a comprehensive description of the quantum properties of the twin beams (including second-order correlations), but is limited to weak emission only, until depletion of the source mode, which is not accounted for, becomes relevant.
- Sec. 4.4 will introduce an alternative approach that concentrates on the single-particle density matrix (see sec. 2.4.4) of the twin-beam modes, the dynamics of which is determined by a hierarchy of correlation functions of increasing order, which can be approximated at an appropriate level by factorization into lower-order correlations. The total number of particles is conserved. While the predictions of this theory are currently limited to single-particle properties (most notably, the population growth of the twin beams), it accounts completely for source depletion and even can include the vibrational excitation dynamics in our experiment. As will be shown in chapter 5, this theory is able to quantitatively describe our observations with only few free paramters.

Apart from those approaches, several techniques based on stochastic numerics have been developed. This includes positive-P and positive-P-Bogoliubov theories [60, 75, 76, 276–281], which were able to predict results in experiments with weak mode populations with high accuracy [74–76]. For the opposite regime of very high final mode populations, truncated Wigner simulations have been proposed [282–284]. Up to now, attempts to apply either of those methods to our (somewhat intermediate) situation have failed, positive-P being too prone to divergence of atom numbers at long emission times [285], and truncated Wigner requiring even higher populations.

4.2. Two-mode model

If we select only one pair of modes (directly labeled as k, k') from the multi-mode system as described in the previous section, eq. (4.8) becomes equal to the Hamiltonian for parametric down-conversion:

$$\hat{H}_{\mathrm{TM}} = \kappa \hat{a}_k^\dagger \hat{a}_{k'}^\dagger \hat{a}_{\mathrm{S}}^2 + \mathrm{H.c.}, \tag{4.12}$$

where $\kappa \equiv \kappa_{kk'}$ is only non-vanishing for $k' = -k$. If initially, only state S is populated with $N_{\mathrm{S}} = N$ atoms, twin atoms will be emitted into k, k' on a timescale on the order of $1/\kappa N$. If we neglect any time-dependent shifts in the total mean-field energy due to elastic scattering $\langle \hat{H}_{\mathrm{den}} \rangle$, i.e., we only regard the dynamics induced by $\hat{H}_{\mathrm{TM}}$ itself, we can solve the equation of motion for the populations N_{S} and $N_k = N_{k'}$ numerically in the Schrödinger picture. For that, we expand the many-body state in terms of bosonic Fock states (permanents):

$$|\psi(t)\rangle = \sum_{m=0}^{N/2} C_m(t) \left(\hat{a}_k^\dagger \hat{a}_{-k}^\dagger\right)^m \left(\hat{a}_{\mathrm{S}}^\dagger\right)^{N-2m} |0\rangle\,, \tag{4.13}$$

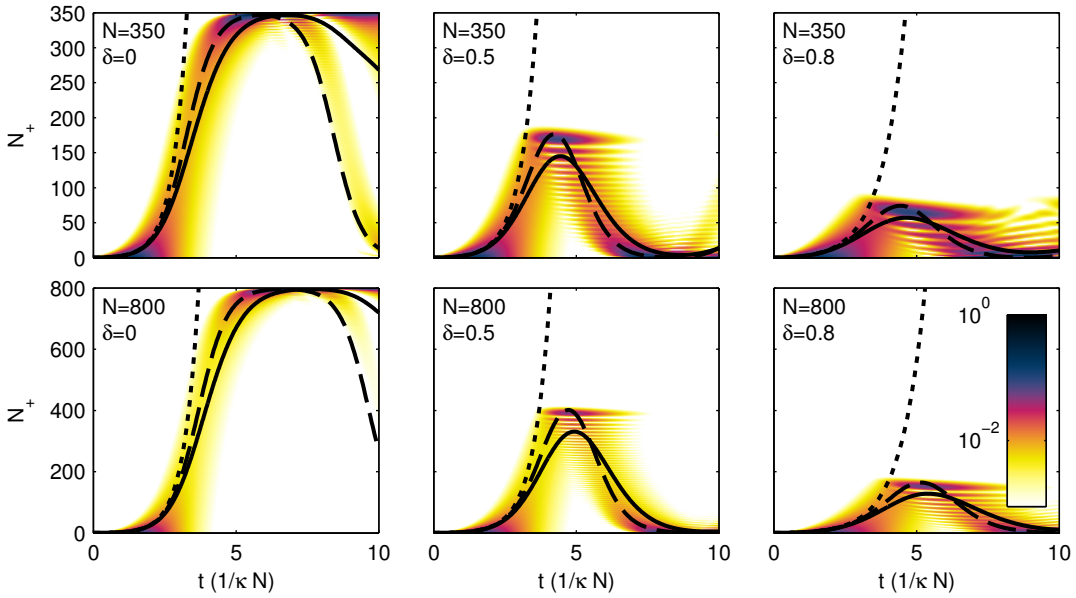

Figure 4.1.: Population dynamics for the two-mode model driven by the coupling of eq. (4.12). In each panel, the respective values of the total atom number N and the detuning δ between source state and twin modes (normalized as defined in the text) are given. False color (logarithmic scale): population of bosonic Fock states as defined in eq. (4.13) from exact solution, normalized to N. Solid lines: expectation value $\langle N_+ \rangle$ of twin beam population from exact solution. Dashed lines: $\langle N_+ \rangle$ from density matrix approximation (section 4.4). Dotted lines $\langle N_+ \rangle$ from Bogoliubov (undepleted) approximation (section 4.3)

where $|0\rangle$ denotes the vacuum state. Assuming all levels to be energetically degenerate, we can now numerically propagate this state using Hamiltonian (4.12) with initially $C_m(0) = \delta_{m0}$ [205].

The result for the populations of the Fock states $|C_m(t)|^2$, along with the expectation value of the total twin-beam population $N_+ = \langle \psi(t)| \hat{a}_k^\dagger \hat{a}_k + \hat{a}_{k'}^\dagger \hat{a}_{k'} |\psi(t)\rangle$, is shown in the leftmost panels of fig. 4.1. The natural time scale for the process is given by the effective coupling $\Omega \equiv \kappa N$, where $N = N_+ + N_S$ denotes the total atom number. One observes an initial slow rise, followed by the onset of strong bosonic amplification that rapidly redistributes the population towards the twin beams, up to complete depletion. Subsequently, a net back-scattering into the source mode occurs, however, the state vector acquires a more complex, branched structure and even exhibits interference phenomena between branches in Fock space.

Additionally, a detuning of the twin beam kinetic energy with respect to the excess energy of state S can be introduced, and defined in a normalized way as $\delta = (\epsilon_S - \hbar^2 k^2/2m)/\Omega$, where m denotes the particle mass. This is easily accomplished by adding a term $\hat{H}_\delta = \delta \cdot \Omega \cdot \hat{a}_S^\dagger \hat{a}_S$ to the total Hamiltonian. In the resulting plots in fig. 4.1, a weaker emission is observed, which completely vanishes at $\delta = 1$, which is consistent with the broadening expected from energy-time uncertainty.

Also, the prediction for the two-mode case from the Bogoliubov and density matrix

approximations are shown. For the former, the twin-beam population can be simply written as [see eq. (4.26) below][3]

$$N_+^{(\mathrm{Bog})} = 2\frac{\sinh^2(\sqrt{1-\delta^2}\Omega t)}{(1-\delta^2)}, \qquad -1 < \delta < 1. \tag{4.14}$$

All three curves show excellent agreement at early times. While the Bogoliubov description fails already at less than 20% of scattered atoms due to negligence of source depletion, the density matrix expansion agrees satisfactorily up to the point of maximum emission, and qualitatively also accounts for the backscattering.

4.3. Bogoliubov approximation

In this section, instead of keeping products of four field operators as in eq. (4.8), we will derive the twin-beam creation dynamics using the Bogoliubov approximation (2.14): $\hat{\Psi}(\mathbf{r},t) \approx \psi_0(\mathbf{r},t) + \hat{\delta}(\mathbf{r},t)$. Here, the source cloud is considered as the (c-number) condensate ψ_0, whereas only the twin beams are contained in the quantum field $\hat{\delta}$. As already mentioned in sec. 2.2, in the Bogoliubov approximation, scattering in and out of the twin beams does not change the amplitude of $|\psi_0|^2$, i.e. the condensate is not depleted accordingly. This is known as undepleted pump approximation in quantum optics and can be safely used for pair generation in optical devices [24], where the yield of the twin-beam emission is negligibly small due to the limited interaction time. Also, this approach has been widely applied to twin-atom creation [278, 279, 286–288], and has been successful in describing numerous experiments [73–76, 280], where the depletion of the source state is small.

In our case, the interaction time can in principle be arbitrarily long, and the conversion into twin beams is mostly limited by depletion. This means, that the Bogoliubov approximation will yield divergent results, and is only valid at the very beginning of the emission process. Still it provides a particularly simple description, that also correctly predicts some basic features (such as the twin-beam kinetic energy and bandwidth). Furthermore, in contrast to the more quantitative theory described below, one obtains the full field operators for the twin-beam modes, giving access to not only the twin-beam populations, but also higher-order correlation functions (as discussed in sec. 2.3).

Our starting point is the Heisenberg equation for $\hat{\delta}$ that is derived from the quadratic excitation Hamiltonian (2.19):

$$i\hbar\frac{\partial\hat{\delta}}{\partial t} = [\hat{H}_0 + 2g|\psi_0(\mathbf{r},t)|^2]\hat{\delta} + g\psi_0^2\hat{\delta}^\dagger, \tag{4.15}$$

with the single-particle Hamiltonian $\hat{H}_0$ as introduced in eq. (2.10). The second term in brackets can be understood as an effective potential for the excitations due to the condensate mean field (with the factor of 2 implicitly arising from symmetrization). The last term allows for production of twin beams. For simplicity, we do not consider a trapped source cloud, but assume a homogeneous one-dimensional gas with line

[3] Compared to eq. (4.26), the notation is slightly different here, which can be resolved by recognizing, that $N_+ = 2N_k, \delta = \Delta/\Omega$.

density $n_{1\mathrm{d}}$ in a box of length L. The source cloud is in vibrational inversion along y, whereas the twin-beam modes, which are assumed as plane waves, reside in the transverse ground state. Thus, we can write:[4]

$$\begin{aligned}\psi_0(\mathbf{r},t) &= \sqrt{n_{1\mathrm{d}}}\phi_1(y)\phi_0(z)\exp[-i(\mu_1/\hbar)t] \\ \hat{\delta}(\mathbf{r},t) &= \phi_0(y)\phi_0(z)L^{-1/2}\sum_q \exp[-iqx]\hat{a}_q(t).\end{aligned} \tag{4.16}$$

We insert those functions into eq. (4.15), multiply the result with $\phi_0^*(y)\phi_0^*(z)L^{-1/2}\cdot\exp(ikx)$, and integrate over all spatial directions. As the mode coupling strengths $\kappa_{k,k'}$ are non-zero only for $k'=-k$ in an infinite system, we obtain:

$$i\hbar\frac{\partial\hat{a}_k}{\partial t} = \left(\frac{\hbar^2k^2}{2m}+2gn_{1\mathrm{d}}\alpha_{01}\right)\hat{a}_k(t) + gn_{1\mathrm{d}}\exp[-2i(\mu_1/\hbar)t]\beta_{01}\hat{a}^\dagger_{-k}(t). \tag{4.17}$$

We now take the time derivative of (4.17), substitute $\partial\hat{a}_{-k}/\partial t$ and $\hat{a}_{-k}(t)$ (by solving eq. (4.17) for those). This gives a second-order differential equation for the dynamics of $\hat{a}_k(t)$:

$$\begin{aligned}&\frac{\partial^2\hat{a}_k}{\partial t^2} + 2i\frac{\mu_1}{\hbar}\frac{\partial\hat{a}_k}{\partial t} \\ &\quad+\hbar^{-2}\left[\left(\frac{\hbar^2k^2}{2m}+2gn_{1\mathrm{d}}\alpha_{01}\right)\left(\frac{\hbar^2k^2}{2m}+2gn_{1\mathrm{d}}\alpha_{01}-2\mu_1\right)-g^2n_{1\mathrm{d}}^2|\beta_{01}|^2\right]\hat{a}_k(t)=0.\end{aligned} \tag{4.18}$$

At this point, let us define some characteristic frequencies/energies of the twin-beam system:

$$\text{Mode kinetic energy:}\qquad \epsilon_k = \hbar^2k^2/(2m) \tag{4.19}$$

$$\begin{aligned}\text{Source excess energy:}\qquad \epsilon_\mathrm{S} &= \mu_1 - 2gn_{1\mathrm{d}}\alpha_{01} \\ &= h\nu_1 - gn_{1\mathrm{d}}(2\alpha_{01}-\alpha_{11})\end{aligned} \tag{4.20}$$

$$\text{Mode detuning:}\qquad \Delta_k = (\epsilon_k-\epsilon_\mathrm{S})/\hbar \tag{4.21}$$

$$\text{Emission rate:}\qquad \Omega = gn_{1\mathrm{d}}|\beta_{01}|/\hbar. \tag{4.22}$$

Eq. (4.20) describes the source excess energy (which is shifted from ν_1 by mean field effects [63, 68, 75]) that will be converted into the twin-beam peak kinetic energy. The typical rate of twin-beam production is given by Ω. We further define $\hat{a}_k(t)\equiv\hat{b}_k(t)\exp[-i(\mu_1/\hbar)t]$ (corresponding to a shift of the energy zero point), and finally write eq. (4.18) in a more meaningful way as:

$$\frac{\partial^2\hat{b}_k}{\partial t^2} + (\Delta_k+\Omega)(\Delta_k-\Omega)\hat{b}_k(t)=0. \tag{4.23}$$

For $|\Delta_k|<\Omega$, the solution reads:

$$\hat{b}_k(t) = \hat{A}\cosh[\omega_k t] + \hat{B}\sinh[\omega_k t], \tag{4.24}$$

[4] In this section, as we will be concerned with plane-wave states with well-defined momenta, we will use the direct notation $\hat{a}_k$, instead of the (enumerated) $\hat{a}_i$.

where we defined $\omega_k^2 = |\Omega_k^2 - \Delta_k^2|$. For $|\Delta_k| > \Omega$, the hyperbolic functions are replaced by cos and sin, giving an oscillating solution, leading to negligible mode populations. This implies, that the amplification bandwidth, i.e. the (kinetic) energy range around ϵ_S where twin beams are produced, is given by Ω (power broadening). The coefficients $\hat{A}, \hat{B}$ can be determined from initial conditions, and we finally obtain for modes within the bandwidth:

$$\hat{b}_k(t) = \hat{a}_k(t)e^{i(\mu_1/\hbar)t} = \hat{a}_k(0)\cosh[\omega_k t] - i\omega_k^{-1}[\Delta_k \hat{a}_k(0) + \Omega \hat{a}_{-k}(0)^\dagger]\sinh[\omega_k t]. \quad (4.25)$$

Thus, if the modes are empty initially, the population dynamics is

$$N_k(t) = \langle \hat{a}_k^\dagger(t)\hat{a}_k(t)\rangle = \left(\frac{\Omega}{\omega_k}\right)^2 \sinh^2[\omega_k t], \quad (4.26)$$

which is obtained from the commutation relations for the $\hat{a}_k(0)$. See fig. 4.1 for a comparison to the exact result for two modes (in the figure, $\delta = \Delta/\Omega$). The peak production rate of twin beams is reached if $\Delta_k = 0$, at a momentum $k_0 = \sqrt{2m\epsilon_S}$.

Similarly, one can derive non-local and higher correlation functions, such as $G^{(1)}$ (or, equivalently, ρ, see sec. 4.4) and the anomalous density M:

$$G^{(1)}_{k,k'}(t) \equiv \rho_{k,k'}(t) = \langle \hat{a}_k^\dagger(t)\hat{a}_{k'}(t)\rangle = \delta_{k,k'}N_k \quad (4.27)$$

$$M_{k,k'}(t) = \langle \hat{a}_k(t)\hat{a}_{k'}(t)\rangle = [-i\sqrt{N_k}\cosh[\omega_k t] - (\Delta_k/\Omega)N_k]\delta_{k,-k'}, \quad (4.28)$$

the latter being nonzero only for modes with opposite momenta. For initially empty modes, Wick's theorem states that the second-order correlation function behaves as $G^{(2)}_{k,k'} = N_k N_{k'} + |G^{(1)}_{k,k'}|^2 + |M_{k,k'}|^2$, and thus:

$$g^{(2)}_{k,k'}(t) = 1 + \delta_{k,k'} + [N_k^{-1}\cosh[\omega_k t] + (\Delta/\Omega)^2]\delta_{k,-k'}, \quad (4.29)$$

indicating excess second-order correlations only at identical same (Hanbury Brown-Twiss bunching) and opposite (back-to-back pair correlations) momenta [286].

As demonstrated in refs. [287, 288], in contrast to the two-mode model, the theory explained in this section can be extended to inhomogeneous systems by choosing appropriate wave functions for ψ_0 and $\hat{\delta}$. In fig. 4.2, numerical results of such calculations for our system, that have been obtained in collaboration with Jan Chwedeńczuk and Tomasz Wasak, are shown.

4.4. Density matrix expansion

While the Bogoliubov approximation provides complete information about the state of the emitted twin beams, it fails to quantitatively describe the experiments presented in this thesis: Quickly after the onset of twin-beam emission, the depletion of the source population becomes dominating, whereas at short times its continuous pumping from the ground state have to be considered. Both is hard to achieve when treating the source state as a classical field. Instead of splitting the matter-wave into a classical part and quantum perturbations, we now describe the system in its entirety in terms of reduced density matrices of increasing order [192, 193], in analogy

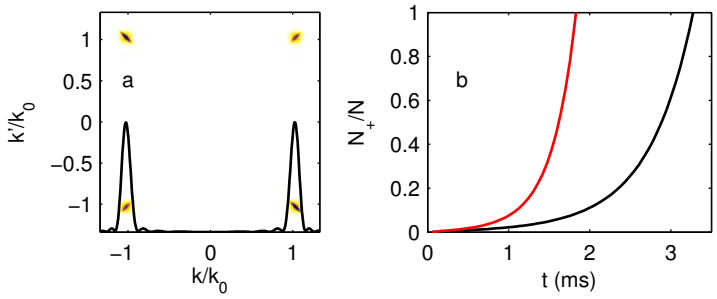

Figure 4.2.: Numerical results obtained from finite-size Bogoliubov calculation. (a) False-color plot (a.u.) of $G^{(2)}_{k,k'}$ at $\lesssim 1\,\mathrm{ms}$ after starting the emission process with $N = 800$ atoms in the source cloud. The superimposed black line indicates the density distribution. Note that the back-to-back peaks at $k = -k' = k_0$ are significantly higher than the bunching peaks at $k = k' = k_0$, indicating violation of the Cauchy-Schwarz inequality (see sec. 5.3.4). (b) Total population of twin-beam modes for $N = 350$ (black) and $N = 800$ (red). As depletion is not accounted for, the twin-beam population grows rapidly, and assumes unphysical values > 1 after few milliseconds.

to a classical BBGKY hierarchy.[5] We start from the single-particle density matrix $\rho[\equiv G^{(1)}]$, which corresponds to tracing out all but one particle from the total system. It is sufficient for describing single-particle observables, such as distribution functions in real or momentum space, single-particle eigenmodes, and their populations. In contrast to symmetry-breaking approaches, the particle number is strictly conserved [289], allowing to treat depletion appropriately.

Using the density matrix description, meaningful approximations can be made by truncating the hierarchy of correlations of increasing order, at some point appropriate for the system under study. This relies on the assumption that those higher correlations become less and less important and can be factorized into densities [as in eq. (2.25)]. Initially developed for approximating problems in classical kinetic theory, this method has been extended to quantum problems early on. A treatment of bosonic Josephson dynamics in a quantum gas beyond mean fields has been demonstrated in ref. [290]; the application to our system, which is formally similar to the one demonstrated in ref. [291], has been conceived by Ulrich Hohenester, and will be outlined in the following.

4.4.1. Equations of motion

Primarily, we want to study the amplified population growth of the twin beams, so we are directly interested in the entries of the single-particle reduced density matrix, expressed in terms of basis states i, j:

$$\rho_{ij} = \langle \hat{a}_i^\dagger \hat{a}_j \rangle \tag{4.30}$$

[5] The concept of reduced density matrices is essentially equivalent to increasing-order non-normalized Glauber correlation functions (sec. 2.3), using a language related rather to statistical physics than quantum optics. For example, the single-particle density matrix ρ, as already used in the context of quasi-condensates [eq. (2.36)] is analogous to the $G^{(1)}$ function.

which has the populations of twin-beam modes i, j on its diagonal, and off-diagonal coherences between them. The source population will be denoted as $N_\mathrm{S} \equiv \rho_\mathrm{SS} = \langle \hat{a}_\mathrm{S}^\dagger \hat{a}_\mathrm{S} \rangle$. An extended description, that also includes the absolute ground state of the system will be given in chapter 5. The Heisenberg equation of motion for $\hat{a}_i^\dagger \hat{a}_j$ and the multi-mode Hamiltonian (4.8), plus free evolution (which contains the *total* twin-beam mode energies ϵ_i', see below) $\hat{H}_0 = \sum_i \epsilon_i' \hat{a}_i^\dagger \hat{a}_i + \mu_1 \hat{a}_\mathrm{S}^\dagger \hat{a}_\mathrm{S}$ leads to the expressions (with $\hbar \equiv 1$):

$$\begin{aligned} \dot{\rho}_{ij} &= -i \left\langle \left[\hat{a}_i^\dagger \hat{a}_j, \hat{H}_0 + \hat{H}_\mathrm{MM} \right] \right\rangle \\ &= -i \left[\epsilon_i' \rho_{ii} - \epsilon_j' \rho_{jj} \right] + \sum_m \left(\kappa_{im} \Delta_{mj} - \Delta_{im}^* \kappa_{mj} \right) \\ \dot{\rho}_\mathrm{SS} \equiv \dot{N}_S &= -\sum_i \rho_{ii}, \end{aligned} \tag{4.31}$$

depending on the two-particle density matrix entries:

$$\Delta_{ij} \equiv \Delta_{ij\mathrm{SS}} = \langle \hat{a}_i^\dagger \hat{a}_j^\dagger (\hat{a}_\mathrm{S})^2 \rangle. \tag{4.32}$$

Truncating the density matrix hierarchy at this level by e.g. factorizing $\Delta_{ij} \approx \sqrt{N_i N_j} N_\mathrm{S}$ would correspond to a mean-field theory, where correlation functions higher than first order are assumed to be that of a coherent state [290]. It can immediately be seen by inserting this approximation into eq. 4.31, that such a description would fail in our case, as $N_i = 0$ for any i in the initial (empty) state, and hence $\dot{\rho}_{ii} = 0$ for all i. Thus, we have to derive an approximate set of equations of motion for the entries Δ_{ij}. Proceeding one step further in the density matrix hierarchy, the Heisenberg equation for $\dot{\Delta}_{ij}$ will contain three-particle correlations. We factorize those into products of lower-order density matrices,[6] e.g.:

$$\left\langle \hat{a}_i^\dagger \hat{a}_j^\dagger \hat{a}_\mathrm{S}^\dagger \hat{a}_l \hat{a}_m \hat{a}_\mathrm{S} \right\rangle \approx \rho_{il} \rho_{jm} N_\mathrm{S}, \tag{4.33}$$

finally leading to

$$\begin{aligned} i\dot{\Delta}_{ij} \approx &- \kappa_{ij} N_\mathrm{S}(N_\mathrm{S} - 1) + (2N_\mathrm{S} + 1) \sum_{m,l} \kappa_{ml} \rho_{im} \rho_{jl} \\ &- N_\mathrm{S}(N_\mathrm{S} - 1) \sum_m \left(\kappa_{im} \rho_{mj} + \kappa_{jm} \rho_{mi} \right) \\ &+ \Delta_{ij} [2\mu_1 - \epsilon_i' - \epsilon_j'] \,. \end{aligned} \tag{4.34}$$

This expression now allows for growth of the twin-beam mode populations ρ_{ii}, due to the first term, which does not depend on any elements ρ_{ij} and hence can account for

[6] The best way to concatenate the field operators is not obvious a priori, and it has been suggested that all possible combinations have to be averaged [289]. However, for our case, factorizing the source population N_S out of the three-particle correlation gave satisfactory results.

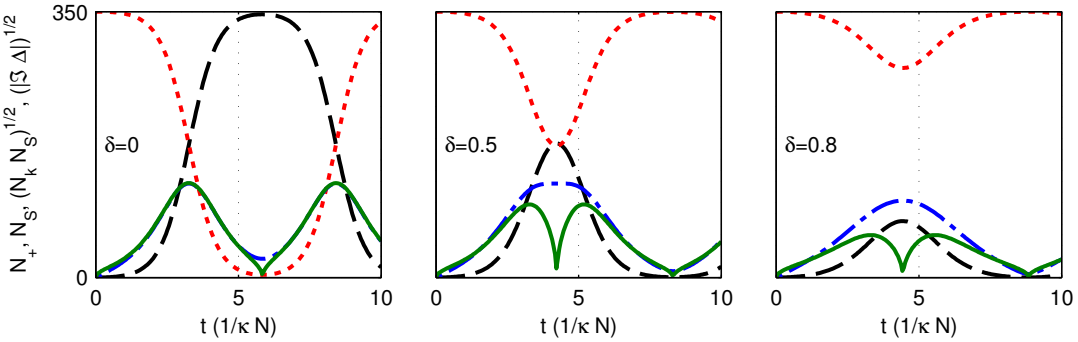

Figure 4.3.: Density matrix elements for the two-mode problem at different detunings δ. Parameters are as in the upper row of fig. 4.1. Black dashed line: twin-beam population $N_+ = 2N_k$. Red dotted line: source population N_S. Blue dash-dotted line: $\sqrt{N_k N_\mathrm{S}}$. Green solid line: $\sqrt{|\Im\Delta|}$. Note, that $|\Im\Delta| > N_k N_\mathrm{S} = 0$ initially, allowing for growth of twin beams.

spontaneous scattering into empty modes. The last term ensures energy conservation, and acts similarly to the detuning Δ_k in the Bogoliubov picture. We can now solve the equations of motion for the single-particle density matrix (4.31). Some results for our system will be presented below.

Before, it is instructive to revisit the two-mode case from sec. 4.1 using the density matrix formalism. In this case, using the nomenclature introduced in that section, eq. 4.34 reduces to:

$$\dot{\Delta} \approx i\kappa \left[N_\mathrm{S}(N_\mathrm{S}-1)(2N_k+1) - 2N_k^2(2N_\mathrm{S}+1) \right], \tag{4.35}$$

with $N_k = \rho_{kk} = \rho_{k'k'}$. The second term in brackets accounts for the backscattering of population into the source state, as also observed in the exact solution (sec. 4.2), even though there are quantitative deviations. For $\epsilon_\mathrm{S} = \epsilon_k$, eq. (4.31) becomes $\dot{N}_k = 2\kappa\Im\Delta$, resulting in the dashed curves in the left column ($\delta = 0$) of fig. 4.1. Initially, $N_k = 0$ and $N_\mathrm{S} = N \gg 1$, and eq. (4.35) reduces to $\dot{\Delta} \approx i\kappa N^2$. Consequently, the emitted population grows quadratically as $N_k \approx (\Omega t)^2$ (with $\Omega = \kappa N$), which for short times t is consistent with the two-mode Bogoliubov approximation, eq. (4.14). If a detuning is present, standard free evolution terms have to be included, leading to the data shown in the $\delta \neq 0$ panels in fig. 4.1, which show good agreement with the exact solution. In fig. 4.3, the matrix elements from the two-mode density matrix model are shown for different detunings.

4.4.2. Results for our system

We now discuss some results obtained from numerically solving the dynamics of the multi-mode single-particle density matrix, eq. 4.31, for the parameters of the experiments shown in this thesis. For the longitudinal source state in eq. (4.10), instead of the homogeneous system in sec. 4.3, we assume a Thomas-Fermi profile corre-

sponding to the longitudinal confinement $V_{\mathrm{ext}}(x)$: $\psi_{\mathrm{S}}(x) = \psi_{\mathrm{TF}}(x) \equiv \sqrt{n_{\mathrm{TF}}(x)}$,[7] i.e. $\kappa_{ij} = g\beta_{01} \int \psi_i^*(x)\psi_j^*(x) n_{\mathrm{TF}} \mathrm{d}x$. We neglect the phase fluctuations present in a realistic quasi-condensate at temperatures $T > T_\phi$ (sec. 2.4.2).

For the longitudinal modes of the twin beams, we can assume trapped eigenstates $\psi_i(x)$, which can be inferred from solving the time-independent Schrödinger equation analogous to eq. (4.15):

$$\epsilon_i' \psi_i(x) = \frac{1}{2m} \nabla^2 \psi_i(x) + \left[V_{\mathrm{ext}}(x) + 2g\alpha_{01} n_{\mathrm{TF}}(x) \right] \psi_i(x). \tag{4.36}$$

The effective potential term within the TF radius is rather flat, as there $n_{\mathrm{TF}}(x) = n_{\mathrm{TF}}(0) - (g\alpha_{00})^{-1} V_{\mathrm{ext}}(x)$, and $2\alpha_{01} \approx \alpha_{00}$. Hence, near the density peak (where the twin beams are mostly emitted) the solutions closely resemble plane waves with kinetic energy $\epsilon_i \approx \epsilon_i' - 2g\alpha_{01} n_{1\mathrm{d}}(0)$, restoring the situation of the Bogoliubov approximation. As a basis set for the calculation, we choose a sufficient number of states around $\epsilon_i' \approx \mu_1$ to cover the expected amplification bandwidth $\Omega = g\beta_{01} n_{\mathrm{TF}}(0)$. Alternatively, we will also consider the case of plane, running waves with periodic boundaries (i.e., ring topology) of length L:

$$\psi_i'(x) = \frac{1}{\sqrt{L}} \exp(ik_i x), \tag{4.37}$$

similar to the treatment shown in the previous section. In this case, we directly assign energies $\epsilon_i' = \epsilon_i + 2g\alpha_{01} n_{\mathrm{TF}}(0)$ in the simulation.

This assumption of stationary basis states (and hence, coupling coefficients κ) only holds for the very onset of emission, where the mean field is mostly given by atoms in the transversely excited state. Currently, the density matrix simulation is limited to static wave functions and energies, however, as $2\alpha_{01} - \alpha_{11} \ll \epsilon_{\mathrm{S}}$ we expect the impact of changing mean fields to be small.

In fig. 4.4, the time evolution of the twin-beam populations predicted by the density matrix expansion are shown for plane waves and trap eigenstates. From the simulated single-particle density matrix entries $\rho_{ij}(t)$, real and momentum space distributions can be inferred as:

$$n(x,t) = \sum_{i,j} \psi_i^*(x)\psi_j(x)\rho_{ij}(t), \qquad \tilde{n}(k,t) = \sum_i \tilde{\psi}_i^*(k)\tilde{\psi}_j(k)\rho_{ij}(t) \tag{4.38}$$

$$\tilde{\psi}_i(k) = \int \psi_i(x) e^{-ikx} \mathrm{d}x.$$

It is observed that twin-beams wave packets are created near the center of the TF distribution, and then propagate outwards with a peak momentum $k_0 = \sqrt{2m\epsilon_{\mathrm{S}}} \approx 5.5\,\mu\mathrm{m}^{-1}$, with $\epsilon_{\mathrm{S}} \approx h\nu_1 - g n_{\mathrm{TF}}(0)[2\alpha_{01} - \alpha_{11}]$ as derived above. While in the plane-wave case, the momentum distribution remains constant and matter-wave packets propagate across the periodic boundaries (as in a ring geometry), for the trapped

[7] As the longitudinal wave function does not have sufficient time to relax according to the changed interaction constant after excitation, we assume a TF potential that is derived from the ground state chemical potential before excitation (i.e., which contains α_{00}, not α_{11}).

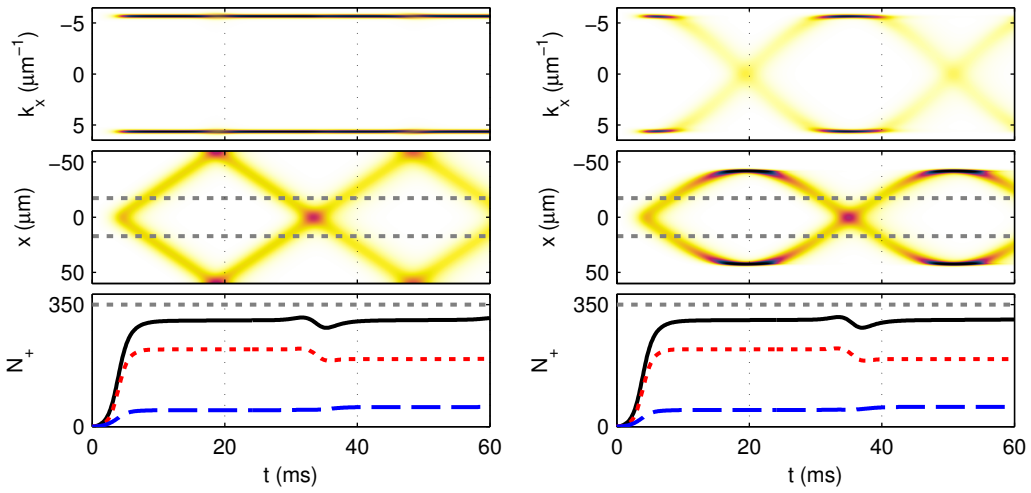

Figure 4.4.: Twin beam evolution in momentum space (top) and real space (middle) for $N = 350$ atoms. Grey lines indicate the Thomas-Fermi radius R of the source cloud. On the bottom, the total population of the twin beams (black, solid), and the populations of the first (red, dotted) and second (blue, dashed) pair of one-body eigenstates are shown. Left: plane-wave basis with periodic boundaries. Right: effective potential eigenstate basis.

states the momentum distribution soon broadens and shifts inwards when the packets approach the turning points of the potential. Near the turning points, the real space density temporarily narrows due to the strong anharmonicity of the mean-field effective potential, and the packets travel inwards again. The bottom panel shows that the total population of the twin beams N_+ remains constant after $\approx 6\,\mathrm{ms}$, which corresponds to the time when the twin-beam packets leave the region of the source cloud. This can be estimated as $\tau_{\max} \sim R \cdot (\hbar k_0/m)^{-1} \approx 4.5\,\mathrm{ms}$ for the TF radius $R \approx 17\,\mu\mathrm{m}$. As can be expected, the population dynamics and initial shape of the wave packets are not noticeably affected by the choice of the twin-beam basis set. After a half oscillation (or round-trip, in the travelling-wave case), the two packets encounter each other, causing a slight modulation in their total population, and a net transfer into the second-largest pair of eigenmodes (see sec. 4.4.3).

4.4.3. Single-particle density matrix and fragmentation

We now take a brief look at the first-order coherence properties predicted for the twin beams by the density matrix calculation. From a statistical mechanics viewpoint, the single-particle density matrix ρ as introduced in eq. (4.30) has all but one of the N particles traced out from the many-body density matrix of the full system [193]:

$$\rho = \mathrm{Tr}_{(2\ldots N)}\{\rho_{\mathrm{tot}}\}. \tag{4.39}$$

Even if the total system, represented by ρ_{tot}, is closed and undergoes a unitary evolution governed by the von-Neumann equation, the single-particle sub-system described by ρ may evolve from a pure state (which we have prepared initially) into a mixed state with respect to single-particle properties. Indeed, once the matrix elements ρ_{ij}

acquire non-zero values, we observe several macroscopic eigenvalues of ρ. They are composed of pairs with equal populations in each, where one pair has significantly larger population than the others (see fig. 4.4, red dotted line). When using the plane-wave basis [fig. 4.4, left panel, and eq. (4.37)], and neglecting all but the largest pair of eigenvalues, we have in momentum space:

$$\rho_0(k,k) = \frac{N_+}{2}|\psi_{\mathrm{L}}(k)|^2 + \frac{N_+}{2}|\psi_{\mathrm{R}}(k)|^2, \tag{4.40}$$

where the orbitals $\psi_{\mathrm{L}}, \psi_{\mathrm{R}}$ are peaked around momenta k_0 and $-k_0$, reflecting momentum conservation. Also the less-populated pairs retain this symmetry. The first-order correlation functions is then given by

$$g_0^{(1)}(k,k') = \begin{cases} 1, & k,k' \in \mathrm{L} \text{ or } k,k' \in \mathrm{R} \\ 0, & \text{otherwise.} \end{cases}, \tag{4.41}$$

where L and R denote the regions in momentum space covered by each of the orbitals. This result is equivalent to that obtained from the Bogoliubov approximation (4.27), taking into account that the latter assumes a homogeneous system, where momentum conservation is strictly obeyed and the mode pairs decouple.[8] In other terms, we move from a single condensate in the Penrose-Onsager sense (sec. 2.4.4) to a fully fragmented state [193], where each of the twin-beams is an independent condensate with respect to single-particle properties. The relative phase between these condensates is undefined (as expected for a twin-Fock state). As the total evolution of the system is unitary, this process must be accompanied by a buildup of higher-order correlations, as predicted by the Bogoliubov approximation [fig. 4.2(a)]. This relation becomes obvious from the viewpoint of each single particle (as represented by ρ), where the other $N-1$ particles act as an environment, and the correlation buildup is perceived as a decoherence process [290]. In our case, while their relative phase is undefined, number squeezing between the twin-beams (which is a two-particle property) is present. However, as the density matrix theory at its current stage of development is limited to calculating single-particle quantities, only the former can be predicted.

[8] Also, in the finite-size Bogoliubov calculations (fig. 4.2), the same pair-wise appearance of eigenstates is observed.

5. Analysis of the experimental results

5.1. Overview

In this chapter, a detailed qualitative and quantitative analysis of experimental data will be presented. As introduced in chapter 1, the two main goals of the investigations are, to prove stronger-than-classical correlations in the twin-atom beams, and to understand the dynamics of the excitation and emission process.

Sequence for twin-beam production All our experiments start with the preparation of a quasi-condensate as laid out in sec. 3.2.3. The final evaporation ramp, which cools the cloud to quantum degeneracy, is performed in the dressed anharmonic trap (see sec. 3.2.2). For the following steps, the anharmonicity of the transverse confinement is crucial for two reasons. First, in a harmonic trap, the quasi-classical center-of-mass motion and the internal dynamics of a cloud completely decouples, even in presence of arbitrary two-body interactions [145, 146]. The desired wave function, which is the first excited solution of the Gross-Pitaevskii equation (GPE), has a different symmetry (odd vs. even parity) and internal structure than the ground state (such as a non-positive Wigner function). Hence, it could not be reached by displacement of the trap, even for an optimized trajectory [251]. The second reason for the anharmonicity relates to the emission process: for our potential, the level spacings are increasing ($\nu_1 = 1.84\,\mathrm{kHz}, \nu_2 = 1.99\,\mathrm{kHz}$, see sec. 3.2.2). This means, that two-particle scattering into combinations of transverse states, other than both atoms going to the ground state, are energetically unfavorable.

Atom numbers in the final trap range between $N \sim 300$ and $N \sim 2000$ (see table 5.1 below), where most data has been taken at around $N \sim 800$, which corresponds to the non-linearity set in the excitation sequence optimization (appendix A). Assuming longitudinal Thomas-Fermi profiles and transverse single-particle states, this latter value corresponds to a Thomas-Fermi peak density of $n_{\mathrm{TF}}(0) \approx 25\ \mu\mathrm{m}^{-1}$, a chemical potential $\mu_0 \approx h \cdot 600$ Hz, and a radius $R \approx 23\ \mu\mathrm{m}$. The temperature of the final clouds is hard to obtain precisely in the experiment, as no thermal cloud is visible in the images, and the temperatures and densities are too low to apply density correlation thermometry [153]. From the cloud width after expansion (appendix B) and the emission dynamics (sec. 5.5), a temperature $T \sim 25\,\mathrm{nK} \approx (h/k_{\mathrm{B}}) \cdot 510\,\mathrm{kHz}$ for most of the data sets is estimated. Hence, the conditions for a 1d description $\mu_0, T < \nu_1 = 1.84\,\mathrm{kHz}$ are fulfilled, and we are in a quasi-condensate regime, as can be read off fig. 2.1.

Having prepared the quasi-condensate in the anharmonic potential, we start the excitation process that transfers the atoms into the source state. In fig. 5.1, the entire twin-beam production sequence is depicted in various experimental and theoretical results. All experimental data has been obtained by switching off all confinement potentials at time t, and taking a time-of-flight image using the light sheet system, as shown in fig. 5.2. At $t = 0$, the motion of the trap along y is started. In panel

(b), the trajectory $\lambda(t)$, along which the trap travels until $t = T = 5\,\mathrm{ms}$, is shown. $\lambda(t)$ has been derived from the optimal control calculation explained in appendix A. The response of the transverse wave function can be obtained by solving the GPE with an additional driving term [eq. (5.27)], the resulting momentum distribution is shown in panel (c). Using the two-level driving model derived in sec. 5.4.3, we can extract effective populations of ground and source state (panel d) from the numerical solution. Experimental data for the transverse momentum distribution of the source is shown in panel (e), which has been derived from time-of-flight fluorescence images, see fig. 5.2. Up to $t \sim 7\,\mathrm{ms}$, the agreement with GPE numerics is excellent (a quantitative comparison is presented in sec. 5.4.1), but degrades at later times due to second-order collisions of the source cloud with the emitted twin-beam atoms not captured by the GPE. In panel (f), the numerically derived (see sec. 4.4) *in-situ* density distribution of the twin-beam packets is shown, which are produced near the peak of the initial condensate, and then propagate outwards. Finally, panel (g) displays experimentally obtained time-of-flight profiles along the longitudinal direction (note the logarithmic color scaling). Soon after starting the excitation sequence, the twin-beam peaks become visible at a position that corresponds to the momentum $k_0 = \sqrt{2m\epsilon_\mathrm{S}}$ (see sec. 4.3). Also, the population of the twin-beams is shown and compared to results of the density matrix expansion model developed in sec. 4.4.

Interpretation of fluorescence images With very few exceptions, all data shown in this thesis have been acquired in expansion, as shown in fig. 5.2, using the light sheet fluorescence imaging system of our experiment (see secs. 3.1.6 and 3.2.4 for details). Even though changing the time-of-flight expansion time is possible by making hardware adjustments, $t_\mathrm{tof} = 46\,\mathrm{ms}$ has been used throughout all measurements. The capability to take slice images by pulsing the light-sheet beams briefly [43, 202] is not used, which means that the density distribution of the clouds is fully integrated over the transverse z direction. The vertical extent of the cloud implies a dependence of the detection time of each atom on its position along z with respect to the center of mass of the falling cloud. While this should cause an additional blur of the images in regions corresponding to high velocities in the lateral xy-plane, a straightforward calculation for typical parameters shows, that this effect is negligible compared to the effect of diffusion of atoms within the light sheet.

For a one-dimensional degenerate gas, as considered here, the fast transverse expansion of the cloud causes atom interactions to vanish rapidly after release from the trap, and the ensuing expansion can be considered ballistic [292]. Along y (i.e., integrating over x), the resulting image represents the initial momentum distribution, as the transverse cloud size before expansion is negligible (far field). If we express momenta as wave numbers k_y, a distance δy in the image hence corresponds to $\delta k_y = \alpha\,\delta y$ with $\alpha = m/\hbar t_\mathrm{tof} \approx 0.030\,\mu\mathrm{m}^{-2}$. The object space pixel size of our camera of $4\,\mu\mathrm{m}$ is then equivalent to momentum space pixels of $0.12\,\mu\mathrm{m}^{-1}$ length.

Along the longitudinal direction x, the far field condition is not fully reached due to the initial condensate radius of $R \approx 20\,\mu\mathrm{m}$ and the typical momenta in the quasi condensate as given by the thermal coherence length λ_T (2.36) $k_\phi = \lambda_\mathrm{T}^{-1} \sim 0.1\,\mu\mathrm{m}^{-1} \approx \alpha L$ (see fig. 2.2). On the other hand, the center momentum of the emitted atoms is $k_0 \approx 5.5\,\mu\mathrm{m}^{-1} \gg (\alpha L, k_\phi)$, hence the longitudinal overlap of the source cloud and the

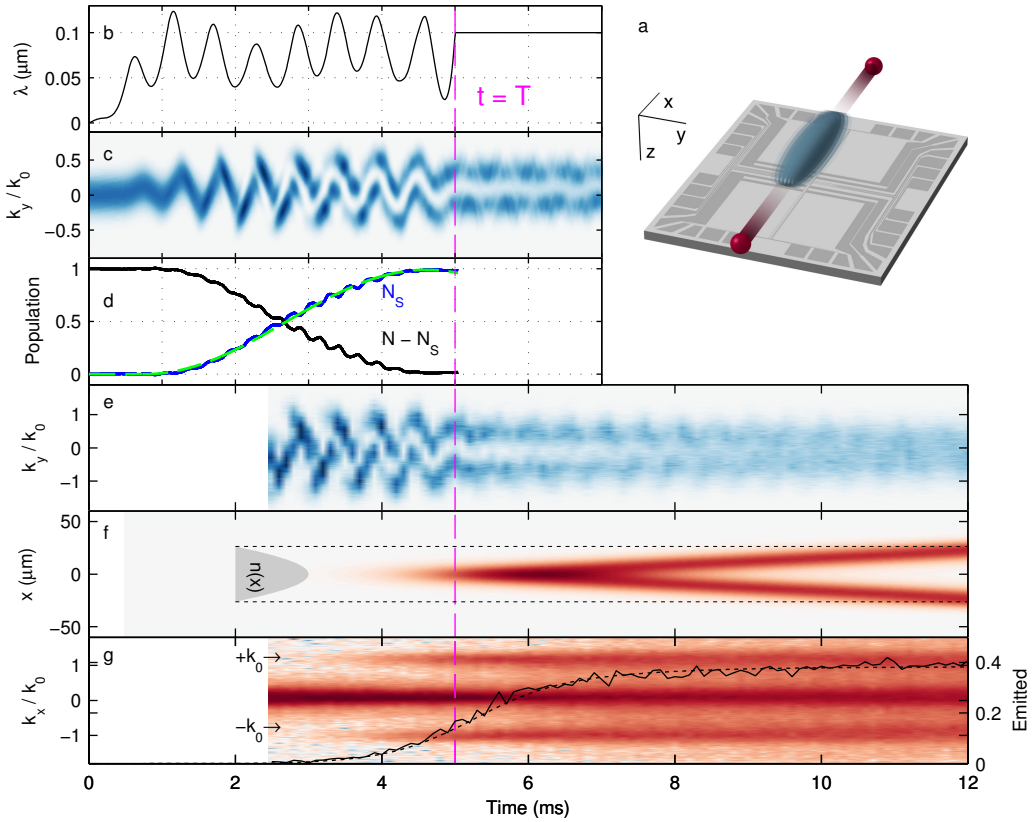

Figure 5.1.: Twin-atom beam production sequence. (a) Illustration of the process (as fig. 1.1). (b) Excitation ramp $\lambda(t)$, which is the displacement of the transverse trapping potential. As a reference, the typical radius of the wave function is $l_y = 0.265\,\mu\text{m}$ (see sec. 3.2.2). (c) Numerically obtained transverse momentum density $\tilde{n}(k_y, t)$ as a function of time, calculated for realistic experimental parameters. The momentum axis is scaled to $k_0 = \sqrt{2m\epsilon_S}$ (see sec. 4.3). (d) Relative population of transverse ground and excited state, as calculated from the two-level model (sec. 5.4.3). (e) Experimental transverse momentum density, obtained from time-of-flight images as depicted in fig. 5.2. (f) Theoretical longitudinal density distribution of the twin-beam modes, calculated as in fig. 4.4. The grey shaded area represents the linear Thomas-Fermi density of the trapped condensate; the dashed lines correspond to the TF-radius R. (g) Longitudinal profile of time-of-flight images, shown on a logarithmic color scale. The vertical axis is scaled to equivalent momenta, as explained in the text. The black solid line (which refers to the right axis) indicates the fraction of atoms emitted into the twin beams as observed in the experiment, the dotted line shows the result of the corresponding calculation as explained in sec. 5.5.

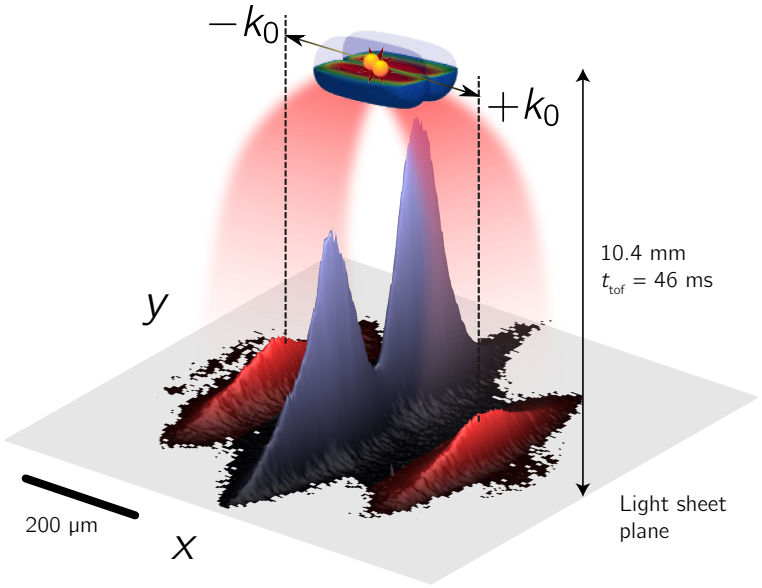

Figure 5.2.: Detection of the source and twin-beam clouds in time of flight. At a time t after starting the excitation sequence, all trapping potentials are switched off, and the cloud expands freely while falling down a distance of $\sim 10.4\,\mathrm{mm}$, corresponding to $t_{\mathrm{tof}} = 46\,\mathrm{ms}$. After this time, the cloud reaches the light sheet (see fig. 3.7), where it is detected by fluorescence. Along the transverse direction y, the distribution of the source cloud (blue) corresponds to the excited state. The twin beams (shown in red), which carry a momentum k_0 that is large compared to the other momentum scales present along x, separate during expansion, and their population can be detected, at only minimal overlap with the source cloud.

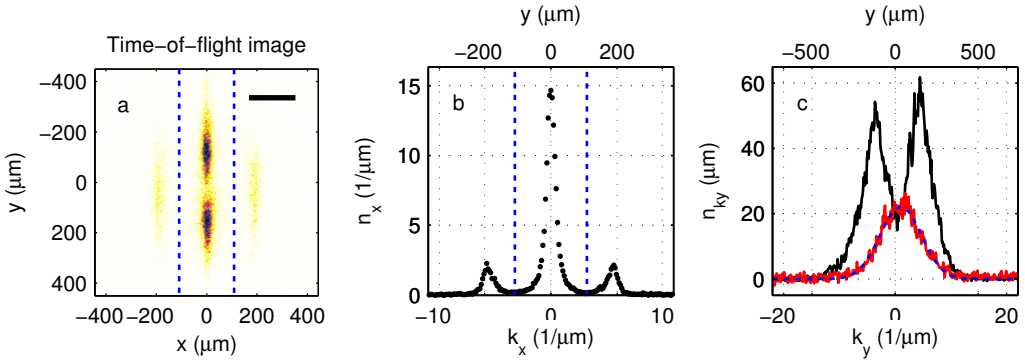

Figure 5.3.: Example image and profiles. Average over 12 experimental runs with identical settings. (a) False-color image as obtained from the light sheet camera. Axes are in *real* space at detection time, the scale bar indicates the spacing corresponding to the typical twin-beam momentum. Dotted blue lines correspond to the regions defined for the source cloud and the twin beams. (b) Longitudinal profile of (a). Top and bottom x-axes correspond to real and equivalent momentum space units, respectively; y-axis refers to real space. (c) Transverse profiles of (a) for source region (black dots) and twin-beam regions (red dots), respectively; y-axis refers to momentum space. The blue dashed line is a Gaussian fit to the twin-beam profiles (as used to extract the co-oscillating coordinate systems in fig. 5.20).

emitted beams is negligible in the images for most of the data sets. However, this does not imply strict equivalence of twin-beam peak momentum and time-of-flight position, due to the in-situ propagation of the twin-beam wave packets. In sec. 5.5.3, this issue will be addressed quantitatively. In fig. 5.3, a typical experimental image, averaged over a few runs with identical settings, and the corresponding profiles are shown. The calibration to absolute densities has been performed as described in sec. 3.2.4. In the profile plots, both real-space and equivalent momentum-space units are given. False-color plots that are used throughout this chapter to depict especially the dynamics of the transverse momentum distribution $\tilde{n}(k_y, t)$ as shown e.g. in fig. 5.1(d), are derived from profiles as the black one in panel (c). In those, usually we normalize each column to its integral.

Analysis approach Quite generally, our approach for understanding the experiment relies on separating the excitation (vibrational inversion) and twin-beam emission dynamics as far as possible. While the *time scales* of excitation and emission overlap, as seen in fig. 5.1, a clear distinction between both parts can be made in terms of their *spatial direction* and, hence, length scales. The excitation occurs along the transverse direction y (with ground state size $l_\mathrm{y} \sim 0.25\,\mu\mathrm{m}$), whereas the twin-atom beams are emitted longitudinally (with TF radius $R \sim 20\,\mu\mathrm{m}$). We thus reduce the complex three-dimensional dynamics to two one-dimensional descriptions, that have been developed largely independently, and are coupled by some effective parameters only.

With respect to the *excitation* process, the twin-beam emission acts as a decay channel of the excited state. However, this does not affect the excitation dynamics

too much, as for $t < T$, the number of "decayed" twin-beam atoms typically remains small. Also, as long as the criteria for a one-dimensional gas are fulfilled, thermal effects play no role for the excitation – the phase fluctuations of the quasi-condensate have a purely longitudinal nature. We can consider the condensate as a single-mode system, and a rather simple mean-field description is appropriate. This justifies the use of the GPE as underlying theory for the numerical simulations, which has been extended by a simple driving term, see eq. (5.27). From comparing panels c and e in fig. 5.1, it becomes evident that this approach is working quite well. In appendix A, it is briefly described how, based on GPE simulations, the optimal control trajectory for the excitation process was found.

Conversely, with respect to the *emission* process, the vibrationally excited source state acts as an effective *internal* state of the atoms, which is collisionally unstable and releases energy into the twin-beam momenta. To describe emission, we apply the (essentially one-dimensional) theory developed in chapter 4, where the transverse degree of freedom only appears in the definition of the overlap parameters in eq. (4.9), and the time-dependent population of the source state. This population [fig. 5.1d] constitutes the connection point between the theories, and will be eventually captured by the two-mode model for the transverse excitation that is developed in sec. 5.4.3. It allows to reduce the excitation dynamics to a simple continuous driving model, which is fully characterized by three parameters, and can be easily used as input to the emission calculations, which eventually agree well with the data [fig. 5.1(g)].

In this chapter After this quick review of the experiment sequence, the following analyses will be presented in this chapter:

- The observation of strongly sub-binomial number fluctuations (squeezing) between the emerging twin beams, which is the principal result of this thesis, is presented in some detail in sec. 5.2.
- A complementary analysis, based on second-order correlation functions, is laid out in sec. 5.3, which will also lead to alternative means to estimate number squeezing. Briefly, position-resolved correlations will be discussed.
- The dynamics of the transverse excitation into the source state (vibrational inversion) is studied and compared to theory in sec. 5.4.
- The dynamics of emission into the twin beams is analyzed in sec. 5.5, using the excitation dynamics results as an effective input parameter, along with the theory developed in sec. 4.4.
- In sec. 5.6, preliminary data on the effects of finite temperature of the source on the emission process is presented and discussed qualitatively.

While specific parameters like timing, atom number, temperature, or number of realizations vary among the different taken data sets, to accommodate the requirements of the various observables of interest, the basic experimental scheme largely remains that described above. In table 5.1, all data sets which have been used in the data treatment are listed for reference, their respective labels will be used in the remainder of this chapter for quick identification.

Table 5.1.: Data sets used for the results presented in this thesis. $K_{\mathrm{tot}}, K_{\mathrm{set}}$ denotes the total number of shots, and the typical number of realizations per parameter setting, respectively.

Label	Date	K_{tot}	K_{set}	t(ms)	N	Used in	Remarks
Sqz	23/08/10	1395	1395	6.5	700	5.2, 5.3	Big number squeezing set
DynA	30/05/11	5571	11	2.5...12	790	5.4, 5.5	Scaled exc. pulses (I-V)
DynB	05/06/11	2061	11	2.5...18	890	5.4	Scaled exc. pulses (B-I, B-II)
Corr	01/06/11	1400	130	5, 6.5	240...2400	5.3	RF knife varied
VarT	06/12/11	1062	7	2.5...15	680	5.6	RF knife varied (compensated)
VarN	04/07/11	1841	7	2...8.5	300...2000	5.4	Plain evap. time varied
Long	07/12/11	550	5	2.5...100	400	5.5	Long holding time after emission
Pot	19/08/10	1300	8	0.1...8	600	5.4	Offset field varied

5.2. Twin-beam atom number squeezing

In this section, we will analyze twin-beam data sets in the most simple way: in terms of atom numbers $\hat{N}_{\mathrm{L}}$ and $\hat{N}_{\mathrm{R}}$, that fall within two appropriately defined longitudinal regions in momentum space on each single shot:

$$\hat{N}_{\mathrm{L}} = \int_{-x_{\max}}^{-x_{\min}} \hat{n}(x)\mathrm{d}x \qquad \hat{N}_{\mathrm{R}} = \int_{x_{\min}}^{x_{\max}} \hat{n}(x)\mathrm{d}x. \tag{5.1}$$

In the following analysis, $\hat{N}_{\mathrm{L}}$, $\hat{N}_{\mathrm{R}}$, $\hat{N}_{+} = \hat{N}_{\mathrm{L}} + \hat{N}_{\mathrm{R}}$, and $\hat{N}_{-} = \hat{N}_{\mathrm{L}} - \hat{N}_{\mathrm{R}}$ denote corresponding random variables of a stochastic process. Expectation value and variance of a variable $\hat{X}$ will be equivalently denoted as $\mathrm{E}(\hat{X}) \equiv \langle \hat{X} \rangle \equiv X$ and $\mathrm{Var}(\hat{X}) \equiv \Delta\hat{X}^2$, respectively.

Number squeezing factor The signature for twin-atom wave packets are suppressed fluctuations of the number imbalance $\hat{N}_{-} = \hat{N}_{\mathrm{L}} - \hat{N}_{\mathrm{R}}$, also termed *number squeezing*. To quantify this, we will analyze the variance of the number imbalance $\Delta\hat{N}_{-}^2 = \langle \hat{N}_{-}^2 \rangle$, assuming that $\langle \hat{N}_{-} \rangle = 0$. For a symmetric, but uncorrelated emission processes into both twin beams, one would expect a binomial distribution, similar to a fair coin flip. The variance of such a process, denoted by $\Delta_b\hat{N}_{-}^2$, is

$$\begin{aligned}
\Delta_{\mathrm{b}}\hat{N}_{-}^2 &= \mathrm{E}(\mathrm{Var}_{\mathrm{b}}(\hat{N}_{-}|\hat{N}_{+})) + \mathrm{Var}_{\mathrm{b}}(\mathrm{E}(\hat{N}_{-}|\hat{N}_{+})) \\
&= \mathrm{E}(\mathrm{Var}_{\mathrm{b}}(2\hat{N}_{\mathrm{L}} - \hat{N}_{+}|\hat{N}_{+})) + 0 \\
&= 4 \cdot \mathrm{E}(\mathrm{Var}_{\mathrm{b}}(\hat{N}_{\mathrm{L}}|\hat{N}_{+})) \\
&= 4 \cdot \mathrm{E}\left(p\,(1-p)\,\hat{N}_{+}\right) \\
&= N_{+}
\end{aligned} \tag{5.2}$$

with the law of total variance invoked in the first line and the success probability $p = N_{\mathrm{L}}/N_{+} = 1/2$. To quantify the degree of number squeezing, the imbalance variance is normalized to its binomial expectation, yielding the *number squeezing factor*:

$$\xi_-^2 \equiv \frac{\Delta \hat{N}_-^2}{\Delta_\mathrm{b} \hat{N}_-^2} = \frac{\Delta \hat{N}_-^2}{N_+}, \tag{5.3}$$

which will be the main quantity of interest in this section.

Estimating number squeezing from photon numbers In the experiment, what we measure is not directly the atom numbers $\hat{N}_\mathrm{L}, \hat{N}_\mathrm{R}$ within the regions defined by $k_\mathrm{min}, k_\mathrm{max}$, but the number of (effective, see sec. 3.2.4) *photons* $\hat{S}_\mathrm{L}, \hat{S}_\mathrm{R}$ registered on the EMCCD camera during fluorescence imaging. Assuming that we detect exactly m photons from each imaged atom (i.e., neglecting any imaging noise), we can write the sum and difference photon numbers as $\hat{S}_\pm = m\hat{N}_\pm$. As for a constant a, $\mathrm{Var}(a\hat{X}) = a^2 \mathrm{Var}(\hat{X})$, the binomial expectation for the imbalance variance is $\Delta_\mathrm{b} \hat{S}_-^2 = m^2 \Delta_\mathrm{b} \hat{N}_-^2 = m^2 N_+ = m S_+$, and we can write the *uncorrected* number squeezing factor as:

$$\tilde{\xi}_-^2 \equiv \frac{\Delta \hat{S}_-^2}{\Delta_\mathrm{b} \hat{S}_-^2} = \frac{\Delta \hat{S}_-^2}{m S_+}. \tag{5.4}$$

This simple relation needs to be modified, if we take into account the additional noise introduced by fluorescence imaging, as discussed in sec. 3.2.4, comprising detection background and photon shot noise, the latter effectively leading to a stochastic value of m for each atom. We can decompose the variance of the difference signal as:

$$\begin{aligned} \Delta \hat{S}_-^2 &= \mathrm{Var}(\mathrm{E}(\hat{S}_-|\hat{N}_-)) + \mathrm{E}(\mathrm{Var}(\hat{S}_-|\hat{N}_-)) \\ &= \xi_-^2 \Delta_\mathrm{b} \hat{S}_-^2 + \Delta_\mathrm{n} \hat{S}_-^2 \\ &= \xi_-^2 m S_+ + \Delta_\mathrm{n} \hat{S}_-^2, \end{aligned} \tag{5.5}$$

the last term representing detection noise. As we assume the noise contributions to $\hat{S}_\mathrm{L}$ and $\hat{S}_\mathrm{R}$ to be independent, we have $\Delta_\mathrm{n} \hat{S}_- = \Delta_\mathrm{n} \hat{S}_+$, and can directly apply the expression for imaging noise derived in sec. 3.2.4, eq. (3.11):

$$\Delta_\mathrm{n} \hat{S}_-^2 = 2S_+ + \Delta \hat{b}^2. \tag{5.6}$$

With this expression at hand, we can write:

$$\Delta \hat{S}_-^2 = \xi_-^2 m S_+ + 2S_+ + \Delta \hat{b}^2 \tag{5.7}$$

$$\xi_-^2 = \frac{\Delta \hat{S}_-^2 - \Delta_\mathrm{n} \hat{S}_-^2}{\Delta_\mathrm{b} \hat{S}_-^2} = \frac{1}{m} \left[\frac{\Delta \hat{S}_-^2 - \Delta \hat{b}^2}{S_+} - 2 \right], \tag{5.8}$$

the latter equation allowing to estimate the number squeezing factor from experimental data. In sec. 5.3.4 an alternative means to obtain the amount of detection noise will be introduced, that yields compatible values.

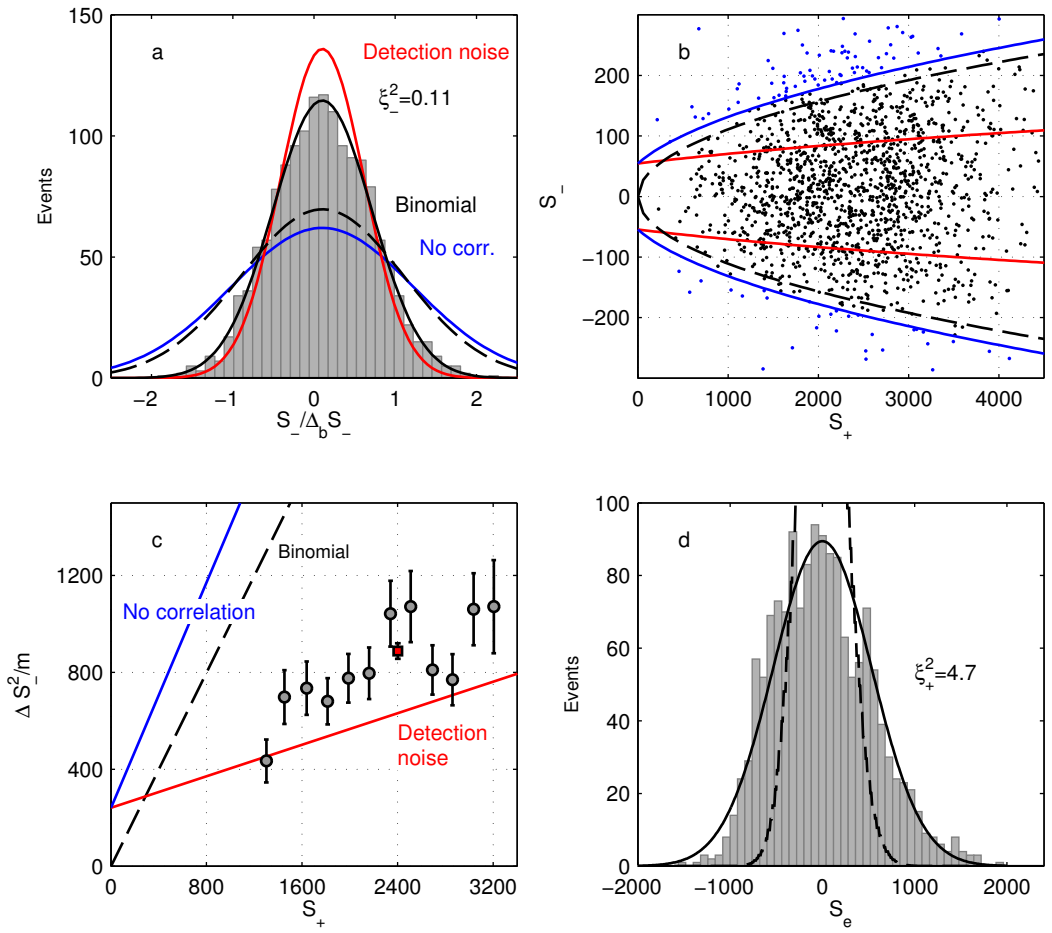

Figure 5.4.: Statistics of twin-beam data set of ≈ 1500 realizations. (a) Histogram of signal imbalances $\hat{S}_-$. Lines represent normal distributions with variances $\Delta_\mathrm{b}\hat{S}_-^2 = mS_+$ (black, dashed), $\Delta_\mathrm{n}\hat{S}_-^2$ (red, dashed), $\Delta_\mathrm{b}\hat{S}_-^2 + \Delta_\mathrm{n}\hat{S}_-^2$ (blue, solid), and $\xi_-^2 mS_+ + \Delta_\mathrm{n}\hat{S}_-^2$ with $\xi_-^2 = 0.11$ (black, solid). (b) Scatter plot of $\hat{S}_-$ vs $\hat{S}_+$ for all experimental realizations. Lines indicate 1σ ranges for the distributions as shown in panel (a). Data points that lie outside the 1σ range for uncorrelated emission are shown in blue. Note, that panels (a) and (d) represent projections of this plot on along its horizontal and vertical axis, respectively. (c) Measured imbalance variances $\Delta\hat{S}_-^2$ for bins of $\hat{S}_+$, divided by the mean photon number per atom m. Lines correspond to the distributions from panel (a), as functions of S_+. The red box corresponds to the total data set, as shown in panel (a). (d) Measured corrected total signal in twin-beam regions $\hat{S}_\mathrm{e} = \hat{S}_+ - r\hat{S}$. Dashed line: Poissonian expectation for pair-wise, shot-noise limited emission from an undepleted source [205]. Solid line: normal distribution with variance exceeding shot noise by a factor of $\xi_+^2 = 4.7$.

In fig. 5.4, the results for $\hat{S}_\pm$ obtained from a data set comprising ≈ 1500 experimental realizations with identical settings are shown in various representations. The total evolution time of $t = 7\,\mathrm{ms}$ (i.e., 2 ms additional holding time after excitation) has been chosen as a compromise between high population of the twin beams, and little broadening of twin beams and source cloud due to higher-order scattering (see sec. 5.5). In the data set, the mean fraction of emitted atoms was $r = N_+/N = S_+/S = 0.27$, at a mean total atom number of $N = S/p = 710$.

As is immediately seen in the histogram shown in panel (a), the distribution of observed $\hat{S}_-$ is much narrower then expected for a binomial distribution with width $\Delta_\mathrm{b}\hat{S}_- = mS_+$ (black dashed line). In fact, its width almost reaches the lower bound, defined by detection noise $\Delta_\mathrm{n}\hat{S}_-$ (red solid line). Invoking eqs. (5.4) and (5.8), we can directly compute the uncorrected and corrected squeezing factors observed in the experiment:

$$\tilde{\xi}_-^2 = \frac{\Delta\hat{S}_-^2}{\Delta_\mathrm{b}\hat{S}_-^2} = 0.37(3)$$
$$\xi_-^2 = \frac{\Delta\hat{S}_-^2 - \Delta_\mathrm{n}\hat{S}_-^2}{\Delta_\mathrm{b}\hat{S}_-^2} = 0.11(2),$$

which is one of the main results of this thesis.

To estimate the given uncertainties, we propagated the standard errors for $\Delta\hat{b}^2$, S_+, $\Delta\hat{S}_-^2$, and m, the latter obtained from an independent measurement as described in sec. 3.2.4. The standard error of the variance $\Delta\hat{S}_-^2 = (K-1)^{-1}\sum_{k=1}^{K}(\hat{S}_-^{(k)} - S_-)^2$, where K denotes the number of experimental runs, is estimated as $\Delta\hat{S}_-^2 \cdot (2/(K-1))^{1/2}$. In sec. 5.3.4, similar results for other data sets (with varied parameters and smaller realization numbers) will be reported.

$\hat{S}_+$-dependent analysis To further analyze the outcome of the measurement, e.g. with respect to the small but finite value of ξ_-^2, we now investigate the signal statistics within bins of the total signal in the twin-beam regions S_+, which is proportional to the emitted atom number. In fig. 5.4(b), a scatter plot of $\hat{S}_-$ vs. $\hat{S}_+$ is shown, each point corresponding to a single observation. Lines indicate 1σ-widths for the distributions as shown in panel (a), i.e., the range within which 68% of the observations should lie if the distribution applies, as a function of S_+. Here, number squeezing is observed in only $\approx 7\% \ll (100-68)\%$ of the observations lying outside the range for uncorrelated emission (blue points). We now bin the observations with respect to $\hat{S}_+$, and calculate $\Delta\hat{S}_+^2$ and S_+ independently for each bin. The result is shown in fig. 5.4(c), again together with lines corresponding to the variances of the distributions in panels (a) and (b) as a function of S_+. The data points are compatible with having a constant distance from the line for detection noise only, suggesting that the nonzero value of ξ_-^2 arises from a constant noise contribution, as opposed to uncorrelated emission. A plausible reason would be a residual overlap of uncorrelated source atoms into the analysis regions; a root-mean-square fluctuation of $\sqrt{\xi_-^2 N_+} \approx 4.5$ atoms (with $N_+ = S_+/m$) would suffice to explain the value. However, as even slight position fluctuations of the entire cloud would cause a strongly super-binomial distribution

near the steep edges of the source cloud peak, this value rather constitutes an upper limit.

Emitted atom number fluctuations In figure 5.4(d), a histogram of the *corrected* signal in the analysis regions $\hat{S}_\mathrm{e} = \hat{S}_+ - r\hat{S}$ is given. Here, $\hat{S}$ denotes the total fluorescence signal (including the source cloud), which corresponds to the total atom number; r is the average emitted atom fraction $S_+/S = N_+/N$ (with the total atom number N). Using $\hat{S}_\mathrm{e}$ instead of $\hat{S}_+$ for the analysis of fluctuations in the number of atoms emitted into twin beams eliminates the influence of total atom number fluctuations [205]. The variance of $\hat{S}_\mathrm{e}$ exceeds its expected value for pair-wise shot-noise limited emission from an undepleted source (following a Poissonian distribution) by a factor of $\xi_+^2 \approx 5$. Furthermore, the distribution is strongly asymmetric (and, hence, non-normal).

Analysis region definition A crucial question for the analysis presented in this section has been the definition of the twin-beam regions [positions $x_\mathrm{min}, x_\mathrm{max}$ in eq. (5.1)]. We proceeded by finding values that minimize the obtained value of ξ_-^2, while keeping the range reasonably small, so that the necessary background correction is kept moderate. Due to the sufficient, but small spacing between the twin beams and the source cloud in the images, the definition of x_min is much more critical for the final results. In fig. 5.5(a), the added density profiles of both twin beams (from outer to inner edge, i.e. right twin beam mirrored) are shown, along with cumulative profiles, corresponding to S_+ and $\Delta\hat{S}_-^2$ in regions from the outer edge of the plot to the position on the horizontal x_min-axis. The squeezing factor obtained in a region defined to a given x_min can be obtained by dividing the two curves, or equivalently subtracting them, if plotted on a logarithmic scale. The result is shown in panel (b). It is observed that, after a steep rise (presumably due to finite imaging resolution) there is a relatively constant, sub-binomial plateau, up to the strong twin-beam peaks. Somewhat unexpectedly, ξ_-^2 first *rises* at this position, which is likely due to position fluctuations of the peaks. Afterwards, it sharply drops to a minimum, the position of which corresponds to the optimal value for the inner limit x_min. The dashed line indicates the value of $x_\mathrm{min} = 112\,\mu\mathrm{m} \hat{=} 28$ pixels chosen for further analysis. It roughly corresponds to the density minimum between twin beams and source cloud. Choosing the outer limit x_max is less critical, in panels (c) and (d) corresponding plots are shown, where the previously determined value of x_min has been used as lower integration limit.

In the plots, a peculiar feature is visible in the density profiles: outside the twin-beam peaks, very weak (~ 1 atom per twin beam) second peaks can be observed on each side. These are likely to be due to emission from higher excited states, that have been inadvertently excited in the mechanical excitation process. In sec. 5.3.5 it will be demonstrated, that the second peaks indeed are strongly correlated to each other, by means of a second-order correlation analysis. Note, that in other data sets taken later (that have been measured with some technical improvements done in the meantime, see sec. 3.1.4), the second peaks are absent. In panel (d) it is seen, that the number squeezing is improved, if the second peaks are included into the analysis. The (within its errors) constant value of ξ_-^2 beyond the second peaks indicates, that the background variance $\Delta\hat{b}^2$ has been estimated appropriately.

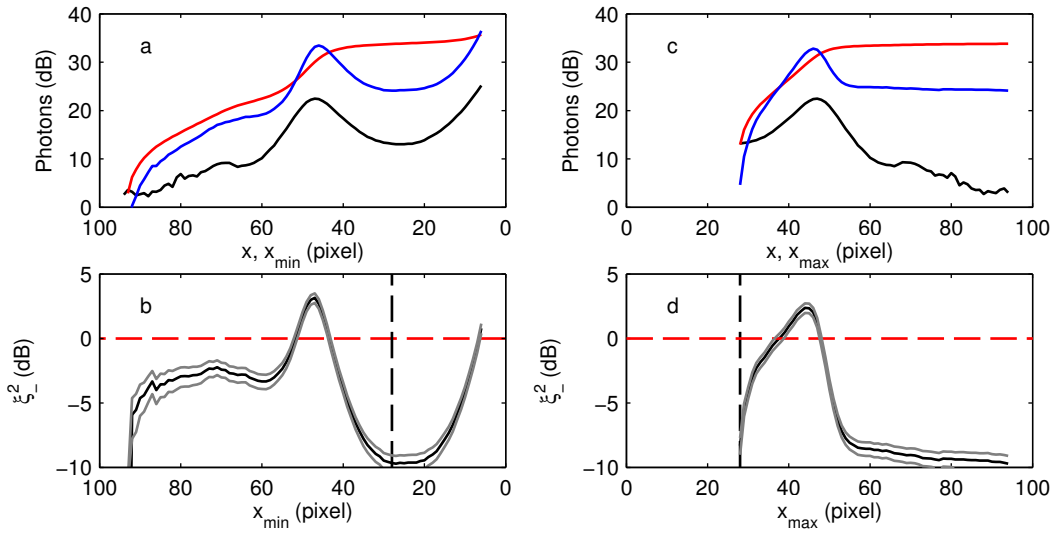

Figure 5.5.: Analysis region definition, note the logarithmic scales in all panels. (a) Black line: (momentum) density profile (in photons per pixel of 4 µm width) of both twin-beams added (right peak inverted), starting from the outer edges of the total density profile, and running towards the central peak (source cloud). Red line: cumulative profile, corresponding to S_+ in a region defined by the outer edge and the position on the horizontal axis. Blue line: cumulative imbalance variance, normalized to m. Number squeezing is present for values of x_{min} where the blue line lies below the red. (b) Number squeezing factor corresponding to inner limit positions given on the horizontal axis. Grey lines are standard errors. Red dashed line: binomial level $\xi^2_- = 1$. Black dashed line: inner limit value corresponding to the x_{min} chosen for analysis. (c) Analogous to (a). However, integration for the cumulative functions is now running from the value for x_{min} given in panel (b) to the position on the horizontal x_{max} axis. (d) Analogous to (c).

A more general approach of analyzing number squeezing, without having to define arbitrary regions, will be presented within the context of second-order correlation functions in sec. 5.3.5.

5.3. Second-order correlation functions of twin beams

We now apply a complementary approach of analyzing the correlation between twin beams, which, instead of atom numbers, is based on second-order correlation functions as introduced in sec. 2.3. The signature of stronger-than-classical correlations in second-order correlation functions is the violation of the Cauchy-Schwarz inquality (CSI) [26, 31], which has recently been demonstrated in matter waves [76], albeit in a strongly multi-mode regime. For twin beams with identical populations, this violation is equivalent to number squeezing (see below) and thus should be present in our experiment. However, the behavior of both approaches with respect to the structure and population of the twin-beam modes differs strongly [293]. For the high populations present in a few-mode scheme based on stimulated emission, number squeezing is the more common measure [10], even though also Cauchy-Schwarz violation has been shown in this regime [294]. Still, for projected experiments extending those presented in this thesis (see sec. 6) more sophisticated means for correlation detection than simple number squeezing might be required, and even for present data some additional insight is obtained. The feasibility of performing such measurements, the relation to number squeezing as found in sec. 5.2, and some first results will be discussed in this section.

5.3.1. The Cauchy-Schwarz inequality for correlation functions

For any pair of variables $\hat{A}, \hat{B}$, the correlation between them $\langle \hat{A}\hat{B} \rangle$ cannot exceed their respective autocorrelations $\langle \hat{A}^2 \rangle, \langle \hat{B}^2 \rangle$. This is easy to see by considering that for the maximally correlated case $\hat{A} \equiv \hat{B}$, all those correlations are exactly equal. As an example, if we consider the intensity $I(x)$ of a field (where x is a point in space and time) at two different positions, this writes

$$| \langle I(x_1)I(x_2) \rangle |^2 \leq \langle I(x_1)I(x_1) \rangle \langle I(x_2)I(x_2) \rangle . \tag{5.9}$$

This *Cauchy-Schwarz inequality* (CSI) also holds for commuting quantum observables, such as the density $\hat{n}(x) = \langle \hat{\Psi}^\dagger(x)\hat{\Psi}(x) \rangle$ of a matter wave field.

However, this is *not* true for coincidences as measured in a quantum optics experiment along the lines of [26], which are given by the higher-order correlation functions as introduced in sec. 2.3. The underlying reason is the quantized nature of the detection process. The definition of quantum correlation functions has to be normally ordered (all annihilation operators are on the right side), to appropriately capture the *coincidence* probability of two (or more) quantized events [24, 25]. The second-order correlation function is hence *not* given by a product of commuting operators, and a commutation relation has to be applied before the CSI. We discuss the simplest case of second-order correlations between two modes, the annihilation operators of which will be denoted as $\hat{a}_1, \hat{a}_2$, with populations $\hat{N}_i = \hat{a}_i^\dagger \hat{a}_i$. The modes shall be symmetric, such that $N = \langle \hat{N}_1 \rangle = \langle \hat{N}_2 \rangle$, and $\langle \hat{N}_1^2 \rangle = \langle \hat{N}_2^2 \rangle$. From the bosonic commutation relation, it follows, that:

$$G_{11}^{(2)} \equiv \langle \hat{a}_1^\dagger \hat{a}_1^\dagger \hat{a}_1 \hat{a}_1 \rangle = \langle \hat{N}_1^2 \rangle - N, \qquad G_{12}^{(2)} \equiv \langle \hat{a}_1^\dagger \hat{a}_1 \hat{a}_2^\dagger \hat{a}_2 \rangle = \langle \hat{N}_1 \hat{N}_2 \rangle \,, \tag{5.10}$$

where the shot noise of magnitude N distinguishes the same-position coincidence probability (autocorrelation) from the mean squared population. The CSI (5.9) can be applied to the commuting populations $\hat{N}_{1,2}$ to obtain

$$\begin{aligned} \langle \hat{N}_1 \hat{N}_2 \rangle &\leq \langle \hat{N}_1^2 \rangle \\ G_{12}^{(2)} &\leq G_{11}^{(2)} + N \\ g_{12}^{(2)} &\leq g_{11}^{(2)} + 1/N, \end{aligned} \tag{5.11}$$

with the normalized second-order correlation $g^{(2)}$ as introduced in eq. (2.27). Thus, due to the quantized nature of detection, second-order correlation functions $g^{(2)}$ *can* violate the CSI by a margin given by $1/N$, restoring eq. (5.9) only in the classical case $N \to \infty$.

The number squeezing factor for two symmetric modes $\xi_-^2 = \langle (\hat{N}_1 - \hat{N}_2)^2 \rangle / N_+$, $N_+ = 2N$ as introduced in sec. 5.2 can be written in terms of second-order correlation functions as:

$$\xi_-^2 = 1 + N(g_{11}^{(2)} - g_{12}^{(2)}), \tag{5.12}$$

which has the remarkable consequence, that for a symmetric two-mode system, number squeezing is equivalent to a violation of the CSI. However, the strength of CSI violation, which can be quantified by

$$v = \frac{g_{12}^{(2)}}{\sqrt{g_{11}^{(2)} g_{22}^{(2)}}} = 1 + \frac{1 - \xi_-^2}{g_{11}^{(2)} N} \tag{5.13}$$

will be decreasing with the mode population N. For the case of twin-beams in the undepleted source approximation (sec. 4.3 and [278]), one expects $g_{11}^{(2)} = 2$, so eq. 5.13 reduces to

$$v = 1 + \frac{1 - \xi_-^2}{2N}, \tag{5.14}$$

which will be a benchmark for the experimental results shown below.

5.3.2. Measuring second-order correlations

A typical experimental scheme used to measure second-order correlations in a light beam is shown in 5.6(a). Here, an incoming beam is split in two using a beam splitter, and coincidences between detection events are recorded as a function of lag time δt between them. It can be shown [25,31], that the normalized coincidence rate is equal to the temporal, averaged $g^{(2)}(\delta t)$ function, as defined in eq. (2.29). Analogously, matter-wave experiments using single-atom detectors (such as micro-channel plates), where each detected atom causes a discrete event, can directly measure normally ordered correlation functions [42, 64, 73, 152, 154]. Here, typically, coincidences are counted

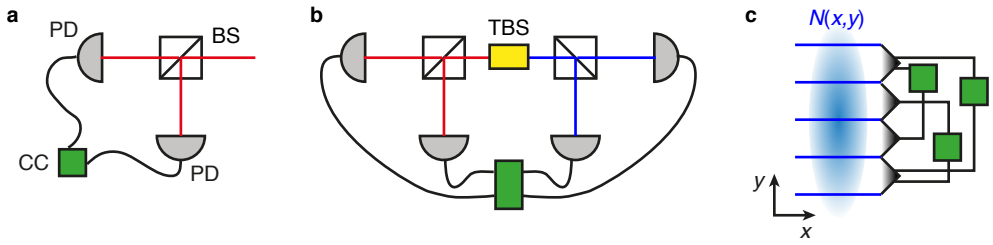

Figure 5.6.: Measurement of second-order correlation functions. (a) Typical measurement setup for the second-order coherence of an incoming light beam [31], using a beam splitter (BS), two single-photon-sensitive photodiodes (PD), and a coincidence counter (CC). (b) Setup for measurement of relative coincidences between two beams originating from a twin-beam source (TBS), allowing to demonstrate violation of the CSI. All beam are sent into a coincidence counter, and second-order correlations are calculated for each combination of input ports. (c) Simplified scheme for measuring the second-order correlation function for one of the twin-atom beams, as described in the text. For each non-adjacent combination of the four transverse bins, coincidences are detected. In the actual experiment, the number of bins corresponds to the number of transverse pixels, which is of the order of 200.

as a function of the spatial distance δx between two detection events, which for long expansion time is equivalent to momenta δk (similar to fig. 5.3).

In cold atom experiments using fluorescence or absorption imaging, atoms are not detected as discrete events, but their density n, integrated along the viewing direction, is inferred from the (usually large) number of photons that is scattered from the imaging light. If the smallest optically resolvable distance is larger than the typical separation of atoms in the image, which is usually the case, it is not possible to uniquely assign the measured detection events (scattered photons) to individual particles. This impedes a direct coincidence measurement. Instead, one obtains a density-density correlation function [43, 153, 178]; if we denote by $\hat{N}(x,y) = \int_{x-l/2}^{x+l/2}\int_{y-l/2}^{y+l/2}\hat{n}(x',y')\mathrm{d}x'\mathrm{d}y'$ the number of atoms[1] seen in a camera pixel of size l, centered at (x,y), it is defined as:

$$\tilde{G}^{(2)}(x,y,x',y') = \langle\hat{N}(x,y)\hat{N}(x',y')\rangle\,; \qquad \tilde{g}^{(2)}(x,y,x',y') = \frac{\tilde{G}^{(2)}(x,y,x',y')}{N(x,y)N(x',y')}, \tag{5.15}$$

where we used the notation $N(x,y) \equiv \langle\hat{N}(x,y)\rangle$. As becomes clear from eq. (5.10), this function is *not* generally equivalent to the second-order correlation, as in a quantum description with $\hat{N}(x,y) = \hat{a}^\dagger(x,y)\hat{a}(x,y)$, the annihilation and creation operators

[1] In contrast to sec. 5.2, we will – for the moment – neglect detection noise, and assume that we can measure atom numbers directly. For our fluorescence imaging this amounts to assuming $\hat{N}(x,y) = \hat{S}(x,y)/m$. This will be justified and discussed further in sec. 5.3.4.

have anomalous order in $\tilde{g}^{(2)}$:

$$\begin{aligned}\tilde{g}^{(2)}(x,y,x',y') &= \frac{\left\langle \hat{a}^\dagger(x,y)\hat{a}(x,y)\hat{a}^\dagger(x',y')\hat{a}(x',y')\right\rangle}{N(x,y)N(x',y')} \\ &= g^{(2)}(x,y,x',y') + g_{\mathrm{sn}}(x,y,x',y').\end{aligned} \tag{5.16}$$

The shot-noise term $g_{\mathrm{sn}}(x,y,x',y')$ is given by a peaked function of $\delta x, \delta y$, with an area defined by the inverse of the mean atom number at a position $x_+/2, y_+/2$ with $x_+ = x + x', y_+ = y + y'$, and a width $\tilde{r}_{\mathrm{a}}$ determined by the auto-correlation of the single-atom fluorescence pattern (sec. 3.2.4). Moreover, detection noise adds a sharp (single pixel) peak at $\delta x = \delta y = 0$ (see sec. 5.3.4). Thus, for close-lying points the density-density correlation deviates from the second-order correlation, and the latter cannot directly be obtained. Also, as $\tilde{g}^{(2)}$ is defined by a product of commuting observables, it obeys the CSI.

In [43], the same detection has been used as for the experiments in this thesis. There, the second-order correlation $g^{(2)}(\delta x, \delta y)$ for small ranges has been inferred from assuming, that in the analyzed clouds, the second-order coherence length along the transverse direction spreads a distance $\delta y \gg \tilde{r}_a$ and only varies slowly on that scale. This is shown to be fulfilled for gases close to or below the condensation threshold. Moreover, in the limit of a perfectly one-dimensional system (see sec. 2.4 and 2.1.2), the occupation of a single transverse mode leads to a coherent transverse correlation function, and hence:

$$G^{(2)}(x,y,x',y') = N(y)N(y') \cdot G^{(2)}(x,x'), \tag{5.17}$$

where the interesting information is only contained in the longitudinal $G^{(2)}(x,x')$. For both cases, $G^{(2)}$ can be recovered from $\tilde{G}^{(2)}$ by extrapolating the region affected by shot noise from the transversely adjacent region with $\delta y > \tilde{r}_{\mathrm{a}}$ (see fig. 5.7). The exact procedure applied is explained in appendix C. As illustrated in figure 5.6(c), this approach is somewhat similar to the measurement of correlation functions with beam splitters and multiple photo detectors, which in this case correspond to multiple transverse domains. In the following, we discuss the application of this method to the twin-beam data.

Notation and normalization The most general density correlation function of four coordinates [eq. (5.15)] is hard to work with practically, due to the required amount of data. In general, our main interest in considering the transverse y-direction is to cut out the shot noise at $\delta y \lesssim \tilde{r}_a$, as described above. As this procedure does not depend on y and y' separately, it seems reasonable to start the analysis from the transversely integrated function:

$$\tilde{G}^{(2)}(x,x',\delta y) = \sum_y \tilde{G}^{(2)}(x,x',y,y+\delta y). \tag{5.18}$$

This function takes sufficiently little memory, while still allowing to obtain correlations between arbitrarily defined longitudinal regions without recalculating (as opposed to e.g. directly calculating $\tilde{G}^{(2)}(\delta x, \delta y)$ for some pre-defined region).

As a convention, capital letters $G^{(2)}$ and $\tilde{G}^{(2)}$ indicate *non-normalized* functions, the absolute values of which depend on the atom number integrated over, and are largely irrelevant. On the other hand, without explicit definition, small letters $g^{(2)}$ and $\tilde{g}^{(2)}$ designate the corresponding *normalized* functions as in eq. (5.15). The appropriate normalization factor for a given correlation function is obtained by replacing all occurrences of $\hat{N}(x)$ with $N(x)$, and performing the same summations, e.g.:

$$\begin{aligned} \tilde{G}^{(2)}(\delta x, \delta y) &= \sum_{x,y} \langle \hat{N}(x,y)\hat{N}(x+\delta x, y+\delta y)\rangle \\ C^{(2)}(\delta x, \delta y) &= \sum_{x,y} N(x,y)N(x+\delta x, y+\delta y) \\ \tilde{g}^{(2)}(\delta x, \delta y) &= [\tilde{G}^{(2)}(\delta x, \delta y)/C^{(2)}(\delta x, \delta y)]/\tilde{g}^{(2)}_{\mathrm{tot}}, \end{aligned} \tag{5.19}$$

where the additional normalization to $\tilde{g}^{(2)}_{\mathrm{tot}} = \langle \hat{N}^2 \rangle / N^2$ with the total atom number N cancels the direct influence of total atom number fluctuations between experimental shots [43]. To correctly account for inhomogeneous densities, all summations have to be performed on the *non-normalized* functions. However, unless otherwise noted, all figures show the physically more relevant normalized functions.

5.3.3. Two-dimensional averaged correlation

Integrating diagonally (with respect to the longitudinal coordinates) over $\tilde{G}^{(2)}(x, x', \delta y)$, yields the two-dimensional averaged density-density correlations:

$$\tilde{G}^{(2)}_{\mathrm{cl}}(\delta x, \delta y) = \sum_x \tilde{G}^{(2)}(x, x+\delta x, \delta y), \qquad \tilde{G}^{(2)}_{\mathrm{bb}}(x_+, \delta y) = \sum_x \tilde{G}^{(2)}(x, x_+ - x, \delta y), \tag{5.20}$$

which differ from each other with respect to the summing direction: The collinear (cl) function is detects HBT-like bunching effects, as has been discussed in great length in [43]. The back-to-back (bb) function, on the other hand, is sensitive to correlations between *opposite* longitudinal positions (with respect to the symmetry axis defined by the source cloud peak), with a center-of-mass offset $x_+/2 = (x + x')/2$ with respect to the symmetry axis at $x = 0$, see fig. 5.7(e). It is typically used for detection of twin-beams in higher-dimensional configurations [73, 76].[2]

If calculated from the entire fluorescence image, the integrated functions are insensitive to locally changing correlation properties, that are present only in certain position combinations, i.e. those only relating one twin-beam peak to the other. In fig. 5.7(a-d), a typical function $\tilde{g}^{(2)}_{\mathrm{cl}}(\delta x, \delta y)$ is shown (data set Corr-III), that has been derived from the full images, i.e. including source cloud and twin beams. Also, the

[2] Note, that eq. (5.20) differs from the typical definition in these studies, in that the transverse direction is still integrated collinearly (i.e., over y_+) even in the back-to-back correlation. Two-dimensional back-to-back integration only is appropriate for point-symmetric two-dimensional correlations as in such collision experiments. In our case, any two-dimensional correlation features might e.g. arise from the transversely asymmetric source cloud or position fluctuations. They should be mirror-symmetric with respect to the x-axis, which is appropriately accounted for by integrating over y_+, not δy.

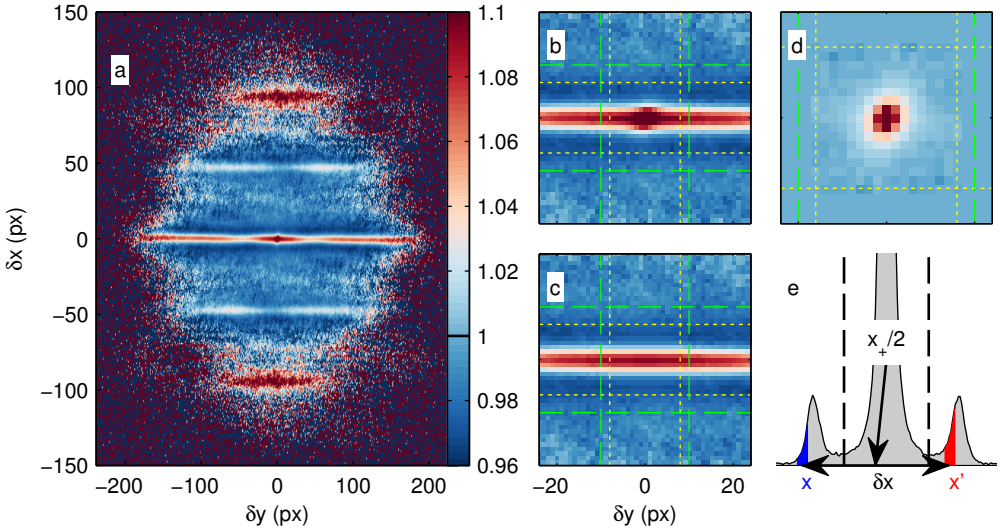

Figure 5.7.: Two-dimensional averaged correlation function, data set Corr-III. (a) Averaged correlation function $\tilde{g}^{(2)}_{\mathrm{cl}}(\delta x, \delta y)$, calculated from the entire images, including source cloud and twin beams. (b) Zoom of (a) into central region with shot noise peak, axes are equally scaled. Yellow dotted lines: region chosen for shot noise removal (r_{sn}). Green dashed lines: region used to interpolate the shot noise region (r_{int}, r_{fit}), see appendix C. (c) Same as (b), with shot noise peak removed. (d) Difference of (c) and (b), color scale shifted by 1. (e) Illustration of variables x_+, δx. In collinear and back-to-back correlation functions, x_+ or δx are summed over, respectively. Dashed lines represent $x_{\mathrm{min}}, x_{\mathrm{max}}$, as in fig. 5.3.

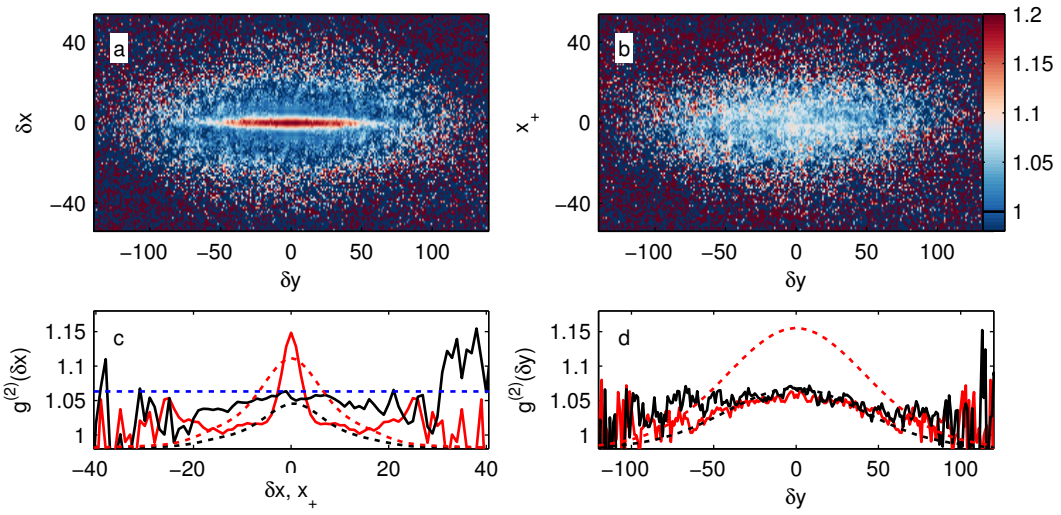

Figure 5.8.: Two- and one-dimensional averaged correlation functions of twin-beam peaks, data set Corr-III. (a,b) Two-dimensional functions $g^{(2)}_{\mathrm{tb}}(\delta x, \delta y)$, and $g^{(2)}_{\mathrm{LR}}(x_+, \delta y)$, respectively. Calculation is performed for regions outside the source, see e.g. dashed lines in figure 5.7(e). (c,d) Longitudinal (c) and transverse (d) correlation functions, for collinear (red) and back-to-back (black) summation, obtained from the same ranges as in panels (a,b). Dotted lines are normalizations, representing the density. The blue dotted line in (c) indicates $\tilde{g}^{(2)}_{\mathrm{tb}}$.

decomposition into second-order correlation $g^{(2)}_{\mathrm{cl}}(\delta x, \delta y)$ and shot noise is shown (panels b-d), as explained in appendix C. Along the longitudinal direction, for small δx, an oscillating structure is visible, that is typical for expanding quasi-condensates [43, 153]. Further outwards (at a distance approximately corresponding to to the twin-beam momentum k_0), peaks are observed, that correspond to correlations between source and twin beams, resulting in transverse structure. At twice that distance the correlation between both twin-beams causes another set of peaks; their large magnitude is caused by the strong fluctuations of the overall emitted fraction [see e.g. fig. 5.4(d)]. Along the transverse direction δy, characteristic double-peak patterns are observed for all peaks involving the source cloud, corresponding to its excited state.

In fig. 5.8, using the same data set, second-order correlations have been derived from twin beam regions [see sec. 5.2, or fig. 5.7(d)] only. Collinear functions $G^{(2)}_{\mathrm{LL}}(\delta x, \delta y)$ and $G^{(2)}_{\mathrm{RR}}(\delta x, \delta y)$ can be obtained from integrating $\tilde{G}^{(2)}(x, x', \delta y)$ collinearly over each of the two twin-beam peaks ($x, x' > x_{\mathrm{min}}; x, x' < -x_{\mathrm{min}}$), respectively, in analogy to eq. (5.20). Next, shot noise is removed as described above. The geometric average $G^{(2)}_{\mathrm{tb}}(\delta x, \delta y) = [G^{(2)}_{\mathrm{LL}}(\delta x, \delta y) \cdot G^{(2)}_{\mathrm{RR}}(-\delta x, \delta y)]^{1/2}$ is shown (as normalized function) in fig. 5.8(a). A clear longitudinal peak (bunching) is visible, that is expected for twin-beam emission in the undepleted limit [73, 278]. Transversely, a slight drop-off is observed (red line in panel d), that might be caused by position fluctuations.

On the other hand, the cross-correlation $G^{(2)}_{\mathrm{LR}}(x_+, \delta y)$ is derived from back-to-back integration of $\tilde{G}^{(2)}(x, x', \delta y)$ in the region $x < -x_{\mathrm{min}}, x' > x_{\mathrm{min}}$. No shot noise subtraction is necessary, as regions with small δx do not contribute. For the data shown

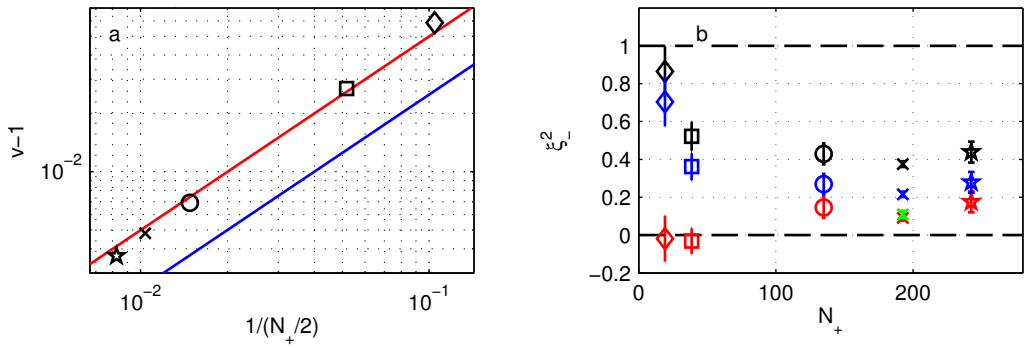

Figure 5.9.: Bulk CSI violation and number squeezing. (a) Amount of Cauchy-Schwarz violation $v-1$ vs inverse population per twin beam peak $N_+/2$ for different data sets Corr-I-IV (diamond, square, circle, star) and Sqz (cross). Lines: Two-mode expectation $v-1=(1-\xi_-^2)/N_+$ for perfect squeezing (red) and $\xi_-^2=0.5$ (blue). (b) Number squeezing for the same data sets, with noise correction as described in the text. Black: uncorrected squeezing factor $\tilde{\xi}_-^2$. Red: corrected squeezing factor ξ_-^2. Blue: corrected by $-2/m$ (as arising from fluctuations of photons emitted per atom). Green: value obtained for set Sqz as in sec. 5.2.

in fig. 5.8(b), only little structure is observed, i.e., there are no significant coincidences of atoms with exactly opposite momenta *within* the twin beams. This is contrast to the findings of ref. [68], where the correlations have been detected in momentum space, however.

Panels c and d show the corresponding one-dimensional averaged functions $g^{(2)}_{\mathrm{LR}}(x_+)$, $g^{(2)}_{\mathrm{LR}}(\delta y)$ (black), and $g^{(2)}_{\mathrm{tb}}(\delta x), g^{(2)}_{\mathrm{tb}}(\delta y)$ (red). In panel (c) it can be clearly observed, that, outside the bunching peak, the back-to-back function exceeds the collinear one, yielding a larger value on average.[3] This corresponds to a violation of the Cauchy-Schwarz inequality, which will be discussed more quantitatively in the next section.

5.3.4. Full twin-beam correlations and number squeezing

Now, we reduce the problem to a two-mode (left and right twin beam) analysis, by discarding most spatial information in $\tilde{G}^{(2)}(x,x',\delta y)$. As strong number squeezing has been shown for such an analysis in sec. 5.2, also a violation of the CSI should be present. Also we discuss an alternative means to determine the number squeezing factor ξ_-^2.

CSI violation of full twin beams Starting from a shot-noise-free $G^{(2)}(x,x',\delta y)$, we could simply obtain the "bulk" cross- and autocorrelation functions between the twin beams, by binning over longitudinal regions L, R, similar to those used above:

$$G^{(2)}_{\mathrm{LL}}=\sum_{\delta y}\sum_{\substack{x\in\mathrm{L}\\x'\in\mathrm{L}}}G^{(2)}(x,x',\delta y),\qquad G^{(2)}_{\mathrm{LR}}=\sum_{\delta y}\sum_{\substack{x\in\mathrm{L}\\x'\in\mathrm{R}}}G^{(2)}(x,x',\delta y). \tag{5.21}$$

[3] Indeed, near the center it approaches the theoretical maximum of $\tilde{g}^{(2)}_{\mathrm{tb}}=(\langle\hat{N}_1^2\rangle\langle\hat{N}_2^2\rangle)^{1/2}/(N_1N_2)$ as imposed by the CSI for atom numbers (blue dotted line).

Table 5.2.: Values shown in fig. 5.9, with total atom number N and hold time t for each data set. Errors for ξ_-^2 have been estimated as in sec. 5.2. For data set Sqz, the result from sec. 5.2 was $\xi_-^2 = 0.11(2)$.

Set	t(ms)	N	$N_+/2$	$v-1(10^{-3})$	$\tilde{\xi}_-^2$	ξ_-^2
Corr-I	5	235	9	59	0.86(13)	-0.02(12)
Corr-II	6.5	235	17	27	0.52(8)	-0.03(7)
Corr-III	5	845	62	6.9	0.43(6)	0.15(5)
Corr-IV	6.5	845	112	3.7	0.44(6)	0.18(5)
Sqz	6.5	700	89	4.8	0.37(2)	0.09(2)

On the other hand, when starting from $\tilde{G}^{(2)}(x, x', \delta y)$, which contains atom shot noise, it is easier to first compute $G_{\mathrm{LL}}(\delta x, \delta y), G_{\mathrm{RR}}(\delta x, \delta y)$, and $G_{\mathrm{LR}}(x_+, \delta y)$ as described above, and then fully integrate over them. While this yields the same result, it allows to remove shot noise at the intermediate stage of the averaged two-dimensional functions. We obtain the correlations $g_{\mathrm{LL}}^{(2)}, g_{\mathrm{RR}}^{(2)}, g_{\mathrm{LR}}^{(2)}$, and finally the two-mode Cauchy-Schwarz violation $v = g_{\mathrm{LR}}^{(2)}/g_{\mathrm{tb}}^{(2)}$, with $G_{\mathrm{tb}}^{(2)} = [G_{\mathrm{LL}}^{(2)} G_{\mathrm{RR}}^{(2)}]^{1/2}$. The calculated values for different data sets are shown in fig. 5.9(a). Even though the violation in a realistic setting is not at all straightforward to estimate [76, 293], the two-mode relation $v - 1 = (1 - \xi_-^2)/N_+$, assuming $\xi_-^2 = 0$ (red line), approximates the data surprisingly well. The agreement is best for small twin-beam populations, which may be due the fact that in those data the overlap between twin beams and source is the least, and a near-perfect sectioning of the twin-beam regions can be made (see below).

It has to be noted, though, that none of the data sets shown has been taken with the explicit goal of measuring second-order correlations. Especially for the most interesting sets with low populations of the twin beams, too little shots (~ 100) are available to allow for a more robust shot noise rejection, and properly estimating the errors of $v-1$ and hence the confidence in CSI violation. Still, the result is clearly compatible with the expected behavior, suggesting validity of the taken approach, and encouraging further measurements in that direction. Especially for weakly populated twin beams, where v can grow large, or for local measurements (see below), the CSI approach might be superior to the direct number squeezing analysis.

Detection noise, and correction of ξ_-^2 Up to now, we have neglected detection noise, as discussed in the context of number squeezing in sec. 5.2. All noise due to fluctuations of the atom distribution is spatially correlated on a scale at least given by the shot noise peak radius $\tilde{r}_{\mathrm{a}}$. Conversely, detection noise (i.e., photon shot noise) between each pair of pixels is uncorrelated (white noise), and thus only contributes to same-pixel fluctuations. If we explicitly consider the two-dimensional averaged photon signal correlations $\tilde{S}^{(2)}(\delta x, \delta y)$ as directly derived from the photon numbers $\hat{S}(\delta x, \delta y)$

in the images, we hence obtain similarly to eq. (5.5):

$$\begin{aligned}\tilde{S}^{(2)}(\delta x,\delta y) &= \sum_{x,y}\langle\hat{S}(x,y)\hat{S}(x+\delta x,y+\delta y)\rangle \\ &= \sum_{x,y}\left\{m^2\langle\hat{N}(x,y)\hat{N}(x+\delta x,y+\delta y)\rangle + \delta(\delta x,\delta y)\Delta_{\mathrm{n}}\hat{S}(x,y)^2\right\} \\ &= m^2\tilde{G}^{(2)}(\delta x,\delta y) + \delta(\delta x,\delta y)\Delta_{\mathrm{n}}\hat{S}^2,\end{aligned} \tag{5.22}$$

where we applied the law of total covariance in the second line. Thus, by correcting for (atom) shot noise in a region $\delta x,\delta y < \tilde{r}_{\mathrm{a}}$ as described, also the detection noise at $\delta x = \delta y = 0$ is rejected, and we can safely replace $\hat{N}$ by $\hat{S}/m$ to apply the relations for $G^{(2)}$ functions to experimental data.

Moreover, this relation enables us to *directly* obtain the detection noise $\Delta\hat{S}^2$ to correct imaging noise when calculating ξ_-^2 using eq. (5.5), without any assumptions about the imaging system as made in sec. 5.2. To split off detection noise, we have to interpolate the central pixel from the rest of the function; $\Delta_{\mathrm{n}}\hat{S}^2$ is then given by the residual. Shot noise removal as described above does not have to be performed before necessarily. However, the most convenient recipe for interpolation is to fit an appropriate peak function to the isolated atom shot noise peak $g_{\mathrm{sn}}^{(2)}(\delta x,\delta y) = \tilde{g}_{\mathrm{tb}}^{(2)}(\delta x,\delta y) - g_{\mathrm{tb}}^{(2)}(\delta x,\delta y)$ (see appendix C), excluding the central pixel. Despite the greater complexity, this method of obtaining $\Delta\hat{S}^2$ should be advantageous especially for low twin beam populations, where the background correction term $\Delta\hat{b}^2$ in eq. (5.8) becomes important and gives rise to a strong uncertainty of the result.[4] In fig. 5.9(b) and table 5.2 results of this noise correction method are shown. Values compatible with perfect squeezing $\xi_-^2 = 0$ are obtained for sets Corr-I and -II, where the overlap between source cloud and emitted twin beams in the images is vanishing. At the same time, the uncorrected value is high for those, due to the large relative contribution of background photons (which could be mitigated by choosing smaller integration regions, though). For the data set Sqz, which has been analyzed in sec. 5.2, we find agreement with the value found there, corroborating the validity of the assumptions made about detection noise.

5.3.5. Longitudinally resolved correlations

We finally proceed to the more general approach of keeping spatial resolution in the longitudinal direction. That is, instead of collinear or back-to-back averaging we will now work with both coordinates (x,x'), or equivalently $(\delta x, x_+)$, explicitly. Most crucially, this makes the results completely independent of choosing arbitrary cutoff regions in the images, such as the border between source and twin beams at $x_{\min}$. Thus, it also allows for analyzing more complex phenomena that are likely to arise in future measurements (see sec. 6), where the correlation behavior is strongly inhomogeneous, but ascribing certain properties to different longitudinal ranges a priori is too restrictive.

[4] Note, that this technique, even though based on information extracted from correlation functions, is not related to the two-mode model $v - 1 = (1-\xi_-^2)/N_+$.

Second-order correlations in (x, x') First we will have a look at the second-order correlation function $G^{(2)}(x, x')$. In contrast to the previous section, we do not explicitly consider the dependence on the averaged transverse coordinate δy, but still apply shot noise correction. The exact method as discussed in appendix C is somewhat simplified as compared to the previous section, and at the current stage does not warrant quantitative validity of the results to better than $\sim 20\%$ for Cauchy-Schwarz violation. Still, qualitative features are captured well, and will be discussed in the following.

It often makes sense, to slightly average over small bins (super-pixels) of size Δ in x, x'; especially given, that for small-scale behavior, the imaging resolution $\tilde{r}_a$ will be dominant. We can write this binned function as:

$$G^{(2)}_{\Delta}(x, x') = \sum_{\xi=-\Delta/2}^{\Delta/2} \sum_{\xi'=-\Delta/2}^{\Delta/2} G^{(2)}(x + \xi, x' + \xi'). \tag{5.23}$$

In the limit of bins encompassing the entire twin-beam peaks, the analysis of the previous sec. 5.3.4 based on $G^{(2)}_{\mathrm{LR}}$ and $G^{(2)}_{\mathrm{tb}}$ is recovered.

In fig. 5.10 (left column), the normalized function $g^{(2)}_{\Delta}(x, x')$ is shown as false-color image for different settings of Δ.[5] The auto- and cross-correlations of the twin beams show up as peaks near each combination of their coordinates (see green lines). Consistently with fig. 5.8, while the auto-correlation peaks are narrow along the δx (i.e., $x + x' = \text{const.}$) direction, the cross-correlation peaks along x_+ are much broader, and no significant sub-structure can be observed.

In fig. 5.10 (center column), the local Cauchy-Schwarz violation ratio

$$v(x, x') = g^{(2)}_{\Delta}(x, x') / \sqrt{g^{(2)}_{\Delta}(x, x) g^{(2)}_{\Delta}(x', x')} \tag{5.24}$$

is shown. The peaks having $v(x, x') > 1$ at low and intermediate Δ show a slightly elongated structure along the $x - x' = \text{const.}$ collinear diagonal, which is explained by bulk position fluctuations of the entire cloud. Also here, no sub-structure is observed that would indicate correlations between atoms of exactly opposite position within the twin beams.

In constrast to higher-dimensional schemes [73, 76], where many transverse modes are available, the lack of such a sub-structure is not surprising for our one-dimensional, "longitudinal-only" scheme. Even in presence of back-to-back correlations, that in a naive picture would arise from the well-defined time and correlated momenta of each pair-collision event, they would be blurred on the scale of the initial cloud size due to the expansion time not being sufficient to reach the far field (sec. 5.1). Also, finite-temperature effects might destroy such correlations, which is however beyond the scope of our current theoretical understanding. In sec. 6, first results from an enhanced scheme, which enforces back-to-back correlations by emission time encoding will be presented.

[5] To connect to the previous sections, it is instructive to note, that the averaged one-dimensional correlations shown in fig. 5.8(c,d) correspond to integrating $G^{(2)}(x, x')$ over appropriate regions along the diagonals $x - x' = \text{const.}$ (collinear: red lines) and $x + x' = \text{const.}$ (back-to-back: black lines).

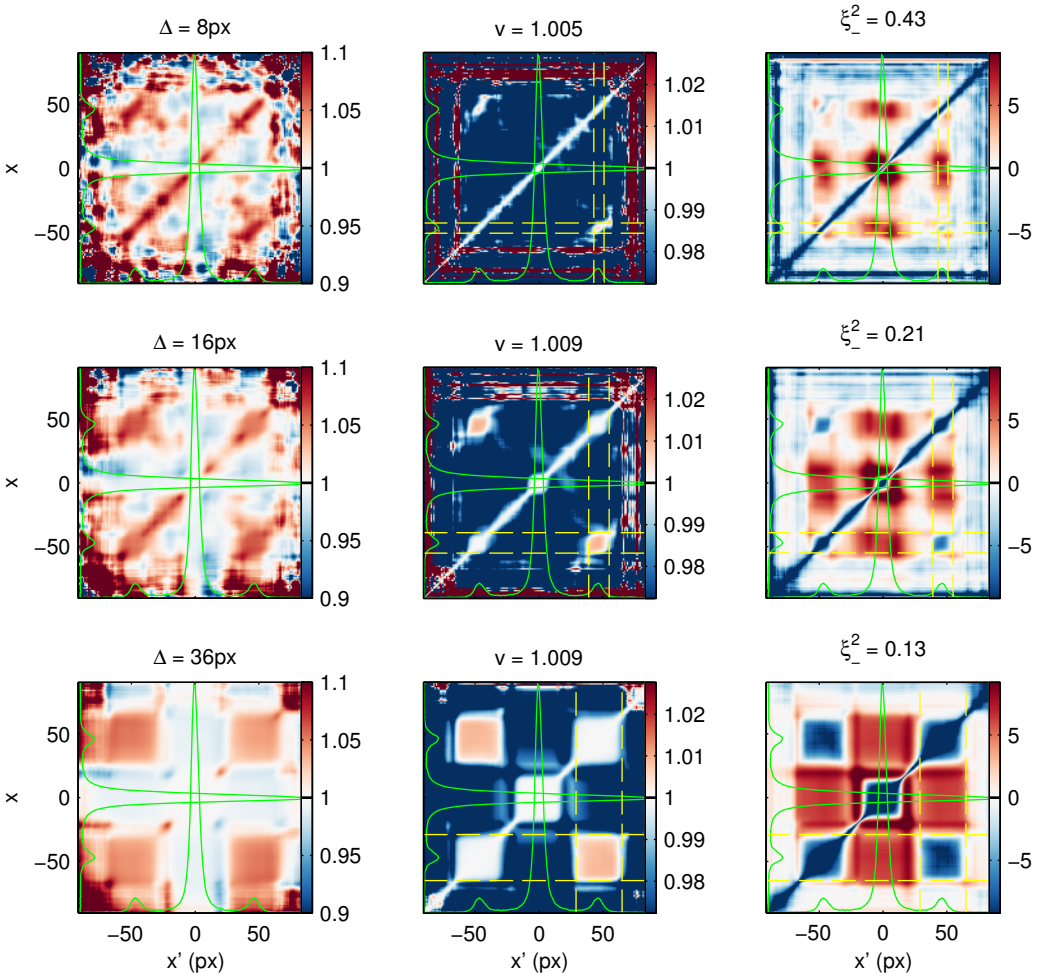

Figure 5.10.: $g^{(2)}_{\Delta}(x, x')$ (left column), local CSI violation $v(x, x')$ (center column), and local squeezing $\xi^2_-(x, x')$ (right column) for data set Cor-III and different binning lengths Δ. Note the logarithmic (dB) color scale for $\xi^2_-(x, x')$. Green lines are the mean longitudinal density profile. Yellow dashed lines indicate the edges of the cross-correlation averaging bin $(x_0, -x_0)$ that is centered on the twin-beam peaks. In the titles, Δ, $v(x_0, -x_0)$, and $\xi^2_-(x_0, -x_0)$ are given, respectively. In the lowest row, the binning region is similar to that used for the fully integrated analysis in sec. 5.3.4 and sec. 5.2.

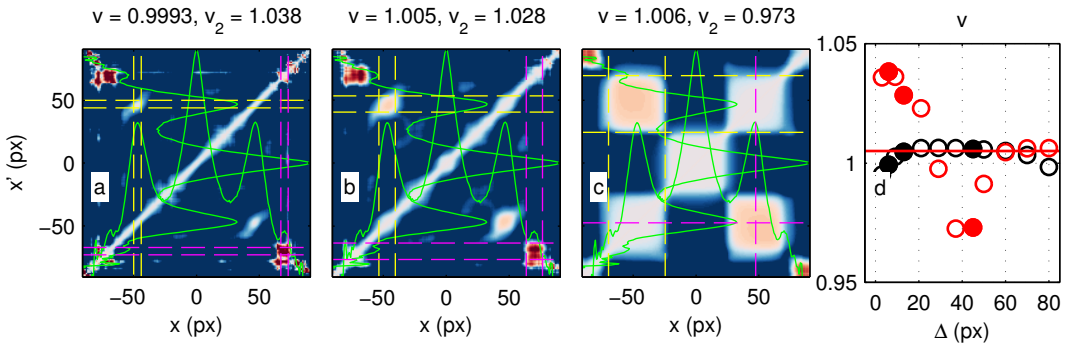

Figure 5.11.: Local CSI violation and number squeezing for data set Sqz. (a-c) Similar to fig. 5.10 (center column), with different values of Δ. Magenta dashed lines indicate the binning range around the *second* twin-beam peaks. In the title, CSI violations are given for the normal and second twin-beam peaks. (d) CSI violation v at center of first (black) and second (red) peak, where the red line reports the value reached for integration over the full twin beams as in sec. 5.3.4. Filled points indicate the values of Δ of the data shown in (a-c).

One notable exception from the lack of sub-structure in current data is present in the data set Sqz. As has been shown in fig. 5.5(a), small second twin-beam peaks, presumably originating from emission from higher vibrational states, are present. Their population is vanishingly weak and hidden in the tails of the first twin-beam peaks, making them less accessible to techniques working on the profiles directly, such as number squeezing detection. On the other hand, by virtue of their weak population, but strong correlation, they create a very large signal in the CSI violation ratio, as seen in fig. 5.11(a-d). This indicates that indeed there have been two independent emission processes present, both populating twin-modes. More importantly, this observation highlights the ability of full second-order correlation functions to detect even tiny sub-structures with non-local correlations, making this method highly attractive for proposed, more complex schemes, e.g. involving superpositions of source states or temporal chirps (sec. 6).

Number squeezing As discussed above, the violation of CSI is equivalent to number squeezing in the case of two balanced modes. In a similar fashion to the longitudinally resolved second-order correlation function, we can analyze the number squeezing between each combination of longitudinal positions (x, x'). In fig. 5.10 (right column), the result is shown for data set Corr-III. At a bin size Δ that fits the width of the twin-beam peaks, the minimum achievable value at the twin-beam peak positions of $\tilde{\xi}^2_-(x, x') = 0.13$ is found, compatible with that obtained in sec. 5.3.4.

As the analysis regions may have a strong mean imbalance $N_-(x, x') = N(x) - N(x')$, the expression for the binomial expectation of its variance deduced in eq. (5.2) is not applicable anymore, as the second term would become non-zero and dependent on fluctuations of the total emitted number $\Delta\hat{N}^2_+(x, x')$. To retain a simple expression for the binomial expectation (i.e., which only depends on expectation values), instead of $\hat{N}_-(x, x') = \hat{N}(x) - \hat{N}(x')$, we subtract the mean imbalance, and analyze the

quantity[6]

$$\hat{N}'_- = \hat{N}_- - \tilde{p}\hat{N}_+, \qquad \tilde{p} = \frac{N_-}{N_+}.$$

The binomial variance for $\hat{N}'_-$ can now easily be derived analogously to the balanced case, eq. (5.2):

$$\begin{aligned}
\Delta_\mathrm{b}\hat{N}'^2_- &= \mathrm{E}(\mathrm{Var}_\mathrm{b}(\hat{N}'_-|\hat{N}_+)) + \mathrm{Var}(\mathrm{E}(\hat{N}'_-|\hat{N}_+)) \\
&= \mathrm{E}(\mathrm{Var}_\mathrm{b}(2\hat{N}(x) - \hat{N}_+|\hat{N}_+)) + \mathrm{Var}(\tilde{p}\hat{N}_+ - \tilde{p}\hat{N}_+) \\
&= 4 \cdot \mathrm{E}(\mathrm{Var}_\mathrm{b}(\hat{N}(x)|\hat{N}_+)) + 0 \\
&= 4 \cdot \mathrm{E}(p\,(1-p)\,\hat{N}_+) \\
&= (1-\tilde{p}^2)N_+,
\end{aligned} \tag{5.25}$$

where we used the relation $p = (\tilde{p}+1)/2$ for the binomial success probability.[7] It is straightforward to derive that this expression can be written in terms of $\tilde{G}^{(2)}(x,x')$:

$$\Delta_\mathrm{b}\hat{N}'^2_- = (1-\tilde{p})^2\tilde{G}^{(2)}(x,x) + (1+\tilde{p})^2\tilde{G}^{(2)}(x',x') - 2(1-\tilde{p}^2)\tilde{G}^{(2)}(x,x').$$

The local number squeezing factor is then given by:

$$\xi^2_-(x,x') = \frac{\Delta\hat{N}'_-}{(1-\tilde{p}^2)N_+} = \frac{1}{2}\left[(1-\tilde{p})\frac{\tilde{G}^{(2)}(x,x)}{N(x)} + (1+\tilde{p})\frac{\tilde{G}^{(2)}(x',x')}{N(x')} - 4\frac{\tilde{G}^{(2)}(x,x')}{N_+}\right]. \tag{5.26}$$

Correcting detection noise can be accomplished in a manner similar to that introduced in the previous section, see appendix C. As for correlation functions, binning over a range Δ has to be applied on each of the $\tilde{G}^{(2)}(x,x')$ and $N(x)$ independently. Some results are shown in fig. 5.10 (right column) and sec. 6.

5.4. Excitation dynamics

Having analyzed, the correlation properties of the emitted twin beams, we now focus on the dynamics of the creation process. As outlined in sec. 5.1, our approach is to split the full dynamics as far as possible into descriptions for the (transverse) excitation and (longitudinal) emission dynamics. For the first part, the goal is to experimentally implement the "shaking" scheme for state transfer with the optimized trajectory (see appendix A), compare the results to theory and find a description for the excitation which is suitable as input for the emission calculation. This will be tackled in the following section.

We will approach the problem of understanding the transverse dynamics in two largely independent, complementary ways, motivated by the goal of developing an effective mapping of the many-body dynamics to a driven two-level system. In sec. 5.4.1

[6] In the following derivations, unless explicitly needed, we will omit the arguments (x,x'), which apply to all used quantites.

[7] Note, that this model does not take into account that $\tilde{p}$ *itself* may fluctuate due to technical instabilities between different experimental realizations (e.g. of total atom number or temperature), that do not necessarily affect both considered points proportionally. Hence, points with strong imbalance are much more prone to effects of technical noise, increasing ξ^2_-.

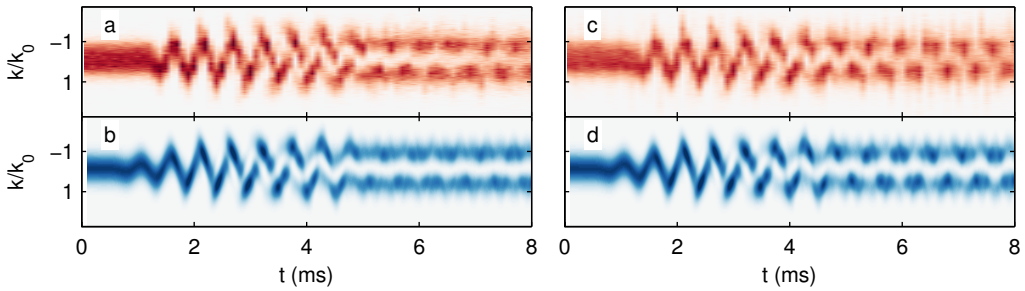

Figure 5.12.: Typical transverse momentum distribution dynamics $\tilde{n}(k_y, t)$, shown as false-color plots (data set Pot). (a) and (c) Experiment. (b) and (d) 1d GPE numerics, including finite bandwidth effects (see text). In (a) and (b), the offset field is detuned by $\sim 1\,\mathrm{mG}$, in (c) and (d) by $\sim 2\,\mathrm{mG}$ with respect to the optimal value, which has been found by minimizing the difference between experimental and numerical result at times before 5 ms. Each single time corresponds to an average of ~ 10 experimental runs, and is normalized to unity.

we will start by comparing GPE numerical results for the time-dependent momentum distribution of the driven condensate wave function to experimental observations. While the excellent agreement indicates, that the theory used to obtain the optimized ramp (appendix A) is accurate, it gives only limited insight into how the excitation process can be understood qualitatively. In sec. 5.4.2 a more phenomenological analysis is performed on the experimental data, which will give hints about how to develop a semi-quantitative understanding that provides more insight than the pure numerical result. In sec. 5.4.3 the GPE simulations are investigated in more detail, using a description based on Wigner quasi-probability functions, and displaced Fock states. It will become evident that all approaches lead to conceptually similar and quantitatively compatible interpretations, which can finally be unified to obtain a two-level interpretation as sought after initially.

5.4.1. Comparison of experiment and numerics

Compared to other driven quantum systems, where optimal control techniques may be applicable, a rather unique advantage of cold atoms is the accessibility of the system response, enabled by the relatively large time and length scales and the abundance of powerful imaging techniques. Probing the performance of a control strategy is not restricted to the final outcome, but the driven system can be monitored even *while* it is being driven, providing direct means to compare experiment and numerical simulations. As explained in sec. 5.1, the light sheet imaging system gives us direct access to the momentum distribution of the gas along its transverse axis. In fig. 5.12(a), a typical momentum distribution dynamics plot as obtained from the experiment is shown.

Numerical solution The numerical simulations shown in this section have been performed using the GPE (2.15), which acquires a time-dependent potential term for the excitation problem, just as in the approach for optimization in appendix A.

Alternatively to the time-dependent potential, we can define the condensate wave function $\phi(y)$ in a frame that is co-moving with the optimized trajectory $\lambda(t)$ [fig. 5.13(d)]. Then, the driving arises from the time-dependent displacement $\psi(y,t) = \exp[-i\lambda(t)\partial/\partial y]\psi_0(y,t)$, where $\psi_0(y,t)$ is defined in a fixed frame, and the GPE reads:

$$i\hbar\frac{\partial}{\partial t}\phi(y,t) = \left[-\frac{\hbar^2}{2m}\frac{\partial^2}{\partial y^2} - \dot{\lambda}(t)\frac{\partial}{\partial y} + V_{\mathrm{ext}}(y) + g_{\mathrm{y}}|\phi(y,t)|^2\right]\phi(y,t) \tag{5.27}$$

where $V_{\mathrm{ext}}(y)$ is now time-independent, and the interaction constant g_{y} is derived similarly to eq. (2.30), averaging over a TF condensate along x:

$$g_{\mathrm{y}} = g\int n_{\mathrm{TF}}(x)^2\mathrm{d}x\int|\phi(z)|^4\,\mathrm{d}z \tag{5.28}$$

As a convention, we will denote the first two GPE eigenstates as ϕ_0', ϕ_1', as opposed to the single-particle (Schrödinger) eigenstates ϕ_0, ϕ_1 as used in chapter 4.

Finite bandwidth effects To compare the experimental data to those obtained from numerical propagation of the GPE, we first need to account for the slight modification of the control sequence imposed by the finite bandwidth of the electronics used in our experiment. The main contribution to this filtering is the isolation amplifier that was used to have a galvanic isolation between the (grounded) waveform generator output and the (floating) chip electronics.[8] The measured transfer function modulus $|\mathcal{M}(\nu)|$ at a frequency ν can be approximated by an exponential $|\mathcal{M}(\nu)| \approx e^{\nu/\nu_{\mathrm{co}}}$ with cutoff frequency $\nu_{\mathrm{co}} \approx 4.4\,\mathrm{kHz}$. Furthermore, a frequency-dependent phase shift is imposed. Effectively, filtering mainly causes a reduction of the driving amplitude near the resonant frequency $\nu_1 \approx 1.8\,\mathrm{kHz}$ by a factor $|\mathcal{M}(\nu_1)|^{-1} \sim 1.6$, and a time delay on the order of 0.1 ms (fig. 5.13d). In fig. 5.13 it is shown, that the filtering due to the electronics can be largely canceled by rescaling and shifting the control sequence by these factors. The difference in the outcome of the simulated momentum distribution is only small and largely given by a slightly enhanced collective oscillation, which does not affect the emission dynamics (see sec. 5.4.3). For more recent experiments (sec. 6), the bandwidth has been greatly improved using a new electronics setup.

Robustness against experiment inaccuracy In OCT, an aspect of high relevance is the sensitivity of the excitation dynamics to deviations of experimental parameters from the ones used for optimization. In our case, this predominantly applies to parameters affecting the trapping potential. We consider small changes of the harmonic and quartic potential parameters ν_{y}, σ_{y} in eq. (3.6). In the experiment such deviations arise from variation of the dressing parameters Ω_0, Δ_0, which, in turn, are caused by inaccuracy of the current in the RF antenna wires δI_{RF}, and of the external offset field along x (defining the atomic Larmor frequency) δB_{x}, respectively (see sec. 3.2.2).

We can linearize the dependence of the potential parameters along y as given in eq. (3.6) around the optimum and write [in units of Hz, mG, mA]:

$$\begin{aligned}\nu_{\mathrm{y}} &= 1655 + 19\times\delta B_{\mathrm{x}} - 106\times\delta I_{\mathrm{RF}}\\ \sigma_{\mathrm{y}} &= 78.1 - 2.3\times\delta B_{\mathrm{x}} + 8.6\times\delta I_{\mathrm{RF}}.\end{aligned} \tag{5.29}$$

[8] Recently, the setup has been changed to a waveform generator having floating outputs, that lifts this restriction and allows for faster control ramps (see sec. 6).

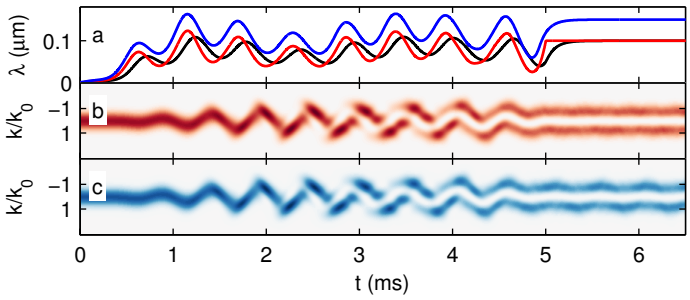

Figure 5.13.: Effect of filtering due to finite electronics bandwidth. (d) Control ramps $\lambda(t)$. Red: original control ramp. Black: control ramp after applying the electronics filtering. Blue: rescaled, filtered and time-shifted control ramp. (b) GPE momentum distribution, simulated without accounting for finite bandwidth. (c) GPE momentum distribution, simulation including finite bandwidth, amplitude rescaling of the control ramp by a factor of 1.6 and a time shift of 0.08 ms.

Fig. 5.12(a,c) shows experimental momentum dynamics for two sets with slightly different offset fields B_x. By comparison with numerical results (panels b,d), a difference of $\sim 1\,\mathrm{mG}$ is found, which already yields a clearly distinguishable result, especially regarding times $t > 5\,\mathrm{ms}$ where the strength of residual dynamics indicates a decrease in excitation fidelity. It is rather elusive to independently characterize the trap (e.g. using RF spectroscopy, see sec. 3.12) at this level of precision, rendering observation of the excited momentum dynamics itself the only sufficiently sensitive tool to optimize the experimental parameters.

Numerical results for a range of parameters are shown in Fig. 5.14. Panels (c-f) correspond to deviations caused by an offset field misalignment of $\pm 2\,\mathrm{mG}$ (b,c) and $\pm 7\,\mathrm{mG}$ (e,f) leading to weaker (positive values) or stronger RF dressing, respectively. It is observed that any deviation leads to a decrease in excitation efficiency, which is defined here as time-averaged overlap with the desired wave function ϕ_1', $\eta = \langle |\langle \phi_1' | \phi(t) \rangle|^2 \rangle_{t>5\,\mathrm{ms}}$. The similarly defined population of higher excited states ζ becomes strong at trap modifications with weaker dressing $\delta\nu_y > 0$ and $\delta\sigma_y < 0$. This effect can be expected, as the protection against excitation to higher states fades with decreasing anharmonicity, while the excursion of the trap relative to the typical length l_y increases. In panel (d), on top of an offset field mismatch of $+3\,\mathrm{mG}$, the current in the RF wire has been adjusted to cancel the effect on ν_y. The weak mismatch in σ_y and ξ_y only leads to a slight reduction of efficiency. Consequently, optimizing the experimental parameters for a strong excitation (e.g. by minimizing residual dynamics at $t > T = 5\,\mathrm{ms}$) may lead to slightly shifted values, which however compensate. Using this method, a sensitivity of better than 1 mG (or an equivalent mismatch of the dressing current) can be reached.

Many-body effects Along the transverse directions, confinement is strong enough ($h\nu_1 \gg \mu_0$) to make interaction-induced effects comparatively small. Still, to achieve the highest possible fidelity of the excitation, it is crucial to keep the nonlinear term in eq. 5.27 for optimization. In fig. 5.15, the excitation dynamics is shown for a data set (VarN), where the atom number has been varied before starting the excitation

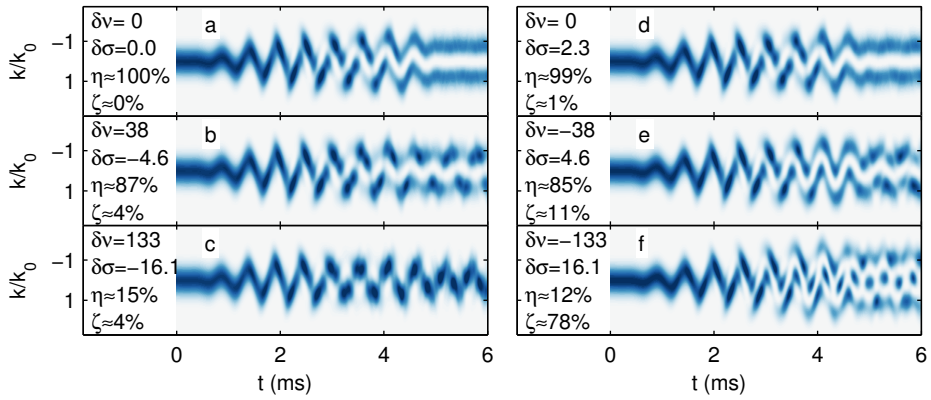

Figure 5.14.: Stability of the excitation sequence against inaccuracy of the trapping potential (numerical result). In each plot, the deviation of the potential terms $\delta\nu_y, \delta\sigma_y$ are given (in units of Hz), as well as the efficiency η and the spurious excitation to higher states ζ as defined in the text.

sequence, by keeping a fixed RF knife for a variable time, which causes plain evaporation. A possible temperature change should be largely irrelevant for the excitation, as long as there is no significant thermal population of transversely excited states. The data is compared to simulations, where the parameter g_y in eq. (5.27) has been calculated using TF profiles matching the respective total atom number N. Especially for high atom numbers, this might not be completely adequate, as the wave function along z, and consequentially the chemical potential and TF radius may be affected by interactions [93].

It is observed, that effective excitation is achieved for a nonlinearity corresponding to an atom number $N \sim 900$, which is close to what has been used in the optimization. For all other atom numbers, stronger residual dynamics after the end of the sequence ($t > T = 5\,\mathrm{ms}$) is found, indicating decreased fidelity, as the desired state is stationary. While the GPE simulations reproduce the general tendencies found in the experiment, the agreement is not as good as e.g. for scaled excitations (see below). For the highest atom number, only rather poor qualitative agreement is reached, indicating insufficiency of a mean-field model such as GPE (necessitating e.g. a MCTDHB ansatz [126, 295]) and strong effects of the rapid decay of the excited state into twin beams.

Scaled excitations In fig. 5.16 the momentum distribution dynamics is shown for data sets DynA/DynB, which will be the main subject of analysis in the remainder of this and the following (sec. 5.5) sections. To achieve different efficiencies, the excitation ramp has been scaled in amplitude by factors s with respect to the optimal control result, resulting in strongly varying wave function dynamics. The approach of simple amplitude scaling has been chosen over using separately optimized ramps for different efficiencies, to allow for easier comparison due to the well-defined relation between the used control sequences. Furthermore, our analysis will show that the main spurious effect of this strategy are collective oscillations at reduced scalings. Comparison between GPE and experimental result (average over $\sim$ 12 realizations)

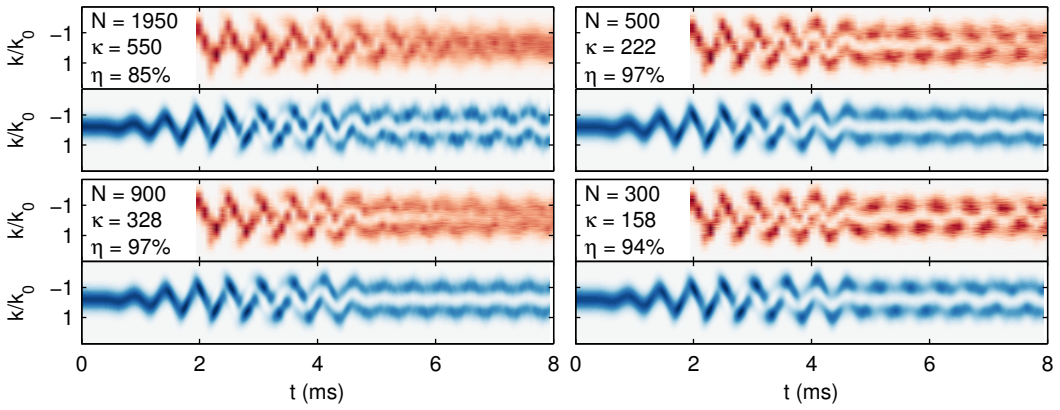

Figure 5.15.: Effect of varied atom numbers on excitation (data set VarN). In each pair of plots (top: experiment, bottom: numerics), the typical experimental atom number is shown alongside the non-linearity $\kappa \equiv g_{\mathrm{y}} N$ (in Hz µm, ordinary frequency). The efficiency η is defined in the text.

shows excellent agreement at early times.[9] At later times, decay of the excited state into twin beams, which is not accounted for in theory, becomes significant (see bottom right panel) and for high values of s, agreement is reduced due to inelastic collisions with the twin beams which reside in a different transverse state. However, for weak excitation, even the shape of single "beating peaks" after the end of the excitation pulse is precisely captured by numerics. Along the k-axis, the GPE result has been convolved with a Gaussian of $m/(\hbar t_{\mathrm{tof}}) \cdot 40\,\mu\mathrm{m} \approx 1.20\,\mu\mathrm{m}^{-1}$ rms width to account for finite imaging resolution and bulk position fluctuations. Apart from a small shift of the t-axis and a slight re-scaling of the k_{y}-axis,[10] the scaling factor s is the only free input parameter of the simulation.

Having established the detection method, and verified that the outcome is consistent with the numerics on which the control optimization has been founded, we now proceed to a more qualitative analysis of the experimental result.

5.4.2. Analysis of experimental momentum dynamics

In this and the following section we will analyze the momentum distribution dynamics beyond a simple comparison to numerical results, focusing on data set DynA/DynB which covers the largest range of parameters, allowing to derive a rather general description. The notion underlying the discussion will be that of a few-level system, comprised by the ground, first and occasionally second excited state of the confinement potential along the excitation direction, with the final goal to reduce the anharmonic

[9] Note that s has been defined including the necessary re-scaling due to finite electronics bandwidth (see Fig. 5.13).

[10] The shift in t is well below the experimental time resolution, and is very probably due to the inaccuracy of the filtering circuit characterization. The necessity for the re-scaling of k_{y} (of the order of 10%) might arise from interaction effects causing weak hydrodynamic effects in expansion [203]. The values of both adjustment are consistent among all sets shown.

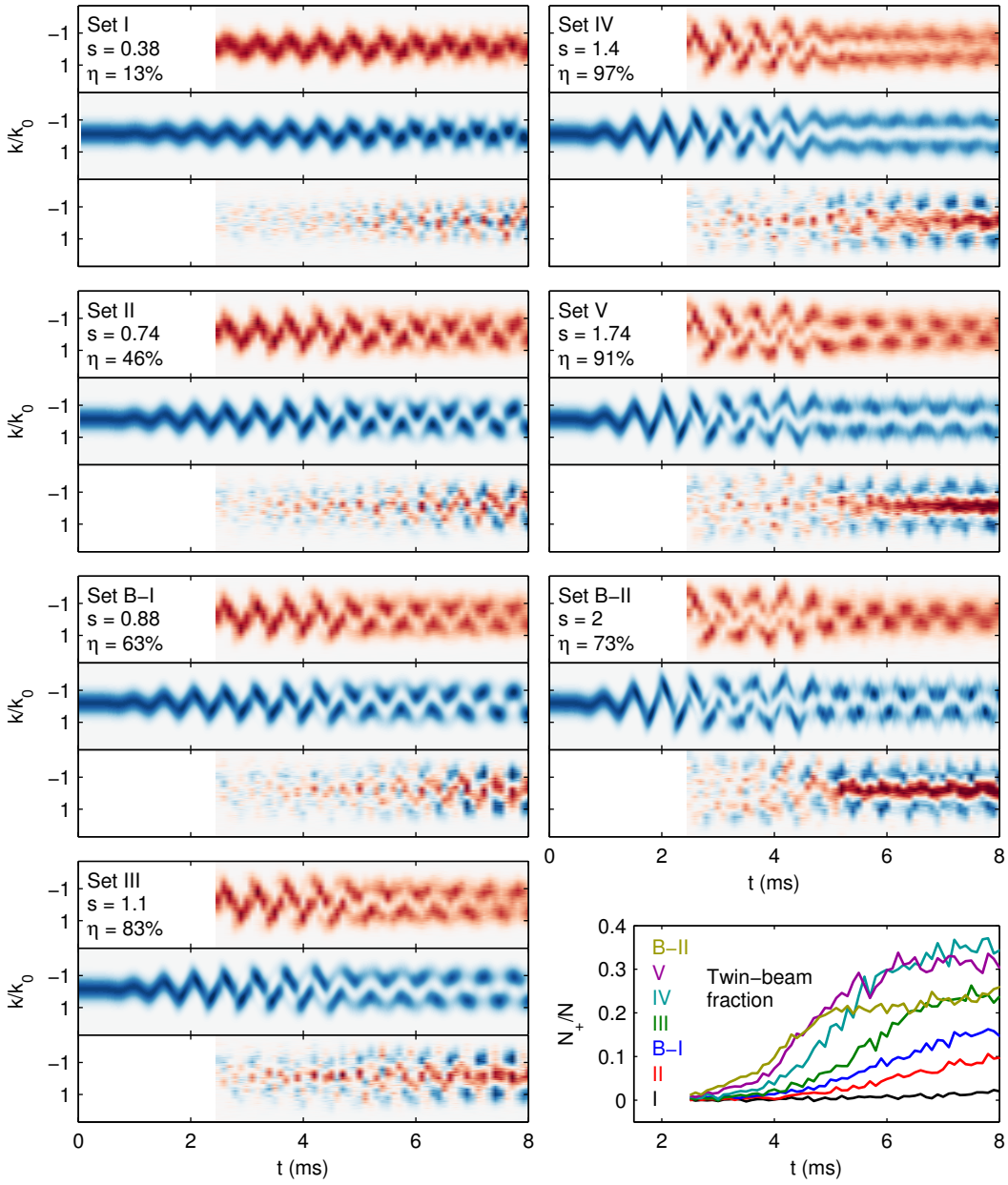

Figure 5.16.: Experimental and numerical results for the transverse momentum distribution dynamics $\tilde{n}(k_y, t)$, data set DynA/DynB. Mean atom number is 770 for sets I-V, and 856 for sets B-I and B-II. For each of the seven sub-sets, the upper image (red false-color) is the experimental result, normalized separately for each time step. The middle image (red false-color) shows the numerical GPE result, including low-pass filtering and scaling by the factor s as given. The bottom image shows the deviation between experiment and theory, expressed as imbalance $\tilde{n}_{\mathrm{ex}} - \tilde{n}_{\mathrm{th}}$; the color scale for the imbalance is enhanced by a factor 3. The bottom right inset shows the relative amount N_{dec}/N of atoms that have decayed from the excited state into twin atom pairs.

oscillator to a closed two-level system.[11] This approach may seem inappropriate, as it relies on the superposition principle, which requires a linear equation of motion and is hence not applicable to a mean-field wave-function as described by the GPE. However, in our case the nonlinearity is weak compared to the oscillator energy, and so is the modification of the dynamics due to many-body effects (see fig. 5.15), suggesting that a description in terms of single-particle states may still provide significant insight. A more involved, but conceptually similar approach, which is directly based on stationary states of the GPE can be found in refs. [94, 251, 309].

Center-of-mass dynamics As the simplest possible observable derivable from the momentum dynamics, we start by analyzing the transverse center-of-mass of the experimental images, corresponding to the momentum expectation value $K(t) \equiv \langle k_\mathrm{y}(t) \rangle$, see black lines in fig. 5.17 (left panels). In the power spectra of $K(t)$ (center panels), two strong peaks are observable near the first two transverse level spacings (see sec. 3.2.2) $\nu_1 = 1.84\,\mathrm{kHz}$ and $\nu_2 = 1.99\,\mathrm{kHz}$, and a weak third at $\nu_3 \approx 2.10\,\mathrm{kHz}$.

Assuming a single-particle level picture, these peaks can be interpreted as beating frequencies between populations of the first three levels of the oscillator, where mean-field effects are causing frequency shifts, as described below. Consequently, the magnitude of oscillations is the strongest for intermediate excitation efficiencies (sets II, III, B-I), where the levels are populated most evenly, maximizing the beating contrast [see below, fig. 5.18(a)].

A crucial observation is, that also the transverse profiles of the twin-beam peaks, which are separated in the images longitudinally (see fig. 5.3), exhibit strong oscillations of $K_\mathrm{t}(t) \equiv \langle k_\mathrm{y}^{(\mathrm{t})}(t) \rangle$ (see red lines in fig. 5.20). Meanwhile, they fully maintain their near-Gaussian shape.

In fig. 5.17, oscillations of the *relative* center-of-mass $K_\mathrm{r}(t) = K(t) - K_\mathrm{t}(t)$ (left), and their power spectrum (center) $f(\nu) = |\mathcal{F}[K_\mathrm{r}(t)](\nu)|^2$, are shown as blue lines. It is observed that, while the oscillations are similarly strong as in a fixed frame, all peaks in the power spectrum, except that near ν_1 are suppressed. This suggests, that in a reference frame co-oscillating with $K_\mathrm{t}(t)$, the dynamics can be understood in terms of two transverse levels, motivating an approach of decomposition into a quasi-classical oscillation, and "internal" dynamics, which remain unaffected by the bulk oscillation.[12] This interpretation is consistent with our understanding of the twin-beam emission process (sec. 5.5), where the transverse state of the twin beams, a Gaussian state displaced by $K_\mathrm{t}(t)$, defines the appropriate ground state for the internal dynamics. In sec. 5.4.3, a more rigorous formalism for the co-oscillating frame will be given, and its position will be independently derived from numerical results.

In the right column of fig. 5.17, spectra are shown which are derived from the oscillations at times $t > 5\,\mathrm{ms}$ only, i.e., where no driving occurs anymore. Hence, they provide a characterization of the final state that is reached after the excitation. Qualitatively, the same features are observed as in the full time spectra, however, peaks

[11] In the literature on quantum control strategies, this problem is occasionally discussed as that of leakage-suppression in a two-level system [106–108, 296].

[12] This decomposition is exactly valid for harmonically confined many-body systems [145, 146]. Obviously, this does not hold for an anharmonic oscillator, which is exactly why our excitation to a non-classical state by displacement can work at all. Being aware of the inconsistency, we still apply the decomposition approach to qualitatively understand the dynamics.

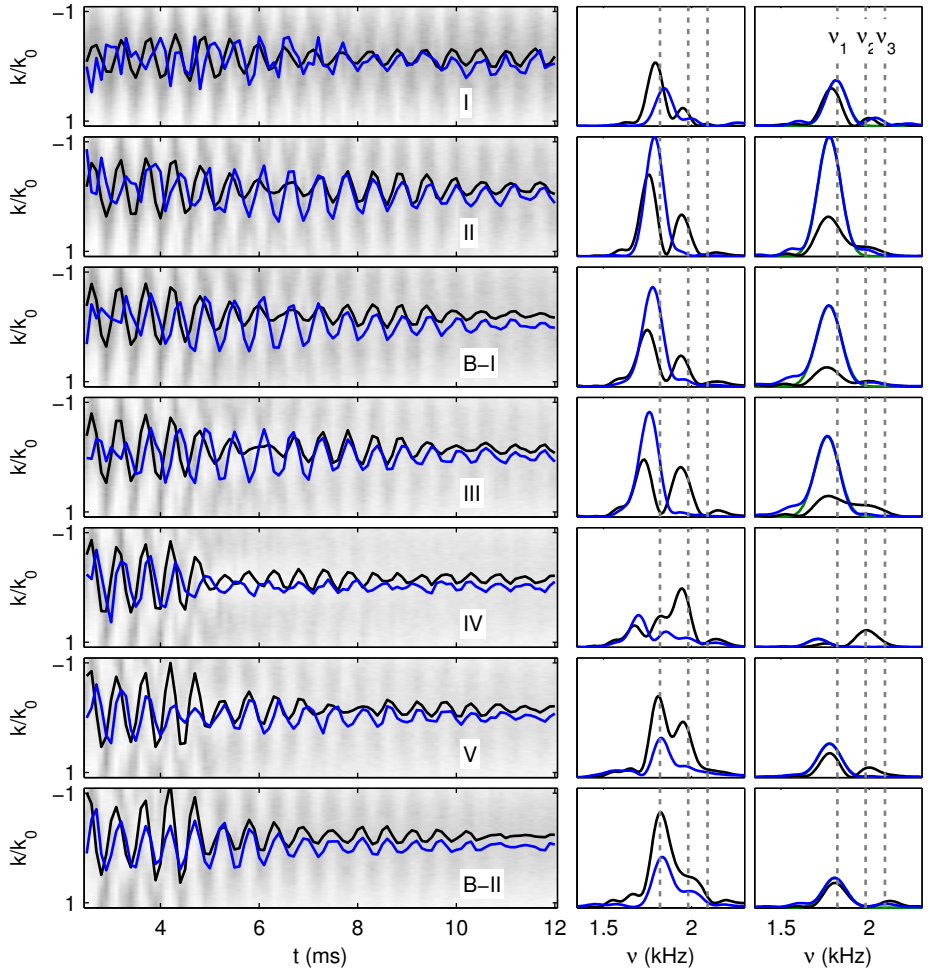

Figure 5.17.: Momentum space center-of-mass dynamics for data set DynA/DynB, as shown in fig. 5.16. Left column: center-of-mass momentum of the source cloud with respect to a fixed frame ($K(t)$, black) and relative to the twin-beam center-of-mass ($K_\mathrm{r}(t)$, blue). (See Fig. 5.20 for the twin-beam center-of-mass.) In the background, the full dynamics is shown (see Fig. 5.16). Middle column: corresponding power spectra $f(\nu)$, taken over the entire time span shown. Right column: spectra, taken over a time span starting from $t > T = 5\,\mathrm{ms}$, i.e., after the end of the excitation. Grey dashed lines in the background indicate the harmonic frequency ν_h, and the first three level spacings, as defined in the previous section. All spectra are in arbitrary units, but normalized identically for each of the columns.

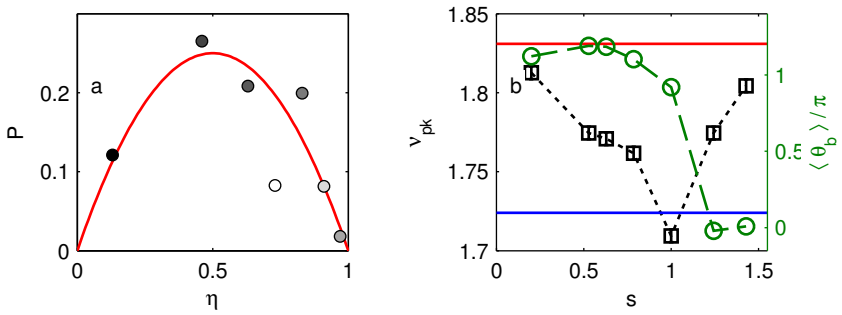

Figure 5.18.: Analysis of post-excitation beating spectra shown in the right column of fig. 5.17. (a) Integrated power of oscillations P. The experimental points have been scaled for best fit to $\eta(1-\eta)$ (red line). η has been derived as described in the previous section. The shading of each point indicates the corresponding scaling s (white is highest). (b) Peak position (black, left axes) and cosine of averaged phase (green, right axes). Red and blue lines correspond to the single-particle level spacing ν_1, and the mean-field-shifted level spacing ν_1', respectively.

at ν_2 are smaller, which is consistent with theory, as will be shown below. Also, in the relative center-of-mass spectrum, the observation of a single-peak structure, with a minimal amplitude for the most efficient excitation is even more evident. However, the observation of a single-peak structure, with a minimal amplitude for the most efficient excitation is even more evident. In Fig. 5.18(a), the integrated power of the oscillations $P \propto \int f(\nu)\mathrm{d}\nu$, measuring the stationarity of the final state, is shown as a function of the numerically obtained excitation efficiency η (see previous section). Apart from the strongest driving, where higher states may become excited more easily, P shows fair agreement with a curve given by $\eta(1-\eta)$, which is the squared amplitude of the interference term in the momentum-space density of a two-level system with momentum-space wave functions $\tilde{\phi}_0, \tilde{\phi}_1$:

$$\begin{aligned}\tilde{n}(k_\mathrm{y}, t; \eta) &= \left|\sqrt{1-\eta}\tilde{\phi}_0(k_\mathrm{y}) + \sqrt{\eta}\tilde{\phi}_1(k_\mathrm{y})\right|^2 \\ &= (1-\eta)|\tilde{\phi}_0(k_\mathrm{y})|^2 + \eta|\tilde{\phi}_1(k_\mathrm{y})|^2 \\ &\quad + 2\sqrt{\eta(1-\eta)}\Re[\tilde{\phi}_0^*(k_\mathrm{y})\tilde{\phi}_1(k_\mathrm{y})]\cos(2\pi\nu_1 t).\end{aligned} \tag{5.30}$$

The positions of the beating peak (obtained from a Gaussian fit) are shown in fig. 5.18(b). For high efficiency, the frequency is shifted downwards from the oscillator level spacing ν_1 (red line). Somewhat similarly to the discussions in chapter 4 and sec. 5.5.3, this is explained by the mean field term in the GPE (5.27). For the boundary case of near-unity efficiency, the shift can be calculated rather easily. As the ground state population is negligible, it does not contribute to the interaction energy, and the chemical potential μ_e for an atom in the excited state is given by the second eigenvalue of the time-independent GPE. The according wave function $\phi_1'(y)$ can now be used to calculate the chemical potential μ_g of a single atom in the ground state ϕ_0^MF, using a Schrödinger equation with effective potential arising from the mean field of the excited

state:

$$\mu_{\mathrm{g}}\phi_0^{\mathrm{MF}}(y) = \left[-\frac{\hbar}{2m}\frac{\partial^2}{\partial y^2} + V_{\mathrm{ext}}(y) + 2g_{\mathrm{y}}|\phi_1'(y)|^2\right]\phi_0^{\mathrm{MF}}(y), \tag{5.31}$$

where the factor of 2 arises from exchange symmetry, similarly to the Bogoliubov-de Gennes equations (2.21).[13] The beating frequency is now given by the difference in chemical potential. Instead of the oscillator level spacing $\nu_1 \approx 1.831\,\mathrm{kHz}$, we obtain $\nu_1' = (\mu_e - \mu_g)/(2\pi\hbar) \approx 1.724\,\mathrm{kHz}$ (blue line).[14] Given the uncertainty in the input parameters of the calculation (such as the assumption of an equilibrium Thomas-Fermi shape longitudinally), this value agrees well with the experimentally obtained one for maximum efficiency (set IV), $\nu_{\mathrm{IV}} = 1.709(1)\,\mathrm{kHz}$.

Finally, we can have a look at the phase of the (relative) center-of-mass oscillation. When comparing the value of $K_{\mathrm{r}}(t)$ for different scalings at a fixed time in fig. 5.17, it is apparent, that the phase inverts at the point of maximum efficiency. We take the averaged phase from the Fourier transform result, weighted by the Lorentzian fit of the peak, and obtain the curve shown in fig. 5.18(b, right axes). The inversion is reminiscent of a two-level system subject to a Rabi driving, where the phase of precession inverts after passing the pole of the Bloch sphere at a pulse area larger than π. As will be shown in the following section, the excitation process can be understood analogously.

5.4.3. Two-level driving model

To understand the physical mechanism governing the optimal excitation protocol, in the following we analyze the time evolution of the condensate wave function in the Wigner quasi-probability representation [57]:

$$W(y,k,t) = \int e^{-iks}\phi(y+\frac{s}{2},t)\phi^*(y-\frac{s}{2},t)\,\mathrm{d}s\,, \tag{5.32}$$

which provides a mixed position-momentum distribution. Integration over all momenta k gives the spatial probability distribution $|\phi(y,t)|^2$. Likewise, integration over y gives the momentum probability distribution.

In fig. 5.19 the Wigner function of the condensate is shown for different times during the excitation sequence. Initially, it approximately corresponds to the ground state of the harmonic oscillator, with equal uncertainty in position and momentum.

The distribution is slightly elongated along y due to the nonlinear atom-atom interactions. The final state (bottom right panel), corresponds to the first excited state of the GPE in the anharmonic trap, ϕ_1'. It has positive and negative values (giving a node at $y = 0$ upon integration over all momenta), and thus differs from a genuine classical distribution function.

[13] Note, that ϕ_0^{MF} is quite different from ϕ_0', which is the mean field wave function (GPE solution) of the entire cloud in the ground state.

[14] To a fair approximation, this shift can also be derived by neglecting the deformation of the oscillator eigenstates due to the mean field. Using their density overlaps $\gamma_{ij} = \int |\phi_i(y)|^2|\phi_j(y)|^2\mathrm{d}y$, we can simply write: $\nu_1' \approx \nu_1 + g_{\mathrm{y}}N(\gamma_{11} - 2\gamma_{01})/(2\pi\hbar) \approx 1.705\,\mathrm{kHz}$. Note also, that this latter value is close, but not equal to that derived in chapter 4 for the mean-field shift of the twin-beam kinetic energy ϵ_{S}, as the latter has been calculated near the peak of the longitudinal TF parabola, whereas here (in computing g_{y}) we average over it.

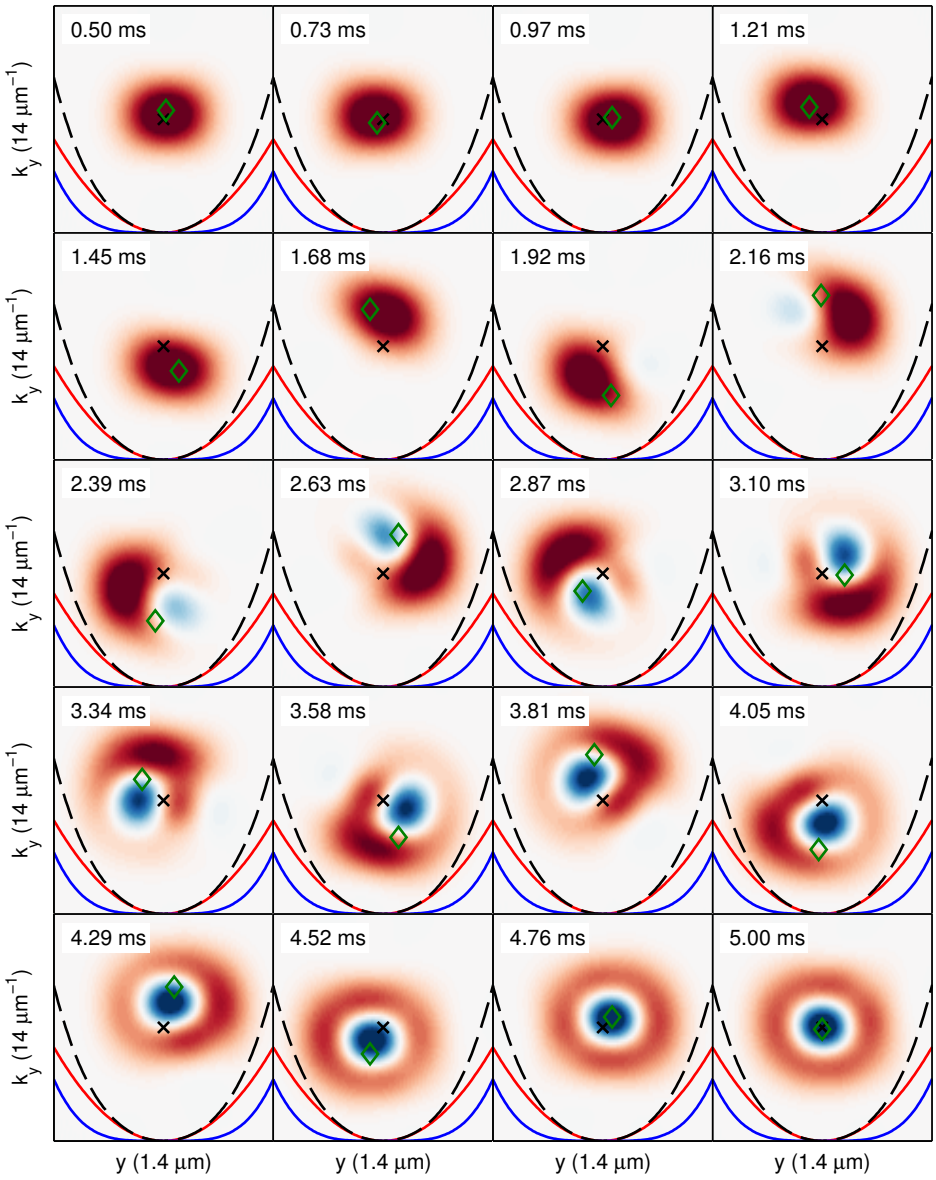

Figure 5.19.: Time evolution of Wigner function. Each panel displays a false-color plot of a Wigner function at the displayed time of the excitation sequence. Red and blue ranges correspond to positive and negative values, respectively. Lines indicate the trapping potential: the harmonic part $\propto \nu_{\mathrm{y}}(y/l_{\mathrm{y}})^2$ is shown in red, the anharmonic part $\propto \sigma_{\mathrm{y}}(y/l_{\mathrm{y}})^4$ is shown in blue. The dashed line corresponds to the total potential. The trap center is marked as black cross, whereas the green diamond indicates the origin $Y_0(t), K_0(t)$ of the co-moving frame.

We observe, that the excitation first brings the condensate into quasi-classical collective oscillations, whose frequency is determined by the harmonic part of the confinement potential. In the Wigner function, they appear as a circling motion around the center. For a large enough displacement, the condensate wave function is brought into the region where the anharmonicity of the confinement becomes significant (see red/blue lines). Now, the internal structure of the wave function (and not just its displacement in phase space) can be modified, and on top of the collective oscillation, the transfer from the ground to the first excited state occurs. Finally, at the terminal time $T = 5\,\mathrm{ms}$, the control process brings the condensate to a complete halt.

Motivated by the observation of the Wigner function behavior and the findings of the previous section, we next suggest a procedure to approximately map the excitation dynamics onto a genuine two-level description of ground and excited condensate states. As in sec. 5.4.2, the main idea is to separate the wave function dynamics into (i) a collective, quasi-classical oscillation, which is needed to bring the condensate into the anharmonic part of the trap, and (ii) an internal conversion between the ground and first excited state, defined in a co-moving frame. The latter conversion is governed by the anharmonic part of the trap, as explained above.

We define wave functions $\varphi_\mathrm{g}(y)$ and $\varphi_\mathrm{e}(y)$ as single-particle eigenfunctions of the *harmonic* part of the trap potential only, i.e. Eq. (3.6) with σ_y and ξ_y set to zero. Also, any modifications due to the nonlinear atom-atom interactions are neglected. This simplification allows us to analyze the dynamics in terms of displaced Fock states [297], that capture well the notion of the separation approach. Let $\hat{D}[\alpha(t)] = \exp[\alpha(t)\hat{a}^\dagger - \alpha(t)^*\hat{a}]$ denote the displacement operator of the harmonic oscillator [57], where $\alpha(t) = [l_\mathrm{y}^{-1}Y_0(t) + il_\mathrm{y}K_0(t)]/\sqrt{2}$ determines the position and momentum of the displacement at time t, and $\hat{a}$ denotes the annihilation operator. For a given displacement $\alpha(t)$, we can compute the overlap between the displaced ground and excited states with the condensate wave function according to

$$\chi(t) = \left| \int \left[\hat{D}[\alpha(t)]\varphi_g(y)\right]^* \phi(y,t)\,\mathrm{d}y \right|^2 + \left| \int \left[\hat{D}[\alpha(t)]\varphi_e(y)\right]^* \psi(y,t)\,\mathrm{d}y \right|^2 . \tag{5.33}$$

Determining the value $\alpha(t)$ which gives the largest overlap at time t allows us the aforementioned decompositions into (i) center-of-mass coordinates $Y_0(t)$ and $K_0(t)$, and (ii) probability amplitudes $\langle\hat{D}[\alpha(t)]\varphi_g|\phi(t)\rangle$ and $\langle\hat{D}[\alpha(t)]\varphi_e|\phi(t)\rangle$ for the ground and excited state within the displaced frame. In all cases we find an overlap $\chi(t)$ well above 90%, which thus justifies the wave function decomposition. In fig. 5.20, the obtained values for $K_0(t)$ are shown as red lines, and compared to experimentally obtained values, as described below. In fig. 5.21 we compare $\chi(t)$ and the obtained excited population $\eta'(t) = [\langle\hat{D}[\alpha(t)]\varphi_g|\phi(t)\rangle|^2$ to results from direct projection of $\phi(y,t)$ on the GPE states $\phi_i'(y)$. The direct projection leads to strong transient population of higher excited states, and a sudden jump near the end of the excitation [fig. 5.21(a)], where they are depopulated again. This is reminiscent of the fixed-frame center-of-mass spectra (black lines in fig. 5.17), where a peak near ν_2 is present when regarding the entire sequence (center column), but mostly vanishes after $t = T$ (right column). In contrast, the two-level approximation in the system displaced by $\alpha(t)$ yields a smooth transition [fig. 5.21(b)], consistent with the continuous appearance of negative values of the Wigner function (fig. 5.19). In the momentum dynamics derived from the two-level model in a similar manner to eq. (5.30) as shown in fig. 5.21(d), a continuous

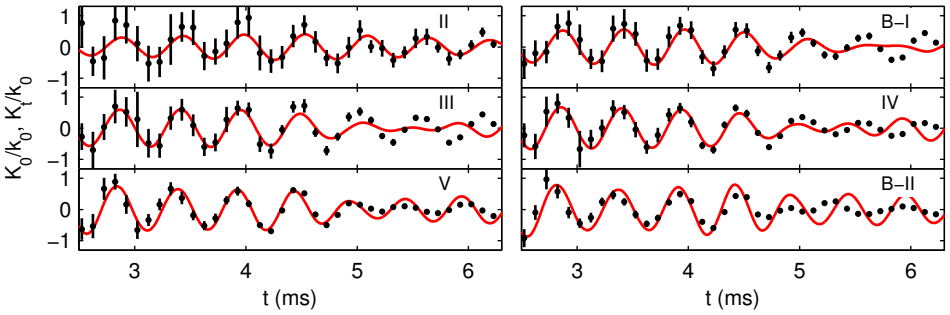

Figure 5.20.: Reference frame for two-level model. Underlying data are the same as shown in Figs. 5.16 and 5.17. Red lines are the momentum-space displacement $K_0(t)$ of the two-mode basis states, as obtained from applying Eq. (5.33) to the GPE result. Black points indicate the experimentally found center-of-mass position of twin beams that have decayed from the excited state K_t, defining the reference frame for the emission process (see sec. 5.4.2). Similar to the momentum space dynamics as shown in Fig. 5.16, agreement reduces at later times, where decay into twin beams becomes strong. Data set I has been omitted due to the emission of twin beams being insufficient to determine K_t.

transfer to the excited state is observed, with strong beating at intermediate excited population. Again, this is consistent with the experimental *relative* center-of-mass spectra (blue lines in fig. 5.17), where only a single peak near ν_1' persists, even during the excitation. Similar to a Rabi pulse with area larger than π, the excited population $\eta'(t)$ is decreasing towards $t = T$ for scaling parameters $s > 1$.

As laid out in sec. 5.4.2, the appropriate ground state for the internal conversion dynamics can also be determined in the experiment from the center-of-mass position $K_\mathrm{t}(t)$ of the twin-atom beams which the excited state is decaying into continuously. For times t, where the decayed fraction becomes perceivable, we can compare the experimentally found $K_\mathrm{t}(y)$ to $K_0(y)$ as in fig. 5.20, and find good agreement without any free parameter over a large range of settings. Together with the absence of decay products from higher excited states in the experiment, this result confirms the validity of the decomposition approach.

In the next section, it will be shown, that the obtained populations of the excited state allow for a quantitative description of the ensuing twin-beam emission process. To facilitate the inclusion of the two-level result η' into the emission dynamics calculation, we approximate the excitation process by a constant, near-resonant Rabi coupling with coupling strength Ω, detuning δ and initial time delay t_0:

$$\tilde{\eta}(t) = \begin{cases} \left(\frac{\Omega}{\Omega'}\right)^2 \sin^2\left[\Omega'(t-t_0)\right] & : t_0 \le t \le T \\ \left(\frac{\Omega}{\Omega'}\right)^2 \sin^2\left[\Omega'(T-t_0)\right] & : t > T \\ 0 & : t < t_0 \end{cases} \tag{5.34}$$

where $\Omega' = \sqrt{\Omega^2 + \delta^2}$. fig. 5.21 (dashed lines) shows, that eq. (5.34) is an appropriate approximation to the numerically obtained $\eta(t)$, if Ω, Δ and t_0 are left as fit parameters. These will be inserted into eq. (5.39) to conveniently include continuous pumping into the density matrix theory (as described in sec. 4.4).

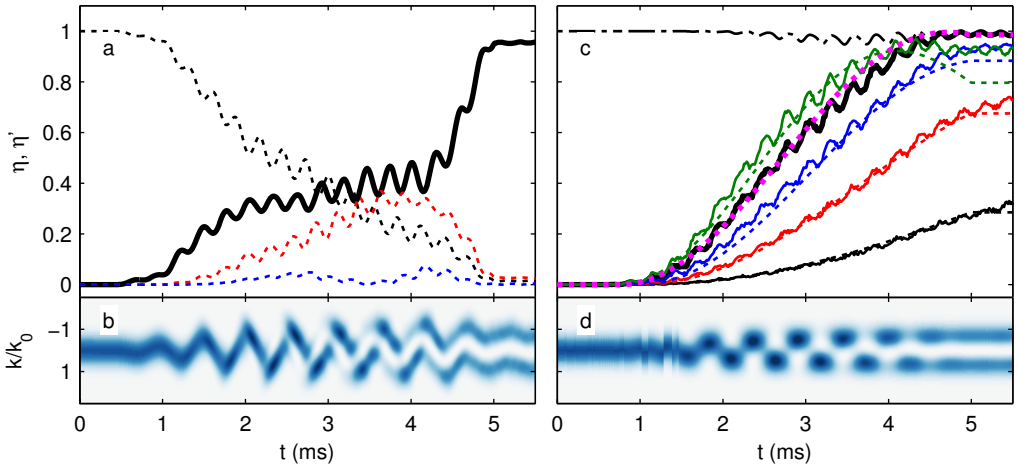

Figure 5.21.: State populations during the excitation process. (a) Populations $\eta(t)$ of excited states of the full anharmonic potential [Eq. (3.6)] as arising from direct projection of the GPE result for data set IV ($s = 1$). The solid line indicates the population of the first excited state, dotted lines represent the ground (black) and first and second excited (red, blue) states. (b) Corresponding momentum dynamics (identical to Fig. 5.16-IV). (c) Population of first excited state in co-oscillating frame within the two-mode model $\eta'(t)$. Solid thick line: data set IV, corresponding to solid line in (a). Solid, colored lines: sets I (black), II (red), III (blue), and V (green). The dash-dotted line indicates the total overlap of the two-level model with the GPE result $\chi(t)$ [see Eq. (5.33)], which exceeds a value of 0.95 at all times t. Dotted lines: corresponding Rabi driving fits, following eq. (5.34). (d) Momentum dynamics arising from time-dependent superposition of ϕ_0, ϕ_1 in the co-oscillating frame, data set V. Note the strong beating at intermediate times/excited fractions.

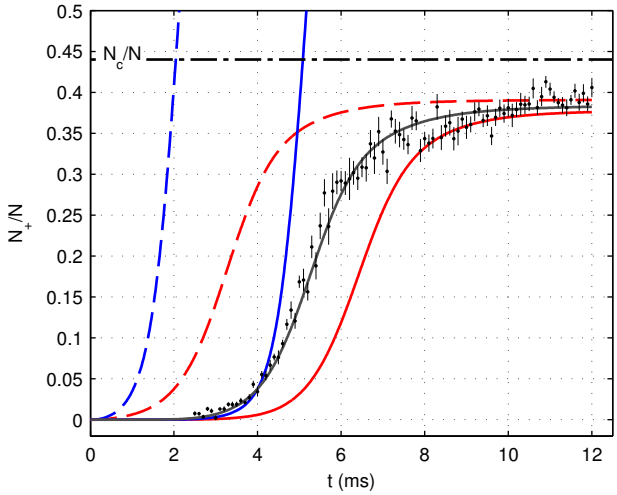

Figure 5.22.: Emission dynamics curves for various modifications of the density matrix theory. All curves are for $N = 800$ atoms. Blue, dashed: instantaneous pumping, zero temperature. Red, dashed: instantaneous pumping, $T = 25\,\mathrm{nK}$, corresponding to $N_c \approx 350$. Blue, solid: finite-time pumping (optimal excitation in 5 ms, see sec. 5.4), zero temperature. Red, solid: finite-time pumping, $T = 25\,\mathrm{nK}$. Black, solid: finite-time pumping, $T = 25\,\mathrm{nK}$, with excess scattering $\Gamma = 0.4\,\mathrm{s}^{-1}$. Dots with errorbars: experimental result for optimal excitation.

5.5. Emission dynamics

In this section we will discuss the dynamics of the twin-beam emission process, i.e., how the time-dependence of the twin-beam properties after starting the excitation sequence, can be understood. In contrast to sections 5.2 and 5.3, where two-particle observables (that depend on products of four field operators) have been discussed, the analysis will be limited to the most accessible of *single-particle* observables, that is, the mean population of the twin beams N_+. This allows for comprehensive quantitative analysis, as the density matrix theory detailed in sec. 4.4 can be applied, whereas there is currently no theory available that can predict two-particle quantities in the regime of strong depletion and long emission times present in our experiment. Moreover, estimation of mean populations only does not necessitate many experimental realizations, allowing to cover a large parameter range while keeping measurement times reasonable. Before experimental results are presented, some extensions of the general density matrix method from sec. 4.4 as required by the peculiarities of our experiment will be discussed.

5.5.1. Extensions of the density matrix theory

In the density matrix theory as laid out in sec. 4.4, several assumptions have been made, that are not necessarily fulfilled in the experiment, but quantitatively alter the emission dynamics:

- It has been assumed, that at $t = 0$, all atoms are already pumped into the

source state S. As discussed in the previous section, in the actual experiment, the pumping from the ground state takes non-negligible time and causes an overlap of excitation and emission time scales. The theoretical treatment of excitation and emission, however, are completely separated, necessitating an effective description to connect them.

- Thermal effects have been neglected entirely. As in an elongated system, thermal effects can be understood as a depletion of the condensate mode (see sec. 2.4.4), this approximation is effectively equivalent to taking for granted, that all atoms in the vibrationally excited state directly take part in a single emission process. Indeed, the populations of the excited state, $N_\mathrm{e} \approx \eta' N$, and the source state, N_S, cannot a priori be expected to be equal: $N_\mathrm{S} \leq N_\mathrm{e}$.

- It is assumed, that the twin-beam modes are completely empty initially, and that there is no other process other than the amplified emission described by the density matrix theory, that can populate them over time. The extreme sensitivity of the population dynamics on the state of the final mode at early times (which triggers Bosonic enhancement) amplifies any spurious effects, even if they appear to be very weak.

- The quantum modes that are relevant for the emission process have been assumed to be static. However, the redistribution of population causes a back-action on the energy of the modes themselves due to changing mean-field shifts, see sec. 4.4.2.. However, as discussed there, this effect is weak quantitatively, as the decreased density overlap between source and twin beams is almost exactly canceled by the bosonic enhancement for elastic scattering between different modes ($\alpha_{11} \approx \alpha_{00} \approx 2\alpha_{01}$).

- Any higher-order inelastic scattering between twin-beam atoms and the transversely excited cloud are neglected. Especially at longer times, this will lead to exchange of particles between the transverse states in the twin beams, transfer of longitudinal momentum due to the finte temperature of the source, and eventually the relaxation of the system towards thermal equilibrium. Those effects are beyond the scope of current theoretical description, despite being of fundamental interest, especially as questions on integrability in a one-dimensional system arise [261, 262, 298–301]. They should not affect the initial population dynamics of the twin beams, which depends only on the initial inelastic scattering out of the source state. However, it is conjectured that this approximation leads to the underestimation of the twin-beam width compared to the experiment (sec. 5.5.3).

It has been found, that the first three of those approximations strongly impact the calculation results and have to be accounted for using some effective theories that will be described in the following. For a quick overview, in fig. 5.22 emission curves are shown, where none, some, or all of the three modifications have been applied.

Thermal source depletion Direct application of the density matrix theory leads to a huge overestimation of both the initial growth rate, and the saturation value that is

reached at longer times, with respect to the experimentally obtained data (blue dashed line).[15] The reason that was found to be the likely cause for the discrepancy are the longitudinal phase fluctuations present in a finite-temperature quasi-condensate (see sec. 2.4.2).

In our theory in sec. 4.4, we assumed all atoms to populate a single source mode with population N_{S}, which is the only non-zero entry of the single-particle density matrix $\rho = \rho_{\mathrm{SS}} \otimes \rho_{ij}$, before emission starts. This is clearly incompatible with the single-particle density matrix of a phase-fluctuating quasi-condensate $\rho(x, x')$, which is given by eq. (2.40). As described in sec. 2.4.4, using the Penrose-Onsager criterion, a *true condensate* can be defined as the mode corresponding to the largest eigenvalue of $\rho(x, x')$, and as a consequence writing the quasi-condensate single-particle density matrix as:

$$\rho(x, x') = N_{\mathrm{c}} \psi_{\mathrm{c}}^*(x) \psi_{\mathrm{c}}(x') + \rho_{\mathrm{th}}(x, x'). \tag{5.35}$$

We now make the somewhat radical step, to completely neglect the thermally excited part ρ_{th}. Hence, in the mode couplings of our theory, eq. (4.10) we replace:

$$\psi_{\mathrm{TF}}(x) \to \psi_{\mathrm{c}}(x) \tag{5.36}$$

and, at the same time set the initial source population to $\rho_{\mathrm{SS}} = N_{\mathrm{c}}$, or, if we include the excitation process (see below), $\rho_{\mathrm{gg}} = N_{\mathrm{c}}$, where ρ_{gg} is the initial ground state population. We also assume, that the excitation process does not depend on the longitudinal mode structure, and hence:

$$\frac{N_{\mathrm{S}}}{N_{\mathrm{c}}} = \frac{N_{\mathrm{e}}}{N}. \tag{5.37}$$

Note that, however, for the calculation of mean-field effects, such as the effective potential of the twin-beam modes (4.36), we keep the full quasi-condensate density $n_{\mathrm{TF}} = |\psi_{\mathrm{TF}}|^2$.

In fig. 5.23(a), emission curves for different temperatures at otherwise identical parameters are shown. While the onset time of emission does not strongly depend on the temperature, slope and saturation value are heavily affected. For the numbers considered, a slight oscillation of population back into the source state is only observed at $T = 0$. As a comparison, emission curves based on the second-largest eigenmode of $\rho(x, x')$ are shown. Note however, that in a full theory for emission from quasi-condensates, the dynamics for emission from each mode would not at all be independent.

Obviously, the PO-mode simplification is only justified in the limit of low temperatures, where the eigenvalues of $\rho_{\mathrm{th}}(x, x')$ remain small enough to prevent significant emission from the respective modes. However, it allows to keep the theoretical description compact and numerically tractable. Moreover, minor contributions of scattering from higher modes can be phenomenologically accounted for by adjusting the excess scattering rate as described below.

[15] As density matrix and Bogoliubov theories agree well at early times for the case of instantaneous pumping, the same should be true for a prospective modified Bogoliubov theory that can include the excitation dynamics and/or source depletion.

Continuous pumping To handle the overlapping time scales of excitation and emission, we can take advantage of the effective two-mode approximation for the transveral states that has been developed in sec. 5.4.3. The reduction of the complex dynamics of a driven many-body system to a simple Rabi coupling allows for a straightforward inclusion of the pumping dynamics into the emission calculation. All we have to do is to add a coupling term to the Hamiltonian in the Heisenberg equation (4.31) that transfers atoms into the transversely excited source state:

$$\hat{H}_{\mathrm{tot}} = \hat{H}_0 + \hat{H}_{\mathrm{MM}} + \hat{H}_{\mathrm{P}}(t). \tag{5.38}$$

In this Hamiltonian, $\hat{H}_0$ accounts for free evolution terms of all involved states, which are the twin-beam modes $\hat{a}_i$, the source mode $\hat{a}_{\mathrm{S}}$, and the initial ground state $\hat{a}_{\mathrm{g}}$. The two latter correspond to the single-particle two-state approximation in sec. 5.4.3, and the twin-beam states correspond to the functions $\psi_i(x)$ as derived in eq.(4.36). Following the sinusoidal fits of the transverse two-level approximation, eq. (5.34), we can write the pumping Hamiltonian as:

$$\begin{aligned} \hat{H}_{\mathrm{P}}(t) &= \frac{\hbar\tilde{\Omega}}{2} \cdot \begin{cases} \hat{a}_{\mathrm{S}}^{\dagger}\hat{a}_{\mathrm{g}} + \mathrm{H.c.} & : t_0 \le t \le t_{\mathrm{exc}} \\ 0 & : \text{otherwise} \end{cases} \\ \tilde{\Omega} &= \Omega \cdot \exp\left[-i\left(\mu_1/\hbar + \delta\right)\left(t - t_0\right)\right], \end{aligned} \tag{5.39}$$

which is the simple Hamiltonian for a near-resonantly driven two-level system [24]. The parameters δ, Ω, t_0 have been obtained from fits as described in sec. 5.4.

For the modified Hamiltonian (5.38), we can again solve the Heisenberg equation for the single-particle density matrices ρ_{ij}, ρ_{SS} and $\rho_{\mathrm{gg}} = \langle \hat{a}_{\mathrm{g}}^{\dagger}\hat{a}_{\mathrm{g}} \rangle$, in analogy to eq. (4.31).

Results are shown in fig. 5.23(b). It is observed that at an excitation duration of 5 ms (blue lines), there is a significant overlap of excitation and emission time scale, indicated by the peak of the population N_{S} not reaching the total PO mode (true condensate) population $N_{\mathrm{c}} \approx 400$. For the total emitted population N_{+}, the main effect of finite-time pumping is a time delay. However, slope and saturation value are only weakly affected.

Note, that $\hat{H}_{\mathrm{P}}$ only couples ground and source state. Hence, it is assumed, that the excitation process does not affect the atoms that have already been emitted into the twin-beam modes. This seems justified from experimental observations (the measured transverse momentum distributions of the twin beams are found to be close to that of a ground state), and the fact that at early times during the excitation process, the final state still resembles a quasi-classical coherent state.

Excess scattering When comparing the calculated twin-beam population, arising from the two-state pumping and thermal source depletion approximations, the saturation value and slope of the emission curve are well captured [red line in fig. 5.22(a)]. However, there is a time delay of $\lesssim 2$ ms in the theory. It is likely, that several factors contribute to this delay:

- While scattering from higher quasi-condensate eigenmodes would not cause a strong contribution to the total twin-beam populations at times considered here,

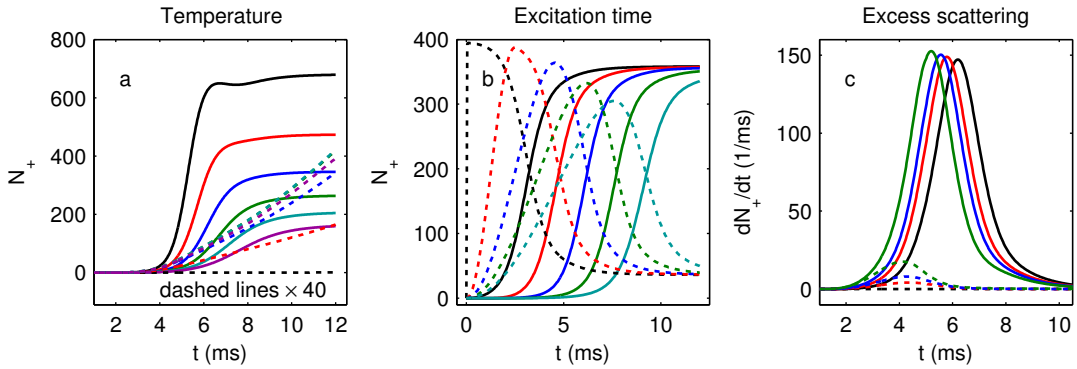

Figure 5.23.: Influence of the theory modifications outlined in this section on the twin-beam emission dynamics. (a) Emission dynamics for $N = 800$ and different temperatures ranging from $T = 0$ (black) to $T = 50\,\mathrm{nK}$ (purple) in steps of $10\,\mathrm{nK}$. Solid lines: emission from Penrose-Onsager (PO) mode, as considered for our simulations. Dashed lines: emission calculated for second-largest eigenmode (without emission from PO mode) of $\rho(x, x')$, magnified by a factor of 40. (b) Emission dynamics for $N = 800$ atoms at $T = 20\,\mathrm{nK}$ ($N_c \approx 400$), for various excitation times ranging between instantaneous excitation (black) and a Rabi π pulse with length $10\,\mathrm{ms}$ (cyan). Dashed lines: source population N_S. Solid lines: twin-beam population N_+. (c) Emission rate into twin-beams for $N = 800$ atoms at $T = 20\,\mathrm{nK}$, and excess scattering strength $\Gamma = 0$ (black) to $\Gamma = 0.35\,\mathrm{s}^{-2}$ (green). Dashed lines: excess emission rate. Solid lines: total emission rate.

it still can have an effect on the dynamics. At early times, where the twin-beam mode population is still below or of the order of unity, even a slight additional population can contribute to trigger strong, stimulated emission, and thus shift its onset in time significantly.

- We have neglected any thermal population of both the source state and the twin-beam modes. For the source state, an estimation following a modified Yang-Yang theory as described in ref. [165], yields ~ 3.2 atoms in the transversely excited state at $T = 25\,\mathrm{nK}$, which, however, should be negligible compared to the population caused by the pumping. More crucially, the quasi-condensate momentum distribution, that can be estimated e.g. directly from a Fourier transform of the single-particle density matrix, eq. (2.40), or from more sophisticated numerical techniques [166] still has a finite value of $\sim 1/\mu\mathrm{m}^{-1}$ at typical twin-beam momenta $\sim 5.5\,\mu\mathrm{m}^{-1}$ and $T \sim 25\,\mathrm{nK}$. At early times some of that population is still in the transverse ground state and, hence, could contribute to premature seeding.

- As seen in fig. 5.23(a), a change in the excitation dynamics mostly causes a shift in time, but hardly affects slope and final value. So, any inaccuracy of the two-level excitation model and its fit (sec. 5.4), e.g. an underestimation of source population at early times during excitation, is likely to manifest itself in a temporal shift. The same is true for a non-thermal population of the source state due to technical noise.

As all these effects are hard to capture in terms of both theory and independent experimental characterization, we decided to introduce an additional, weak scattering channel, that spontaneously transfers atoms from the source into the twin-beam states ψ_i, with an empirically determined rate Γ. They act as an additional seed in excess of vacuum fluctuations.

Technically this is implemented as an additional term in the equation of motion for the density matrices ρ_{ij}:

$$\dot{\rho}_{ij} = -i\left\langle\left[\hat{a}_i^\dagger \hat{a}_j, \hat{H}_{\mathrm{tot}}\right]\right\rangle + \Gamma\eta_{ij}N_{\mathrm{S}}^2, \tag{5.40}$$

$$\eta_{ij} = \sqrt{f(\epsilon_i)\cdot f(\epsilon_j)}\frac{\kappa_{ij}}{\mathrm{Tr}(\kappa)} \tag{5.41}$$

where $f(\epsilon)$ is a normalized distribution function for the energy of the twin-beam modes, peaked around μ_1, and having a width of the order of the twin-beam emission rate Ω (see sec. 4.3). For typical parameters, $\sum_i \eta_{ii} \approx 0.5$, so that the resulting absolute scattering rate is $\sim \Gamma N_S^2$. If we assume $N_{\mathrm{S}} \approx N_{\mathrm{c}}$, for $\Gamma \approx 0.4\,\mathrm{s}^{-1}$ and $N = 400$, this yields a maximum scattering rate of $\lesssim 30\,\mathrm{ms}^{-1}$. Realistically, $N_{\mathrm{S}} < N_{\mathrm{c}}$ at all times, and the rate stays below that value [see fig. 5.23(c)]. Similarly to the excitation driving strength, the excess scattering value mostly shifts the emission onset time, but does not affect saturation value and slope of the emission dynamics (see fig. 5.22).

5.5.2. Emission dynamics: matching experiment and theory

With the extensions to the density matrix theory described above, we can now compare experiment and theory results on the population dynamics. Detailed experimental

data have been taken for five different excitation sequences as described in sec. 5.4: one optimized sequence that achieves near-uni efficiency, as well as rescaled excitation ramps, that transfer only a limited amount of atoms into the vibrationally excited state. All data (data set DynA) has been acquired in a single measurement session, and the same data is used for both the transverse excitation (sec. 5.4) and longitudinal emission analysis, ensuring consistency between both parts of the full description.[16]

Several input parameters to the theory are needed to obtain quantitative results, most of which are known from independent characterization:

- The total atom number N an be obtained from fluorescence images, which in turn have been calibrated using resonant absorption imaging (see sec. 3.2.4).
- As described in sec. 5.4, the transverse trapping potential (and, hence, the excess energy of the source state) is well-defined due to the extreme sensitivity of the excitation process, which would detect any deviation from the expected potential.
- The longitudinal confinement frequency is known from sloshing measurements (see sec. 3.2.2). The excellent agreement of the long-time twin-beam oscillation period (see sec. 5.5.3) to theory corroborates the value obtained by this method.
- The temperature T of the source cloud can be roughly estimated from fits, which is however challenging at the low temperatures and atom numbers used in the experiment; even more so, as the shape of the source cloud drastically changes during emission (see sec. 5.6).
- From the fits of the effective source state population 5.4.3, the excitation parameters Ω, δ, t_0 needed as input to eq. (5.39) are known within the approximation of the transverse two-state model.
- The excess scattering parameter Γ, which has been introduced ad hoc into our theory to effectively cancel some of its limitations, is inherently inaccessible to direct measurements.

Hence, Γ and, within certain limits, T are left as free parameters of the theory. As explained above, the effects of those quantities are rather independent of each other; while Γ shifts the emission onset, T can adjust the saturation value and slope of the emission curve. For fitting the theory to experimental data, it has been enforced, that both T and Γ are consistent among all of the different excitation sequences, which is justified, as all experimental data has been taken in interleaved order during a single measurement session. Apart from the modifications introduced in the previous section, the simulation now follows the technique detailed in sec. 4.4, where we use a basis set of 41 Hartree-Fock potential eigenstates [eq. (4.36)] at energies ϵ_i' centered around μ_1.

In fig. 5.24, experimental results for the relative twin-beam population N_+/N are shown with their standard errors, obtained from typically 12 realizations at each of the recorded times. For the weakest (set I), strongest (set V) and optimal (set IV) excitation sequences, good theory agreement (solid lines) is reached for $T = 25\,\mathrm{nK}$,

[16] Data set DynB (curves B-I and B-II in sec. 5.4) is not analyzed in this section, as it has been taken in another measurement session with higher atom numbers, and somewhat worse stability.

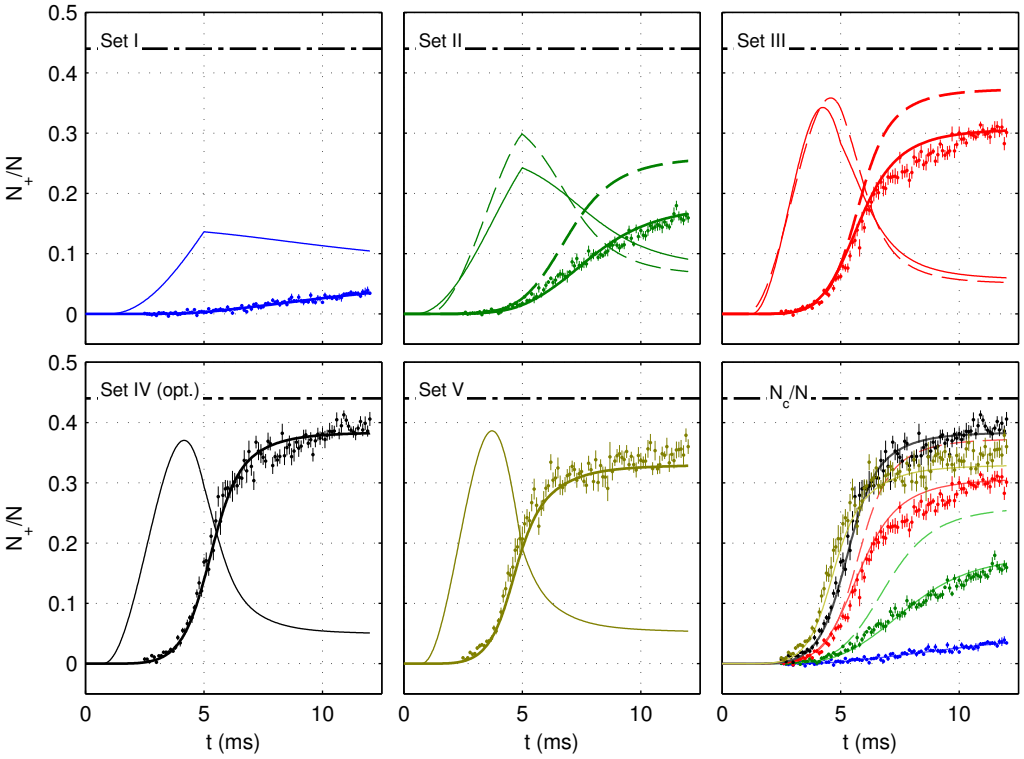

Figure 5.24.: Population of twin beams for different excitation sequences. Dots with error bars: experimental results for N_+/N Thick solid lines: theory curves obtained from the modified density matrix model. Thin solid lines: population of source state N_S assumed for the simulations. Dashed lines: theory curves for data sets II and III obtained from directly using the fitted excitation dynamics. Dash-dotted line: relative population of the PO mode. The last panel shows all excitation curves for easy comparison.

and $\Gamma = 0.4\,\mathrm{s}^{-1}$, and the excitation parameters obtained from fitting the transverse momentum dynamics (sec. 5.4.3). At this temperature and an atom number of 800, the population of the PO mode is $N_\mathrm{c}/N \approx 0.44$, setting an upper limit to the fraction of emitted atoms within our model. It is observed that for the strongest excitation (set V), the onset of emission is faster, than for the optimal excitation (set IV), but the saturation value is lower, due to the smaller population of the source state at the end of the excitation. Furthermore, even for optimal excitation, the emitted fraction does not reach the maximum possible value of N_c/N, which is similar to the observation for the unmodified density matrix model (fig. 4.4) and likely due to the decreasing overlap between source and twin beams.

However, for the intermediate sequences (II and III), using the the directly obtained excitation parameters led to poor agreement (green and red dashed lines). We attribute this to the extreme sensitivity on details of the excitation, if the system is just on the verge of strong stimulated emission. For this case, the accuracy of the transverse two-level approximation might not be sufficient. To be able to still apply our theory, we left the excitation parameters as free parameters for fitting curves II and III (keeping T and Γ fixed). Such, we could obtain results that match the experiment well, but still have excitation curves not too different from the directly fitted ones, further underlining the extreme sensitivity of the emission on a precise knowledge of the excitation.

5.5.3. Twin-beam momentum and long-time behavior

Apart from the twin-beam population, the single-particle density matrix ρ_{ij} also directly allows to infer distribution functions, by invoking eq. (4.38). Apart from density and momentum distribution, it is also possible to obtain the distribution functions for the intermediate case of long, but finite expansion time, similarly to the expansion of multi-mode quasi-condensates, eq. (2.43). As discussed in sec. 5.1, on a large momentum scale the obtained density profiles almost correspond to momentum distributions. However, a small deviation due to the real space distribution is still present, for the case of twin beams mostly because of the finite propagation length of the wave packets while still being trapped. At $t = 10\,\mathrm{ms}$ the real-space peaks are already at $13\,\mu\mathrm{m}$ distance from the trap center, which adds to the time-of-flight position of the peaks according to their momentum. We can account for this by directly calculating the time-of-flight distribution from $\rho_{ij}(t)$ as in eq. (2.43). Using momentum wave functions $\tilde{\psi}(k)$ (4.38), this reads:

$$
\begin{aligned}
n(x, t; t_\mathrm{tof}) &= \sum_{i,j} \psi_i^*(x; t_\mathrm{tof}) \psi_j(x; t_\mathrm{tof}) \rho_{ij}(t), \qquad (5.42)\\
\psi_i(x; t_\mathrm{tof}) &= \int \tilde{\psi}_i(k) e^{i[kx - \hbar k^2 t_\mathrm{tof}/(2m)]} \mathrm{d}k \\
&\approx \int \tilde{\psi}_i \left(\frac{mx}{\hbar t_\mathrm{tof}} + \kappa \right) e^{-i \frac{\hbar t_\mathrm{tof}}{m} \kappa^2} \mathrm{d}\kappa.
\end{aligned}
$$

In the last line the exponent has been expanded around its maximum at $k = \frac{mx}{\hbar t_\mathrm{tof}}$, where the contribution to the integral is the largest due to the oscillations of the

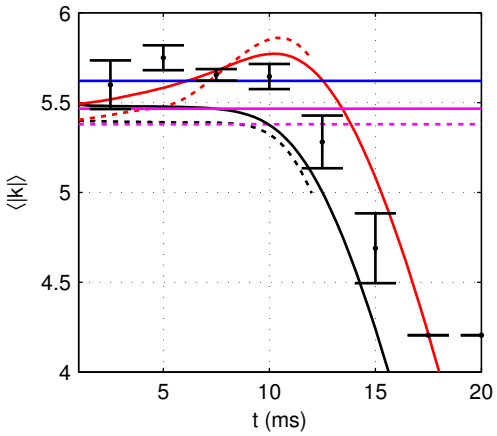

Figure 5.25.: Twin-beam momenta vs time. Solid black line: absolute momentum expectation value of twin beams (410 atoms). Solid red line: twin-beam position after 46 ms time-of-flight, normalized to $\hbar t_{\mathrm{tof}}/m$. Black dots: experimental three-peak fit results for data set Long (410 atoms). Dotted lines: analogously for 800 atoms. Magenta lines: expected initial momentum $\sqrt{2m\epsilon_{\mathrm{S}}}$, including mean field shift for 410 (800) atoms following eq. (4.20). Blue line: expected initial momentum without mean field shift $\sqrt{2mh\nu_1}$.

exponential at higher $|\kappa|$.[17] Note, that inserting the definition of $\tilde{\psi}(k)$ [eq. (4.38)] into the equation would again recover the Green's integral for free motion for the in-situ real space function $\psi(x)$ [again, as in eq. (2.43)]. In fig. 5.25, the expectation value for the longitudinal momentum (black), and the spatial position (red) of the twin beams is shown for short times and the parameters considered below. The initial twin-beam momentum corresponds well to what is expected from the transverse level spacing and the mean field of the source cloud (magenta), see sec. 4.3.

In fig. 5.26, longitudinal time-of-flight and in-situ distributions $n(x,t;t_{\mathrm{tof}})$, $n(x,t)$ are shown and compared to an experimental data set (Long), where the spatial dynamics have been measured to longer times. In comparison to the data shown earlier, the atom number is reduced further ($N \approx 410$) to minimize inelastic scattering with the central cloud, and also to achieve a lower temperature. The experimental in-situ distribution has been obtained by taking absorption images along the y-direction at a short expansion time of 1 ms. Qualitatively, both in-situ and time-of-flight distributions agree to the theory. However, as both still include the source cloud, quantitative comparison is difficult. Also, secondary scattering leads to thermalization with the transversely excited source cloud, which mostly reside in the higher thermal states of the quasi-condensate, as the PO mode has been depleted. This manifests itself in an increasing broadening of both twin-beams and source. As seen from panel (e), the oscillation frequency of in-situ ($\nu_{\mathrm{is}} = 15.2(14)\,\mathrm{Hz}$) and time-of-flight ($\nu_{\mathrm{tof}} = 15.7(8)\,\mathrm{Hz}$) data agree to the theory value of $\nu_{\mathrm{t}} = 15.86(2)\,\mathrm{Hz}$, even though there is a slight phase

[17] For states with a momentum wave function that is only slowly changing on a scale $\delta k \gg \sqrt{m/(\hbar t_{\mathrm{tof}})}$, this restores the far field limit $n(x,t;t_{\mathrm{tof}}) \propto n(k,t)$. However, the single-particle twin-beam eigenstates do *not* fulfill this criterion, as they have rapid oscillations in momentum space due to their spatial offset.

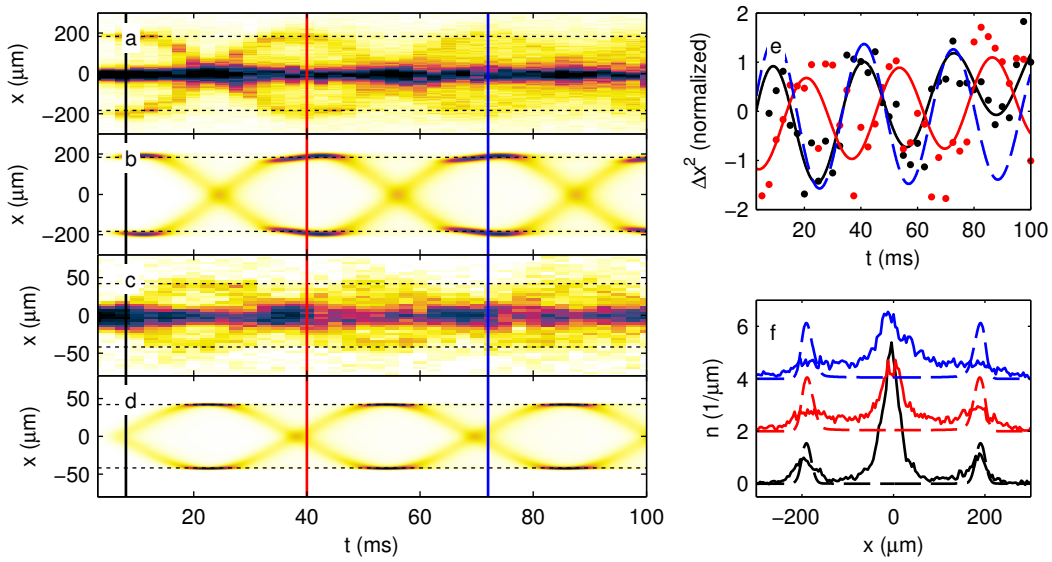

Figure 5.26.: Twin beam spatial dynamics, data set Long (410 atoms). (a), (b), (f) Time-of-flight distributions in analogy to fig. 5.27. (c) In-situ density distribution measured by absorption imaging 1 ms after trap switch-off. (e) Normalized density distribution variance. Black, solid: time-of-flight experimental data. Blue, dashed: time-of-flight theory data. Red, solid: in-situ experimental data.

mismatch (for time-of-flight data) of 9(6)°. This can also be observed more quantitatively in the twin-beam peak position as obtained from three-peak fits at early times (fig. 5.25). In time-of-flight images, twin-beam peaks are still clearly observed after a half and a full oscillation, even though strongly broadened in the latter case.

In fig. 5.27 a similar analysis is shown for data set DynA-IV (optimal excitation). This data set uses a larger atom number and higher temperature, and is measured with a higher time resolution for short times. It is observed, that, while the peak position of the twin beams is correctly predicted, confirming the twin-beam momentum predicted by the theory, their width is underestimated. Also, in contrast to the model which even predicts an initially increasing distance from the source cloud due to the in-situ movement of the twin-beam packets (see fig. 5.25), in the experiment it is observed, that the twin-beam peaks are even shifting to lower distances. Both effects again hint at inelastic secondary scattering processes with atoms in the transversely excited state.

5.6. Finite-temperature effects

In this section, we briefly discuss some experimental results on twin-beam emission using clouds of identical atom number, but different temperatures. As currently neither a sufficiently versatile thermometry method for the regime under study, nor a quantitative emission theory for higher temperatures are available, the discussion will remain mostly qualitative.

To prepare the initial state, the final values of the evaporation radio frequency (RF)

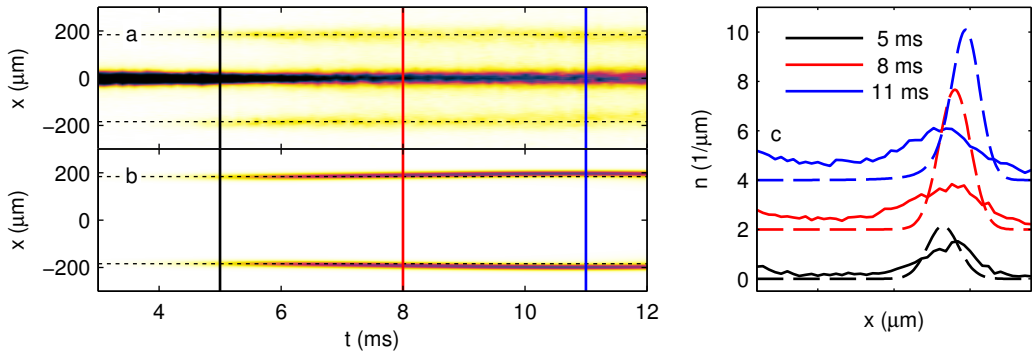

Figure 5.27.: Twin beam spatial dynamics in time-of-flight images, data set DynA-IV (800 atoms). (a) Experimentally obtained longitudinally integrated densities vs. time. (b) Corresponding theory calculation as obtained from the simulated $\rho_{ij}(t)$ and eq. (5.42). Furthermore, the imaging resolution has been accounted for by convolving with the imaging PSF (see sec. 3.2.4). (c) Longitudinal time-of-flight distribution around one of the twin-beam peaks. Solid line: experiment, dashed line: theory. Times correspond to the lines in panels (a) and (b).

ν_f has been increased from its normal value, in six steps of $0.5\,\mathrm{kHz} \approx 0.3\nu_1$ each. The resulting increase in atom number has been compensated by decreasing the power of the evaporation RF during an earlier phase (copper Z trap) of the experiment cycle, degrading the cooling efficiency and ensuring a constant atom number among the settings ($N \sim 680$). After evaporation and dressed trap preparation, the standard excitation sequence has been run.

In fig. 5.28, longitudinal profiles are shown for different times t and RF frequencies ν_f, together with an independently measured set of reference profiles without excitation. For the coldest cloud ($\nu_\mathrm{f} = 957.5\,\mathrm{kHz}$), the usual appearance of twin-beam peaks after several milliseconds is observed, as well as a broadening and inwards motion at longer times. For higher values of ν_f, the peaks become less pronounced and hidden in the (now broader) source cloud distribution, until for the highest ν_f, twin-beam emission is mostly reflected in a distinctive broadening up to the typical momentum range. In qualitative agreement to the assumption of twin-beam emission being strongly dependent on the coherence (and hence, thermal) properties of the source (sec. 5.5), the effect of twin-beam emission is much weaker here. In fig. 5.29(a,b), two observables readily available from longitudinal profiles are presented: in (a), a corrected emitted fraction $r' = (N_+ - N_+^{(0)})/N$ is shown. Here, N_+ has been counted in the usual twin beam ranges (see sec. 5.2), and corrected for the atom number $N_+^{(0)}$, which is present in that range already without any excitation and emission. For the highest value of ν_f, this value reaches $N_+^{(0)}/N = 0.1$, whereas it is negligibly small for the coldest cloud. It is observed, that the excess population in the twin-beam range grows significantly less for the initially warmer clouds than for the coldest, the latter reaching its typical value of $N_+/N \lesssim 0.4$. In (b), as a more model-independent measure, the RMS width $w = [\int n(x)x^2\mathrm{d}x/N]^{1/2}$ is shown, normalized to the width w_0 of the reference profiles (grey areas in fig. 5.28). Here, it is observed also that the impact of the excitation

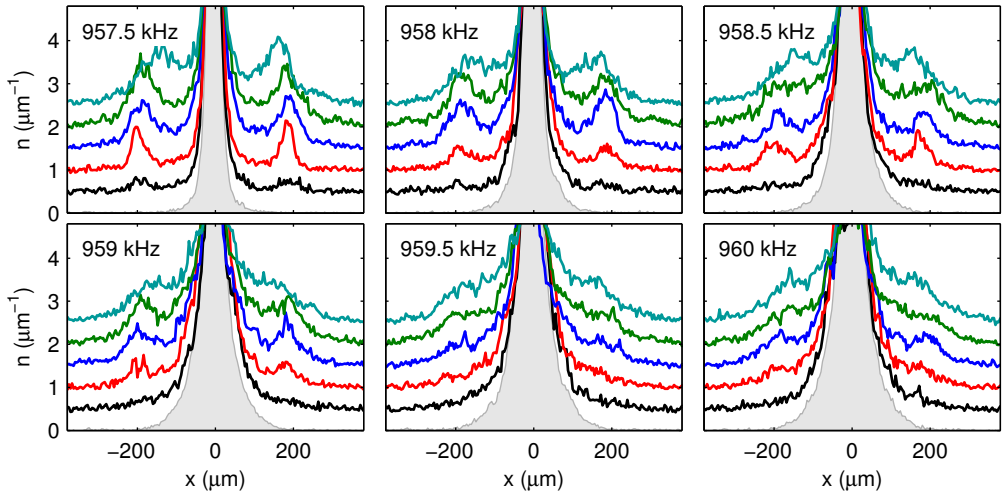

Figure 5.28.: Longitudinal time-of-flight profiles for twin-beam emission at different initial temperatures (data set VarT), as given by the final value of the RF knife (see caption of each panel). Atom number is $N \sim 680$ for all data shown. Grey areas correspond to the time-of-flight distribution of non-excited reference clouds. Colored lines (shifted by $0.5\,\mu\mathrm{m}^{-1}$ each) correspond to times $t = 4\,\mathrm{ms}$ (black), $t = 5\,\mathrm{ms}$ (red), $t = 7\,\mathrm{ms}$ (blue), $t = 10\,\mathrm{ms}$ (green), $t = 14\,\mathrm{ms}$ (cyan).

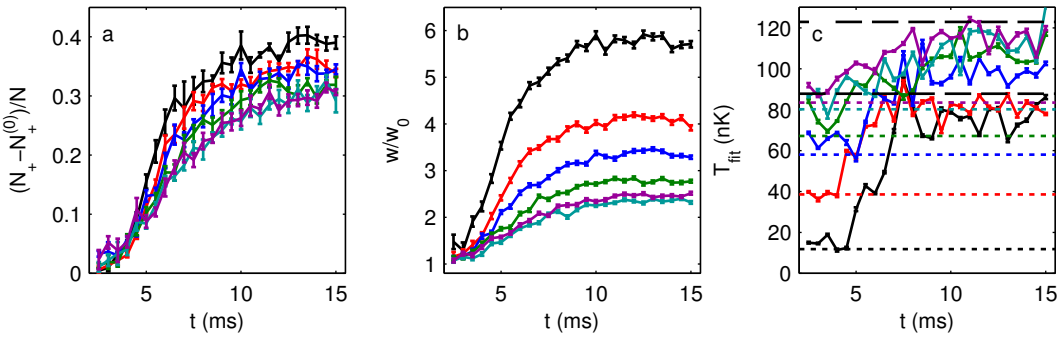

Figure 5.29.: Twin-beam emission for sources at different temperatures. Colors correspond to values $\nu_\mathrm{f} = 957.5\,\mathrm{kHz}$ (black), $\nu_\mathrm{f} = 958\,\mathrm{kHz}$ (red), $\nu_\mathrm{f} = 958.5\,\mathrm{kHz}$ (blue), $\nu_\mathrm{f} = 959\,\mathrm{kHz}$ (green), $\nu_\mathrm{f} = 959.5\,\mathrm{kHz}$ (cyan), $\nu_\mathrm{f} = 960\,\mathrm{kHz}$ (magenta). (a) Corrected emitted fraction $r' = (N_+ - N_+^{(0)})/N$ (see text). (b) RMS width of time-of-flight distributions (see fig. 5.28, normalized to values for reference measurements. (c) Temperatures obtained from fits to the center and the far-out tails of the momentum distributions. Dotted lines are values for the reference data set. Black dashed lines indicate the temperatures corresponding to the first transversely excited states.

on initially cold clouds exceeds by far the excess excitation imposed on the initially warmer clouds. An interpretation of this value as the increase of average longitudinal kinetic energy (or, in that case, its square root) is not strictly valid, as the far-field condition is not fulfilled (see sec. 5.1).

In fig. 5.29(c), approximate temperatures of non-excited source clouds for each ν_t are shown as dashed lines, which have been obtained from fitting the density distribution after expansion using a quasi-condensate model (appendix B). Note, however, that an appropriate fitting method for the entire temperature range (which actually extends beyond a quasi-condensate regime) still has to be developed, and especially for the higher temperatures, the given values should be understood merely as a very rough estimate. Furthermore, similar fits were applied to the twin-beam profiles in fig. 5.28, where the twin-beam region has been excluded from the fits and the obtained density is re-scaled to compensate for the emitted atoms. While this approach may even be less valid quantitatively than the fits to the reference clouds (e.g. given the breathing oscillations that should be excited due to the rapidly changing mean fields), it allows to qualitatively capture the rapid heating of the source cloud once the emission starts.

6. Future directions

The experiments presented in this thesis rather mark the beginning of several new research directions at the Rb-II machine. First proof-of-principle results have been obtained in the fields of both quantum atom optics, and condensate optimal control:

- We have shown, that using optimal control theory and experimental tools readily available in an atom chip experiment, it is possible to bring a condensate wave function into an exotic, vibrationally inverted state. A simple, semi-quantitative model has been developed to intuitively understand the dynamics of this process.
- It has been demonstrated, that the inverted state can be efficiently used as a source for the production of twin-atom beams by means of collisional de-excitation. Using time-of-flight fluorescence imaging, we found strong quantum correlations between the twin beams.
- The production dynamics of the twin-beams was described quantitatively, using a newly developed theoretical model.

With those results at hand, several promising directions of prospective research can be imagined; for some of those, first results have been obtained already.

Vibrational state engineering

In the context of the experiments presented above, the modulated dressed trap scheme has been developed with the goal of achieving vibrational state inversion. However, the possibilities of the method reach far beyond that, especially considering that up to now we have been using only a single degree of freedom out of many more that are readily available, such as two-dimensional motion, confinement strength modulation (up to brief repulsive periods) or rotation of the trap eigenaxes. Apart from significant interest in using the cold atom system (with the excellent control and detection means it offers) as a test bed for optimal control schemes [11], the final states themselves may open up a whole range of interesting physics [94, 251]. One may e.g. wonder, if a (transverse) GPE eigenstate exists, that is stable against collisional decay; one idea would be a two-dimensionally excited state in the yz-plane carrying angular momentum, similarly to a Laguerre mode in beam optics. An imaging system that will give access to the full transverse momentum distribution is currently being planned. Furthermore, schemes going beyond the mean-field level, e.g. for generation of entanglement [124, 125], cooling [127] or squeezed states [126] seem an exciting perspective.

Recently, using specifically developed electronics, the bandwidth of the control modulation (see secs. 3.1.5 and 5.4.1) could be increased to $\sim 100\,\mathrm{kHz}$, and bipolar ramps have been enabled. Also, other than depicted in fig. 3.2, the modulation can now be applied to the symmetric RF wires on top of the dressing current, which eliminates the residual motion along z, enabling much larger excursions of the trap without spurious excitation. In fig. 6.1, some preliminary results obtained with the new setup are shown.

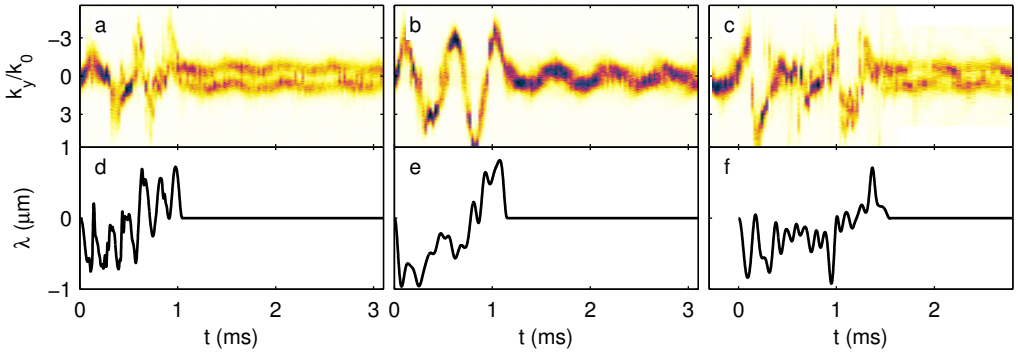

Figure 6.1.: Recent results on fast vibrational state optimal control. Top row: measured momentum distribution dynamics, bottom row: displacement $\lambda(t)$. (a,d) Fast vibrational inversion ramp, $T = 1.1\,\mathrm{ms}$. (b,e) 50/50 "beam splitter" ramp. (c,f) $\pi/2$ "Ramsey" ramp, applied 0.25 ms after 50/50 ramp. Note, that the amplitude of the ramps is larger by a factor ~ 10 compared to the previous $T = 5\,\mathrm{ms}$ inversion ramp (fig.5.13).

In contrast to the excitation sequence mostly used in this thesis (see appendix A), the control ramps $\lambda(t)$ have been obtained using a stochastic optimization (CRAB [302]) in collaboration with Antonio Negretti. Panels (a,d) shows a vibrational inversion sequence, which (using significantly higher frequencies and amplitude) achieves near-unity fidelity in just $T = 1.1\,\mathrm{ms}$, albeit with slightly increased collective oscillations in the final state. In contrast to the $T = 5\,\mathrm{ms}$ ramp used up to now, twin-beam emission during the excitation process shown in fig. 6.1 is negligible, simplifying the theoretical description considerably. Especially, it allows measuring correlations in the regime of very weakly populated twin beams ($N_+ \ll N_S$), where the Bogoliuov description (sec. 4.3) remains valid, and strongly non-classical second-order correlations are expected (sec. 5.3.4).

In panels (b,e), another fast sequence is presented, which is optimized to prepare a state with equal projections on ground and excited state, similar to a superposition state in a non-interacting system. As in the scaled ramps in sec. 5.4.2, strong beating peaks are visible. Panels (c,d) show a pulse, which can act on the state created by (b,e) in a phase-sensitive manner, where the final outcome state depends on the phase of the beating pattern, completing a sequence similar to a Ramsey or Mach-Zehnder interferometer, but acting on a mean-field wave function. This last pulse is a first step towards a different class of optimal control schemes, that implement evolution operators instead of state transfers [11, 107, 296].

Designing correlations

Up to now, correlation measurements with twin-atoms in motional states have either operated in the regime of multi-mode scattering with weak populations and a distinct spatial correlation structure [73–75], or with few strongly populated modes [64, 67, 68] having a rather fixed structure imposed by the specific production process. However, to employ schemes such as time-based entanglement [303, 304], or higher-order interference [30, 89], it would be desirable to have more control over the mode structure of

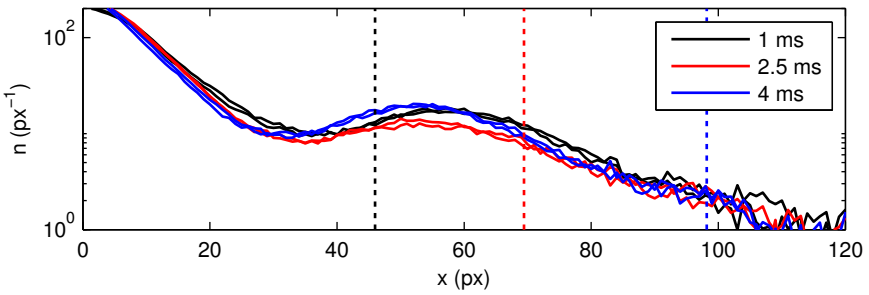

Figure 6.2.: Averaged longitudinal profiles of clouds after chirped emission (with parts at $x < 0$ mirrored). Numbers in legend correspond to the chirp time t_c. Dashed lines correspond to momenta k_0, $\sqrt{\nu_0/\nu_1}k_0$, and $\sqrt{2\nu_0/\nu_1}k_0$.

the emitted twin beams, without going to an unrestricted multi-mode situation. Also the relation between number squeezing, entanglement, and correlation functions in a controlled multi-mode system would be of theoretical interest [293]. In our experiment, one way of doing so would be to prepare more complex transverse source states with multiple decay channels, which inadvertently happened in one data set (Sqz), and indeed produced structured spatial correlations (fig. 5.11). Considering the recent progress in transverse state control (see above), this seems a promising scheme.

Another approach that has already been implemented, is to invert the condensate using the fast excitation pulse [fig. 6.1(a,d)], and then chirp the transverse level spacings in a (transversely) near-adiabatic way, by decreasing the dressing strength (fig. 3.11). This corresponds to steadily going left from the green lines in fig. 3.11, continuously shifting the parameters of the emission process as introduced in chapter 4. Specifically, the source excess energy ϵ_S follows the level spacing, yielding a time-dependent energy profile of the amplification process. Obviously, the dynamics of the process gets much more complex: For example, there is a competition between stimulated emission into the modes populated in the beginning, and emission near the momentary point of highest coupling, and it is not trivial to estimate the maximum rate of change at which stimulated emission can persist at all. Still, the problem seems tractable in Bogoliubov approximation.

In fig. 6.2, averaged longitudinal profiles are shown. Total emission time after fast excitation [as in fig. 6.1(a)] was 5 ms in all cases, with a linear chirp of the trap to zero dressing, i.e. degenerate transverse level spacings of $\nu_0 = 4.1$ kHz. The chirp was done during the first phase t_c of the emission time, as given in the figure. It can be observed that the twin beam peaks lie somewhere between the limits given by the energies $\sim \nu_1$ and $\sim \nu_0$, where the fastest chirp (black line) has its peak shifted the furthest towards higher momenta. Interestingly, overall emission is the weakest for the *intermediate* chirp time (red line), suggesting, that on its time scale the stimulated emission process is affected the most by the continuously changing situation. In all sets, significant residual population is found at momenta corresponding to energies $\sim 2\nu_0$, indicating that other relaxation channels are open, either due to non-adiabaticity of the chirp, or the finally degenerate level spacings allowing higher-order processes.

The intuitive notion, that the kinetic energy of each atom pair within the twin beams is correlated (and encodes the emission time) appears to be corroborated

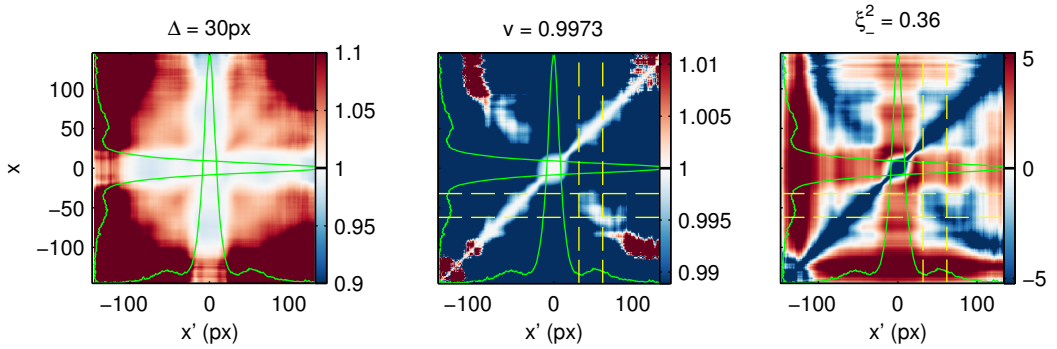

Figure 6.3.: Correlations in the chirped cloud for 2.5 ms hold time (red line in fig. 6.2), shown in a way similar to fig. 5.10.

by first experiments. In fig. 6.3 it can be observed, that in the longitudinally resolved correlations v and ξ^2_- (see sec. 5.3.5), structures on the anti-diagonal appear. For the latter, it remains to be investigated, to which extent this is determined by technical fluctuations (see footnote on pg. 104), or actual non-local squeezing. The high values of $g^{(2)}$ near the outer edges indicate strong shot-to-shot fluctuations in the outer regions. Note the high value of the relative second-order correlation (left) $v = g^{(2)}(x,x')/[g^{(2)}(x,x)g^{(2)}(x',x')]^{1/2}$ (Cauchy-Schwarz violation) near $x \lesssim 100\,\mathrm{px}$, corresponding to emission with energy $\sim 2\nu_0$; again indicating that higher-order vibrational de-excitation is occuring.

Modifying the transverse levels along specifically optimized paths (possibly even using non-adiabatic schemes), together with a sufficient understanding of the creation dynamics might allow to design the structure of the second-order correlations between the twin beams. One objection here is, that this kind of correlations will appear in momentum space only, and the relatively short expansion time in our experiment will impose a blur due to the finite initial size of the cloud. This may be less of a concern for matter-wave optics elements operating in actual momentum space, as will be sketched next.

Twin-beam optics

Now that a source of twin-atom beams is available, the logical next step would be to perform actual matter-wave quantum optics experiments with it, as sketched in sec. 1.1. Many schemes to construct linear optics elements for matter waves, such as mirrors and beam splitters are known [15, 259]. The most important tools necessary to build e.g. a Mach-Zehnder setup with our twin-beam source would be mirrors to reflect the twin-beam packets back towards each other, beam splitters to mix them, and some means to shift their relative phase. In this case, one could e.g. implement a twin-Fock state interferometer [80, 81], essentially an external-state equivalent of the internal-state experiment presented in ref. [70]. Probing continuous-variable entanglement of the twin-beams [71, 91] could possibly be performed along the lines of ref. [92]. Also, a combination of such schemes with controlled creation of multi-mode beams (see previous paragraph) would be of high interest, addressing fundamental questions on

entanglement in a many-mode system.

The most obvious solution for a simple reflection would be to leave the twin beams trapped, and have them propagate back towards each other, such as in the data shown in fig. 5.26. However, this is hindered by the presence of the residual source cloud in its strongly non-equilibrium state, the interaction of which with the twin beams is not yet understood. As becomes clear from the red line in fig. 5.26(f), even after the first half-oscillation the twin-beam peaks become strongly smeared out. Attempts to selectively remove the source cloud, e.g. using a microwave transition to the $F = 2$ hyperfine manifold (where the discrete transverse levels show up as side bands) had only limited success so far. Even if the source cloud could be disposed, a longitudinal in-situ beam-splitter is not readily available in our experiment; schemes implementing a simple central barrier (as in ref. [52]) might be possible, however.

An alternative way to achieve recombination of the twin-beam packets would be to run only the production sequence in the trap, and then perform all further operations during expansion of the cloud. In this case, one could use a pair of far-detuned laser beams along x as a Bragg grating [305, 306], to perform momentum-sensitive manipulations, before the cloud is detected in the light sheet. The recoil momentum of e.g. a Nd-YAG laser ($\lambda = 1064\,\mathrm{nm}$, $\frac{2\pi}{\lambda} = 5.9\,\mu\mathrm{m}^{-1} \approx k_0$) could mirror and recombine twin-beam packets using a simple standing wave, if a slightly increased twin-beam momentum is produced. Using a slight detuning between the beams would allow to resolve the momentum distribution of the gas [189, 190], and specifically, removing the source cloud, which is localized near $k_\mathrm{x} = 0$. Also, the mode properties of the twin-beams themselves could be studied in more detail. While a suitable laser is available in the lab, practical integration of Bragg beams in the experiment will require some major rearrangements of optics around the vacuum chamber, due to optical access becoming more and more scarce. Also, the presence of the reflecting atom chip surface might give rise to stray light issues.

Amplification using a multi-mode source

In the main theoretical model of this thesis – the density matrix expansion – the problem of the multi-mode nature of the quasi-condensate source has been dealt with in a rather radical way, by effectively reducing the description to a single mode with reduced atom number. While this worked satisfactory at the level of the twin-beam population dynamics (though necessitating the ad-hoc parameter Γ to account for the omission of other modes), correlation properties of the twin beams may be strongly affected [293]. At the current stage, this is acceptable, as the density matrix theory makes no statement about higher-order correlations anyway. For future theory developments, be it in the direction of a higher-order density matrix expansion, a number-conserving version of the linearized Bogoliubov approach, or stochastic methods, the multi-mode source will almost with certainty become an important, and potentially interesting, issue. The most promising approach might be, to couple the emission calculation to a numerical result for the initial system [166, 175, 307, 308].

On the experimental side, finite-temperature measurements, which are at a rather preliminary stage still (see sec. 5.6) will have to be taken in a more systematic way, and with sufficient statistics to allow for correlation measurements. Even more urgently, a more reliable and consistent thermometry technique than that given in appendix B

will have to be found.

Probing thermalization with high-momentum atoms

One of the most intriguing theoretical aspects of the one-dimensional Bose gas is the integrability of the Lieb-Liniger model, eq. (2.31) [159], which in principle should preclude the relaxation of such a system from non-equilibrium to a thermal state. Indeed, for the case of a strongly interacting gas ($\gamma \gg 1$, see sec. 2.4.1) a persistent "Newton's cradle" state has been observed [298]. The dynamics of thermalization in the weakly interacting case has been a major subject of experimental [199, 255] and theoretical [261, 299–301] study in our group. The twin-atom system is in a well-defined, strongly out-of-equlibirium state, and observing its thermalization (or absence thereof on accessible time scales) would be an excellent scheme to probe the involved relaxation mechanisms.[1] Apart from the momentum distribution, also the dynamics of the non-classical correlations present in the initial state should give deep insight into the process.

Again, the problem here is the remaining source cloud, impeding a proper one-dimensional description. Other than removing the source cloud somehow (see above), a way around this could be to perform a very weak excitation only, which places only few atoms in the transverse state and the twin-beams. One might also consider constructing an optimal control for a transient population of transverse states only (not dissimilar to a low-efficiency version of the "Ramsey"-scheme in fig. 6.1). While such a system would not be as far from equilibrium as the pure twin-beam states, the high sensitivity of the light sheet imaging should still make it possible to observe the ultimate fate of the twin-beam packets.

[1] In earlier experiments, where population of transverse states (and their decay) was caused by technical noise, indeed a persisting non-thermal distribution was found [216], which however has not been investigated further, yet.

Appendices

A. Optimization of the excitation ramp

The excitation trajectory used for pumping the condensate into the first excited GPE state (sometimes referred to as nonlinear coherent mode [94, 309]) has been derived using an optimal control theory [11, 95, 96] algorithm, which will briefly be described here. The explanation closely follows that given in refs. [114, 206].

In contrast to the rest of this thesis, only dimensionless coordinates will be used in this section, which are matched with the typical scales of the problem, defining $\hbar \equiv 1\,\mu\mathrm{m} \equiv m \equiv 1$.[1] Furthermore, as compared to eq. (5.27), we will define all wavefunctions in a fixed frame, and normalize them to one instead of the atom number N, which leads to an interaction constant $\kappa \equiv g_{\mathrm{y}} N$. The transverse Gross-Pitaevskii equation [equivalent to eq. (5.27)] then reads

$$i\frac{\partial\phi(y,t)}{\partial t} = \left(-\frac{1}{2}\frac{\partial^2}{\partial y^2} + V_\lambda(y,t) + \kappa\,|\phi(y,t)|^2\right)\phi(y,t)\,. \tag{A.1}$$

The anharmonic confinement potential is now moving as $V_\lambda(y,t) = V_6(y-\lambda(t),0)$ (see secs. 3.2.1, and 3.2.2). The objective of the control problem can now be formulated as follows. Let λ_0 be the control parameter at the initial time $t = 0$, and λ_1 the control parameter at the final time $t = T$ of the control process. Likewise, we denote the initial ground state of the GPE with $\phi_0'(y)$. The *desired* final wave function is the first excited state of the GPE $\phi_1'(y)$. The OCT algorithm then seeks for the optimal time variation of $\lambda(t)$ that brings the final wave function as close as possible to ϕ_1'.

To gauge the success of the excitation process for a given control field $\lambda(t)$, we define a cost function

$$J(\phi(T),\lambda) = \frac{1}{2}\left[1 - \left|\langle\phi_1'|\phi(T)\rangle\right|^2\right] + \frac{\gamma}{2}\int_0^T \left[\dot{\lambda}(t)\right]^2 \mathrm{d}t\,. \tag{A.2}$$

The first term of the cost function becomes minimal when the final wave function precisely matches the desired wave function, apart from a global (irrelevant) phase. The second term favors smooth control fields and is needed to make the OCT problem well posed [310]. γ is a parameter that weights the relative importance of the two control objectives of smooth control fields and of wave function matching. As our experimental implementation allows fast and precise control of $\lambda(t)$ (see sec. 3.2.1), the parameter γ can be set such that the control penalization is always much smaller than the first term in eq. (A.2). OCT is now seeking for an "optimal control" that minimizes the cost function $J(\phi(T),\lambda)$, under the condition that the final wave function $\phi(T)$ has to be obtained from the Gross-Pitaevskii equation of Eq. (A.1) with the initial wave function $\phi_0'(y)$. There exists a multitude of approaches to perform the optimization (see e.g. ref. [11] for a recent review). For the vibrational inversion problem, we use a (deterministic) Lagrangian framework, in contrast to the stochastic methods [99, 302, 311] which were used for some more recent experiments (sec. 6).

[1] It follows, that times are measured in units of 1.37 ms, and energies in units of $\hbar \cdot (1.37\,\mathrm{ms})^{-1} = h \cdot 116\,\mathrm{Hz}$.

In this approach, to turn the constrained minimization problem into an unconstrained one, one introduces a Lagrange function [11]:

$$L(\phi, p, \lambda) = J(\phi, \lambda) + \Re \int_0^T \left\langle p \middle| i\frac{\partial \phi}{\partial t} - \left(-\frac{1}{2}\frac{\partial^2}{\partial y^2} + V_\lambda(y,t) + \kappa\,|\phi|^2 \right) \phi \right\rangle \mathrm{d}t\,, \quad \text{(A.3)}$$

where the adjoint function $p(y,t)$ acts as a generalized Lagrange parameter. Here and in the following we will, for the sake of brevity, often omit parameters y and t. At the minimum of $J(\phi,\lambda)$ the Lagrange function has a saddle point, where all three derivatives $\delta L/\delta\psi$, $\delta L/\delta p$ and $\delta L/\delta\lambda$ must vanish. Performing the usual functional derivatives, we obtain after some variational calculation the following *optimality system*:

$$i\frac{\partial \phi}{\partial t} = \left(-\frac{1}{2}\frac{\partial^2}{\partial y^2} + V_\lambda + \kappa|\phi|^2 \right) \phi \quad \text{(A.4a)}$$

$$i\frac{\partial p}{\partial t} = \left(-\frac{1}{2}\frac{\partial^2}{\partial y^2} + V_\lambda + 2\kappa|\phi|^2 \right) p + g\,\phi^2\,p^* \quad \text{(A.4b)}$$

$$\gamma\ddot{\lambda} = -\Re\langle\phi|\frac{\partial V_\lambda}{\partial \lambda}|p\rangle\,, \quad \text{(A.4c)}$$

which has to be solved together with the initial condition $\phi(0) = \phi_0'$, as well as with the constraints on the control field $\lambda(0) = \lambda_0$ and $\lambda(T) = \lambda_1$. To obtain the equation for the adjoint function p, we have performed an integration by parts for the term involving the time derivative of ϕ prior to working out the functional derivative $\delta L/\delta\phi$. This procedure gives, in addition to eq. (A.4b), the terminal condition

$$ip(y,T) = -\langle\phi_1'|\phi(T)\rangle\,\phi_1'(y)\,. \quad \text{(A.5)}$$

Quite generally, the Lagrange parameter determines the sensitivity of the system with respect to the external control. In our case, the dynamic equation (A.4b) describes the propagation of fluctuations around the Gross-Pitaevskii solution and has the same form as a Bogoliubov-de Gennes equation (2.21).

In most cases of interest it is impossible to guess $\lambda(t)$ such that eqs. (A.4a–c) are fulfilled simultaneously, and one has to employ a numerical solution scheme. Suppose that $\lambda(t)$ is some guess for a viable control field. We can now solve Eq. (A.4a) forward in time to obtain the final wave function $\phi(T)$, which, in turn, allows us to compute the adjoint function $p(T)$ from eq. (A.5). In the ensuing step, the time evolution of $p(t)$ is solved backwards in time. Since $\lambda(t)$ is not the optimal control, eq. (A.4c) is no longer fulfilled. However, the functional derivative

$$\frac{\delta L}{\delta \lambda} = -\gamma\ddot{\lambda} - \Re\langle\phi|\frac{\partial V_\lambda}{\partial \lambda}|p\rangle \quad \text{(A.6)}$$

provides us with a search direction for $\lambda(t)$. Adding a fraction of $\delta L/\delta\lambda$ to $\lambda(t)$ leads to a control that performs better and brings the final wave function $\phi(T)$ closer to the desired one. The improved control field is then used in the next iteration. In our simulations we typically perform a time discretization of the interval $[0,T]$ and use a generic optimization routine, such as the nonlinear conjugate gradient [312, 313] or a quasi-Newton method, together with eq. (A.6) for computing the appropriate search

directions. One shortcoming of Eq. (A.6) is that in general $\delta L/\delta\lambda$ does not vanish at the boundary points of the time interval, although the control field is fixed to the values of λ_0 and λ_1 there. To overcome this problem, one rewrites the penalization term of the control field $(\gamma/2)\left(\dot{\lambda},\dot{\lambda}\right)_{\mathrm{L}^2}$ as $(\gamma/2)\left(\lambda,\lambda\right)_{\mathrm{H}^1}$, where the definition of the H^1 inner product is $(u,v)_{\mathrm{H}^1}=(\dot{u},\dot{v})_{\mathrm{L}^2}$ [295]. It is important to realize that this different norm does neither affect the value of the cost function nor the Gross-Pitaevskii or adjoint equations. However, it does affect the equation for the control field in case of a non-optimal $\lambda(t)$, which now satisfies a Poisson equation

$$-\frac{\mathrm{d}^2}{\mathrm{d}t^2}\frac{\delta L}{\delta\lambda}=-\gamma\frac{\mathrm{d}^2\lambda}{\mathrm{d}t^2}-\Re\langle\psi|\frac{\partial V_\lambda}{\partial\lambda}|p\rangle\,. \tag{A.7}$$

The advantages of Eq. (A.7) are that the boundary conditions for $\lambda(t)$ are automatically fulfilled and that changes due to large values of the second term on the right-hand side are distributed, through the solution of the Poisson equation, over the whole time interval. In all our OCT calculations we use Eq. (A.7) instead of Eq. (A.6).

Our OCT implementation relies on a numerical optimization routine and a differential equation solver. As for the optimization routine, one can use any generic code that, starting from some initial guess for the control field, requires a function value (the cost function) together with the derivative of the evaluated function $\delta L/\delta\lambda$ to compute a new, improved $\lambda(t)$. When using the H^1 norm of eq. (A.7) one must ensure that all inner products in the generic code are evaluated as $(u,v)_{\mathrm{H}^1}$ rather than $(u,v)_{\mathrm{L}^2}$. In general we observed the best performance for the quasi-Newton BFGS optimization [314], which outperforms the nonlinear conjugate gradient method for larger number of iterations in the optimization loop. As for the differential equation solver, we usually employ a split operator technique [114] because of its robustness and simplicity.

With increasing iterations, the cost function $J(\phi,\lambda)$ and the derivative measure $|\delta L/\delta\lambda|$ decrease. Note that the "optimal control" corresponds to a minimum of the control landscape, associated with a derivative equal to zero, but it is generally not guaranteed that also the cost is small there. However, there are indications that under quite broad conditions the OCT loop will come up with a $\lambda(t)$ that fulfills the control objective of wave function matching almost perfectly [315]. In our simulations we typically stop after a given number of iterations or when the derivative has become sufficiently small. The resulting $\lambda(t)$ sequence, as shown e.g. in fig. 5.1(b), is then called the optimal control. With the control we closely match the desired wave function at the terminal time, with a fidelity of $|\langle\phi_1'|\phi(T)\rangle|^2\approx 1-3\cdot 10^{-3}$. Up to a global phase, the wave function remains stationary for $t>T$.

B. Fits of finite-temperaure data

An obvious prerequisite for a more quantitative analysis of the temperature dependence of emission dynamics as in sec. 5.6 is a reliable and accurate thermometry method for the regime under consideration. For our case, which is characterized by low temperatures and unusually low atom numbers, methods developed in previous works on thermometry in one-dimensional Bose gases [153, 165, 166, 202, 307, 308] fail. Due to the low temperature and chemical potential, there is little population of transversely excited states (~ 100 atoms even for the warmest clouds), which would allow fitting a thermal cloud around the source [202]. Measuring density-density correlations after intermediate expansion times [153, 216] would necessitate higher temperatures and densities; for the coldest clouds, characteristic density ripples, from which temperatures can be inferred, are hardly present. On the other hand, at higher temperatures, the quasi-condensate regime, in which this method is valid, is left. Focusing techniques as used in various experiments to reveal the momentum distribution of the gas [165, 166] will be challenging to implement due to the poor control of longitudinal confinement in our experiment (sec. 3.2.1). Once temperatures get large enough to make the deviation of the in-situ density profile discernible from a Thomas-Fermi parabola, a fit of a Yang-Yang model [183] could be used [165]. However, such in-situ images have poor signal-to-noise ratio due to the low atom number and distortions due to the adjacent chip surface [224], impeding a sufficiently precise measurement.

Developing a truly appropriate thermometry technique for our situation is beyond the scope of this thesis. To still obtain a very coarse estimate to the temperature range of the analyzed data, we deduce an approximation to the finite-temperature time-of-flight distribution as seen in light sheet imaging. We proceed by combining an in-situ density profile $n_{\mathrm{YY}}(x; N, T)$ as obtained from solving the Yang-Yang integral equations [183] with a simple estimation of the momentum distribution of a quasi-condensate. For a homogeneous one-dimensional Bose gas in the quasi-condensate regime (i.e., having suppressed density fluctuations), the expression for the exponentially decaying first-order correlation function leads to a Lorentzian momentum distribution [see eq. (2.36)]:

$$\tilde{n}(k; n, T) = \mathcal{F}[g^{(1)}(\delta x)] = \frac{\lambda_{\mathrm{T}}/\pi}{1 + \lambda_{\mathrm{T}}^2 k^2}, \qquad \lambda_{\mathrm{T}} = \frac{2\hbar^2 n}{m k_{\mathrm{B}} T}. \tag{B.1}$$

Using the local density approximation (LDA), we can average $\tilde{n}(k)$ over the initial density $n_{\mathrm{YY}}(T, N, x)$ and directly account for the broadening due to finite expansion time:

$$n(x; t_{\mathrm{tof}}) \propto \int n(x - x') \cdot \tilde{n}\left(\frac{m x'}{\hbar t}\right) \mathrm{d}x'. \tag{B.2}$$

Additionally, population of transversely excited states is accounted for as thermal gases with chemical potential shifted by the appropriate transverse energy, which expand freely and are added on top of the density distribution [165].

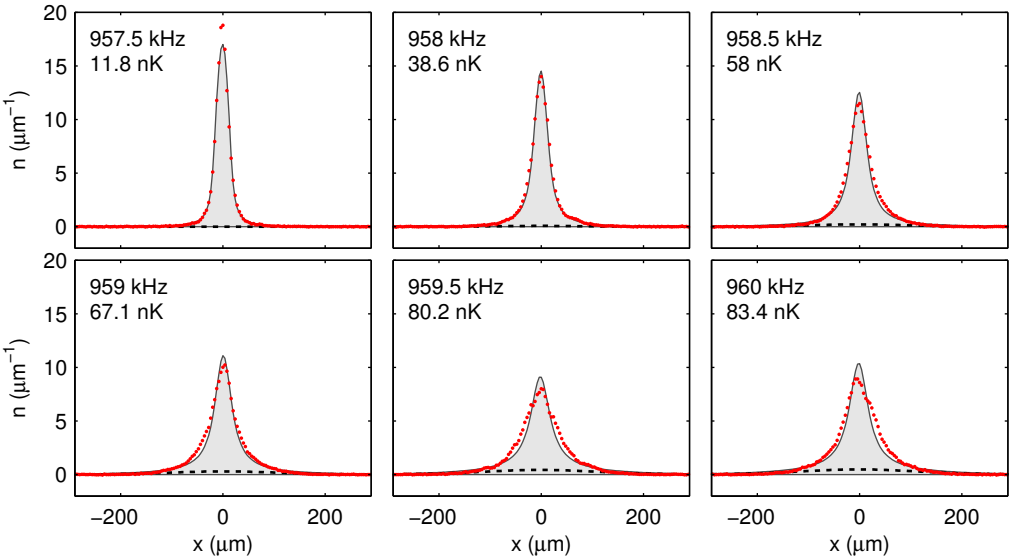

Figure B.1.: Fits of the model explained in the text to time-of-flight longitudinal profiles of non-excited reference clouds, which have been prepared in the same way as those in sec. 5.6. Dotted lines are the contribution from thermally populated higher transverse states. The given values correspond to dotted lines in fig. 5.29(d).

This strategy is somewhat inconsistent, as in regions, where the Yang-Yang profile actually deviates from an inverted parabola (arising from a quasi-condensate equation of state), the quasi-condensate theory is obviously not applicable anymore. However it gave more reasonable results compared to a direct propagation of a quasi-condensate density matrix (fig. 2.2). Still, the agreement with experimental data as shown in fig. B.1 is rather poor and does not warrant any truly quantitative interpretation.

C. Shot-noise rejection in correlation functions

Two-dimensional averaged function To exclude the shot noise peak in the two-dimensional (2d) averaged density correlation functions $\tilde{g}^{(2)}(\delta x, \delta y)$, a region with $|\delta y|, |\delta x| \leq r_{\mathrm{sn}}$ (yellow box in fig. C.1(a) and yellow dotted lines in fig. 5.7) is replaced by interpolated values. As outlined in sec. 5.3, this strategy relies on the function being slowly changing along the δy axis, and factorizing the correlation function within the region affected by shot noise into functions, that depend only on δx and δy, respectively. The basic protocol is performed as follows (note, that $1\,\mathrm{px} \approx 4\,\mu\mathrm{m}$):

- As a source for interpolation, a "stripe" along the longitudinal axis $\tilde{g}^{(2)}_{\mathrm{int}}(\delta x)$ is extracted from averaging the (normalized) correlation function transversely over regions directly adjacent to shot noise, $r_{\mathrm{sn}} < |\delta y| \leq r_{\mathrm{int}}$ (vertical green dashed lines in fig. 5.7). It is assumed, that up to a scalar factor, the δx-dependence of $\tilde{g}^{(2)}$ in that range matches that in the range $\delta y \leq r_{\mathrm{sn}}$. A trade-off between the validity of this assumption and noise in $\tilde{g}^{(2)}_{\mathrm{int}}(\delta x)$ has to be made when determining the range r_{int}. Depending on the transverse correlation behavior, r_{int} can extend up to ~ 4 pixels beyond r_{sn} without distorting the result.

- To interpolate the region with $\delta y \leq r_{\mathrm{sn}}$, $\tilde{g}^{(2)}_{\mathrm{int}}(\delta x)$ is scaled to account for the slow transverse variation of $g^{(2)}$, with a scaling factor $F(\delta y)$ that is dependent on the transverse offset. This factor is found by minimizing the mean square deviation $\langle[\tilde{g}^{(2)}(\delta x, \delta y) - F(\delta y)\tilde{g}^{(2)}_{\mathrm{int}}(\delta x)]^2\rangle$, taken over a domain $|\delta y| \leq r_{\mathrm{int}}$, and $r_{\mathrm{sn}} < |\delta x| \leq r_{\mathrm{fit}}$.[1] That means, that the scaling of the interpolation source function at position δy is determined from a range that lies outside (but close to) the shot noise region *longitudinally* (horizontal green dashed lines in fig. 5.7). Similarly to r_{int}, values of $r_{\mathrm{fit}} \sim r_{\mathrm{sn}} + 4\,\mathrm{px}$ lead to satisfying results. For data with little noise (e.g. high atom numbers or many experimental runs), the optimization can be run independently for each pixel along δy. However, especially when calculating the correlation between weakly populated twin beams in sec. 5.3, it is helpful to require some smoothness of the function $F(\delta y)$, e.g. by adding a term $\propto \langle[\partial/\partial(\delta y)F(\delta y)]^2\rangle$ to the cost function that penalizes discontinuities.

- Finally, we can estimate the second-order correlation function using:

$$g^{(2)}(\delta x, \delta y) = \begin{cases} F(\delta y)\tilde{g}^{(2)}_{\mathrm{int}}(\delta x) & : \delta x \leq r_{\mathrm{sn}} \wedge \delta y \leq r_{\mathrm{sn}} \\ \tilde{g}^{(2)}(\delta x, \delta y) & : \text{otherwise} \end{cases}, \tag{C.1}$$

$$G^{(2)}(\delta x, \delta y) = g^{(2)}(\delta x, \delta y)/\tilde{g}^{(2)}(\delta x, \delta y) \cdot \tilde{G}^{(2)}(\delta x, \delta y) \tag{C.2}$$

  i.e., by applying an interpolated "patch" on the region affected by atom shot noise. The residuum of the interpolation in the central region corresponds to

[1] While in principle a fit up to $|\delta y| \leq r_{\mathrm{sn}}$ would suffice, extending the range slightly simplifies ensuring consistency at the boundaries of the shot noise region.

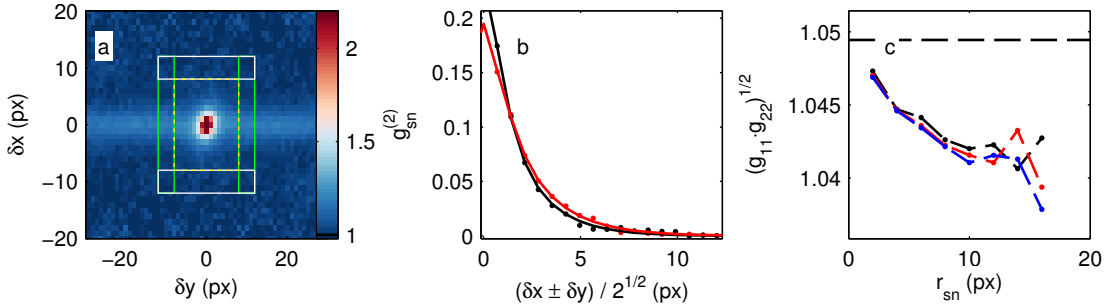

Figure C.1.: Shot noise rejection, data set Corr-III. (a) Two-dimensional averaged $\tilde{g}^{(2)}_{\mathrm{cl}}(\delta x, \delta y)$ between twin beams, same data as in fig. 5.8(a). Yellow dotted box: shot noise range. Green boxes: interpolation source range $r_{\mathrm{sn}} < |\delta y| \leq r_{\mathrm{int}}$. White boxes: fitting range $r_{\mathrm{sn}} < |\delta x| \leq r_{\mathrm{fit}}$. (b) Points: shot noise peak (difference between original and interpolated function), summed diagonally, i.e., along the eigen-axes of the light sheet. Lines: fits as described in the text. In this plot, the central pixel (including detection noise) has a value of ~ 0.75. (c) Dependence of full twin-beam auto-correlation $(g^{(2)}_{11} g^{(2)}_{22})^{1/2}$ on r_{sn} for $r_{\mathrm{int}} = 2\,\mathrm{px}$ (black), 4 px (red), 6 px (blue). The dashed line indicates $g^{(2)}_{12}$.

the shot noise peak $g^{(2)}_{\mathrm{sn}}(\delta x, \delta y) \approx \tilde{g}^{(2)}(\delta x, \delta y) - g^{(2)}_{\mathrm{int}}(\delta x, \delta y)$, see fig. C.1(b) and fig. 5.7(d). It has an elliptical shape with eigen-axes that are rotated by 45° with respect to the trap axes, due to the geometry of the light sheet illumination (see sec. 3.2.4).

In the ideal one-dimensional case, where only a single transverse mode is occupied and eq. (5.17) holds, this technique gives a fully correct result, and $F \equiv 1$. This is not completely valid under experimental circumstances, e.g. when calculating the correlations in the entire images, which contain both twin beams and source, or if position fluctuations occur. Still, $F(\delta y)$ usually varies slowly enough to allow for finding a set of parameters $r_{\mathrm{sn}}, r_{\mathrm{fit}}, r_{\mathrm{int}}$ that leads to a function which is insensitive to small changes of these parameters, and varies smoothly in both directions.

For the estimation of the detection noise $\Delta_{\mathrm{n}}\hat{S}^2$ as described in sec. 5.3.4, we can fit a two-dimensional peak function to the obtained shot noise $g^{(2)}_{\mathrm{sn}}(\delta x, \delta y)$, excluding the central pixel. Comparing various peak shapes it was found that a generic product of Gaussian and Lorentzian distributions of the form $a \cdot \exp[-\delta x^2/(2w_x^2) - \delta y^2/(2w_y^2)]/[1 + \delta x^2/u_x^2 + \delta y^2/u_y^2]$ models the data well. Using the fit coefficient a, we can write:

$$\Delta_{\mathrm{n}}\hat{S}^2 = [\tilde{g}^{(2)}_{\mathrm{sn}}(0,0) - a] \cdot C^{(2)}(0,0).$$

with $C^{(2)}(\delta x, \delta y)$ as defined in eq. (5.19).

Longitudinally averaged function Obtaining the longitudinally resolved function $G^{(2)}(x, x')$ from the non-corrected $\tilde{G}^{(2)}(x, x', \delta y)$ relies on connecting to the results found in the previous section. To this end it is convenient to parametrize the transversely averaged functions such as $G^{(2)}(x, x', \delta y)$ as $G^{(2)}(x_+, \delta x, \delta y) \equiv G^{(2)}(x \equiv$

$(x_+ + \delta x)/2, x' \equiv (x_+ - \delta x)/2, \delta y)$. We start by defining:

$$\tilde{G}^{(2)}(x_+, \delta x, \delta y) = g_{\mathrm{sn}}^{(2)}(x_+, \delta x, \delta y) \cdot C^{(2)}(x_+, \delta x, \delta y) + G^{(2)}(x_+, \delta x, \delta y) \tag{C.3}$$

$$g_{\mathrm{sn}}^{(2)}(x_+, \delta x, \delta y) \equiv \frac{N \cdot F(x_+, \delta x, \delta y)}{N(x_+/2)} g_{\mathrm{sn}}^{(2)}(\delta x, \delta y). \tag{C.4}$$

As the shot noise peak in the normalized functions is expected to scale with $N(x_+/2)^{-1}$ while retaining its shape, the function $F(x_+, \delta x, \delta y)$ should ideally be a constant. Furthermore, we can require the relation:

$$\sum_{x_+} G^{(2)}(x_+, \delta x, \delta y) = G^{(2)}(\delta x, \delta y) \tag{C.5}$$

to be fulfilled, where $G^{(2)}(\delta x, \delta y)$ is known from eq. (C.2).

For the data shown in this thesis, we take the simplest possible approach and set $F(x_+, \delta x, \delta y) \equiv F_0$, where F_0 is obtained from minimizing $\sum_{\delta x, \delta y} P(\delta x, \delta y)^2$ with

$$P(\delta x, \delta y) = G^{(2)}(\delta x, \delta y) - \sum_{x_+} \Big[\tilde{G}^{(2)}(x_+, \delta x, \delta y) - \frac{N \cdot F_0}{N(x_+/2)} g_{\mathrm{sn}}^{(2)}(\delta x, \delta y) \cdot C^{(2)}(x_+, \delta x, \delta y) \Big], \tag{C.6}$$

where the central pixel (which is affected by detection noise) has to be excluded. Detection noise is finally corrected similarly to eq. 3.11 by subtracting $\delta(\delta x, \delta y) \cdot (2mN(x_+/2) + \Delta\hat{b}^2)/m^2$ from $G^{(2)}(x_+, \delta x, \delta y)$, where the background variance $\Delta\hat{b}^2$ for one full transverse pixel row has to be used.

The values for $g_{\mathrm{tb}} - 1$ xfrom summing over appropriate regions differ from those obtained by specifically fitting the shot noise in the twin-beam regions (as described above) by typically $\sim 5\%$, leading to a mismatch of $\sim 15\%$ in $v - 1$. Within the qualitative discussion in sec. 5.3.5 this may be acceptable, however, quantitative conclusions will require a more involved scheme, where the requirement of a constant F_0 is lifted. One possible approach to do so would be consider various ranges of x_+ separately, and using appropriately determined functions for $g_{\mathrm{tb}}^{(2)}(\delta x, \delta y)$, respectively.

D. Publications

The following publications are related to this thesis:

- R. Bücker, T. Berrada, S. van Frank, J.-F. Schaff, T. Schumm, J. Schmiedmayer, G. Jäger, J. Grond, and U. Hohenester. *Vibrational state inversion of a Bose-Einstein condensate: optimal control and state tomography.* arXiv:1212.4173, (accepted for publication in Journal of Physics B, special issue *20th Anniversary of Quantum State Engineering*).

- R. Bücker, U. Hohenester, T. Berrada, S. van Frank, A. Perrin, S. Manz, T. Betz, J. Grond, T. Schumm, and J. Schmiedmayer. *Dynamics of parametric matter-wave amplification.* Physical Review A 86 (2012): 013638.

- A. Perrin, R. Bücker, S. Manz, T. Betz, C. Koller, T. Plisson, T. Schumm, and J. Schmiedmayer. *Hanbury Brown and Twiss correlations across the Bose–Einstein condensation threshold.* Nature Physics 8 (2012): 195.

- R. Bücker, J. Grond, S. Manz, T. Berrada, T. Betz, C. Koller, U. Hohenester, T. Schumm, A. Perrin, and J. Schmiedmayer. *Twin-atom beams.* Nature Physics 7 (2011): 608.

- T. Betz, S. Manz, R. Bücker, T. Berrada, C. Koller, G. Kazakov, I. Mazets, H.-P. Stimming, A. Perrin, T. Schumm, and J. Schmiedmayer *Two-Point Phase Correlations of a One-Dimensional Bosonic Josephson Junction.* Physical Review Letters 106 (2011): 020407.

- T. Schumm, S. Manz, R. Bücker, D. A. Smith, and J. Schmiedmayer. *Interferometry with Bose-Einstein Condensates on Atom Chips.* In: Atom Chips, edited by J. Reichel and V. Vuletić, 211–264. Wiley-VCH Verlag GmbH & Co. KGaA, 2011.

- S. Manz, R. Bücker, T. Betz, Ch. Koller, S. Hofferberth, I. E. Mazets, A. Imambekov, E. Demler, A. Perrin, J. Schmiedmayer, and T. Schumm *Two-point density correlations of quasicondensates in free expansion.* Physical Review A 81 (2010): 031610.

- R. Bücker, A. Perrin, S. Manz, T. Betz, C. Koller, T. Plisson, J. Rottmann, T. Schumm, and J. Schmiedmayer. *Single-particle-sensitive imaging of freely propagating ultracold atoms.* New Journal of Physics 11 (2009): 103039.

- W. Rohringer, R. Bücker, S. Manz, T. Betz, C. Koller, M. Göbel, A. Perrin, J. Schmiedmayer, and T. Schumm. *Stochastic optimization of a cold atom experiment using a genetic algorithm.* Applied Physics Letters 93 (2008): 26410.

E. List of symbols

	Physical constants
h	Planck constant (6.63×10^{-26} Js)
$\hbar$	Reduced Planck constant (1.06×10^{-26} Js)
k_B	Boltzmann constant (1.38×10^{-23} J/K)
μ_B	Bohr magneton (9.27×10^{-28} J/T)
m	Mass of a ^{87}Rb atom (1.44×10^{-25} kg)
a_s	Scattering length of ^{87}Rb in $F = 1$ (5.31×10^{-9} m)
	Lengths and momenta
λ_dB	Thermal de Broglie wave length
λ_T	Quasi-condensate coherence length
l_ϕ	Quasi-condensate phase correlation length
ξ_h	Healing (correlation) length
R	Thomas-Fermi radius
l_i	Harmonic oscillator length along i-th direction
$l_\perp$	Transverse oscillator length
k_0	Peak twin beam momentum
$\lambda(t)$	Excitation trajectory
$x_\mathrm{min}, x_\mathrm{max}$	Edges of counting regions for twin beams in time of flight
$K, K_\mathrm{t}, K_\mathrm{r}$	Transverse center-of-mass momenta: source, twin-beams, and relative
Y_0, K_0, α	Origin of co-oscillating frame along y in two-level model (sec. 5.4.3)
	Energies/frequencies and coupling constants
μ	Chemical potential (general)
$\mu_0, \mu(x)$	Global and local chemical potential in LDA
μ_1	Global chemical potential of condensate in vibrational inversion
$\mu_\mathrm{e}, \mu_\mathrm{g}$	Chemical potentials of transverse two-level model (sec. 5.4.2)
ω_i	Trap (angular) frequency along i-th direction
ω_h	Geometrically averaged trap (angular) frequency
$\bar{\omega}$	Arithmetically averaged trap (angular) frequency
$\omega_\perp$	Mean transverse trap (angular) frequency
ϵ_S	Source excess/twin beam peak kinetic energy
ϵ_i	Total (chapter 2)/kinetic (chapter 4) energy of i-th longitudinal mode
ϵ_i'	Total energy of i-th longitudinal mode (chapter 4)
E_nm	Energy of n-th/m-th single-particle transverse state along y/z, respectively
ν_x, ν_y, ν_z	Frequency of harmonic contribution to trapping potentials
$\sigma_{y,z}, \xi_{y,z}$	Quartic and sixth-order contributions to trapping potentials
$\nu_i, \nu_i^{(z)}$	i-th transverse potential level spacing along y or z
ν_0	Level spacing of static (harmonic) trap
ν_i'	Transverse mean-field shifted level spacing
g	3d interaction constant
g_1d	Longitudinal 1d interaction constant
g_y	Transverse (along y) 1d interaction constant
κ	General mode coupling constant (relating to populations, not densities)
κ_{ij}	Coupling of longitudinal mode pair i, j to source mode S
δ	Relative detuning of twin-beam modes (sec. 4.2)

Ω	Twin-beam emission rate (chapter 4)
Δ_k, ω_k	Detuning and effective emission rate for twin-beam mode k (sec. 4.3)
Γ	Excess scattering rate for twin-beam emission model (sec. 5.5)
V	Potential (general)
V_{ext}	Trap potential (general)
V_{mag}	Static field trap potential
V_{RF}	Dressed potential
V_6	Polynomial approximation to dressed potential

Populations

N	Total atom number
N_0	Condensate (ideal)
N_{S}	Source state
N_i	Longitudinal mode i
N_{c}	Penrose-Onsager mode
N_{e}	Transversely excited state
$N_{\mathrm{L}}, N_{\mathrm{R}}$	Population in each of the twin beams
N_+	Twin-beam total population $N_{\mathrm{L}} + N_{\mathrm{R}}$
N_-	Twin-beam imbalance $N_{\mathrm{L}} - N_{\mathrm{R}}$
$\tilde{p}$	Normalized imbalance N_+/N_- (sec. 5.3.5)
$S, S_+, \ldots$	Fluorescence signal corresponding to $N, N_+, \ldots$

Wave functions and densities

$\psi_{\mathrm{TF}}(x)$	Thomas-Fermi wave function (total, or longitudinal)
$\psi_i(x), \tilde{\psi}_i(k)$	Wave function of mode i (total, or longitudinal)
$\psi_0(x)$	Condensate wave function
$\psi_{\mathrm{c}}(x)$	Wave function of Penrose-Onsager mode
$\phi_n(y), \phi_m(z)$	Wave function of n-th/m-th transverse single-particle state
$\phi'_n(y)$	Transverse GPE eigenfunction
$\phi_0^{\mathrm{MF}}(y)$	Single-particle ground state, affected by mean field in ϕ'_1
$\varphi_{\mathrm{e}}, \varphi_{\mathrm{g}}$	Transverse harmonic-oscillator wave functions (sec. 5.4.3)
α_{mn}, β_{mn}	Normalized transverse density overlaps
$n(\ldots)$	Density (general)
n_0	3d peak density
$n_{1\mathrm{d}}(x), \tilde{n}_{1\mathrm{d}}(k)$	Line density (longitudinal)
$N(x,y), S(x,y)$	Atom number/photons detected in pixel at (x,y) (sec. 5.3)

Correlation functions

$\rho(x,x'), \tilde{\rho}(k,k')$	Single-particle reduced density matrix (long.)
ρ_{ij}	Single-particle density matrix expressed in modes i,j (long.)
$\rho_{i\mathrm{S}}$	Single-particle density matrix between mode i and source mode
$\Delta_{ij} \equiv \Delta_{ij\mathrm{SS}}$	Two-particle density matrix between modes i,j and source mode
$G^{(n)}(\ldots)$	Non-normalized n-th order correlation function
$g^{(n)}(\ldots)$	Normalized n-th order correlation function
M	Anomalous density (sec. 4.3)
$\tilde{G}^{(2)}(\ldots), \tilde{g}^{(2)}(\ldots)$	Density-density correlations (non-normally ordered)
$g^{(2)}_{\mathrm{sn}}$	Shot-noise peak in density-density correlations
$\tilde{G}^{(2)}_{\mathrm{cl}}, \tilde{G}^{(2)}_{\mathrm{bb}}$	Collinear and back-to-back averaged density-density correlations
$G^{(2)}_{\mathrm{LL}}, G^{(2)}_{\mathrm{RR}}, G^{(2)}_{\mathrm{LR}}, G^{(2)}_{\mathrm{tb}}$	Second-order correlation within/between twin-beam peaks

Operators

$\hat{H}_{\mathrm{tot}}$	Total Hamiltonian (in various contexts)
$\hat{H}_{\mathrm{P}}$	Pumping Hamiltonian

$\hat{H}_0$	Single-particle Hamiltonian
$\hat{H}_\delta$	Effective quadratic Hamiltonian for excitations
$\hat{H}_{\mathrm{el}}, \hat{H}_{\mathrm{sc}}$	Elastic and inelastic scattering Hamiltonian
$\hat{H}_{\mathrm{MM}}, \hat{H}_{\mathrm{TM}}$	Multi-mode and two-mode twin-beam Hamiltonian
$\hat{\Psi}(\mathbf{r}, t)$	Total field operator
$\hat{\delta}$	Bogoliubov excitation field operator
$\hat{a}_i$	Annihilation operator for (longitudinal) field modes
$\hat{a}_{\mathrm{S}}, \hat{a}_{\mathrm{g}}$	Annihilation operators for source mode and initial ground state
$\hat{D}$	Harmonic oscillator displacement operator
	Temperatures
T	Temperature (general)
β	Inverse temperature $(\mu_{\mathrm{B}} T)^{-1}$
$T_{3\mathrm{d}}$	3d ideal gas critical
$T_{1\mathrm{d}}$	1d ideal gas critical
t	Normalized for 1d
T_{d}	1d degeneracy
T_{co}	Quasi-condensate crossover
T_ϕ	Finite-size condensate crossover
	Others
c	Speed of sound
γ	Lieb-Liniger parameter
v	Cauchy-Schwarz violation ratio
ξ_-^2	Number squeezing factor
$\tilde{\xi}_-^2$	Uncorrected number squeezing factor
$\Delta \hat{X}^2$	Variance of random variable $\hat{X}$
$\Delta_{\mathrm{b}} \hat{S}_-^2$	Binomial twin-beam imablance variance
$\Delta_{\mathrm{n}} \hat{S}_-^2$	Detection noise contribution to twin-beam imbalance variance
η	Transverse excitation efficiency, from overlap with ϕ_1'
η'	Transverse excitation efficiency, from two-level model (sec. 5.4.3)
s	Scaling factor of excitation ramp
T	Total duration of excitation ramp
$\Omega, \delta, \Omega', t_0$	Effective results of two-level driving model
J, L, p	Cost, Lagrange, and adjoint function for the OCT algorithm (appendix A)
	Experimental quantities
t_{tof}	Time of flight
ν_{L}	Larmor frequency at trap minimum
ν_{eff}	Effective trap bottom for dressed trap
ν_{f}	Final frequency of evaporation RF knife
$F, m_{\mathrm{F}}, g_{\mathrm{F}}$	Hyperfine and magnetic quantum number, Landé factor
$I_{\mathrm{t}}, I_{\mathrm{H}}, I_{\mathrm{RF}}$	Currents in trap, H, and RF wires
B_x, B_y	External offset fields (Ioffe, Bias)
$\nu_{\mathrm{RF}}, B_{\mathrm{RF}}$	Parameters of RF dressing field
Ω, Δ	Rabi frequency and detuning of RF dressing (sec. 3.2.2)
$r_{\mathrm{a}}, \tilde{r}_{\mathrm{a}}$	Typical imaging PSF, and typical radius of the PSF auto-correlation
I_{sat}	Saturation intensity
v_{r}	Recoil velocity
$\hat{b}$	Light sheet background signal
m	Average number of fluorescence photons per atom

Bibliography

[1] D. Jaksch, C. Bruder, J. I. Cirac, C. W. Gardiner, and P. Zoller. Cold Bosonic Atoms in Optical Lattices. *Physical Review Letters* 81 (1998), 3108.

[2] M. Greiner, O. Mandel, T. Esslinger, T. W. Hänsch, and I. Bloch. Quantum phase transition from a superfluid to a Mott insulator in a gas of ultracold atoms. *Nature* 415 (2002), 39.

[3] W. S. Bakr, A. Peng, M. E. Tai, R. Ma, J. Simon, J. I. Gillen, S. Fölling, L. Pollet, and M. Greiner. Probing the superfluid-to-Mott insulator transition at the single-atom level. *Science* 329 (2010), 547.

[4] J. Simon, W. S. Bakr, R. Ma, M. E. Tai, P. M. Preiss, and M. Greiner. Quantum simulation of antiferromagnetic spin chains in an optical lattice. *Nature* 472 (2011), 307.

[5] W. H. Zurek. Cosmological experiments in superfluid helium? *Nature* 317 (1985), 505.

[6] J. Anglin and W. Zurek. Vortices in the Wake of Rapid Bose-Einstein Condensation. *Physical Review Letters* 83 (1999), 1707.

[7] B. Nowak, D. Sexty, and T. Gasenzer. Superfluid turbulence: Nonthermal fixed point in an ultracold Bose gas. *Physical Review B* 84 (2011).

[8] W. Ketterle, D. S. Durfee, and D. M. Stamper-Kurn. Making, probing and understanding Bose-Einstein condensates. In *Proceedings of the 1998 Enrico Fermi summer school on Bose-Einstein condensation*, p. 90 (1999). 9904034.

[9] K. Mø lmer. Quantum atom optics with Bose-Einstein condensates. *New Journal of Physics* 5 (2003), 55.

[10] A. Heidmann, R. Horowicz, S. Reynaud, E. Giacobino, C. Fabre, and G. Camy. Observation of Quantum Noise Reduction on Twin Laser Beams. *Physical Review Letters* 59 (1987), 2555.

[11] C. Brif, R. Chakrabarti, and H. Rabitz. Control of quantum phenomena: past, present and future. *New Journal of Physics* 12 (2010), 075008.

[12] L. De Broglie. *Recherches sur la théorie des quanta.* Ph.D. thesis, Paris (1924).

[13] C. Davisson and L. Germer. Diffraction of Electrons by a Crystal of Nickel. *Physical Review* 30 (1927), 705.

[14] I. Estermann and O. Stern. Beugung von Molekularstrahlen. *Zeitschrift für Physik* 61 (1930), 95.

[15] A. Cronin, J. Schmiedmayer, and D. Pritchard. Optics and interferometry with atoms and molecules. *Reviews of Modern Physics* 81 (2009), 1051.

[16] M.-O. Mewes, M. R. Andrews, D. M. Kurn, D. S. Durfee, C. G. Townsend, and W. Ketterle. Output coupler for Bose-Einstein condensed atoms. *Physical Review Letters* 78 (1997), 582.

[17] I. Bloch, T. W. Hänsch, and T. Esslinger. An atom laser with a cw output coupler. *Physical Review Letters* 82 (1999), 3008.

[18] M. R. Andrews, C. G. Townsend, H.-J. Miesner, D. S. Durfee, D. M. Kurn, and W. Ketterle. Observation of interference between two Bose condensates. *Science* 275 (1997), 637.

[19] Y. Castin and J. Dalibard. Relative phase of two Bose-Einstein condensates. *Physical Review A* 55 (1997), 4330.

[20] Y. Shin, M. Saba, T. A. Pasquini, W. Ketterle, D. E. Pritchard, and A. E. Leanhardt. Atom Interferometry with Bose-Einstin Condensates in a Double-Well Potential. *Physical Review Letters* 92 (2004), 50405.

[21] T. Schumm, S. Hofferberth, L. M. Andersson, S. Wildermuth, S. Groth, I. Bar-Joseph, J. Schmiedmayer, and P. Krüger. Matter-wave interferometry in a double well on an atom chip. *Nature Physics* 1 (2005), 57.

[22] M. Lewenstein and L. You. Quantum Phase Diffusion of a Bose-Einstein Condensate. *Physical Review Letters* 77 (1996), 3489.

[23] J. Javanainen and M. Wilkens. Phase and phase diffusion of a split Bose-Einstein condensate. *Physical Review Letters* 78 (1997), 4675.

[24] M. O. Scully and M. S. Zubairy. *Quantum Optics* (Cambridge University Press) (1997).

[25] R. Glauber. The Quantum Theory of Optical Coherence. *Physical Review* 130 (1963), 2529.

[26] J. Clauser. Experimental distinction between the quantum and classical field-theoretic predictions for the photoelectric effect. *Physical Review D* 9 (1974), 853.

[27] H. Kimble, M. Dagenais, and L. Mandel. Photon Antibunching in Resonance Fluorescence. *Physical Review Letters* 39 (1977), 691.

[28] A. Aspect, P. Grangier, and G. Roger. Experimental Tests of Realistic Local Theories via Bell's Theorem. *Physical Review Letters* 47 (1981), 460.

[29] C. K. Hong, Z. Y. Ou, and L. Mandel. Measurement of subpicosecond time intervals between two photons by interference. *Physical Review Letters* 59 (1987), 2044.

[30] J. Rarity and P. Tapster. Experimental violation of Bell's inequality based on phase and momentum. *Physical Review Letters* 64 (1990), 2495.

[31] M. D. Reid and D. F. Walls. Violations of classical inequalities in quantum optics. *Physical Review A* 34 (1986), 1260 .

[32] D. P. DiVincenzo. Quantum Computation. *Science* 270 (1995), 255.

[33] N. Gisin and R. Thew. Quantum communication. *Nature Photonics* 1 (2007), 165.

[34] C. Caves. Quantum-mechanical noise in an interferometer. *Physical Review D* 23 (1981), 1693.

[35] M. Xiao, L.-A. Wu, and H. Kimble. Precision measurement beyond the shot-noise limit. *Physical Review Letters* 59 (1987), 278.

[36] P. Grangier, R. Slusher, B. Yurke, and A. LaPorta. Squeezed-light–enhanced polarization interferometer. *Physical Review Letters* 59 (1987), 2153.

[37] M. Holland and K. Burnett. Interferometric detection of optical phase shifts at the Heisenberg limit. *Physical Review Letters* 71 (1993), 1355.

[38] H. Kimble, Y. Levin, A. Matsko, K. Thorne, and S. Vyatchanin. Conversion of conventional gravitational-wave interferometers into quantum nondemolition interferometers by modifying their input and/or output optics. *Physical Review D* 65 (2001), 022002.

[39] J. Abadie and Others. A gravitational wave observatory operating beyond the quantum shot-noise limit. *Nature Physics* 7 (2011), 962.

[40] M. Naraschewski and R. Glauber. Spatial coherence and density correlations of trapped Bose gases. *Physical Review A* 59 (1999), 4595.

[41] A. Öttl, S. Ritter, M. Köhl, and T. Esslinger. Correlations and Counting Statistics of an Atom Laser. *Physical Review Letters* 95 (2005), 90404.

[42] M. Schellekens, R. Hoppeler, A. Perrin, J. V. Gomes, D. Boiron, A. Aspect, and C. I. Westbrook. Hanbury Brown Twiss effect for ultracold quantum gases. *Science* 310 (2005), 648.

[43] A. Perrin, R. Bücker, S. Manz, T. Betz, C. Koller, T. Plisson, T. Schumm, and J. Schmiedmayer. Hanbury Brown and Twiss correlations across the Bose–Einstein condensation threshold. *Nature Physics* 8 (2012), 195.

[44] M. Kitagawa and M. Ueda. Squeezed spin states. *Physical Review A* 47 (1993), 5138.

[45] D. Wineland, J. Bollinger, W. Itano, and D. Heinzen. Squeezed atomic states and projection noise in spectroscopy. *Physical Review A* 50 (1994), 67.

[46] A. Sorensen, L.-M. Duan, J. I. Cirac, and P. Zoller. Many-particle entanglement with Bose-Einstein condensates. *Nature* 409 (2001), 63.

[47] C. Gross. Spin squeezing, entanglement and quantum metrology with Bose-Einstein condensates (2012). 1203.5359.

[48] C. Gross, T. Zibold, E. Nicklas, J. Estève, and M. K. Oberthaler. Nonlinear atom interferometer surpasses classical precision limit. *Nature* 464 (2010), 1165.

[49] M. F. Riedel, P. Böhi, Y. Li, T. W. Hänsch, A. Sinatra, and P. Treutlein. Atom-chip-based generation of entanglement for quantum metrology. *Nature* 464 (2010), 1170.

[50] C. Orzel, A. K. Tuchman, M. L. Fenselau, M. Yasuda, and M. A. Kasevich. Squeezed states in a Bose-Einstein condensate. *Science* 291 (2001), 2386.

[51] J. Esteve, C. Gross, A. Weller, S. Giovanazzi, and M. K. Oberthaler. Squeezing and entanglement in a Bose-Einstein condensate. *Nature* 455 (2008), 1216.

[52] K. Maussang, G. Marti, T. Schneider, P. Treutlein, Y. Li, A. Sinatra, R. Long, J. Estève, and J. Reichel. Enhanced and Reduced Atom Number Fluctuations in a BEC Splitter. *Physical Review Letters* 105 (2010), 080403.

[53] J. Hald, J. L. Sø rensen, C. Schori, and E. S. Polzik. Spin Squeezed Atoms: A Macroscopic Entangled Ensemble Created by Light. *Physical Review Letters* 83 (1999), 1319.

[54] I. D. Leroux, M. H. Schleier-Smith, and V. Vuletić. Implementation of Cavity Squeezing of a Collective Atomic Spin. *Physical Review Letters* 104 (2010).

[55] M. H. Schleier-Smith, I. D. Leroux, and V. Vuletić. States of an Ensemble of Two-Level Atoms with Reduced Quantum Uncertainty. *Physical Review Letters* 104 (2010), 073604.

[56] C. D. Hamley, C. S. Gerving, T. M. Hoang, E. M. Bookjans, and M. S. Chapman. Spin-nematic squeezed vacuum in a quantum gas. *Nature Physics* 8 (2012), 305.

[57] D. F. Walls and G. J. Milburn. *Quantum Optics, 2nd Edition* (Springer) (2007).

[58] S. Dürr, T. Volz, and G. Rempe. Dissociation of ultracold molecules with Feshbach resonances. *Physical Review A* 70 (2004), 031601.

[59] M. Greiner, C. A. Regal, J. T. Stewart, and D. S. Jin. Probing Pair-Correlated Fermionic Atoms through Correlations in Atom Shot Noise. *Physical Review Letters* 94 (2005), 110401.

[60] K. V. Kheruntsyan, M. K. Olsen, and P. D. Drummond. Einstein-Podolsky-Rosen Correlations via Dissociation of a Molecular Bose-Einstein Condensate. *Physical Review Letters* 95 (2005), 150405.

[61] L. Deng, E. W. Hagley, J. Wen, M. Trippenbach, Y. Band, P. S. Julienne, J. E. Simsarian, K. Helmerson, S. L. Rolston, and W. D. Phillips. Four-wave mixing with matter waves. *Nature* 398 (1999), 218.

[62] J. Vogels, K. Xu, and W. Ketterle. Generation of Macroscopic Pair-Correlated Atomic Beams by Four-Wave Mixing in Bose-Einstein Condensates. *Physical Review Letters* 89 (2002), 020401.

[63] R. G. Dall, L. J. Byron, A. G. Truscott, G. R. Dennis, M. T. Johnsson, and J. J. Hope. Paired-atom laser beams created via four-wave mixing. *Physical Review A* 79 (2009), 011601.

[64] W. RuGway, S. Hodgman, R. Dall, M. Johnson, and A. Truscott. Correlations in Amplified Four-Wave Mixing of Matter Waves. *Physical Review Letters* 107 (2011), 075301.

[65] N. Gemelke, E. Sarajlic, Y. Bidel, S. Hong, and S. Chu. Parametric Amplification of Matter Waves in Periodically Translated Optical Lattices. *Physical Review Letters* 95 (2005), 170404.

[66] K. Hilligsø e and K. Mø lmer. Phase-matched four wave mixing and quantum beam splitting of matter waves in a periodic potential. *Physical Review A* 71 (2005).

[67] G. K. Campbell, J. Mun, M. Boyd, E. W. Streed, W. Ketterle, and D. E. Pritchard. Parametric Amplification of Scattered Atom Pairs. *Physical Review Letters* 96 (2006), 020406.

[68] M. Bonneau, J. Ruaudel, R. Lopes, J.-C. Jaskula, A. Aspect, D. Boiron, and C. I. Westbrook. A tunable source of correlated atom beams (2012). 1212.6315.

[69] C. Klempt, O. Topic, G. Gebreyesus, M. Scherer, T. Henninger, P. Hyllus, W. Ertmer, L. Santos, and J. J. Arlt. Parametric Amplification of Vacuum Fluctuations in a Spinor Condensate. *Physical Review Letters* 104 (2010), 195303.

[70] B. Lücke, M. Scherer, J. Kruse, L. Pezzé, F. Deuretzbacher, P. Hyllus, O. Topic, J. Peise, W. Ertmer, J. Arlt, L. Santos, A. Smerzi, and C. Klempt. Twin matter waves for interferometry beyond the classical limit. *Science* 334 (2011), 773.

[71] C. Gross, H. Strobel, E. Nicklas, T. Zibold, N. Bar-Gill, G. Kurizki, and M. K. Oberthaler. Atomic homodyne detection of continuous-variable entangled twin-atom states. *Nature* 480 (2011), 290.

[72] E. Bookjans, C. Hamley, and M. Chapman. Strong Quantum Spin Correlations Observed in Atomic Spin Mixing. *Physical Review Letters* 107 (2011), 210406.

[73] A. Perrin, H. Chang, V. Krachmalnicoff, M. Schellekens, D. Boiron, A. Aspect, and C. Westbrook. Observation of Atom Pairs in Spontaneous Four-Wave Mixing of Two Colliding Bose-Einstein Condensates. *Physical Review Letters* 99 (2007), 150405.

[74] J.-C. Jaskula, M. Bonneau, G. Partridge, V. Krachmalnicoff, P. Deuar, K. Kheruntsyan, A. Aspect, D. Boiron, and C. Westbrook. Sub-Poissonian Number Differences in Four-Wave Mixing of Matter Waves. *Physical Review Letters* 105 (2010), 190402.

[75] V. Krachmalnicoff, J.-C. Jaskula, M. Bonneau, V. Leung, G. B. Partridge, D. Boiron, C. I. Westbrook, P. Deuar, P. Ziń, M. Trippenbach, and K. V. Kheruntsyan. Spontaneous Four-Wave Mixing of de Broglie Waves: Beyond Optics. *Physical Review Letters* 104 (2010), 150402.

[76] K. Kheruntsyan, J.-C. Jaskula, P. Deuar, M. Bonneau, G. Partridge, J. Ruaudel, R. Lopes, D. Boiron, and C. Westbrook. Violation of the Cauchy-Schwarz Inequality with Matter Waves. *Physical Review Letters* 108 (2012), 260401.

[77] I. B. Spielman, P. R. Johnson, J. H. Huckans, C. D. Fertig, S. L. Rolston, W. D. Phillips, and J. V. Porto. Collisional deexcitation in a quasi-two-dimensional degenerate bosonic gas. *Physical Review A* 73 (2006), 020702.

[78] R. Bücker, J. Grond, S. Manz, T. Berrada, T. Betz, C. Koller, U. Hohenester, T. Schumm, A. Perrin, and J. Schmiedmayer. Twin-atom beams. *Nature Physics* 7 (2011), 608.

[79] R. Campos, C. Gerry, and A. Benmoussa. Optical interferometry at the Heisenberg limit with twin Fock states and parity measurements. *Physical Review A* 68 (2003), 023810.

[80] P. Bouyer and M. Kasevich. Heisenberg-limited spectroscopy with degenerate Bose-Einstein gases. *Physical Review A* 56 (1997), R1083.

[81] J. Dunningham, K. Burnett, and S. Barnett. Interferometry below the Standard Quantum Limit with Bose-Einstein Condensates. *Physical Review Letters* 89 (2002), 150401.

[82] L. Pezzé and A. Smerzi. Entanglement, Nonlinear Dynamics, and the Heisenberg Limit. *Physical Review Letters* 102 (2009), 100401.

[83] A. Einstein, B. Podolski, and N. Rosen. Can quantum-mechanical description of physical reality considered complete? *Physical Review* 47 (1935), 777.

[84] M. Reid. Demonstration of the Einstein-Podolsky-Rosen paradox using nondegenerate parametric amplification. *Physical Review A* 40 (1989), 913.

[85] H. Pu and P. Meystre. Creating Macroscopic Atomic Einstein-Podolsky-Rosen States from Bose-Einstein Condensates. *Physical Review Letters* 85 (2000), 3987.

[86] L.-M. Duan, G. Giedke, J. I. Cirac, and P. Zoller. Inseparability Criterion for Continuous Variable Systems. *Physical Review A* 84 (2000), 2722.

[87] P. Kwiat, K. Mattle, H. Weinfurter, A. Zeilinger, A. Sergienko, and Y. Shih. New High-Intensity Source of Polarization-Entangled Photon Pairs. *Physical Review Letters* 75 (1995), 4337.

[88] M. A. Horne, A. Shimony, and A. Zeilinger. Two-particle interferometry. *Physical Review Letters* 62 (1989), 2209.

[89] J. Kofler, M. Singh, M. Ebner, M. Keller, M. Kotyrba, and A. Zeilinger. Einstein-Podolsky-Rosen correlations from colliding Bose-Einstein condensates. *Physical Review A* 86 (2012), 032115.

[90] S. L. Braunstein. Quantum information with continuous variables. *Reviews of Modern Physics* 77 (2005), 513.

[91] M. Olsen and M. Davis. Entanglement properties of degenerate four-wave mixing of matter waves in a periodic potential. *Physical Review A* 73 (2006), 063618.

[92] A. J. Ferris, M. K. Olsen, and M. J. Davis. Atomic entanglement generation and detection via degenerate four-wave mixing of a Bose-Einstein condensate in an optical lattice. *Physical Review A* 79 (2009), 43634.

[93] F. Gerbier. Quasi-1D Bose-Einstein condensates in the dimensional crossover regime. *Europhysics Letters* 66 (2004), 771.

[94] V. Yukalov, E. Yukalova, and V. Bagnato. Non-ground-state Bose-Einstein condensates of trapped atoms. *Physical Review A* 56 (1997), 4845.

[95] A. P. Peirce and M. A. Dahleh. Optimal control of quantum-mechanical systems: Existence, numerical approximation, and applications. *Physical Review A* 37 (1988), 4950.

[96] H. Rabitz. Whither the Future of Controlling Quantum Phenomena? *Science* 288 (2000), 824.

[97] T. E. Skinner, T. O. Reiss, B. Luy, N. Khaneja, and S. J. Glaser. Application of optimal control theory to the design of broadband excitation pulses for high-resolution NMR. *Journal of Magnetic Resonance* 163 (2003), 8.

[98] T. E. Skinner, T. O. Reiss, B. Luy, N. Khaneja, and S. J. Glaser. Reducing the duration of broadband excitation pulses using optimal control with limited RF amplitude. *Journal of Magnetic Resonance* 167 (2004), 68.

[99] N. Khaneja, T. Reiss, C. Kehlet, T. Schulte-Herbrüggen, and S. J. Glaser. Optimal control of coupled spin dynamics: design of NMR pulse sequences by gradient ascent algorithms. *Journal of Magnetic Resonance* 172 (2005), 296.

[100] A. Assion. Control of Chemical Reactions by Feedback-Optimized Phase-Shaped Femtosecond Laser Pulses. *Science* 282 (1998), 919.

[101] C. Tesch and R. de Vivie-Riedle. Quantum Computation with Vibrationally Excited Molecules. *Physical Review Letters* 89 (2002), 157901.

[102] G. Vasilev, A. Kuhn, and N. Vitanov. Optimum pulse shapes for stimulated Raman adiabatic passage. *Physical Review A* 80 (2009), 13417.

[103] M. Hofheinz, E. M. Weig, M. Ansmann, R. C. Bialczak, E. Lucero, M. Neeley, A. D. O'Connell, H. Wang, J. M. Martinis, and A. N. Cleland. Generation of Fock states in a superconducting quantum circuit. *Nature* 454 (2008), 310.

[104] U. Hohenester. Optimal quantum gates for semiconductor qubits. *Physical Review B* 74 (2006).

[105] S. Safaei, S. Montangero, F. Taddei, and R. Fazio. Optimized single-qubit gates for Josephson phase qubits. *Physical Review B* 79 (2009), 064524.

[106] H. Jirari, F. W. J. Hekking, and O. Buisson. Optimal control of superconducting N-level quantum systems. *Europhysics Letters* 87 (2009), 28004.

[107] P. Rebentrost and F. Wilhelm. Optimal control of a leaking qubit. *Physical Review B* 79 (2009), 060507.

[108] B. Khani, J. M. Gambetta, F. Motzoi, and F. K. Wilhelm. Optimal generation of Fock states in a weakly nonlinear oscillator. *Physica Scripta* T137 (2009), 014021.

[109] M. V. Berry. Transitionless quantum driving. *Journal of Physics A: Mathematical and Theoretical* 42 (2009), 365303.

[110] M. G. Bason, M. Viteau, N. Malossi, P. Huillery, E. Arimondo, D. Ciampini, R. Fazio, V. Giovannetti, R. Mannella, and O. Morsch. High-fidelity quantum driving. *Nature Physics* 8 (2011), 147.

[111] V. Giovannetti. The quantum speed limit. In D. Abbott, J. H. Shapiro, and Y. Yamamoto, eds., *Fluctuations and Noise in Photonics and Quantum Optics*, pp. 1–6 (Proc. SPIE 5111) (2003). 0303085.

[112] T. Caneva, M. Murphy, T. Calarco, R. Fazio, S. Montangero, V. Giovannetti, and G. E. Santoro. Optimal Control at the Quantum Speed Limit. *Physical Review Letters* 103 (2009), 240501.

[113] A. del Campo, I. L. Egusquiza, M. B. Plenio, and S. F. Huelga. Quantum speed limits in open system dynamics (2012). 1209.1737.

[114] U. Hohenester, P. K. Rekdal, A. Borzì, and J. Schmiedmayer. Optimal quantum control of Bose-Einstein condensates in magnetic microtraps. *Physical Review A* 75 (2007), 23602.

[115] A. Couvert, T. Kawalec, G. Reinaudi, and D. Guéry-Odelin. Optimal transport of ultracold atoms in the non-adiabatic regime. *Europhysics Letters* 83 (2008), 13001.

[116] G. De Chiara, T. Calarco, M. Anderlini, S. Montangero, P. Lee, B. Brown, W. Phillips, and J. Porto. Optimal control of atom transport for quantum gates in optical lattices. *Physical Review A* 77 (2008), 052333.

[117] J. G. Muga, X. Chen, A. Ruschhaupt, and D. Guéry-Odelin. Frictionless dynamics of Bose-Einstein condensates under fast trap variations. *Journal of Physics B* 42 (2009), 241001.

[118] J.-F. Schaff, X.-L. Song, P. Capuzzi, P. Vignolo, and G. Labeyrie. Shortcut to adiabaticity for an interacting Bose-Einstein condensate. *Europhysics Letters* 93 (2011), 23001.

[119] A. del Campo, A. Retzker, and M. B. Plenio. The inhomogeneous Kibble–Zurek mechanism: vortex nucleation during Bose–Einstein condensation. *New Journal of Physics* 13 (2011), 083022.

[120] J.-F. Schaff, P. Capuzzi, G. Labeyrie, and P. Vignolo. Shortcuts to adiabaticity for trapped ultracold gases. *New Journal of Physics* 13 (2011), 113017.

[121] A. del Campo and M. G. Boshier. Shortcuts to adiabaticity in a time-dependent box. *Scientific Reports* 2 (2012), 648.

[122] Y. Kagan, E. Surkov, and G. V. Shlyapnikov. Evolution of a Bose-condensed gas under variations of the confining potential. *Physical Review A* 54 (1996), R1753.

[123] Y. Castin and R. Dum. Bose-Einstein condensation in time dependent traps. *Physical Review Letters* 77 (1996), 5315.

[124] F. Platzer, F. Mintert, and A. Buchleitner. Optimal Dynamical Control of Many-Body Entanglement. *Physical Review Letters* 105 (2010), 020501.

[125] T. Caneva, T. Calarco, and S. Montangero. Entanglement-storage units. *New Journal of Physics* 14 (2012), 093041.

[126] J. Grond, J. Schmiedmayer, and U. Hohenester. Optimizing number squeezing when splitting a mesoscopic condensate. *Physical Review A* 79 (2009), 21603.

[127] A. Rahmani, T. Kitagawa, E. Demler, and C. Chamon. Cooling through optimal control of quantum evolution (2012), 5. 1210.5244.

[128] K. Huang. *Statistical Mechanics* (Wiley, New York) (1987).

[129] V. Bagnato, D. E. Pritchard, and D. Kleppner. Bose-Einstein condensation in an external potential. *Physical Review A* 35 (1987), 4354.

[130] C. J. Pethick and H. Smith. *Bose-Einstein condensation in dilute atomic gases.* (Cambridge University Press) (2002).

[131] V. Bagnato and D. Kleppner. Bose-Einstein condensation in low-dimensional traps. *Physical Review A* 44 (1991), 7439.

[132] W. Ketterle and N. van Druten. Bose-Einstein condensation of a finite number of particles trapped in one or three dimensions. *Physical Review A* 54 (1996), 656.

[133] I. Bouchoule, K. V. Kheruntsyan, and G. V. Shlyapnikov. Interaction-induced crossover versus finite-size condensation in a weakly interacting trapped one-dimensional Bose gas. *Physical Review A* 75 (2007), 31606.

[134] N. van Druten and W. Ketterle. Two-Step Condensation of the Ideal Bose Gas in Highly Anisotropic Traps. *Physical Review Letters* 79 (1997), 549.

[135] J. Armijo, T. Jacqmin, K. Kheruntsyan, and I. Bouchoule. Mapping out the quasicondensate transition through the dimensional crossover from one to three dimensions. *Physical Review A* 83 (2011), 021605(R).

[136] N. P. Proukakis and B. Jackson. Finite-temperature models of Bose–Einstein condensation. *Journal of Physics B* 41 (2008), 203002.

[137] N. N. Bogoliubov. On the theory of superfluidity. *Journal of Physics - USSR* 11 (1947), 23.

[138] F. Dalfovo, L. Pitaevskii, and S. Stringari. The condensate wave function of a trapped atomic gas. *Journal of Research of the National Institute of Standards and Technology* 101 (1996), 537.

[139] L. Salasnich, A. Parola, and L. Reatto. Effective wave equations for the dynamics of cigar-shaped and disk-shaped Bose condensates. *Physical Review A* 65 (2002).

[140] M. Edwards, R. Dodd, C. Clark, and K. Burnett. Zero-temperature, mean-field theory of atomic Bose-Einstein condensates. *Journal of Research of the National Institute of Standards and Technology* 101 (1996), 553.

[141] M. Edwards, P. A. Ruprecht, K. Burnett, R. J. Dodd, and C. W. Clark. Collective Excitations of Atomic Bose-Einstein Condensates. *Physical Review Letters* 77 (1996), 1671.

[142] D. S. Jin, M. R. Matthews, J. R. Ensher, C. E. Wieman, and E. A. Cornell. Temperature-Dependent Damping and Frequency Shifts in Collective Excitations of a Dilute Bose-Einstein Condensate. *Physical Review Letters* 78 (1997), 764.

[143] S. Stringari. Collective Excitations of a Trapped Bose-Condensed Gas. *Physical Review Letters* 77 (1996), 2360.

[144] F. Dalfovo, S. Giorgini, L. P. Pitaevskii, and S. Stringari. Theory of Bose-Einstein condensation in trapped gases. *Reviews of Modern Physics* 71 (1999), 463.

[145] J. García-Ripoll, V. Pérez-García, and V. Vekslerchik. Construction of exact solutions by spatial translations in inhomogeneous nonlinear Schrödinger equations. *Physical Review E* 64 (2001), 056602.

[146] I. Bialynicki-Birula and Z. Bialynicka-Birula. Center-of-mass motion in the many-body theory of Bose-Einstein condensates. *Physical Review A* 65 (2002), 063606.

[147] A. Aspect, P. Grangier, and G. Roger. Experimental Realization of Einstein-Podolsky-Rosen-Bohm Gedankenexperiment: A New Violation of Bell's Inequalities. *Physical Review Letters* 49 (1982), 91.

[148] A. Aspect, J. Dalibard, and G. Roger. Experimental Test of Bell's Inequalities Using Time- Varying Analyzers. *Physical Review Letters* 49 (1982), 1804.

[149] U. Titulaer and R. Glauber. Correlation Functions for Coherent Fields. *Physical Review* 140 (1965), B676.

[150] R. H. Brown and R. Q. Twiss. Correlation between photons in two coherent beams of light. *Nature* 177 (1956), 27.

[151] U. Fano. Quantum theory of interference effects in the mixing of light from phase-independent sources. *American Journal of Physics* 29 (1961), 539.

[152] T. Jeltes, J. M. McNamara, W.Hogervorst, W. Vassen, V. Krachmalnicoff, M. Schellekens, A. Perrin, H. Chang, D. Boiron, A. Aspect, and C. I. Westbrook. Comparison of Hanbury Brown-Twiss effect for bosons and fermions. *Nature* 445 (2007), 402.

[153] S. Manz, R. Bücker, T. Betz, C. Koller, S. Hofferberth, I. E. Mazets, A. Imambekov, E. Demler, A. Perrin, J. Schmiedmayer, and T. Schumm. Two-point density correlations of quasicondensates in free expansion. *Physical Review A* 81 (2010), 031610.

[154] R. Dall, S. Hodgman, A. Manning, M. Johnsson, K. Baldwin, and A. Truscott. Observation of atomic speckle and Hanbury Brown–Twiss correlations in guided matter waves. *Nature Communications* 2 (2011), 291.

[155] H. Moritz, T. Stöferle, M. Köhl, and T. Esslinger. Exciting Collective Oscillations in a Trapped 1D Gas. *Physical Review Letters* 91 (2003), 250402.

[156] T. Kinoshita, T. Wenger, and D. S. Weiss. Observation of a one-dimensional Tonks-Girardeau gas. *Science* 305 (2004), 1125.

[157] B. L. Tolra, K. M. O'Hara, J. H. Huckans, W. D. Phillips, S. L. Rolston, and J. V. Porto. Observation of reduced three-body recombination in a correlated 1D degenerate Bose gas. *Physical Review Letters* 92 (2004), 190401.

[158] B. Parades, A. Widera, V. Murg, O. Mandel, S. Fölling, I. Cirac, G. V. Shlyapnikov, T. W. Hänsch, I. Bloch, and B. Paredes. Tonks-Girardeau gas of ultracold atoms in an optical lattice. *Nature* 429 (2004), 277.

[159] E. H. Lieb and W. Liniger. Exact Analysis of an Interacting Bose Gas. I. The General Solution and the Ground State. *Physical Review* 130 (1963), 1605.

[160] E. H. Lieb. Exact Analysis of an Interacting Bose Gas. II. The Excitation Spectrum. *Physical Review* 130 (1963), 1616.

[161] C. N. Yang. Thermodynamics of a One-Dimensional System of Bosons with Repulsive Delta-Function Interaction. *Journal of Mathematical Physics* 10 (1969), 1115.

[162] D. S. Petrov, G. V. Shlyapnikov, and J. T. M. Walraven. Phase-Fluctuating 3D Bose-Einstein Condensates in Elongated Traps. *Physical Review Letters* 87 (2001), 50404.

[163] F. Gerbier, J. H. Thywissen, S. Richard, M. Hubgart, P. Bouyer, A. Aspect, and M. Hugbart. Momentum distribution and correlation function of quasicondensates in elongated traps. *Physical Review A* 67 (2003), 51602.

[164] C. Menotti and S. Stringari. Collective oscillations of a one-dimensional trapped Bose-Einstein gas. *Physical Review A* 66 (2002), 043610.

[165] A. Van Amerongen, J. Van Es, P. Wicke, K. Kheruntsyan, and N. Van Druten. Yang-Yang thermodynamics on an atom chip. *Physical Review Letters* 100 (2008), 90402.

[166] T. Jacqmin, B. Fang, T. Berrada, T. Roscilde, and I. Bouchoule. Momentum distribution of one-dimensional Bose gases at the quasicondensation crossover: Theoretical and experimental investigation. *Physical Review A* 86 (2012), 043626.

[167] E. Haller, M. J. Mark, R. Hart, J. G. Danzl, L. Reichsöllner, V. Melezhik, P. Schmelcher, and H.-C. Nägerl. Confinement-Induced Resonances in Low-Dimensional Quantum Systems. *Physical Review Letters* 104 (2010), 153203.

[168] M. Olshanii. Atomic Scattering in the Presence of an External Confinement and a Gas of Impenetrable Bosons. *Physical Review Letters* 81 (1998), 938.

[169] I. Bouchoule, N. J. van Druten, and C. I. Westbrook. Atom chips and one-dimensional Bose gases. In J. Reichel and V. Vuletić, eds., *Atom Chips*, chap. 11, pp. 331–363 (Wiley-VCH Verlag GmbH & Co. KGaA, Weinheim) (2011).

[170] K. V. Kheruntsyan, D. M. Gangardt, P. D. Drummond, and G. V. Shlyapnikov. Pair Correlations in a Finite-Temperature 1D Bose Gas. *Physical Review Letters* 91 (2003), 40403.

[171] K. V. Kheruntsyan, D. M. Gangardt, P. D. Drummond, and G. V. Shlyapnikov. Finite-temperature correlations and density profiles of an inhomogeneous interacting one-dimensional Bose gas. *Physical Review A* 71 (2005), 53615.

[172] P. Deuar, A. G. Sykes, D. M. Gangardt, M. J. Davis, P. D. Drummond, and K. V. Kheruntsyan. Nonlocal pair correlations in the one-dimensional Bose gas at finite temperature. *Physical Review A* 79 (2009), 043619.

[173] L. Mathey, A. Vishwanath, and E. Altman. Noise correlations in low-dimensional systems of ultracold atoms. *Physical Review A* 79 (2009), 013609.

[174] A. Imambekov and L. I. Glazman. Universal Theory of Nonlinear Luttinger Liquids. *Science* 323 (2009), 228.

[175] H.-P. Stimming, N. Mauser, J. Schmiedmayer, and I. Mazets. Fluctuations and Stochastic Processes in One-Dimensional Many-Body Quantum Systems. *Physical Review Letters* 105 (2010), 015301.

[176] D. Gallucci, S. P. Cockburn, and N. P. Proukakis. Phase coherence in quasicondensate experiments: an ab initio analysis via the stochastic Gross-Pitaevskii equation. *Physical Review A* 86 (2012), 013627. 1205.6075.

[177] M. Hugbart, J. A. Retter, F. Gerbier, A. F. Varón, S. Richard, J. H. Thywissen, D. Clément, P. Bouyer, and A. Aspect. Coherence length of an elongated condensate. *The European Physical Journal D* 35 (2005), 155.

[178] J. Esteve, J.-B. Trebbia, T. Schumm, A. Aspect, C. I. Westbrook, and I. Bouchoule. Observations of density fluctuations in an elongated Bose gas: ideal gas and quasi-condensate regimes. *Physical Review Letters* 96 (2006), 130403.

[179] S. Hofferberth, I. Lesanovsky, T. Schumm, A. Imambekov, V. Gritsev, E. Demler, and J. Schmiedmayer. Probing quantum and thermal noise in an interacting many-body system. *Nature Physics* 4 (2008), 489.

[180] E. Haller, M. Gustavsson, M. J. Mark, J. G. Danzl, R. Hart, G. Pupillo, and H.-C. Nägerl. Realization of an excited, strongly correlated quantum gas phase. *Science* 325 (2009), 1224.

[181] J. Armijo, T. Jacqmin, K. Kheruntsyan, and I. Bouchoule. Probing three-body correlations in a quantum gas using the measurement of the third moment of density fluctuations. *Physical Review Letters* 105 (2010), 230402. 1007.3713.

[182] T. Jacqmin, J. Armijo, T. Berrada, K. Kheruntsyan, and I. Bouchoule. Sub-Poissonian Fluctuations in a 1D Bose Gas: From the Quantum Quasicondensate to the Strongly Interacting Regime. *Physical Review Letters* 106 (2011), 230405.

[183] C. Yang. Concept of Off-Diagonal Long-Range Order and the Quantum Phases of Liquid He and of Superconductors. *Reviews of Modern Physics* 34 (1962), 694.

[184] M. Girardeau. Relationship Between Systems of Impenetrable Bosons and Fermions in One Dimension. *Journal of Mathematical Physics* 1 (1960), 516.

[185] F. D. M. Haldane. Effective harmonic-fluid approach to low-energy properties of one-dimensional quantum fluids. *Physical Review Letters* 47 (1981), 1840.

[186] N. D. Mermin and H. Wagner. Absence of Ferromagnetism or Antiferromagnetism in One- or Two-Dimensional Isotropic Heisenberg Models. *Physical Review Letters* 17 (1966), 1133.

[187] P. Hohenberg. Existence of Long-Range Order in One and Two Dimensions. *Physical Review* 158 (1967), 383.

[188] C. Mora and Y. Castin. Extension of Bogoliubov theory to quasicondensates. *Physical Review A* 67 (2003), 53615.

[189] S. Richard, F. Gerbier, J. H. Thywissen, M. Hugbart, P. Bouyer, and A. Aspect. Momentum Spectroscopy of 1D Phase Fluctuations in Bose-Einstein Condensates. *Physical Review Letters* 91 (2003), 10405.

[190] N. Fabbri, D. Clément, L. Fallani, C. Fort, and M. Inguscio. Momentum-resolved study of an array of one-dimensional strongly phase-fluctuating Bose gases. *Physical Review A* 83 (2011), 031604.

[191] D. S. Petrov, G. V. Shlyapnikov, and J. T. M. Walraven. Regimes of Quantum Degeneracy in Trapped 1D Gases. *Physical Review Letters* 85 (2000), 3745.

[192] P.-O. Löwdin. Quantum Theory of Many-Particle Systems. I. Physical Interpretations by Means of Density Matrices, Natural Spin-Orbitals, and Convergence Problems in the Method of Configurational Interaction. *Physical Review* 97 (1955), 1474.

[193] K. Sakmann, A. Streltsov, O. Alon, and L. Cederbaum. Reduced density matrices and coherence of trapped interacting bosons. *Physical Review A* 78 (2008).

[194] O. Penrose and L. Onsager. Bose-Einstein condensation and liquid helium. *Physical Review* 104 (1956), 576.

[195] S. Wildermuth, P. Krüger, C. Becker, M. Brajdic, S. Haupt, A. Kasper, R. Folman, and J. Schmiedmayer. Optimized magneto-optical trap for experiments with ultracold atoms near surfaces. *Physical Review A* 69 (2004), 030901(R).

[196] S. Wildermuth, S. Hofferberth, I. Lesanovsky, E. Haller, L. M. Andersson, S. Groth, I. Bar-Joseph, P. Krüger, and J. Schmiedmayer. Microscopic magnetic-field imaging. *Nature* 435 (2005), 440.

[197] S. Hofferberth, I. Lesanovsky, B. Fischer, J. Verdu, and J. Schmiedmayer. Radiofrequency-dressed-state potentials for neutral atoms. *Nature Physics* 2 (2006), 710.

[198] S. Hofferberth, B. Fischer, T. Schumm, J. Schmiedmayer, and I. Lesanovsky. Ultracold atoms in radio-frequency dressed potentials beyond the rotating-wave approximation. *Physical Review A* 76 (2007), 13401.

[199] S. Hofferberth, I. Lesanovsky, B. Fischer, T. Schumm, and J. Schmiedmayer. Non-equilibrium coherence dynamics in one-dimensional Bose gases. *Nature* 449 (2007), 324.

[200] M. Trinker, S. Groth, S. Haslinger, S. Manz, T. Betz, S. Schneider, I. Bar-Joseph, T. Schumm, and J. Schmiedmayer. Multilayer atom chips for versatile atom micromanipulation. *Applied Physics Letters* 92 (2008), 254102.

[201] W. Rohringer, R. Bücker, S. Manz, T. Betz, C. Koller, M. Göbel, A. Perrin, J. Schmiedmayer, and T. Schumm. Stochastic optimization of a cold atom experiment using a genetic algorithm. *Applied Physics Letters* 93 (2008), 264101.

[202] R. Bücker, A. Perrin, S. Manz, T. Betz, C. Koller, T. Plisson, J. Rottmann, T. Schumm, and J. Schmiedmayer. Single-particle-sensitive imaging of freely propagating ultracold atoms. *New Journal of Physics* 11 (2009), 103039.

[203] P. Krüger, S. Hofferberth, I. Mazets, I. Lesanovsky, and J. Schmiedmayer. Weakly Interacting Bose Gas in the One-Dimensional Limit. *Physical Review Letters* 105 (2010), 265302.

[204] T. Betz, S. Manz, R. Bücker, T. Berrada, C. Koller, G. Kazakov, I. Mazets, H.-P. Stimming, A. Perrin, T. Schumm, and J. Schmiedmayer. Two-Point Phase Correlations of a One-Dimensional Bosonic Josephson Junction. *Physical Review Letters* 106 (2011), 020407.

[205] R. Bücker, U. Hohenester, T. Berrada, S. van Frank, A. Perrin, S. Manz, T. Betz, J. Grond, T. Schumm, and J. Schmiedmayer. Dynamics of parametric matter-wave amplification. *Physical Review A* 86 (2012), 013638.

[206] R. Bücker, T. Berrada, S. van Frank, J.-F. Schaff, T. Schumm, J. Schmiedmayer, G. Jäger, J. Grond, and U. Hohenester. Vibrational state inversion of a Bose-Einstein condensate: optimal control and state tomography (2012), 27. 1212.4173.

[207] P. Krüger. *Coherent matter waves near surfaces.* Ph.D. thesis, University of Heidelberg (2004).

[208] S. Wildermuth. *One-dimensional Bose-Einstein condensates in micro-traps.* Ph.D. thesis, Univserity of Heidelberg (2005).

[209] H. Gimpel. *Magnetische Oberflächenfallen für Atom-Interferometer.* Diploma thesis, University of Heidelberg (2002).

[210] C. Becker. *Eine neuartige magneto-optische Falle für Atomchip-Experimente.* Diploma thesis, University of Heidelberg (2002).

[211] S. Haupt. *Setup of a new Experiment with ultracold 87Rb Atoms: Towards Quantum Information Processing on an Atom Chip.* Ph.D. thesis, University of Heidelberg (2003).

[212] S. Hofferberth. *Experiments with ultracold atoms and Bose-Einstein condensated in microtraps near surfaces.* Diploma thesis, University of Heidelberg (2004).

[213] T. Schumm. *Bose-Einstein condensates in magnetic double well potentials.* Ph.D. thesis, Université Paris 11 (2005).

[214] S. Hofferberth. *Coherent manipulation of Bose-Einstein condensates with radio-frequency adiabatic potentials on atom chips.* Ph.D. thesis, University of Heidelberg (2007).

[215] S. Groth. *Development, fabrication, and characterisation of atom chips.* Ph.D. thesis, University of Heidelberg (2006).

[216] S. Manz. *Density correlations of expanding one-dimensional Bose gases.* Ph.D. thesis, Vienna University of Technology (2010).

[217] T. Betz. *Phase correlations of coupled one-dimensional Bose gases.* Ph.D. thesis, Vienna University of Technology (2011).

[218] R. Bücker. *Fluorescence imaging of ultracold atoms.* Master's thesis, University of Heidelberg (2008).

[219] M. Brajdic. *Entwicklung einer Computersteuerung und ihre Anwendung in einem Experiment zur vereinfachten Bose-Einstein Kondensation in einer Oberflächenfalle.* Diploma thesis, University of Heidelberg (2003).

[220] W. Rohringer. *Stochastic Optimization in an Ultracold Atom Experiment.* Ph.D. thesis, Vienna University of Technology (2008).

[221] J. Reichel and V. Vuletic, eds. *Atom Chips* (Wiley-VCH Verlag GmbH & Co. KGaA, Weinheim) (2011).

[222] S. Schneider. *Bose-{{Einstein}} {Kondensation} in {einer} {magnetischen} {Z}-{Falle}.* Ph.D. thesis, Universit{ä}t Heidelberg (2003).

[223] T. Berrada, S. van Frank, R. Bücker, T. Schumm, J.-F. Schaff, and J. Schmiedmayer. Mach-Zehnder interferometry with number-squeezed Bose-Einstein condensates. *to be published in 2013* .

[224] D. A. Smith, S. Aigner, S. Hofferberth, M. Gring, M. Andersson, S. Wildermuth, P. Krüger, S. Schneider, T. Schumm, and J. Schmiedmayer. Absorption Imaging of Ultracold Atoms on Atom Chips. *Optics Express* 19 (2011), 8471. 1101.4206.

[225] J. Schmiedmayer. Guiding and trapping a neutral atom on a wire. *Physical Review A* 52 (1995), R13.

[226] J. D. Weinstein and K. G. Libbrecht. Microscopic magnetic traps for neutral atoms. *Physical Review A* 52 (1995), 4004.

[227] J. Denschlag and J. Schmiedmayer. Scattering a neutral atom from a charged wire. *Europhysics Letters* 38 (1997), 405.

[228] J. Denschlag, G. Umshaus, and J. Schmiedmayer. Probing a Singular Potential with Cold Atoms: A Neutral Atom and a charged Wire. *Physical Review Letters* 81 (1998), 737.

[229] J. Denschlag, D. Cassettari, A. Chenet, S. Schneider, and J. Schmiedmayer. A Neutral Atom and a Wire: Towards Mesoscopic Atom Optics. *Applied Physics B* 69 (1999), 291.

[230] J. Denschlag, D. Cassettari, and J. Schmiedmayer. Guiding Neutral Atoms with a Wire. *Physical Review Letters* 82 (1999), 2014.

[231] J. Reichel, W. Hänsel, and T. W. Hänsch. Atomic Micromanipulation with Magnetic Surface Traps. *Physical Review Letters* 83 (1999), 3398.

[232] R. Folman, P. Krüger, D. Cassettari, B. Hessmo, T. Maier, and J. Schmiedmayer. Controlling Cold Atoms using Nanofabricated Surfaces: Atom Chips. *Physical Review Letters* 84 (2000), 4749.

[233] W. Hänsel, P. Hommelhoff, T. W. Hänsch, and J. Reichel. Bose-Einstein condensation on a microelectronic chip. *Nature* 413 (2001), 498.

[234] H. Ott, J. Fortagh, G. Schlotterbeck, A. Grossmann, and C. Zimmermann. Bose-Einstein Condensation in a Surface Microtrap. *Physical Review Letters* 87 (2001), 230401.

[235] R. Folman, P. Krüger, J. Schmiedmayer, J. Denschlag, and C. Henkel. Microscopic atom optics: from wires to an atom chip. *Advances in atomic, molecular, and optical physics* 48 (2002), 263.

[236] J. Fortágh, C. Zimmermann, and J. Fortagh. Magnetic microtraps for ultracold atoms. *Reviews of Modern Physics* 79 (2007), 235.

[237] W. H. Wing. On neutral particle trapping in quasistatic electromagnetic fields. *Progress in Quantum Electronics* 8 (1984), 181.

[238] E. Majorana. Atomi Orientati Incampo Magnetico Variabile. *Nuovo Cimento* 9 (1932), 43.

[239] D. Pritchard. Cooling Neutral Atoms in a Magnetic Trap for Precision Spectroscopy. *Physical Review Letters* 51 (1983), 1336.

[240] J. Schmiedmayer. A wire trap for neutral atoms. *Applied Physics B* 60 (1995), 169.

[241] E. A. Hinds, M. G. Boshier, and I. G. Hughes. Magnetic Waveguide for Trapping Cold Atom Gases in Two Dimensions. *Physical Review Letters* 80 (1998), 645.

[242] M. Wilzbach, D. Heine, S. Groth, X. Liu, T. Raub, B. Hessmo, and J. Schmiedmayer. Simple integrated single-atom detector. *Optics Letters* 34 (2009), 259.

[243] J. Estève, C. Aussibal, T. Schumm, C. Figl, D. Mailly, I. Bouchoule, C. I. Westbrook, and A. Aspect1. Role of wire imperfections in micromagnetic traps for atoms. *Physical Review A* 70 (2004), 43629.

[244] T. Schumm, J. Estève, C. Figl, J.-B. Trebbia, C. Aussibal, H. Nguyen, D. Mailly, I. Bouchoule, C. I. Westbrook, and A. Aspect. Atom chips in the real world: the effects of wire corrugation. *European Physical Journal D* 32 (2005), 171.

[245] P. Krüger, L. Andersson, S. Wildermuth, S. Hofferberth, E. Haller, S. Aigner, S. Groth, I. Bar-Joseph, and J. Schmiedmayer. Potential roughness near lithographically fabricated atom chips. *Physical Review A* 76 (2007), 063621.

[246] Y. Japha, O. Entin-Wohlman, T. David, R. Salem, S. Aigner, J. Schmiedmayer, and R. Folman. Model for organized current patterns in disordered conductors. *Physical Review B* 77 (2008), 201407.

[247] J.-B. Trebbia, C. L. G. Alzar, R. Cornelussen, C. I. Westbrook, and I. Bouchoule. Roughness Suppression via Rapid Current Modulation on an Atom Chip. *Physical Review Letters* 98 (2007), 263201.

[248] I. Bouchoule, J.-B. Trebbia, and C. L. G. Alzar. Limitations of the modulation method to smooth wire-guide roughness. *Physical Review A* 77 (2008), 23624.

[249] P. Krüger, Z. Hadzibabic, and J. Dalibard. Critical Point of an Interacting Two-Dimensional Atomic Bose Gas. *Physiscal Review Letters* 99 (2007), 40402.

[250] S. Aigner, L. D. Pietra, Y. Japha, O. Entin-Wohlman, T. David, R. Salem, R. Folman, and J. Schmiedmayer. Long-range order in electronic transport through disordered metal films. *Science* 319 (2008), 1226.

[251] V. Yukalov, K.-P. Marzlin, and E. Yukalova. Resonant generation of topological modes in trapped Bose-Einstein gases. *Physical Review A* 69 (2004), 023620.

[252] O. Zobay and B. M. Garraway. Atom trapping and two-dimensional Bose-Einstein condensates in field-induced adiabatic potentials. *Physical Review A* 69 (2004), 23605.

[253] Y. Colombe, E. Knyazchyan, O. Morizot, B. Mercier, V. Lorent, and H. Perrin. Ultracold atoms confined in rf-induced two-dimensional trapping potentials. *Europhysics Letters* 67 (2004), 593.

[254] I. Lesanovsky, T. Schumm, S. Hofferberth, L. M. Andersson, P. Krüger, and J. Schmiedmayer. Adiabatic radio-frequency potentials for the coherent manipulation of matter waves. *Physical Review A* 73 (2006), 33619.

[255] M. Gring, M. Kuhnert, T. Langen, T. Kitagawa, B. Rauer, M. Schreitl, I. Mazets, D. A. Smith, E. Demler, and J. Schmiedmayer. Relaxation and prethermalization in an isolated quantum system. *Science* 337 (2012), 1318.

[256] J. H. Shirley. Solution of the Schrödinger Equation with a Hamiltonian Periodic in Time. *Physical Review* 138 (1965), B979.

[257] P. Amore and R. A. Sáenz. The period of a classical oscillator. *Europhysics Letters* 70 (2005), 425.

[258] C. L. G. Alzar, H. Perrin, B. M. Garraway, and V. Lorent. Evaporative cooling in a radio-frequency trap. *Physical Review A* 74 (2006), 53413.

[259] H. J. Metcalf and P. van der Straten. *Laser Cooling and Trapping* (Springer Verlag, Heidelberg Berlin New York) (1999).

[260] O. J. Luiten, M. W. Reynolds, and J. T. M. Walraven. Kinetic theory of the evaporative cooling of a trapped gas. *Physical Review A* 53 (1996), 381.

[261] I. E. Mazets, T. Schumm, and J. Schmiedmayer. Breakdown of Integrability in a Quasi-1D Ultracold Bosonic Gas. *Physical Review Letters* 100 (2008), 210403.

[262] I. Mazets. Dynamics and kinetics of quasiparticle decay in a nearly-one-dimensional degenerate Bose gas. *Physical Review A* 83 (2011), 043625.

[263] S. Kuhr, W. Alt, D. Schrader, M. Muller, V. Gomer, and D. Meschede. Deterministic Delivery of a Single Atom. *Science* 293 (2001), 278.

[264] N. Schlosser, G. Reymond, I. Protsenko, and P. Grangier. Sub-{p}oissonian loading of single atoms in a microscopic dipole trap. *Nature* 411 (2001), 1024.

[265] K. D. Nelson, X. Li, and D. S. Weiss. Imaging single atoms in a three-dimensional array. *Nature Physics* 3 (2007), 556.

[266] W. S. Bakr, J. I. Gillen, A. Peng, S. Fölling, and M. Greiner. A quantum gas microscope for detecting single atoms in a Hubbard-regime optical lattice. *Nature* 462 (2009), 74.

[267] J. F. Sherson, C. Weitenberg, M. Endres, M. Cheneau, I. Bloch, and S. Kuhr. Single-atom-resolved fluorescence imaging of an atomic Mott insulator. *Nature* 467 (2010), 68.

[268] T. Gericke, P. Wurtz, D. Reitz, T. Langen, and H. Ott. High-resolution scanning electron microscopy of an ultracold quantum gas. *Nature Physics* 4 (2008), 949.

[269] W. Vassen, C. Cohen-Tannoudji, M. Leduc, D. Boiron, C. Westbrook, A. Truscott, K. Baldwin, G. Birkl, P. Cancio, and M. Trippenbach. Cold and trapped metastable noble gases. *Reviews of Modern Physics* 84 (2012), 175.

[270] M. Gring. *Prethermalization in an Isolated Many Body System.* Ph.D. thesis, Technische Universiät Wien (2012).

[271] D. A. Steck. Rubidium 87 D Line Data. *available online at http://steck.us/alkalidata* (2008).

[272] C. Cohen-Tannoudji, J. Dupont-Roc, and G. Grynberg. *Atom-Photon Interactions* (Wiley, New York) (1992).

[273] G. Reinaudi, T. Lahaye, Z. Wang, and D. Guéry-Odelin. Strong saturation absorption imaging of dense clouds of ultracold atoms. *Optics Letters* 32 (2007), 3143.

[274] E. technologies. Low Light Technical Note 5: An Overview of the Ageing Characteristics of L3VisionTM Sensors. available from www.e2v.com.

[275] A. G. Basden, C. A. Haniff, and C. D. Mackay. Photon counting strategies with low-light-level CCDs. *Montly Notices of the Royal Astronomical Society* 991 (2003), 985.

[276] K. Kheruntsyan and P. Drummond. Quantum correlated twin atomic beams via photodissociation of a molecular Bose-Einstein condensate. *Physical Review A* 66 (2002), 031602.

[277] K. Kheruntsyan. Matter-wave amplification and phase conjugation via stimulated dissociation of a molecular Bose-Einstein condensate. *Physical Review A* 71 (2005), 053609.

[278] C. Savage, P. Schwenn, and K. Kheruntsyan. First-principles quantum simulations of dissociation of molecular condensates: Atom correlations in momentum space. *Physical Review A* 74 (2006).

[279] C. Savage and K. Kheruntsyan. Spatial Pair Correlations of Atoms in Molecular Dissociation. *Physical Review Letters* 99 (2007), 220404.

[280] A. Perrin, C. M. Savage, D. Boiron, V. Krachmalnicoff, C. I. Westbrook, and K. V. Kheruntsyan. Atomic four-wave mixing via condensate collisions. *New Journal of Physics* 10 (2008), 045021.

[281] P. Deuar, J. Chwedeńczuk, M. Trippenbach, and P. Ziń. Bogoliubov dynamics of condensate collisions using the positive-P representation. *Physical Review A* 83 (2011), 063625.

[282] A. Norrie, R. Ballagh, and C. Gardiner. Quantum Turbulence in Condensate Collisions: An Application of the Classical Field Method. *Physical Review Letters* 94 (2005), 040401.

[283] A. Norrie, R. Ballagh, and C. Gardiner. Quantum turbulence and correlations in Bose-Einstein condensate collisions. *Physical Review A* 73 (2006), 043617.

[284] P. Deuar and P. Drummond. Correlations in a BEC Collision: First-Principles Quantum Dynamics with 150 000 Atoms. *Physical Review Letters* 98 (2007), 120402.

[285] I. Carusotto, Y. Castin, and J. Dalibard. N-boson time-dependent problem: A reformulation with stochastic wave functions. *Physical Review A* 63 (2001), 023606.

[286] R. Bach, M. Trippenbach, and K. Rzążewski. Spontaneous emission of atoms via collisions of Bose-Einstein condensates. *Physical Review A* 65 (2002), 063605.

[287] P. Ziń, J. Chwedeńczuk, A. Veitia, K. Rzążewski, and M. Trippenbach. Quantum Multimode Model of Elastic Scattering from Bose-Einstein Condensates. *Physical Review Letters* 94 (2005), 200401.

[288] P. Ziń, J. Chwedeńczuk, and M. Trippenbach. Elastic scattering losses from colliding Bose-Einstein condensates. *Physical Review A* 73 (2006), 033602.

[289] S. Wang and W. Cassing. Explicit treatment of N-body correlations within a density-matrix formalism. *Annals of Physics* 159 (1985), 328.

[290] A. Vardi and J. Anglin. Bose-Einstein Condensates beyond Mean Field Theory: Quantum Backreaction as Decoherence. *Physical Review Letters* 86 (2001), 568.

[291] F. Rossi and T. Kuhn. Theory of ultrafast phenomena in photoexcited semiconductors. *Reviews of Modern Physics* 74 (2002), 895.

[292] A. Imambekov, I. Mazets, D. Petrov, V. Gritsev, S. Manz, S. Hofferberth, T. Schumm, E. Demler, and J. Schmiedmayer. Density ripples in expanding low-dimensional gases as a probe of correlations. *Physical Review A* 80 (2009), 1. 0904.1723.

[293] P. Deuar, T. Wasak, P. Zin, J. Chwedenczuk, and M. Trippenbach. Multimode number-squeezing in collisions of two Bose-Einstein condensates (2013), 12. 1301.3726.

[294] A. Marino, V. Boyer, and P. Lett. Violation of the Cauchy-Schwarz Inequality in the Macroscopic Regime. *Physical Review Letters* 100 (2008), 233601.

[295] J. Grond, G. von Winckel, J. Schmiedmayer, and U. Hohenester. Optimal control of number squeezing in trapped Bose-Einstein condensates. *Physical Review A* 80 (2009), 053625.

[296] F. Motzoi, J. Gambetta, P. Rebentrost, and F. Wilhelm. Simple Pulses for Elimination of Leakage in Weakly Nonlinear Qubits. *Physical Review Letters* 103 (2009), 110501.

[297] F. de Oliveira, M. Kim, P. Knight, and V. Buek. Properties of displaced number states. *Physical Review A* 41 (1990), 2645.

[298] T. Kinoshita, T. Wenger, and D. S. Weiss. A quantum Newton's cradle. *Nature* 440 (2006), 900.

[299] I. E. Mazets and J. Schmiedmayer. Restoring integrability in one-dimensional quantum gases by two-particle correlations. *Physical Letters A* 79 (2009), 61603.

[300] I. E. Mazets and J. Schmiedmayer. Thermalization in a quasi-one-dimensional ultracold bosonic gas. *New Journal of Physics* 12 (2010), 055023.

[301] P. Grisins and I. Mazets. Thermalization in a one-dimensional integrable system. *Physical Review A* 84 (2011).

[302] T. Caneva, T. Calarco, and S. Montangero. Chopped random-basis quantum optimization. *Physical Review A* 84 (2011), 022326.

[303] C. Gneiting and K. Hornberger. Bell Test for the Free Motion of Material Particles. *Physical Review Letters* 101 (2008), 260503.

[304] C. Simon and J.-P. Poizat. Creating Single Time-Bin-Entangled Photon Pairs. *Physical Review Letters* 94 (2005).

[305] J. Stenger, S. Inouye, A. P. Chikkatur, D. M. Stamper-Kurn, D. E. Pritchard, and W. Ketterle. Bragg spectroscopy of a Bose-Einstein condensate. *Physical Review Letters* 82 (1999), 4569.

[306] M. Kozuma, L. Deng, E. W. Hagley, J. Wen, R. Lutwak, K. Helmerson, S. L. Rolston, and W. D. Phillips. Coherent splitting of Bose-Einstein condensed atoms with optically induced Bragg diffraction. *Physical Review A* 82 (1999), 871.

[307] S. Cockburn, D. Gallucci, and N. Proukakis. Quantitative study of quasi-one-dimensional Bose gas experiments via the stochastic Gross-Pitaevskii equation. *Physical Review A* 84 (2011), 023613.

[308] M. Davis, P. Blakie, A. van Amerongen, N. van Druten, and K. Kheruntsyan. Yang-Yang thermometry and momentum distribution of a trapped one-dimensional Bose gas. *Physical Review A* 85 (2012), 031604.

[309] V. Yukalov, E. Yukalova, and V. Bagnato. Nonlinear coherent modes of trapped Bose-Einstein condensates. *Physical Review A* 66 (2002), 043602.

[310] A. Borzì, G. Stadler, and U. Hohenester. Optimal quantum control in nanostructures: Theory and application to a generic three-level system. *Physical Review A* 66 (2002), 053811.

[311] P. Doria, T. Calarco, and S. Montangero. Optimal Control Technique for Many-Body Quantum Dynamics. *Physical Review Letters* 106 (2011), 190501.

[312] R. Kosloff, S. Rice, P. Gaspard, S. Tersigni, and D. Tannor. Wavepacket dancing: Achieving chemical selectivity by shaping light pulses. *Chemical Physics* 139 (1989), 201.

[313] W. H. Press, S. A. Teukolsky, W. T. Vetterling, and B. P. Flannery. *Numerical Recipes in C++: The Art of Scientific Computing* (Cambridge Univ. Press, Cambridge), 2 ed. (2002).

[314] D. P. Bertsekas. *Nonlinear Programming* (Athena Scientific, Cambridge, UK) (1999).

[315] H. A. Rabitz, M. M. Hsieh, and C. M. Rosenthal. Quantum Optimally Controlled Transition Landscapes. *Science* 303 (2004), 1998.

Dipl.-Phys. Robert Bücker
Lerchenfelder Str. 88-90/15
1080 Wien, Austria
+43 681 10617144
rbueck@ati.ac.at

Curriculum Vitae

Personal Information

Date of Birth	February 20, 1983
Place of Birth	Bad Nauheim, Hesse, Germany
Citizenship	German
Employment	Projektassistent (FWF), TU Wien

Education

Summer 2011	Visiting PhD student (3 months) at Center for Ultracold Atoms, Massachusetts Institute of Technology (group of Vladan Vuletić)
2008 - 2012	PhD student at Atominstitut, Vienna / CoQuS graduate school
February 2008	Diplom/diploma in Physics (secondary subject Physiology, final grade 1.0)
2006 - 2007	Diploma thesis at Atominstitut, Vienna (group of Jörg Schmiedmayer) Thesis topic: *Fluorescence Imaging of Ultracold Atoms*
March 2005	Five-week internship ('Miniforschung') at DKFZ (German Cancer Research Center), research on physical models in radiation oncology (group of Uwe Oelfke)
October 2004	Vordiplom/pre-diploma (secondary subject Computer Science, final grade 1.6)
2002 - 2008	Physics studies, Ruprecht-Karls-Universität, Heidelberg
June 2002	Abitur, Viktoriaschule, Darmstadt (intensive courses Physics and Music, final grade 1.0)

Scholarships

2008	Admission to CoQuS doctoral programme
2006	Foreign scholarship (Austria) from Studienstiftung des Deutschen Volkes
2002	Admission to *Studienstiftung des Deutschen Volkes* (German National Academic Foundation)